A study of manganites using the Magnetorefractive Effect

Paul Richard Abernethy

PhD Thesis

Submitted: September, 2006

Department of Physics, The University of York

Abstract

This thesis is concerned with the magnetotransport properties of manganite perovskites. It explores the use of infrared (IR) spectroscopy to measure the Magnetorefractive Effect (MRE), which relates changes in the reflectivity in an applied field to changes in the high frequency conductivity. This measurement technique is contactless and it also provides spectral information over the IR wavelength range 2-25 μm. The results of experiments on bulk samples of $La_{1-x}Sr_xMnO_3$ (LSMO) ($x = 0$ to 0.3) and thin film samples of $La_{1-x}Ba_xMnO_3$ (LBMO) ($x = 0.14$ to 0.34) on $SrTiO_3$ (STO) substrates are presented. The IR spectra succeed in showing that the a.c. conductivity depends on the temperature, the magnitude of the applied magnetic field and the wavelength of excitation. A comparison of MRE and four–point probe measurements as a function of temperature for two LBMO thin film on STO shows that there is a strong correlation between the two measurement techniques. Simulations of the MRE in these materials show that their spectra are governed by the behaviour of the material's complex dielectric function, ε. In the thin films, the MRE was found to be enhanced at wavelengths where $\sqrt{\varepsilon} \rightarrow 1$. Its magnitude strongly depends on the growth parameters, the film thickness and the choice of substrate.

Contents

Abstract **i**

Contents **vii**

List of figures **xiv**

List of tables **xv**

List of accompanying material **xvi**

Acknowledgements **xviii**

Author's Declaration **xix**

1 Introduction **1**

1.1 Overview of the field of research 1

1.2 The aims of the research 3

1.3 Outline of the thesis 5

2 The properties of the mixed-valence manganites **8**

2.1 Introduction 8

2.2 Basic structure 9

2.3 The Jahn-Teller distortion 10

2.4 Magnetic phase changes 12

2.5 Carrier mobility in the mixed-valence manganites 14

2.5.1 Double exchange 14

2.5.2 The influence of the crystal structure on carrier mobility 16

2.5.3 An introduction to polarons 18

2.5.4 Competing theories of CMR 26

2.6 Infrared spectra and optical phonons 29

2.7 Thin film properties 33

2.7.1 Structural effects 34

2.7.2 CMR and the Curie temperature 35

2.7.3 Magnetic domains and grain boundary MR 40

2.7.4 Optical properties 49

2.8 Conclusions 50

3 The Magnetorefractive Effect 52

3.1 Introduction 52

3.2 Modelling the Magnetorefractive Effect 53

3.3 The complex dielectric function 54

3.3.1 The Drude term and the plasma frequency 54

3.3.2 The Resonance term 56

3.3.3 Magnetic field dependence 57

3.4 Reflection coefficients 58

3.5 Calculating the MRE(%) 59

3.6 Modelling results for a bulk manganite sample 59

3.6.1 Model parameters 59

3.6.2 Modelled IR spectra 61

3.6.3 Modelled MRE spectra 61

3.6.4 The consequences of changing parameter values on the IR and MRE spectra 63

3.7 Modelling the MRE in a thin film sample 69

3.7.1 Modelling an $SrTiO_3$ substrate 69

3.7.2 Modelling the thin film 73

3.7.3 Modelling the thin film-substrate system 75

3.7.4 Modelled MRE spectra 77

3.7.5 The consequences of changing parameter values on the IR spectra 79

3.8 Conclusions 85

4 Experimental Techniques 88

4.1 Introduction 88

4.2 Measuring the magnetorefractive effect 89

4.2.1 Room temperature measurements 89

4.2.2 The consequences of polarization 95

4.2.3 Temperature controlled MRE measurements 97

4.3 Additional experiments 106

4.3.1 Vibrating sample magnetometer measurements 106

4.3.2 Four-point probe measurements of CMR 106

4.3.3 Temperature controlled CMR measurements 107

4.3.4 Scanning Electron Microscope measurements 108

5 Experimental results for bulk samples of $La_{1-x}Sr_xMnO_3$ 110

5.1 Introduction 110

5.2 The samples 111

5.3 Surface topography 112

5.4 Magnetization measurements 113

5.5 IR and MRE spectra 115

5.5.1 Room temperature measurements 115

5.5.2 Temperature induced effects 122

5.5.3 Polarization dependence 124

5.5.4 Magnetization dependence 125

5.6 A comparison between four-point probe and MRE measurements of the magnetoresistance 127

5.7 Conclusions 129

6 Experimental results for thin film manganite samples 131

6.1 Introduction 131

6.2 The samples 132

6.3 The substrates $SrTiO_3$, $LaAlO_3$ and $NdGaO_3$ 133

6.3.1 Reflection spectra at room temperature 135

6.3.2 Reflection spectra below room temperature 140

6.4 IR and MRE spectra of thin manganite films 142

6.4.1 Samples of $La_{1-x}Ba_xMnO_3$ 142

6.4.2 Samples of $La_{1-x}Ca_xMnO_3$ 151

6.5 Temperature controlled experiments 154

6.5.1 Temperature controlled four-point probe measurements for LBMO_1155_STO and LBMO_1154_STO 155

6.5.2 Temperature controlled MRE measurements for LBMO_1155_STO and LBMO_1154_STO 160

6.6 Conclusions 168

7 Conclusions and future work **172**

Appendices **180**

A **180**

A.1 Modelling IR and MRE spectra using MathCAD 180

A.2 SEM images 183

A.3 Polarization dependence 183

A.4 Modelling the response of FELIX 183

A.5 Skin depth 184

A.6 Calibration of the magnet and power supply 185

B Electron-lattice interactions: a study of carrier dynamics at FELIX 188

B.1 Introduction 188

B.2 Experimental setup 189

B.2.1 A brief overview of FELIX 189

B.2.2 Pump-probe in a reflection geometry 190

B.2.3 Corrections for attenuation 192

B.2.4 Samples 193

B.3 Experimental results 193

B.3.1 Power dependence 193

B.3.2 Wavelength dependence 196

B.3.3 Temperature dependence 199

B.3.4 Field dependence 206

B.4 Interpreting the FELIX results 207

B.4.1 Understanding the positive and negative signals 207

B.4.2 Understanding the temperature dependence 210

B.4.3 Understanding the magnetic field dependence 214

B.5 Conclusions 215

Definitions 218

Bibliography 224

List of Figures

2.1 The basic perovskite structure. 9

2.2 Possible magnetic modes for the Mn cations 10

2.3 Energy level splitting in the mixed-valence manganites 11

2.4 Phase diagram for $La_{1-x}Sr_xMnO_3$ 12

2.5 Illustration of the orbital overlap in a plane of the perovskite structure 15

2.6 Schematic diagram of the double-exchange mechanism 15

2.7 Dependency of the phase transition temperature on the tolerance factor. 18

2.8 Temperature dependence of the resistivity for single crystals of $La_{1-x}Sr_xMnO_3$. 20

2.9 Typical phonon modes observed in the mixed-valence manganites 21

2.10 Schematic picture of the different types of polaron 22

2.11 Illustration of localization of an extended wave packet by potential fluctuations due to A^{3+} and B^{2+} ions and localization of an extended wave packet by fluctuations of the spin dependent potential. 24

2.12 Reflectivity spectra of $La_{1-x}Sr_xMnO_3$. 31

2.13 Phase diagram and temperature dependent magnetoresistance of tensile strained LBMO on STO. 37

2.14 Temperature dependence of magnetoresistance ratio for LBMO (x=0.05 to 0.3) thin films with thickness of 50 nm. 39

2.15 Resistivity and MR as a function of temperature for polycrystalline LCMO and LSMO films. 41

2.16 Kerr hysteresis loop of a polycrystalline LSMO film sample averaged over a number of grains. 43

2.17 Energy level diagram comparing the conduction band of Ni with $La_{2/3}Sr_{1/3}MnO_3$. 45

2.18 Topographic and MFM image of a $La_{0.77}Sr_{0.23}MnO_3$ film grown on a bicrystal $SrTiO_3$ substrate around an artificial grain boundary. 48

2.19 MFM images of a 60-nm-thick $La_{0.77}Sr_{0.3}MnO_3$ film above the Curie temperature. 49

2.20 Optical conductivity spectra for LCMO prepared on $SrTiO_3$, $LaAlO_3$ and $YAlO_3$. 50

3.1 Modelled IR reflection spectra for a generic bulk manganite sample 61

3.2 Modelled MRE spectra for a generic bulk manganite sample 62

3.3 The effect of changing the effective carrier mass on the modelled IR and MRE spectra for a generic bulk perovskite sample. 63

3.4 The effect of changing the oscillator strength on the IR spectra of a generic bulk perovskite sample 65

3.5 The effect of changing the damping factor γ in the Drude-like term of the complex dielectric function on the IR spectra of a generic perovskite sample 67

3.6 The effect of changing the damping factor γ_j in the resonance term of the complex dielectric function on the IR spectra of a generic perovskite sample 68

3.7 The effect of shifting the resonance position on the modelled IR spectra of a generic bulk perovskite sample 69

3.8 Modelled IR spectra using the three parameter models of the $SrTiO_3$ dielectric function for s- and p-polarized incident light. 72

3.9 Normalized experimental IR spectrum for an $SrTiO_3$ substrate 74

3.10 Modelled IR spectrum for a thin film perovskite 76

3.11 Modelled IR spectra for the film-substrate system 77

3.12 Modelled MRE spectra for a thin film perovskite sample 78

3.13 The effect of changing the effective carrier mass on the modelled IR spectra for a generic thin film perovskite sample 79

3.14 The effect changing the weighting of the substrate to film ratio in the dielectric function of a thin film sample has on the IR spectra 80

3.15 The effect changing the oscillator strength in the dielectric function of a thin film sample has on the IR spectra 81

3.16 The effect changing γ in the Drude term of the dielectric function of a thin film sample has on the IR spectra 82

3.17 The effect changing γ_j in the resonance term of the dielectric function of a thin film sample has on the IR spectra 83

3.18 The effect changing k_j in the resonance term of the dielectric function of a thin film sample has on the IR spectra 84

3.19 The relationship between the reflectivity and the dielectric function for a lorentzian oscillator. 86

4.1 Overhead view of the room temperature MRE experimental setup. 89

4.2 A close-up, side-view of the sample position for the room temperature MRE experiments. 93

4.3 IR spectrum for a Ag reference sample 94

4.4 Schematic showing the electric field vectors of light in reflection 95

4.5 Normalised reflectivity as a function of the angle of incidence θ for s- and p-polarized light. 96

4.6 The Joule-Thomson effect and its use in a micro-miniature refrigerator. 98

4.7 Schematic diagram showing the dimensions and connections for vacuum chamber of the micro-miniature refrigeration system. 99

4.8 Photograph showing the vacuum chamber 102

4.9 A comparison of the MRE spectra measured inside and outside of the vacuum chamber for a spin valve sample. 103

4.10 MRE spectra measured for a thin film $La_{0.7}Sr_{0.3}MnO_3$ sample. 104

4.11 MRE(%) spectra measured inside and outside of the vacuum chamber for a bulk $La_{0.8}Sr_{0.2}MnO_3$ sample. 105

4.12 Schematic of the setup for a Vibrating Sample Magnetometer 106

4.13 Schematic of the four-point probe experimental setup 107

4.14 Schematic of the temperature controlled CMR experimental setup. 108

5.1 Scanning electron micrograph of $La_{0.8}Sr_{0.2}MnO_3$ prepared by a) the sol-gel technique and b) the solid state reaction method. 113

5.2 Room temperature normalised magnetization curves for $La_{1-x}Sr_xMnO_3$ ($x = 0, 0.1, 0.2$ and 0.3) 114

5.3 Infrared spectra in randomly polarized light for $La_{1-x}Sr_xMnO_3$, $x = 0, 0.1, 0.2$ and 0.3 in zero applied magnetic field at room temperature. 116

5.4 Experimental and modelled IR spectra for $La_{0.9}Sr_{0.1}MnO_3$, $La_{0.8}Sr_{0.2}MnO_3$ and $La_{0.7}Sr_{0.3}MnO_3$ 120

5.5 Experimental and modelled MRE (%) spectra for $La_{0.9}Sr_{0.1}MnO_3$, $La_{0.8}Sr_{0.2}MnO_3$ and $La_{0.7}Sr_{0.3}MnO_3$ 121

5.6 Infrared spectra for $La_{0.8}Sr_{0.2}MnO_3$ 123

5.7 MRE(%) spectra for $La_{0.8}Sr_{0.2}MnO_3$ 124

5.8 MRE(%) as a function of wavelength for $La_{0.8}Sr_{0.2}MnO_3$ using p-polarized incident light at room temperature 125

5.9 Magnetization dependence of the MRE(%) at 10 μm for the LSMO samples. . . 126

5.10 A comparison between four-point probe and MRE measurements of the magnetoresistance in an $La_{0.8}Sr_{0.2}MnO_3$ sample. 128

6.1 Normalised infrared reflection spectra of the substrates $SrTiO_3$, $LaAlO_3$ and $NdGaO_3$ at room temperature and random polarization of the IR light. 135

6.2 Randomly polarized IR spectra for a NGO substrate for different rotations around the normal of the substrate surface 138

6.3 Normalised reflection spectra of the substrates at room temperature in perpendicular (s) and parallel (p) polarized light. 139

6.4 Modelled IR spectra using the four parameter model of the STO dielectric function for s- and p-polarized incident light. 140

6.5 Temperature dependence of the normalised reflection spectra of the substrates in randomly polarised IR light in zero applied field 141

6.6 IR and MRE spectra for the LBMO_1191 a-c samples. 143

6.7 IR and MRE spectra showing the thickness dependence for LBMO (x=0.3) for randomly polarized incident light. 145

6.8 Modelled IR spectra that shows the effect of changing the number of free carriers and the film/substrate contribution to the dielectric function. 147

6.9 A comparison between the MRE spectra predicted by our model and the MRE spectra measured experimentally for LBMO_1207_STO. 150

6.10 A comparison between the MRE spectra measured experimentally for LCMO_03A_LAO with the MRE spectra predicted by our model. 153

6.11 Plot of CMR(%) versus applied field for two LBMO samples as measured using the four-point probe method. 156

6.12 A plot of electrical resistance versus temperature for two LBMO samples as measured using the four-point probe method. 158

6.13 A plot of CMR(%) versus temperature for two LBMO samples as measured using the four-point probe method. 159

6.14 Temperature dependence of the infrared spectra for LBMO_1154_STO 160

6.15 A plot of MRE(%) versus wavelength for two LBMO samples for a variety of temperatures. 162

6.16 A comparison between temperature and field induced changes in the IR spectra for LBMO_1154. 163

6.17 A plot comparing the IR spectra and electrical resistance to changes in the CMR(%) and absolute MRE(%) versus temperature for two LBMO samples 165

6.18 A plot of the wavelength of the maximum positive MRE versus temperature . . 167

A.1 Current and voltage versus magnetic field characteristics of the electromagnet's power supply 187

B.1 Schematic illustrating the time structure of the FELIX electron beam. 189

B.2 A schematic showing a typical pump-probe experimental setup at FELIX for a transmission geometry 190

B.3 Power dependent measurements at 4K for several LBMO thin film samples. . . 194

B.4 Change in transmission as a function of temperature for $La_{0.7}Ca_{0.3}MnO_3$ close to T_C 195

B.5 Power dependence of the negative and positive signal for LBMO_1154 196

B.6 Wavelength dependent measurements for LBMO_1191a at FELIX. 197

B.7 Plots showing how the signal amplitude varies as a function of delay time and how the maximum signal amplitude varies with wavelength for the LBMO_1155 sample. 199

B.8 Temperature dependent measurements for LBMO_1155 at FELIX. 200

B.9 Amplitude of the negative signal for LBMO_1155 at 13.3 μm 200

B.10 Temperature dependent measurements for LBMO_1191a at FELIX. 202

B.11 Amplitude of the positive and negative signals observed for LBMO_1191a at 11.7 μm 202

B.12 Temperature dependent measurements for LBMO_1154 at FELIX. 203

B.13 Amplitude of the negative and positive signals observed for LBMO_1154 at 11.7 μm 204

B.14 Normalised equilibrium IR reflectivity for LBMO_1154 at a) 13.3 μm and b) 11.7 μm as a function of temperature. 205

B.15 Signal amplitude versus delay time at 4K for field cooled and zero field cooled samples of LBMO 206

B.16 Modelled profile for f(t) versus time 209

B.17 The change in sample temperature induced by the FELIX micropulse 212

List of Tables

2.1 Ionic radii of rare earth ions, alkali ions and transition metal ions in perovskite crystals 17

2.2 In-plane lattice constants in pseudo cubic notation, structures and lattice mismatches for a doping concentration of x=2/3 34

3.1 Parameters used in the modelling of a bulk manganite sample 60

3.2 A summary of the parameters used to model an STO substrate 73

3.3 Parameters used in the modelling of a thin film manganite sample 75

5.1 The bulk LSMO samples that were studied. 112

5.2 Parameters used in the modelling of a bulk LSMO samples 119

6.1 The thin film perovskite samples 134

6.2 Parameters used in the modelling of LBMO_1207 on STO 149

6.3 Parameters used in the modelling of LCMO_03A on LAO 152

A.1 Calibration data for the power supply of the electromagnetic 186

List of accompanying material

1 CD-ROM

Contents:

Bulk samples

This folder contains three subfolders named ‘LSMO’, ‘SEM images’ , and ‘Polarization dependence’:

LSMO This subfolder contains MathCAD simulations of the IR and MRE spectra for the bulk LSMO samples. Please refer to Appendix A.1 for details.

SEM images This subfolder contains SEM images of the bulk LSMO samples. Please refer to Appendix A.2 for details.

Polarization dependence This subfolder contains a MathCAD model that describes the polarization dependence of the reflectivity on the angle of incidence. Please refer to appendix A.3 for details.

Thin film samples

This folder contains three subfolders named ‘LBMO’, ‘LCMO’ and ‘FELIX model’:

LBMO This subfolder contains MathCAD simulations of the IR and MRE spectra for the thin film LBMO samples. Please refer to Appendix A.1 for details.

LCMO	This subfolder contains MathCAD simulations of the IR and MRE spectra for a thin film LCMO sample. Please refer to Appendix A.1 for details.
FELIX model	This subfolder contains a MathCAD model that simulates the response of thin film LBMO sample at FELIX. Please refer to Appendix A.4 for details.

Acknowledgements

I would like to thank all of the people who have helped me to complete this thesis:

Firstly, I would like to thank my supervisor, Sarah Thompson, for her invaluable advice and constant enthusiasm which has inspired me to greater heights. Her levels of patience and understanding are truly remarkable (and she also bakes a good cake).

I would also like to thank all of the people who have provided me with samples over the course of this project. In particular I would like to thank Rodrigo Marques, Kathryn Dörr and Peter Wright for providing me with all the samples I could wish for. I would also like to thank Gillian Gehring, Jon-Paul Wells, James Neal and Harry Blythe at the University of Sheffield, not only for providing me with samples, but also for helping me to develop a better understanding of the FELIX data.

I would like to thank all of the people at FELIX who helped me to acquire my data. In particular I would like to thank Jonathan Phillips, Damian Carder and Vinh for all of their help in setting up the experiments.

I would also like to thank all of the technical and administrative support staff in the Department of Physics at the University of York. In particular, I would like to express my gratitude to Dave Coulthard and Richard Armitage, who have helped me to get everything working time and time again. Furthermore, I would like to thank Moira Penny and Yvonne Cook for their help with all things administrative.

Last, but by no means least, I would like to thank my parents for putting up with me for a few more years. I appreciate all of the sacrifices you have made to allow me to complete this work.

Author's Declaration

I hereby declare that the work presented in this thesis is based on my own research, unless otherwise stated. It has neither been submitted nor accepted for any degree at this or any other university before.

Paul R. Abernethy
York 2006

Chapter 1

Introduction

1.1 Overview of the field of research

To paraphrase Coey *et al.* (1) "Mixed-valence manganites with the perovskite structure have been studied for almost 60 years. The manganites exhibit a variety of properties, such as ferroelectricity and colossal magnetoresistance (CMR), which makes them appealing to study both in terms of basic research and from a technological viewpoint. Research in this field has been driven by a desire to understand and exploit the large negative magnetoresistance effects which appear near and below the Curie temperature of these materials. The manganites are also of great scientific interest because they exhibit rich electronic and magnetic phase diagrams." Indeed, these compounds have been said by Coey 'to represent, in microcosm, the interplay of experiment, theory and application which is at the heart of solid state physics'.

The broad features of the mixed-valence manganese perovskites were described for polycrystalline ceramic samples by Jonker and van Santen (2), van Santen and Jonker (3) and Jonker (4) working at Phillips in the early 1950s (1). They recorded unexpected ferromagnetism in polycrystalline ceramic samples of (La,Ca)MnO_3, (La,Sr)MnO_3 and (La,Ba)MnO_3 (2) and a distortion from the perovskite lattice structure for compositions near 100% La (5), which was later attributed to the Jahn Teller effect. Furthermore they proposed that both trivalent and tetravalent manganese oxides belong under the terminology 'manganites'. Jonker and van Santen (2), and later Volger (6), found anomalies in the electrical conductivity at the Curie temperature, but CMR remained undiscovered. In

1955, Wollan and Koehler (7) supplemented the structural research for $La_{1-x}Ca_xMnO_3$ by applying the then very new technique of neutron scattering. They gave a remarkably complete description of the magnetic structure for all doping concentrations, which included the antiferromagnetic phases and the first evidence of charge ordering. Around this time Zener's (8; 9) and Anderson's and Hasegawa's (10) theory of the ferromagnetism in manganites, which is today known as the double exchange theory, had encountered widespread acceptance, and at that point research on manganites fell into a decline.

Interest in the mixed-valence manganites was revived in 1989 when Kusters *et al.* demonstrated a large magnetoresistance in $Nd_{50}Pb_{50}MnO_3$ (11). Within a short period colossal magnetoresistance was found in Ba doped (12), Ca doped (13) and Sr doped (14) lanthanum manganites following the preparation of high-quality thin films. Optimized films were found to show remarkable magnetoresistance effects near the Curie point (T_C) which were epitomized by Jin *et al* (15) as the 'colossal magnetoresistance' (CMR). The mixed-valence manganites are typically ferromagnetic and metallic for $x \approx 0.2 - 0.4$. However, above the Curie temperature many of the manganites become insulating, and this metal-insulator transition is unlike anything that occurs in ordinary ferromagnetic metals such as Fe, Co or Ni. There are competing theories for this behaviour, and of the detailed exchange mechanism responsible for the ferromagnetism. Also, the importance of electron-phonon coupling, and the possible existence of small polarons, is hotly debated (16). All of these topics will be discussed in the next chapter.

In 1995, the first magnetoresistive sensors were deployed in commercial magnetic memory systems which triggered the research on manganites for technological applications in addition to research about their fundamental properties (17). However, despite the fact that the magnetoresistive behaviour and the influence of intrinsic inhomogenities in these materials has been studied extensively both experimentally and theoretically for the last 15 years, a complete model of the magnetotransport properties in manganites has not yet been realised.

That same year (1995), Jacquet and Valet predicted that a change in the electrical conductivity of magnetic metallic multilayers would lead to a change in the optical reflectivity (and hence conductivity) if an external magnetic field is applied. They referred to this phenomenon as the Magnetorefractive Effect (MRE) and demonstrated it successfully

in infrared transmission spectra of ($Ni_{80}Fe_{20}$/Cu/Co/Cu) multilayers (18). Since then the MRE has been observed in many other metallic systems (18)–(22). In recent years, infrared spectroscopy has also proved to be an effective probe of the metal-insulator phase transition in manganites (23). Such spectra also yield information about phonon modes and local lattice distortions. The optical conductivity of doped lanthanum manganites has been studied extensively (24)–(43) as a function of temperature and pressure, but surprisingly, there has been very little work regarding the influence of an applied external magnetic field.

There is evidence for a Magnetorefractive Effect in manganites which exhibit colossal magnetoresistance (CMR). A first evidence of this magneto-optical effect can be found in the work of Loshkareva *et al.* (44), who in 1997 observed a decrease of the infrared transmittance through a single crystal of $La_{0.9}Sr_{0.1}MnO_3$ under the application of an external magnetic field of 0.8 T at 140 K . Two years later, Boris *et al.* (45) observed an increase in the reflectivity from a $La_{0.67}Ca_{0.33}MnO_3$ single crystal on the application of an external magnetic field, a phenomenon they referred to as the 'optical CMR effect' . In 2002, using infrared spectroscopy, Sukhorokov *et al.* (46) made the first measurements of the response of a thin film to an applied magnetic field. Their $La_{0.67}Ca_{0.33}MnO_3$ film, grown on a $LaAlO_3$ substrate, showed a 'giant' decrease in the transmittance, which could be related to the Magnetorefractive Effect.

Since 2003, the MRE has been studied by our Magnetic Materials Research Group at the University of York in thin film Ba, Sr and Ca doped lanthanum manganites and also in bulk Sr doped samples. In our first studies of bulk $La_{0.8}Sr_{0.2}MnO_3$, a direct correlation between the Magnetorefractive Effect and colossal magnetoresistance was demonstrated (47). This work has been extended to thin film systems, and the results and modelling of the magnetotransport in these materials is the subject of this thesis.

1.2 The aims of the research

The aims of the research presented in this thesis have evolved over the course of the project. By the time I started this project, our research group had already successfully shown quantitatively that there was a correlation between the giant magnetoresistance and

the MRE in $Co_{1-x}Ag_x$ granular systems (48). We, therefore, wanted to see if our MRE measurement technique could be extended to other magnetic materials. Initially we were interested to see if we could observe an MRE in bulk samples of $La_{1-x}Sr_xMnO_3$ that had been donated to us by R.F.C. Marques, a visiting student from the Instituto de Química de Araraquara in Brazil.

Interestingly, the bulk samples of $La_{1-x}Sr_xMnO_3$, did show a MRE. The aim then was to understand what the IR and MRE spectra were telling us about the magnetotransport properties of these materials. Consequently, I developed a model based upon the work of Boris *et al.* (24) that could simulate the experimental results, allowing me to understand the important features of the spectra.

In 2003, we were given a thin film sample of $La_{0.7}Ba_{0.3}MnO_3$ on a $SrTiO_3$ substrate by Professor Gehring's group at the University of Sheffield, the aim being to see how the IR and MRE spectra of such a high quality thin film sample compared to the bulk samples. The results took us all by surprise since the spectra were completely different from those observed in the bulk samples. The aim of the research then, therefore, was to understand what made the spectra so different in the thin film samples. I was fortunate in that I met P. Wright from QinetiQ at a conference on the mixed-valence manganites, and he was able to provide me with a wide range of thin film Ba and Ca doped lanthanum samples on which to experiment. Consequently, it has been possible to develop a model to explain the features of the thin film samples and establish the influence doping and the sample's thickness has on the spectra. Through the development of this model, I have been able to establish the cause of all of the main spectral features that are observed experimentally and this is one of the key findings of the work presented in this thesis. The model developed in this thesis is an extension and combination of models proposed by Boris *et al.* (24), who modelled the thin film contribution, and Gervais's (138) four-parameter model for a $SrTiO_3$ substrate.

As we shall see in the next chapter, the transport properties of the mixed-valence manganites are temperature dependent. This is due to the phase changes observed in these materials as a function of doping and temperature. When I first started looking at the MRE of the bulk and thin film samples, it was only possible to make measurements at room temperature, which, given the significant role that temperature plays in these mate-

rials, was unsatisfactory. Hence, a primary goal of the project was to develop the MRE experimental setup to allow us to make temperature controlled measurements.

The MRE offers the unique possibility of a contactless, and thus contamination free, probe of the magnetotransport properties of thin film manganite samples. A possible application of this experimental technique is as an instrument for industrial quality control testing of future CMR devices. An additional aim of the research, therefore, has been to investigate and evaluate the applicability of infrared spectroscopy to the characterisation of the magnetotransport properties in the thin film samples provided by QinetiQ.

1.3 Outline of the thesis

This thesis is structured as follows:

In the next chapter, I will discuss the properties of the mixed-valence manganites as they have been presented in the literature. Starting with a review of their basic structure, I will then discuss the magnetic phase changes observed in these materials before moving on to a discussion of various aspects of the carrier mobility in these materials, ranging from the influence the crystal structure has on the conductivity, to double-exchange and the concept of polarons. After a discussion on the possible origins of CMR in these materials, the chapter will conclude with a review of the properties of thin film manganite samples, paying particular attention to the influence the substrate has on the film's properties.

In Chapter 3, I will discuss the model that has been used to simulate the infrared and MRE spectra in bulk and thin film manganite samples. I will establish the origins of the model and will show how the complex dielectric function of these materials can be related to changes in their reflectivity through the inversion of the Fresnel equations. Initially I will discuss the applicability of such a model to bulk samples of $La_{1-x}Sr_xMnO_3$ ($x = 0.1$, 0.2 and 0.3). Once the basic model has been established, I will then discuss how the model needs to be adapted in order to successfully model the infrared and MRE spectra of thin film manganite samples, where the addition of a substrate greatly increases the complexity of the model. One of the advantages of simulating the infrared and MRE spectra of these materials is that it allows us to explore what happens when we change the values of certain parameters in the model, thus allowing us to establish how the various parameters relate

to one another. The consequences that changing the parameters in the model has on the spectra will be the topic of an extended discussion in this chapter.

In Chapter 4, I will introduce the reader to the various experimental methods I have used to characterise the magnetic and magnetotransport properties of bulk and thin film mixed-valence manganite samples. Most of the experimental techniques employed will be familiar to readers with a background in magnetism, for example hysteresis measurements made using a Vibrating Sample Magnetometer (VSM), four-point probe measurements of the magnetoresistance and measurements of the surface topography using a Scanning Electron Microscope (SEM). However, the majority of the measurements made for this thesis have been measurements of the Magnetorefractive Effect in the mixed-valence manganites, and it is likely that this experimental technique will not be familiar to the reader. This chapter, therefore, will start by introducing the reader to the basic MRE experimental setup. Since the mixed-valence manganites have such an interesting magnetic phase diagram that depends on the temperature as well as the amount of doping, a lot of time has been spent developing the basic MRE setup to allow us to make temperature controlled MRE measurements. The design considerations and problems associated with these temperature controlled measurements will be also be discussed.

In Chapter 5, I will present the results of a variety of experiments performed on bulk samples of $La_{1-x}Sr_xMnO_3$ ($x = 0.1$, 0.2 and 0.3). The chapter will begin with a brief description of the preparation techniques used to produce the samples before demonstrating with SEM images how the preparation technique influences the surface topography of the samples. After showing magnetization curves, I will then discuss how well the model introduced in Chapter 3 represents the real IR and MRE spectra obtained from these samples, and will demonstrate how it is the balance of the terms in the sample's complex dielectric function that determines the spectral features we observe experimentally. Towards the end of the chapter, I will compare the results obtained from traditional four-point probe measurements with those obtained using our MRE technique and I hope to convince the reader that the contactless MRE measurement technique is a viable alternate to the standard four-point probe method of measuring a sample's magnetoresistance.

In Chapter 6, I will present the experimental IR and MRE spectra for a variety of thin film manganite samples to determine how successful the model I have developed for the

thin film samples is at reproducing the experimental data. The chapter will begin with a brief description of the preparation techniques used to prepare the thin film samples before examining the IR spectra of the substrates. I will then present the IR and MRE spectra for a selection of our thin film samples, and observe how the substrate and the film's thickness influences the results. Towards the end of the chapter, I will present the results of temperature controlled MRE experiments on thin film samples of $La_{1-x}Ba_xMnO_3$. The results of these temperature controlled experiments will then be compared to temperature controlled four-point probe measurements of the magnetoresistance. By the end of the chapter I will demonstrate that, just as for the bulk samples, it is the balance of the terms in the complex dielectric function that determines the spectral features of these samples.

The thesis will be concluded in Chapter 7, where I will summarize the key findings of my work and I will identify avenues for future research in this field.

Chapter 2

The properties of the mixed-valence manganites

2.1 Introduction

A full literature review of the mixed-valance manganites is a daunting task. Since the revival of interest in these materials in the early 90's there has been extensive research into the properties of these materials and the number of publications in this field has grown at a very rapid rate. There have been several long review papers published by Coey *et al.* (1), Edwards (16) and Dagotto *et al.* (49) and these provide a good starting point for newcomers to the field.

The aim of this chapter is to familiarize the reader with some of the basic concepts that provide the foundation for this field of research. Hence, in this chapter I shall review the basic properties of the mixed-valence manganites, starting with their basic structure. The mixed-valence manganites are very interesting materials since they exhibit magnetic and structural phase changes as a function of temperature and doping. I shall then examine how these magnetic phase changes influence conduction. This will include a review of double exchange and the tolerance factor, as well as the formation of polarons. Differing theories explaining the colossal magnetoresistance in these materials will be outlined before we look at the optical response of these materials to an external stimulus. The chapter will close by considering the properties of thin films of these materials.

2.2 Basic structure

The mixed-valence manganese oxides can be regarded as solid solutions between end members such as $LaMnO_3$ and $SrMnO_3$ with formal valence states $La^{3+}Mn^{3+}O_3^{2-}$ and $Sr^{2+}Mn^{4+}O_3^{2-}$, leading to mixed-valence compounds such as $(La_{1-x}^{3+}Sr_x^{2+})(Mn_{1-x}^{3+}Mn_x^{4+})O_3$, with the relative fraction of Mn^{3+} and Mn^{4+} being controlled by 'x'. The nominal electronic configurations of the Mn^{3+} and Mn^{4+} are $3d^4$ and $3d^3$ respectively.

The manganese oxides have a structure similar to the cubic perovskite structure of $CaTiO_3$ and can exhibit charge ordering, orbital ordering and magnetic ordering. Chemically the system is characterized by the wide range of cations which can occupy the A-site in the perovskite structure (e.g. La, Pr, Nd and by substitution for these, Sr, Ca, Ba etc.), on the cube corner. A good way to regard the structure is as a cubic closed packed array formed of O^{2-} anions and large A cations, with the small B (Mn) cations in the octahedral interstitial sites (1). This structure can be seen in Figure 2.1.

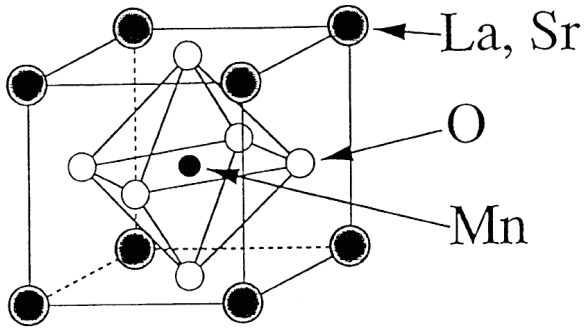

Figure 2.1: The basic perovskite structure. Taken from (1)

The magnetic ordering can occur in several magnetic modes. Some of the simplest magnetic modes are illustrated in Figure 2.2. Mode B is ferromagnetic (FM), but all the others are antiferromagnetic (AFM) and require an enlarged unit magnetic cell. Modes A, C and G consist of oppositely aligned FM planes of the type $\{001\}$, $\{110\}$ and $\{111\}$ respectively. Modes C and E can be combined into a composite CE mode composed of a chequerboard of alternating C and E blocks.

The charge and orbital ordering are prominent for values of $x \gtrsim 0.5$. The samples we

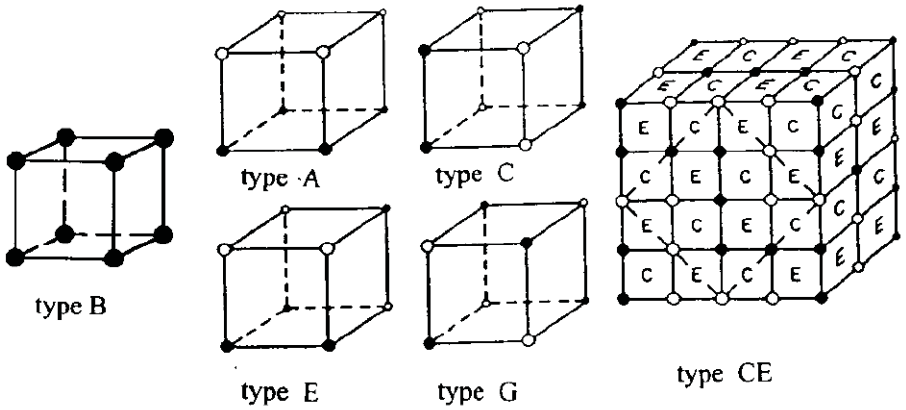

Figure 2.2: Some possible magnetic modes for the B-site cations in the perovskite structure (solid and open circles represent the two antiferromagnetic sublattices). Taken from (1).

have examined so far (see Chapters 5 and 6) are limited to $x \lesssim 0.3$, where neither charge nor orbital ordering is expected (16).

2.3 The Jahn-Teller distortion

In general, the $3d$ atomic levels are five-fold degenerate. The cubic crystal structure, illustrated in Figure 2.1, has an associated crystal field which partially lifts the five-fold degeneracy of the $3d$-orbitals of an isolated ion due to the six oxygen ions surrounding the manganese forming an octahedron. Analysis using the ligand field theory shows that the five-fold degeneracy is lifted into doubly degenerate e_g-orbitals ($d_{x^2+y^2}$ and $d_{3z^2-r^2}$) and triply degenerate t_{2g}-orbitals (d_{xy}, d_{yz} and d_{zx}). This can be seen in Figure 2.3. The energy difference between those two levels is usually expressed as 10 Dq (based on the traditional notation in the ligand field theory [Gerloch and Slade, 1973 (50)]). Estimations by Yoshida (51), suggest that 10 Dq is about 1.3–1.8 eV.

The valence of the Mn ions in this context is either four (Mn^{3+}) or three (Mn^{4+}) and their relative fraction is controlled through chemical doping. The spins of the four d-electrons associated with Mn^{3+} are aligned, due to Hund's first rule (maximum S), so the Mn^{3+} ions adopt a $t_{2g}^3 e_g^1$ configuration with spin, $S = 2$. This is shown in Figure 2.3.

The remaining degeneracy is due to the symmetry of the cubic crystal structure. To

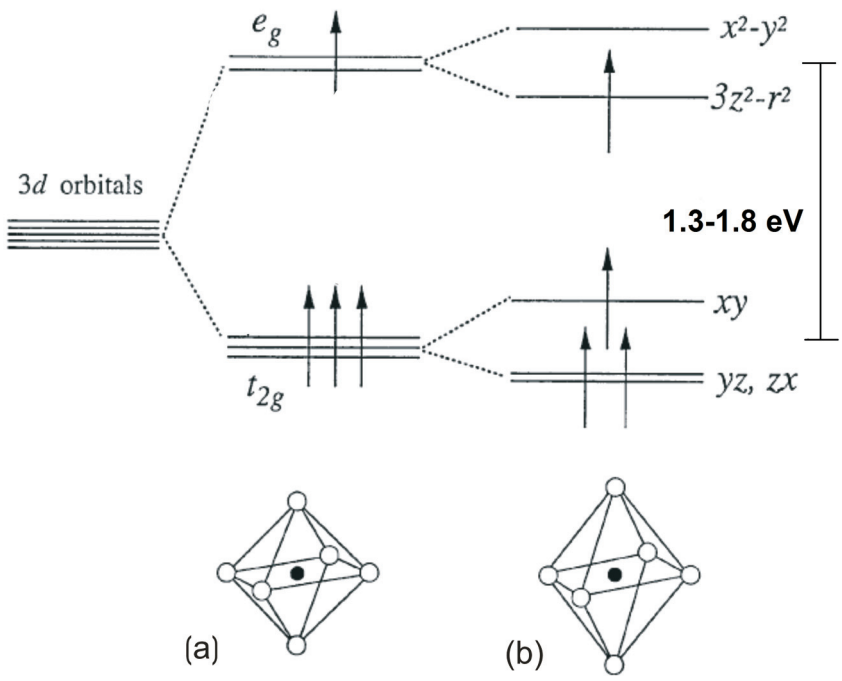

Figure 2.3: Field splitting of the five-fold degenerate atomic $3d$ levels into lower t_{2g} and higher e_g levels, (a) corresponds to a cubic environment while (b) corresponds to a tetragonal environment where $a = b \neq c$ known as the Jahn-Teller distortion. The estimated energy splitting between the t_{2g} and e_g levels is 1.3–1.8 eV (51). Taken from (52).

lift the degeneracy further, the oxygen octahedra surrounding each Mn ion can undergo two types of distortion. The first is a rotation and tilting due to the La^{3+} ion being smaller than the O^{2-} ion, the second is a tetragonal distortion, known as the Jahn-Teller distortion, where each octahedron is stretched along one of the axes in the basal plane (16). When the crystal structure is distorted into a tetragonal shape, the lattice spacing along one direction (say the z-axis) is changed relative to the other two (i.e. $a = b \neq c$, and as a consequence, the energy levels will change. For example, in such a case, the orbitals d_{yz} and d_{zx} would remain degenerate due to symmetry, but d_{xy} will have a different energy. The same will occur with the $d_{x^2+y^2}$ orbital (which has most of its relevant weight on the x-y plane) and the $d_{3z^2-r^2}$ orbital, which elongates along the z-axis. In Figure 2.3, a tetragonal splitting is shown for the case where the lattice spacing c is longer than $a(= b)$. The splitting would be opposite if c were shorter than $a(= b)$ (52). The distorted cubic structures observed in the paramagnetic phase (see below) are frequently orthorhombic, whereas the cubic structures in the ferromagnetic phase are typically rhombohedral (1).

2.4 Magnetic phase changes

The crystallographic and magnetic structures for the $(La_{1-x}Ca_x)MnO_3$ compounds were determined in 1955 by Wollan and Koehler (7) in a remarkably complete neutron and X-ray diffraction study as a function of Mn^{4+} content. In particular, the neutron data revealed a very rich magnetic phase diagram where, for different doping levels, antiferromagnetism can take different configurations (A, C, CE and G types {see Figure 2.2}) and can even coexist with ferromagnetism (B type). Figure 2.4 shows the magnetic phase diagram for the related compound, $La_{1-x}Sr_xMnO_3$ (for $x = 0$ to 0.6). This phase diagram was determined by Tokura and Tomioka (53) from data obtained by Urushibara *et al.* (54).

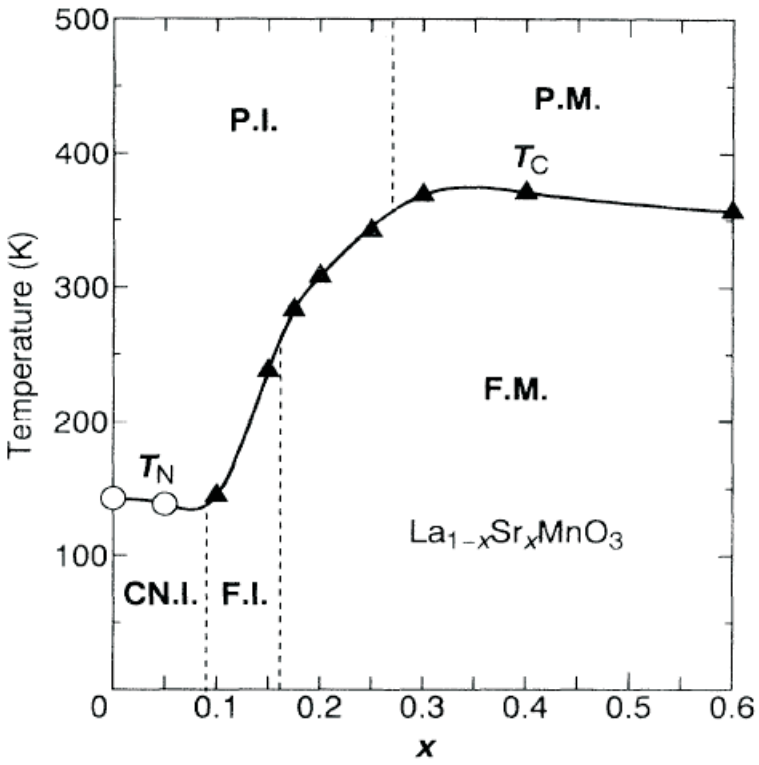

Figure 2.4: Phase diagram for $La_{1-x}Sr_xMnO_3$. PM, PI, FM, FI and CI denote paramagnetic metal, paramagnetic insulator, ferromagnetic metal, ferromagnetic insulator and spin-canted antiferromagnetic insulator states, respectively. Open circles and filled triangles are Néel temperature (T_N) and the Curie temperature (T_C) respectively. Taken from (54). I have studied bulk samples of $La_{1-x}Sr_xMnO_3$ with $x = 0$ to 0.3 (see Chapter 5)

.

From magnetization and susceptibility results, Jonker (4) concluded that the exchange is weakly positive (ferromagnetic) between two $3d^4$ Mn^{3+} ions, negative (antiferromag-

netic) between two $3d^3$ Mn^{4+} ions and positive between a $3d^4$ Mn^{3+} and a $3d^3$ Mn^{4+} ion. These measurements provided the first clear evidence for a ferromagnetic exchange interaction in an oxide.

At intermediate hole concentrations, the system is metallic even above T_C. At densities above $x = 0.5$, an interesting A-type antiferromagnetic metallic state is stabilized. [Actually this state is ferromagnetic within the planes and antiferromagnetic only between the planes.] However, at concentrations below $x = 0.26$, the region above T_C becomes paramagnetic and insulating. This unexpected property of a paramagnetic state, that transforms into a metal upon reducing the temperature, is a key property of all mixed-valence manganites (49). One would normally expect to observe metallic behaviour at high temperature acting as a precursor to the ferromagnetic metallic phase that is to be stabilized at low temperature.

It is normally assumed that at values of $x \approx 0.3$, the system is homogeneous. However, it has been argued by Moreo *et al.* (55) and Nagaev (56), that charge inhomogeneity is widespread in the manganites with a tendency for holes, produced by doping, to segregate into ferromagnetic clusters. Unfortunately, most quantitative work along these lines has employed models in which the long range Coulomb forces are neglected (16). This has led to unrealistic predictions of the macroscopic phase separations since it assumes that the ferromagnetic and metallic samples are single domain. The Coulomb interaction will tend to misalign the spins on longer length scales due to the electron-electron repulsion, thus allowing domains to form (55).

The phase changes are not limited to changing the temperature and/or the level of doping. A study by Asamitsu *et al.* (1995) (57) of $La_{1-x}Sr_xMnO_3$ ($x = 0.17$), which included resistivity, magnetostriction and x-ray diffraction measurements as a function of temperature and magnetic field, suggested that the structural phase transition observed in these materials could be induced, at a fixed temperature, by the application of a magnetic field. A more recent series of single-crystal neutron-diffraction experiments by Campbell *et al.* (1997) (58) have confirmed that this is the case.

Resistivity measurements, performed by Jonker in 1956 (4), revealed a strong correlation between electron transport and magnetic properties. He found that the resistivity is lowest for the $x \approx 0.3$ composition, which is in a ferromagnetic phase, whereas high

resistivities are associated with the antiferromagnetic compositions. A theoretical explanation for this behaviour, and the ferromagnetic exchange observed in these oxides, had been offered by Zener in 1951 (8; 9) in terms of his theory of indirect magnetic exchange between $3d$ atoms. This theory is often known as double exchange.

2.5 Carrier mobility in the mixed-valence manganites

The mobility of the free carriers in the mixed-valence manganites is governed by different mechanisms than the reader will perhaps be familiar with from materials that utilise metallic conduction. Hence, in this section we will discuss the conduction of the free carriers in these materials starting with the theory of double-exchange. We will then examine the effect the crystal structure can have on the carrier mobility before discussing perhaps the most interesting, and controversial, aspect of conduction in the manganites: the formation of polarons.

2.5.1 Double exchange

In the mixed-valence manganites, the three t_{2g} orbitals (see Figure 2.3) are all occupied. These electrons are considered localised and play no part in the electronic transport in these materials. The e_g electrons, however, are non-localised and it is these that are responsible for the electronic transport. This can be understood in terms of the orbital overlap between the t_{2g} orbitals and the oxygen orbitals (Figure 2.5). The t_{2g} orbitals overlap relatively little with the orbitals of the nearby oxygen or lanthanum ions, so these electrons tend to form a localized $t_{2g}^{3\uparrow}$ ion core. However, the e_g orbitals overlap directly with the p-orbitals of the oxygen neighbours, so they tend to form a σ^* antibonding band. i.e. the two orbitals overlap but the bonding between them is such that their electron densities tend to repel one another.

The e_g electrons move through the system by hopping from one ion to the next, with a hopping amplitude, t. Zener (8; 9) considered that the intra-atomic Hund rule exchange, J_H, was strong ($J_H \gg t$) and that the carriers do not change their spin orientation when hopping from one ion to the next, so they can only hop if the spins of the two ions are parallel. On minimising the total free energy of the system, Zener found that ferromagnetic

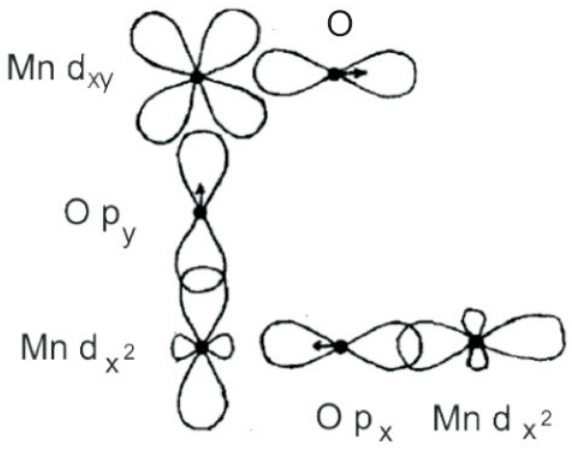

Figure 2.5: Illustration of the orbital overlap in a plane of the perovskite structure. The d_{xy} orbital (t_{2g} orbital) has little overlap with the 2p orbitals of the oxygen neighbours, whereas the d_{x^2} and d_{y^2} (e_g) orbitals overlap strongly with the oxygen p_x or p_y orbitals to form a σ^* antibonding band. Displacements of the oxygen atoms in the plane are indicated by arrows. After (1).

interactions are favoured when the magnetic atoms are fairly well separated and conduction electrons are present.

This theory was then applied to the manganese perovskites (9) with the aim of explaining the strong correlation between conductivity and ferromagnetism. Starting from the insulating antiferromagnetic $LaMnO_3$ end member, where electrons are localized on the atomic orbitals, Zener showed how the system should gradually become more ferromagnetic upon hole doping (i.e. by introducing Mn^{4+}, or increasing x). He considered the problem of the exchange between Mn^{3+} and Mn^{4+} ions via an oxygen ion and introduced the concept of the *simultaneous* transfer of an electron from the Mn^{3+} to the oxygen and from the oxygen to the neighbouring Mn^{4+} (Figure 2.6). Such a transfer was called *double exchange*.

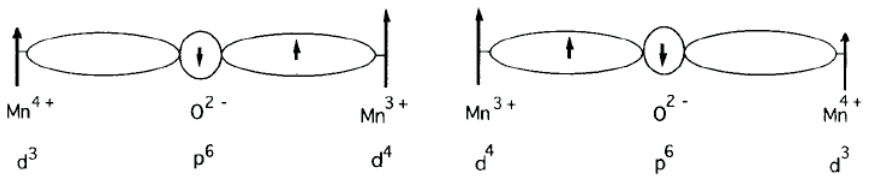

Figure 2.6: Schematic diagram of the double-exchange mechanism. The two states Mn^{3+} – Mn^{4+} and Mn^{4+} – Mn^{3+} are degenerate if the manganese spins are parallel. From (1).

In the case of magnetic atoms, the configurations Mn^{3+} – O^{2-} – Mn^{4+} and Mn^{4+} – O^{2-} – Mn^{3+} are degenerate if the spins of the two d shells are parallel, and the lowest energy of the system at low temperature corresponds to a parallel alignment of the spins of the two adjacent cations. This means that the hopping will only occur if the spins are aligned parallel to one another. In the ferromagnetic metallic region, the spin polarisation of the e_g electron due to the strong Hund coupling ensures that the spins are aligned and allows conduction by the double exchange mechanism. In the paramagnetic insulating phase, however, we are above the magnetic ordering temperature, T_C, and so the spins are randomly aligned i.e we have magnetic disorder. This means that above T_C the material is insulating since the hopping of the e_g electrons is severely limited by the random alignment of their spins.

In 1955, Anderson and Hasegawa (10) showed that the effective hopping for the electron to move from one Mn site to the next is proportional to the square of the hopping between the p-oxygen and the d-manganese orbitals. In addition, if the localized spins are considered classically with an angle ϕ between nearest-neighbours, the effective hopping becomes proportional to cos (ϕ/2). This is quite unlike superexchange where the coupling is proportional to cos ϕ. If $\phi = 0$, the hopping is largest, while if $\phi = \pi$, corresponding to an antiferromagnetic background, then there is no hopping. A quantum mechanical version of this process has been described by Kubo and Ohata (1972) (59).

2.5.2 The influence of the crystal structure on carrier mobility

The ease with which the e_g electrons can hop between the manganese ions (or hopping amplitude) also depends upon the bond angles and bond lengths between the A-site, oxygen and manganese ions. These two factors are controlled by the tolerance factor and the atomic radius of the A site ion, R_0. The tolerance factor, Γ, is defined as:

$$\Gamma = \frac{1}{\sqrt{2}} \frac{d_{R_0-O}}{d_{Mn-O}} \approx \frac{1}{\sqrt{2}} \frac{< r_A > + r_O}{< r_{Mn} > + r_O} \tag{2.1}$$

Here d_{R_0-O} is the distance between the A-site, where the trivalent or divalent non-Mn ions are located, to the nearest oxygen and d_{Mn-O} is the shortest Mn-O distance; $< r_A >$ is the mean radius of the A-site cation, r_O is the radius of the oxygen ion and r_{Mn} is the radius of

the manganese ion. Since for an undistorted cube with a straight Mn-O-Mn link, d_{R_0-O} = $\sqrt{2}$ and d_{Mn-O} = 1 in units of Mn-O distance, then $\Gamma = 1$ in this perfect system. However, the substitution of divalent ions for trivalent ions (e.g. the substitution of strontium for lanthanum) distorts the perfect cubic structure, reducing d_{R_0-O}. Hence, the tolerance factor becomes less than unity as R_0 changes, and the Mn-O-Mn bond angle, ϕ, becomes less than $180°$. As Γ decreases, there is an increase in charge localization as there is a reduction in carrier mobility or conduction bandwidth (W). Although the Mn-Mn distance is reduced in this situation, the hopping amplitude is also reduced. This is counterintuitive since one would expect that having the Mn ions closer together would increase the hopping between them. However, the hopping amplitude is not only proportional to the distance between the Mn and oxygen ions, but also to $cos(\phi)$ due to the fact that it is the p-orbital of the oxygen that is involved in the process. If the p-orbital points toward one of the manganese ions, it cannot point toward the other one simultaneously for $\phi \neq 180°$ (49).

Table 2.1 shows the average ion radii of several commonly used rare earth ions, dopants and transition metal ions that are used to produce perovskite samples. These values can be substituted in equation 2.1 to calculate the tolerance factor.

Rare Earth ions		Dopants		Transition metal ions	
Y^{3+}	$1.19\mathring{A}$	Ca^{2+}	$1.34\mathring{A}$	Mn^{3+}	$0.645\mathring{A}$
La^{3+}	$1.34\mathring{A}$	Sr^{2+}	$1.44\mathring{A}$	Mn^{4+}	$0.530\mathring{A}$
Pr^{3+}	$1.29\mathring{A}$	Ba^{2+}	$1.61\mathring{A}$	Fe^{3+}	$0.645\mathring{A}$
Nd^{3+}	$1.27\mathring{A}$	Pb^{2+}	$1.49\mathring{A}$	Fe^{4+}	$0.590\mathring{A}$
Sm^{3+}	$1.24\mathring{A}$	Cd^{2+}	$1.31\mathring{A}$	Ti^{3+}	$0.605\mathring{A}$
Gd^{3+}	$1.22\mathring{A}$	Sn^{2+}	$1.20\mathring{A}$	Ni^{3+}	$0.690\mathring{A}$

Table 2.1: Ionic radii of rare earth ions, alkali ions and transition metal ions in perovskite crystals with an oxygen ion radius of $1.40\mathring{A}$. Taken from (60)

In Figure 2.7 we see the how the Curie temperature changes depending on the tolerance factor. From the figure, it is interesting to note that although Ba has a larger ionic radius than Ca and Sr, Ba doped $LaMnO_3$ has a Curie temperature that lies between that measured for LCMO and LSMO. There is still some debate about the extent of the effect the ionic radii have on the physical properties of the crystal. For example, while Attfield *et al.* (62) maintain that the transition temperature shows a linear dependence with the A-site cation radius distribution, others, like García-Muñoz *et al.* (63), have demonstrated using neutron diffraction data on $La_{2/3}A_{1/3}MnO_3$ (A=Sr, Ca), that the Mn-O bond length is actually

independent of the ionic radius and it is only the bond angle that is changed, and further it is this change in bond angle that is responsible for the differing transition temperatures. On the other hand, a systematic analysis of Mn-O bond lengths versus average A-site ionic radius by Radaelli *et al* (64) using transport and neutron diffraction data has shown that increasing the static MnO_6 distortion, results in an associated increase in insulating behaviour and a decrease in T_C.

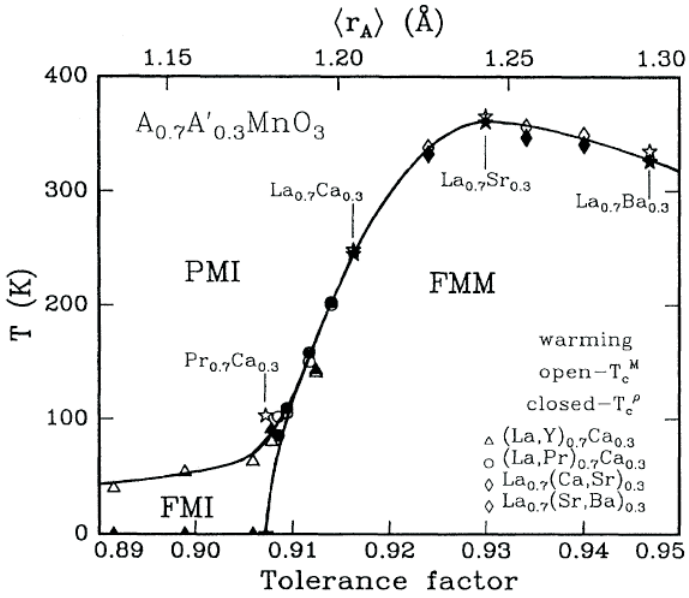

Figure 2.7: Dependency of the phase transition temperature on the tolerance factor. Taken from (61)

It is clear from Figure 2.7 that the tolerance factor plays a crucial role in determining the transition temperature of doped lanthanum manganites. It is not clear, however, whether this is due to changes in the ionic radius modulating the bond lengths or whether it is the change to the bond angles that is more important.

2.5.3 An introduction to polarons

While Zener's theory of double exchange has been very successful in explaining the conductivity of the manganites in the ferromagnetic state, the transport observed in the paramagnetic state cannot be explained by this theory. Also, since the revival of interest in this field in the mid-1990's, it has been revealed that double exchange by itself is insufficient to explain several of the properties of the mixed valence manganites (65). In

particular, colossal magnetoresistance and the 'stabilization of the competing ferromagnetic and paramagnetic phases' near T_C (49), cannot be fully accounted for by this theory. To explain colossal magnetoresistance new concepts have had to be introduced: strong electron-phonon coupling and the formation of polarons.

2.5.3.1 Electron phonon coupling

Interest in the mixed-valence manganites revived in the 1990s following the preparation of optimized thin films which showed remarkable magnetoresistance effects near the Curie point (T_C). The first study of the mixed-valence manganese perovskites by Santen and Jonker (3) and Jonker (66), on ceramic samples of $(La_{1-x}A_x)Mn0_3$ (A = Ba, Ca or Sr), reported resistivity measurements as a function of temperature and composition. As Coey *et al.* noted (1), the main result of this research was the striking correlation between the magnitude of the resistivity and the magnetic state of the compounds. Outside the ferromagnetic concentration range, resistivities are high and are thermally activated, but a resistance anomaly appears around T_C for the ferromagnetic compositions, where there is a transition from thermally activated conduction (polaron hopping, see below) to metallic-like conduction (via double exchange). An example of the resistivity as a function of x and temperature for $La_{1-x}Sr_xMnO_3$ can be seen in Figure 2.8.

In Figure 2.8, the gradient of the resistivity versus temperature curve can tell us a lot about the state of the material at a given temperature. For $x \lesssim 0.1$ the gradient, $d\rho/dT < 0$, is consistent with insulating behaviour. As can be seen in Figure 2.4, for this range of doping, the material is indeed insulating. As x is increased beyond $x \gtrsim 0.15$, we observe that $d\rho/dT > 0$ for temperatures $T \leqslant T_C$, signifying that the sample is exhibiting metallic behaviour, as we would expect from reference to Figure 2.4. This all changes above T_C, where we observe a return to an insulating state. From Figure 2.8, it is clear that the Curie temperature, T_C is vitally important. Not only is there a change in the resistivity of the sample, often of more than an order of magnitude, but there is also a change in the magnetic phase of the sample as we go through the metal-insulator transition.

'The magnitude of the resistivity in the paramagnetic phase', observed in Figure 2.8, 'cannot be understood in terms of double exchange alone'. This conclusion was arrived at by Millis *et al.* (65) who presented estimations of the critical Curie temperature and of

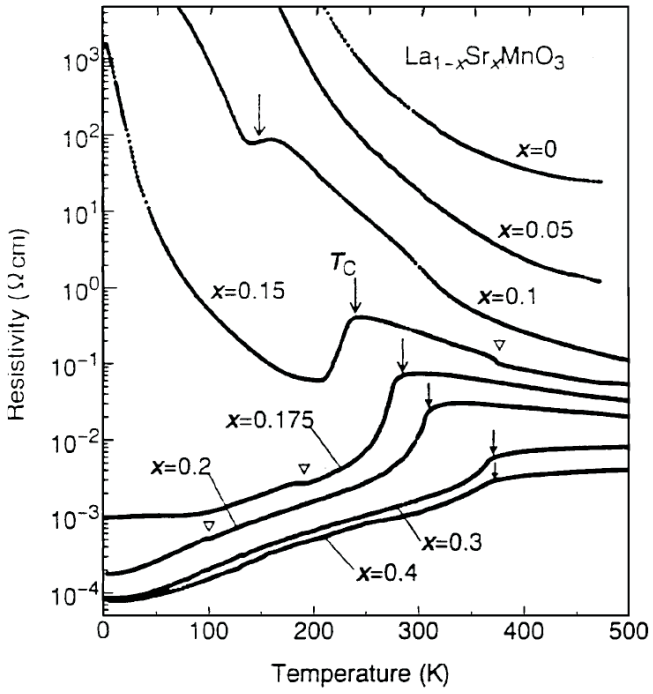

Figure 2.8: Temperature dependence of the resistivity for single crystal $La_{1-x}Sr_xMnO_3$. Arrows indicate the Curie temperature. Open triangles indicate anomalies due to structural transitions. For more details see Urushibara *et al.* (54). From (49).

the resistivity using the double exchange framework. With regard to the ferromagnetism, their calculations for a model that only had a large Hund coupling between the e_g and t_{2g} electrons for an interaction, led to a T_C prediction between 1100 and 3500K. This is an order of magnitude higher than the experimental results. Thus, it was argued that double exchange produces the wrong T_C by a large factor. Millis *et al.* also found a resistivity that grew as the temperature decreased (i.e. insulating behaviour) even below T_C. For this reason Millis *et al.* concluded that a model based only on large J_H is not adequate for the manganites. They argued that the double exchange framework needs to be extended to include coupling between the electrons and the local phonon modes, which arises due to the Jahn-Teller splitting of the Mn^{3+} ion.

The local phonon modes are related to the lattice degrees of freedom. As demonstrated by Edwards (16), the oxygen octahedra can distort in three ways, normally labelled Q_1, Q_2 and Q_3. Q_2 and Q_3, shown in Figure 2.9, represent the Jahn-Teller distortion of the basal plane and an octahedral stretching mode respectively. Q_1 is a breathing mode that incorporates Q_2 and Q_3 simultaneously. The Q_1 mode occurs due to the presence of two

formally different valence states, Mn^{3+} and Mn^{4+}. The Q_2, Jahn-Teller, mode is usually regarded as the most important and was emphasized by Millis *et al.* (65)

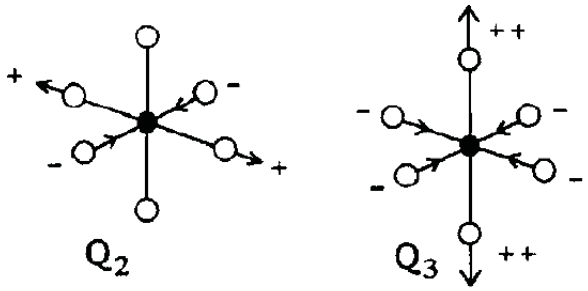

Figure 2.9: Typical phonon modes observed in the mixed-valence manganites. Q_2 is the basal-plane distortion mode and Q_3 is the octahedral stretching mode. Adapted from (16).

2.5.3.2 The formation of polarons

Edwards (16) describes a polaron as follows:

'For a sufficiently strong coupling to the local phonon modes, an electron can produce a strong localized distortion of the lattice if the bare bandwidth is narrow enough. This distortion moves with the electron and the whole structure is called a small polaron.'

In essence, if there is strong electron-phonon coupling, the free-carriers can become trapped and we will observe an increased resistance in the sample. Such a change in resistance is observed at the metal-insulator transition. Above T_C, the carriers are speculated to be bound in polarons, but below T_C this is thought not to be the case. Millis *et al.* believe that this is due to the fact that the criterion for polaron formation (narrow bandwidth) is only just satisfied, thanks to double exchange, as the system enters the paramagnetic state. In the low temperature ferromagnetic state, where small polarons cannot form, the system is metallic and the electron-phonon interaction merely produces a small enhancement of the quasi-particle mass; the quasi-particles in this Fermi liquid are sometimes called large polarons. As T_C is approached, small polarons are formed and their motion is governed by an activation energy that is related to the polaron binding energy.

According to Young Sun *et al.* (67), the carriers are trapped in localized states as small polarons in the paramagnetic phase due to the incorporation of three different localization

features. The first is associated with the strong electron-phonon coupling described above. The second is due to variations in the Coulomb potential due to the presence of trivalent and divalent ions in the lattice. This may be comparable to the one-electron bandwidth and can lead to Anderson localization (68). The third is magnetic localization due to spin disorder on an interatomic scale ($\sim$ 1 nm) in the paramagnetic phase. The carriers can become trapped in regions that are locally ferromagnetic within the paramagnetic phase.

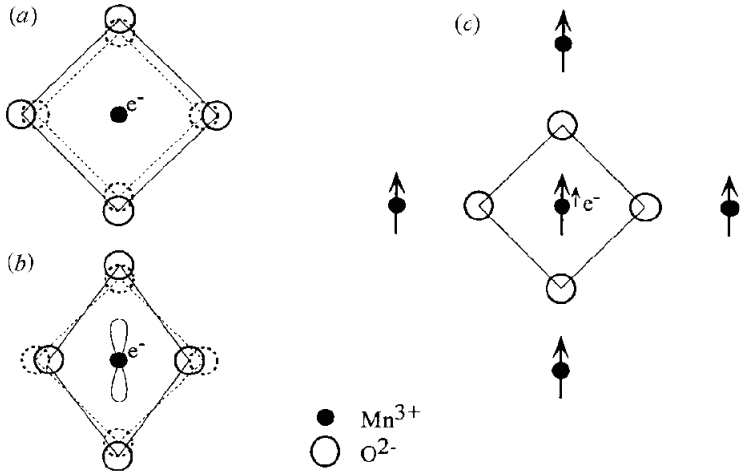

Figure 2.10: Schematic picture of (a) a small dielectric polaron, (b) a Jahn-Teller polaron and (c) a magnetic (spin) polaron. Taken from (1)

Hence, polarons are thought to take one of three forms (see Figure 2.10). The first is a dielectric polaron where the electron bears with it a dilation of the MnO_6 octahedron associated with the breathing mode (Figure 2.10a). The second is the Jahn-Teller polaron (Figure 2.10b) where the electron carries with it an axial distortion of the MnO_6 octahedron. The third is a magnetic (spin) polaron (Figure 2.10c) where there is a ferromagnetic polarisation of the surrounding manganese core spins.

When polarons were first introduced they were a purely theoretical construct. However, there is a growing amount of observational evidence confirming the existence of polarons in a variety of doped lanthanum manganites. For example, Louca *et al* (69) and Billinge *et al.* (70), have both observed lattice polaron formation when they used pair-distribution-function analysis of neutron diffraction data for samples of $La_{1-x}Sr_xMnO_3$ (x<0.4) and $LaCaMnO_3$, respectively. Tyson *et al.* (71), have observed a a significant change in the local structure of $La_{2/3}Ca_{1/3}MnO_3$ as they heated the sample from 80K to

above T_C (270K) which they argued was consistent with proposed small polaron related local Jahn-Teller distortions for $T>T_C$.

There is also optical evidence for the Jahn-Teller effect. Kaplan *et al.* (72) studied the optical properties of $Nd_{0.7}Sr_{0.3}MnO_3$ and found that the data are consistent with models like Millis *et al's* that include both double exchange and the Jahn-Teller effect on the Mn^{3+} e_g levels.

2.5.3.3 Magnetic polarons

The importance of the magnetic phase changes to the material properties of the mixed-valence manganites makes the study of this type of polaron particularly relevant. The concept of a magnetic polaron, with reference to the mixed-valence manganites, was first introduced by de Gennes in 1960 (73). The basic premise of a magnetic polaron (also, occasionally, referred to as a ferron) is not that difficult to visualize. As discussed above, a magnetic polaron consists of a carrier (either an electron or a hole, or indeed a wavepacket of electrons/holes (68)), which becomes localized in the paramagnetic phase. This carrier (or carriers) will have a certain spin alignment. Once trapped the carrier then spin-polarizes the electrons around it, creating a volume in the paramagnetic phase that is locally ferromagnetic.

Electron transfer with spin memory is an essential ingredient for an understanding of the transport properties of mixed-valence manganites, but something more is needed to account for the metal-insulator transition near the Curie point. The change of conduction regime below T_C appears to be brought about by the onset of ferromagnetism. As the temperature decreases, the magnetization increases and the resistivity drops. However, in the paramagnetic phase, the double exchange is limited due to the random alignment of the Mn spins. Double exchange requires the spins to all be aligned. However, experimental results suggest that the conduction bandwidth is comparable in the FM and PM regions (74) meaning that some other process is assisting the conduction in the paramagnetic regime.

Coey *et al.* (68) have suggested that the electrons in the PM phase may be localized in ferromagnetic wave packets. It is possible for an electron wave packet of extent ξ to be weakly localized by the variations in the Coulomb potential due to A^{3+} and B^{2+} ions,

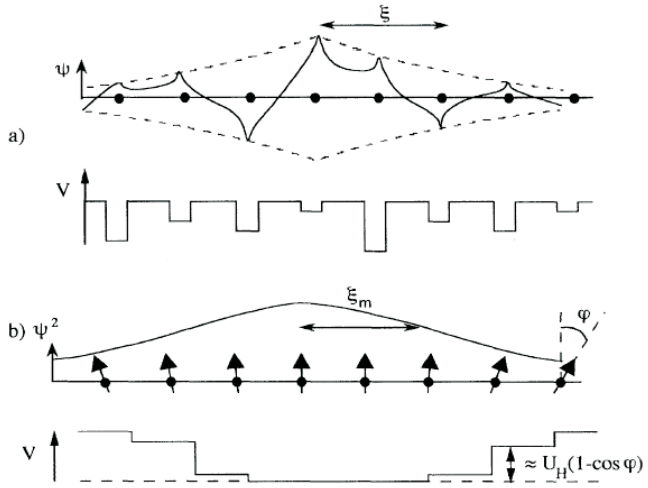

Figure 2.11: Illustration of (a) localization of an extended wave packet by potential fluctuations due to A^{3+} and B^{2+} ions and (b) localization of an extended wave packet by fluctuations of the spin dependent potential. Together these fluctuations produce an immobile large magnetic polaron. Electron transport is by individual electrons tunnelling or hopping from one wave packet to the next across potential barriers at the edges. Taken from (68)

as indicated in Figure 2.11a. The $e_g\uparrow$ electrons can be trapped further by fluctuations in the spin-dependent potential due to local deviations from ferromagnetic order. When the electrons are already trapped, the potential well is deepened by local deviations from collinearity on the periphery of the wave packet (Figure 2.11b) where there are fewer electrons and weaker FM interactions. Coey *et al.* believe that lattice modes play some part in triggering magnetic localization, for localization is more probable for larger cations, and varies with Mn-O-Mn bond lengths.

The wave packet in Figure 2.11b may be regarded as a 'large spin polaron' or a 'giant spin molecule' but it is thought unlikely that this entity can diffuse as a whole. Instead, individual electrons will hop or tunnel across the surface barriers between one wave packet and the next (68). Hence, in the PM regime, one can envision many such wave packets, with the electronic conduction occurring as electrons hop from one immobile FM cluster to the next. For this to occur, there would need to be some coherence between the wave packets, i.e. to preserve spin and enable DE to occur, the wave packets would need to have the same spin alignment. The application of an external magnetic field should cause more of these wave packets to align in the same direction as the applied field. A larger applied field will result in more of these clusters aligning with the field, thus facilitating

the conduction due to DE.

Theoretical models based upon Monte Carlo calculations in a 3D lattice model by Hongsuk *et al.* (75) have clearly demonstrated the formation of magnetic polarons with short-range ferromagnetic ordering in the paramagnetic state. Moreover, the ferromagnetic correlation length was estimated to be $3 - 4$ lattice spacings which is in good agreement with recent neutron scattering experiments by De Teresa *et al.* (76) who used Small-Angle polarized Neutron Scattering (SANS) to estimate the size of the ferromagnetic clusters in the paramagnetic state. De Teresa detected the spontaneous formation of localized 12Å magnetic clusters above T_C that, on application of a magnetic field, were found to grow in size, but decrease in number, as the field was increased.

Varma (77) has used a ferromagnetic spin-polaron picture to estimate the ferromagnetic correlation length, ξ. Using the approximation $\xi \approx (at/T)^{3/5}$, Varma estimated that at the temperature range of the paramagnetic state, in particular at a room temperature of $\sim$ 300 K, the size of the spin polaron is a few lattice spacings. Varma suggested that this implies that the spin polarized carriers can be trapped into local ferromagnetic surroundings due to the spatially fluctuating spin correlations, resulting in the formation of the magnetic polarons in the paramagnetic phase.

It is known that magnetism, electronic transport and crystal structure are closely linked in the manganites due to the very nature of the magnetic interaction, i.e. double exchange. Also, it has been shown that Jahn-Teller polarons play an important role in the Ca-doped compounds (78). A dynamic Jahn-Teller effect is known to accompany Mn^{3+} - Mn^{4+} transitions during electron hopping and Viret *et al.* (79) believe that this could create dynamically fluctuating regions of varying density on the time scale of the neutron-matter interaction ($\approx 10^{-11}$ s).

From a structural point of view, Jahn-Teller polarons and magnetic clusters are difficult to study, due to their local and dynamic nature. However, diffraction techniques have been successfully used, not only to determine the average structural and magnetic properties of the manganese perovskites (structural phase transitions, 'tuning' of the electronic bandwidth, effects of disorder, etc.), but also to study the more unusual and local features of these systems (80). For example, Radaelli *et al.* (80) have used the study of neutron diffraction data to allow them to determine the size and abundance of the magnetic clus-

ters in the PM phase. Radaelli *et al.* found that the integrated diffuse intensity was almost constant above T_C, and interpreted this as being indicative of the presence of stable magnetic clusters, 5–10 Å in size, well above T_C. This is in good agreement with the results previously obtained, in a narrower temperature range, using inelastic neutron scattering by Lynn *et al.* (81) and the SANS results of De Teresa *et al.* (76).

Viret *et al.* (79) also had to develop a model that described an average magnetic coherence that extended over a number of Mn spins in order to get a good fit to their data. Even at temperatures 100 K above T_C, they found that the magnetic coherence still extended over groups of about 10 Mn ions. Viret *et al.* believe that it is possible that three or four associated charge carriers are delocalised on this scale, thereby mediating the double-exchange interaction. Viret *et al.* have ascribed transport above T_C to electron hopping between small delocalised regions, which could be of the variable range hopping (VRH) type (82). Since the ferromagnetic exchange in these systems is mediated by the charge carriers, Viret *et al.* think that the exceptionally large magnetic coherence at high temperatures and the long magnetic correlation range could be an indication in favour of a VRH conduction above T_C between magnetically aligned clusters.

2.5.4 Competing theories of CMR

As discussed above, electron-phonon coupling and the formation of polarons seem to be required to understand the CMR observed in the mixed valence manganites. However, the type of polarons that are formed and the extent of the electron-phonon coupling are still hotly debated. In this section I will briefly highlight the current theories that have been proposed in the literature to explain CMR in these materials.

2.5.4.1 Jahn-Teller polarons and phase separation

The Jahn-Teller polaron is thought to be important in the understanding of the mixed-valence manganites since it carries with it an anisotropic local distortion that removes the degeneracy of the electronic ground state. However, while Millis *et al.* (65) consider the electron-lattice interaction arising from the dynamic Jahn-Teller distortion to be important for the understanding of overall trends of CMR phenomena, they, and others, agree that

lattice polaron formation is incomplete to explain the transport properties in connection with the observed CMR phenomena (93; 94; 95) since it does not fully explain the experimentally observed results, for example, the magnetic characteristics of the polarons as determined from neutron diffraction data (76; 80).

In the manganites, the Hund coupling J_H is much stronger than the kinetic energy of the electrons. Consequently, configurations are very unlikely in which the electronic spin is antiparallel to the local core spin. Magnetic domains form within the manganites, just like any other magnetic material. Hence, on longer length scales, the spins must become misaligned via the Coulomb interaction (like charges repel) so that the domains can form. Phase separation at the metal-insulator transition has been argued to lead to either small (96) or large (55) nanoscale clusters (alternative known as magnetic polarons), which have been the basis for a possible, though controversial, explanation of CMR (49). These clusters are randomly distributed and are thought to have fractalic shapes (49), leading naturally to percolative transitions from one competing phase to the other, as couplings or densities are varied. The resistivity obtained in this context is similar to that found in experiments: Near the critical amount of metallic fraction for percolation, at room temperature the charge conduction can occur through the insulating regions since their resistivity at that temperature is very similar to that of the metallic state. Thus, the system behaves as an insulator. However, at low temperatures, the insulator regions have a huge resistivity and, thus, conduction is through the percolative metallic filaments which have a large intrinsic resistivity. Finally, it is expected that in a percolative regime there must be a high sensitivity to magnetic fields and other naively 'small' perturbations, since tiny changes in the metallic fraction can induce large conductivity modifications. According to Dagotto *et al.* (49), this provides the best explanation of the CMR effect in these materials.

However, in a more recent paper, Koller *et al.* (74) presented a numerical and analytical study of a one-dimensional ferromagnetic Kondo model with classical core spins in which they argued that the correct physical interpretation of the features which have previously been interpreted as phase separation in the one-dimensional model is, rather, given by ferromagnetic polarons, i.e. small FM regions with one single trapped charge carrier. From their findings, they believe it seems sensible to reassess the explanations of CMR based on phase separation since these explanations are primarily based on percolation ideas, which can equally well be applied to FM polarons as percolating units. They believe that

it appears plausible that the FM polarons will exist in symbiosis with lattice deformations (Jahn-Teller polarons)

2.5.4.2 Bipolarons

A competing theory has been proposed by Alexandrov and Bratovsky (97). They assume that the holes in the mixed-valence manganites are associated with the oxygen p-orbitals instead of the manganese ions and that double exchange is, therefore, unnecessary. The antiferromagnetic interaction between the local Mn ions and the carriers is then assumed to be weak enough to treat within a mean field theory. Alexandrov and Bratovsky then suppose that small polarons are the carriers even in the ferromagnetic state, but near T_C they mostly combine to form bipolarons. This leads to a rapid rise in the resistivity near T_C which then falls slowly above T_C as the bipolarons thermally dissociate. An applied magnetic field would tend to split up the immobile bipolarons and reduce the resistivity giving the CMR effect. This theory is in reasonable agreement with some of the key features observed experimentally in these materials, such as the huge drop in resistivity at the Curie point and an anomaly in their specific heat, but there is no direct experimental evidence of bipolaron formation.

Indeed, Nagaev (98) strongly disagrees with the view of Alexandrov and Bratovsky and this has led to a public argument between them (99; 100; 101). In particular, Nagaev argues that the polaron binding energy is insufficient to allow small polarons to form in the manganites, let alone bipolarons. Hence, Nagaev considers Jahn-Teller phonons as irrelevant for the specific properties of these materials since the hole-phonon coupling is too weak to allow the formation of polarons. Millis *et al.* also disagree with the bipolaron theory proposed by Alexandrov and Bratovsky, and cite the Pauli principle which says that two electrons can only occupy the same orbital if they have opposite spin. This is prevented in the manganites due to the strong Hund's rule coupling which aligns the spins, thus quashing the bipolaron theory.

2.5.4.3 Magnetic polarons

It has been suggested the formation of magnetic polarons in the vicinity of T_C is important. (77). Indeed, a lot of theoretical works (68; 102; 103; 104; 105) have demonstrated that the magnetic polaron formation plays a crucial role in CMR phenomena in the paramagnetic state.

For CMR oxides, Saitoh *et al.* (106) have investigated the temperature dependence of angle-resolved photoemission spectra (ARPES) for the phase transition from FM to PM order. Their studies show that a pseudogap develops above T_C, which they argue can be rationalized in the polaron picture. In the PM phase we have the competition of ferromagnetism, driven by the DE mechanism, and spin disorder due to thermal fluctuations. Therefore, FM polarons will form in the paramagnetic background. They will, however, be more extended because the PM force is less pronounced than the AFM force at low temperatures (102). With increasing temperature, the core spin fluctuations become stronger and the competition of the FM polarons with the PM background gets tougher and eventually, for high enough temperatures, the core spin fluctuations dominate.

Theoretical models, such as those based upon Monte Carlo calculations in a 3D lattice model by Hongsuk *et al.* (75), imply that the spin polarized carriers can be trapped into local ferromagnetic surroundings due to the spatially fluctuating spin correlations, resulting in the formation of the magnetic polarons in the paramagnetic phase. From these results, it has been suggested that the magnetic polaron formation is responsible for the magnetic transition and the magnetotransport properties in doped CMR manganites.

2.6 Infrared spectra and optical phonons

A detailed description of how the optical properties of these materials can be determined is given in Chapter 3, where I model the IR spectra in bulk and thin film samples of a generic perovskite. In this section, I shall therefore concentrate on the experimental and theoretical results that have been described by others in the literature.

The spectral properties of the mixed-valence manganites have been studied extensively. The reason for this is that IR phonon spectra are sensitive to local lattice distortions and

hence, these studies can help to develop an understanding of the transport properties of these materials (93).

The IR spectra reflect the vibrational modes of the lattice in the crystal. Kebin Li *et al.* (107) have used IR transmittance spectra from $La_{2/3}Ca_{1/3}MnO_3$ to show that the internal phonon modes associated with the bending and stretching modes of the MnO_6 octahedra are evident in the spectra.

Kim, Jung and Noh (26) have measured IR reflectivity spectra for a polycrystalline $La_{0.7}Ca_{0.3}MnO_3$ sample. They found that the internal phonon modes i.e., the bending and stretching modes of the MnO_6 octahedra, showed significant frequency shifts near the Curie temperature T_C. The frequency shifts of the internal phonon modes were found to have a linear relationship with the lattice expansion above T_C. These frequency shifts were attributed to a strong electron-phonon coupling and a crossover from small to large polaronic states as the temperature decreases through T_C. Using the same sample, Kim *et al.* (30) then measured temperature dependent optical conductivity spectra. In the metallic regime, at very low temperatures, the spectra clearly showed two types of absorption features: a sharp Drude-like peak and a broad mid-infrared absorption band which they attributed to the coherent and incoherent motion of large polarons, respectively.

In a study similar to Kim *et al.*'s, Okimoto *et al* (25) looked at the optical spectra of $La_{1-x}Sr_xMnO_3$ and considered their temperature dependence. The reflectivity spectra as a function of photon energy for a range of temperatures are shown in Figure 2.12. Corresponding to the change of the electrical conduction (see inset Figure 2.12), the reflectivity spectra below 3 eV show a large variation with temperature. The reflectivity spectra above and near T_C (283 K) are typical for a non-metal, with sharp far-infrared features due to the optical phonons at 0.02, 0.04 and 0.08 eV, or $\lambda = 61.88$, 30.94 and 15.47 μm, respectively. As the temperature decreases, the lower energy reflectivity is gradually increased and then the spectra turn into metallic reflectance bands (where the incident radiation can no longer propagate in the medium of the sample and is hence reflected) at low temperatures. The phonon structures were observed to provide a smaller relative contribution with decreasing temperature and this was attributed to a dielectric screening effect.

Hartinger *et al.* (43) have also studied how the phonon modes change with temperature in thin films of $La_{1-x}CaMnO_3$ (LCMO) and $La_{1-x}SrMnO_3$ (LSMO). They found that

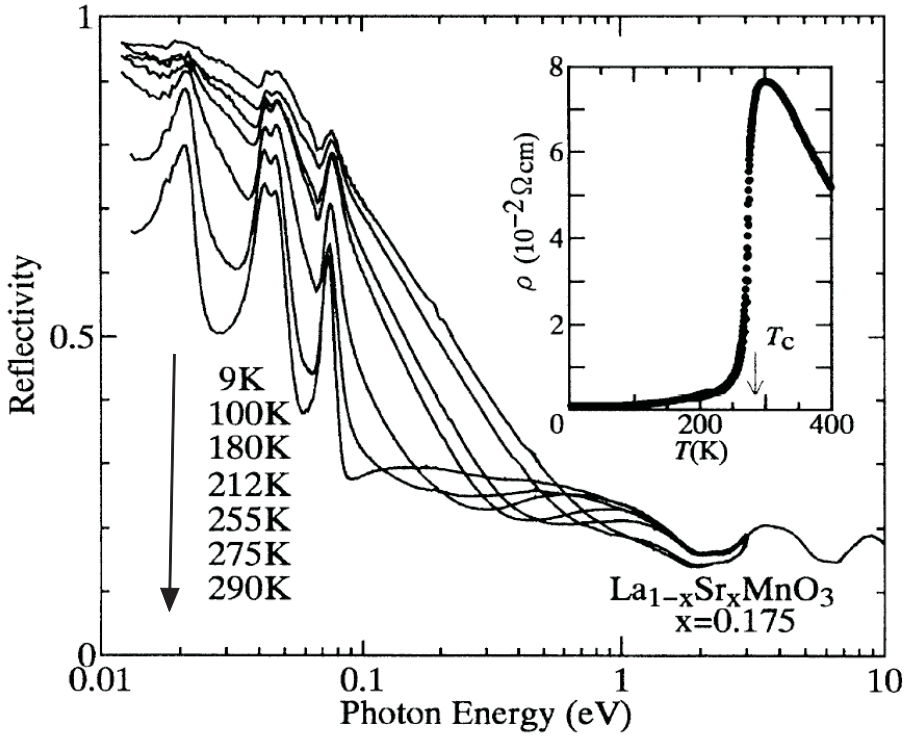

Figure 2.12: Reflectivity spectra of $La_{1-x}Sr_xMnO_3$ ($x = 0.175$ and $T_C = 283$ K) at various temperatures in the photon energy range 0.01 to 3.0 eV and at 290 K above 3.0 eV. The inset shows the temperature dependence of the resistivity for the same crystal. Taken from (25).

the manganites provide an interesting opportunity to study the coupling between lattice degrees of freedom and charge and spin effects. In normal metals, the dominant effect of mobile electrons on lattice vibrations is to screen out the phonon resonances. However, since the manganites are such 'bad' metals, the phonon resonances are still well pronounced and can still be resolved in the conducting low temperature ferromagnetic phase.

Like Okimoto *et al.*, Hartinger *et al.* observed that the phonon modes decrease as the temperature decreases. However, Hartinger *et al.* also observed that the phonon modes in LCMO reacted differently to cooling than those in the LSMO sample. In LCMO the stretching and bending modes become more pronounced with cooling than in LSMO. They also reported that the stretching phonon mode at 580 cm^{-1} shifts significantly to lower frequency with decreasing temperature in LCMO whereas almost no shift is observable in LSMO. However, they also reported irregularities within the LCMO sample itself, for although the stretching mode at 580 cm^{-1} was shifted, the one at 520 cm^{-1} was not. After

fitting their spectra to a polaron model by Emin (108), Hartinger *et al.* concluded that the differences in the spectra are caused by the different character of the polarons in LCMO and LSMO. They attributed a small polaron picture to the LCMO thin film and a large polaron picture to the LSMO thin film.

Alexandrov and Bratovsky (99) believe that the frequency dependence of the optical conductivity can be explained in terms of their bipolaron theory, where one has bipolarons in the paramagnetic phase and small polarons in the ferromagnetic phase. They believe that the optical conductivity at high temperature is well described by small-bipolaron absorption, while the low-temperature mid-infrared band is due to absorption by small polarons. The frequency shifts near T_C, that are associated with a shift in spectral weight from the bipolaronic peak to the polaronic one, are thought to occur because of the dissociation of the bipolarons as the temperature is reduced below T_C.

Perroni *et al.* (109) have studied $La_{1-x}A_xMnO_3$ perovskites with $0 < x < 0.5$, near the metal-insulator transition temperature. They found that the combined effect of the magnetic and electron-phonon interactions pushes the system toward a regime of two coexisting phases: A low electron density phase, made by itinerant large polarons, forming ferromagnetic domains and a high electron density phase, made by localized small polarons, giving rise to paramagnetic or antiferromagnetic domains depending on the temperature. Employing a variational scheme, Perroni *et al.* derived the spectral and optical properties of manganites for $x = 0.3$ at different temperatures. They found that the phase separation regime induces a robust pseudogap in the excitation spectrum of the system and that the conductivity spectra were characterized by a transfer of spectral weight from high to low energies, as the temperature decreases. Like Kim, Jung and Noh (30), they found that in the metallic, ferromagnetic phase, at low T, two types of IR absorption were apparent: a Drude term and a broad absorption band which they also attributed to the coherent and incoherent motion of large polarons, respectively.

Perroni *et al.*(110) have subsequently studied the effects of a magnetic field on the IR absorption. They found that the introduction of a magnetic field is able to modify the IR response of the system. The presence of an external magnetic field favours the alignment of the core spins, making the ferromagnetic phase more stable, and increases the coherent motion of the charge carriers. At low temperatures, in the ferromagnetic phase, the system

shows a Drude response due to the coherent motion of large polarons. However, at high T, the IR absorption becomes associated with the incoherent dynamics of small polarons. The introduction of a magnetic field was also found to have dramatic consequences for the resistivity near T_C. Perroni *et al.* found that the magnetic field shifts the peak of the resistivity as a function of temperature. Since the formation of small polarons around T_C leads to a localisation of the free carriers, this can lead to a rapid increase in the resistivity as we enter the paramagnetic phase. A large difference between resistivities at different magnetic fields can occur due to the fact that as the applied magnetic field is increased, the polarons can become delocalised, thus increasing the conduction bandwidth and reducing the resistivity. As we shall see in Chapter 5, this is similar to observations I have made in bulk samples of $La_{1-x}Sr_xMnO_3$ near the Curie temperature.

2.7 Thin film properties

The tolerance factor described in 2.5.2 illustrates the influence the ionic radius of the dopant ion can have on the physical properties of the sample. Thin film samples have additional strains that are introduced due to the presence of the substrate. While most of the strain is due to a lattice mismatch between the film and the substrate, the preparation method can also introduce additional strain.

A variety of preparation methods can be employed to grow thin film samples including: reactive sputtering, ion beam sputtering coevaporation, chemical vapour deposition and pulsed laser deposition. The latter two techniques have been used to prepare the thin films of $La_{1-x}Ba_xMnO_3$ (LBMO), $La_{1-x}Ca_xMnO_3$ (LCMO) and $La_{1-x}Sr_xMnO_3$ (LSMO) we have studied, the results of which can be found in Chapter 6. Each growth technique has different growth parameters and these can heavily influence the resulting film. Indeed, even films grown at the same laboratory under similar conditions can have different physical properties depending on the growth parameters.

The lattice distortion introduced by strain can change the Mn-O bond lengths and bond angles, and this can cause drastic changes to the electric and magnetic properties of the film in comparison to bulk samples of the same material. These changes will also manifest themselves in the sample's IR optical spectra, and in section 3.7.5 of Chapter 3, I model

the possible consequences strain can have on the sample's IR spectra.

I shall now present an overview that considers the influence the thin film nature can have on the structure, Curie temperature, magnetoresistance and optical properties of doped lanthanum manganites.

2.7.1 Structural effects

The choice of substrate used in the preparation of thin films of LBMO, LCMO and LSMO is usually selected to minimise the lattice mismatch between the film and the substrate. For example, LBMO is typically grown on STO. In Table 2.2 we summarise the typical lattice parameters and mismatches for the most commonly used substrates $SrTiO_3$, $LaAlO_3$ and $NdGaO_3$ (STO, LAO and NGO, respectively).

			LCMO orthorhombic 3.86 Å	LSMO rhombohedral 3.873 Å	LBMO rhombohedral 3.91 Å
STO	cubic	3.905 Å	1.17%	0.83%	-0.13%
NGO	orthorhombic	3.857 Å	-0.08%	-0.41%	-1.36%
LAO	rhombohedral	3.79 Å	-1.81%	-2.14%	-3.07%

Table 2.2: In-plane lattice constants in pseudo cubic notation, structures and lattice mismatches for a doping concentration of x=2/3 after (111; 112; 113; 114). Positive values are associated with tensile strain and negative values with compressive strain.

The typical unit cell size for LAO is smaller than the unit cell size of the film. This causes an in-plane compression which leads to an elongation of the oxygen octahedra normal to the film surface. STO, on the other hand, generally has a larger unit cell size and so this leads to in-plane tensile stress and an out-of-plane compression of the oxygen octahedra.

These stresses and strains change the symmetry of the crystal structure and can cause the thin films to have a different crystal structure than bulk samples of the same material. For example, Vlasko-Vlasov *et al.* (115) observed a stretched tetragonal structure in $La_{2/3}Ca_{1/3}MnO_3$ films grown on STO, whereas the bulk sample had an orthorhombic crystal structure.

2.7.2 CMR and the Curie temperature

The Curie temperature in strained thin films can differ significantly from the Curie temperature measured in bulk samples of the same material. As we have seen, it can be argued that the physics of CMR in these materials is governed by the interplay of Mn e_g electron itineracy (with its "double exchange" connection to magnetism) and the localizing effect of a strong electron lattice coupling. One particular mechanism for this coupling is the JahnTeller effect: the e_g level is two-fold degenerate in a cubic environment but the degeneracy is split by a biaxial distortion.

Millis *et al.* (116) argue that this suggests that there are two different types of strain dependence that are applicable to these materials. The first is a uniform bulk compression which they argue will tend to increase the "bare" electron hopping amplitude, increasing the conductivity, and thereby reducing the relative importance of the electron-lattice coupling. This will have a tendency to increase T_C. The second is a biaxial distortion. This will increase the JahnTeller splitting between the t_{2g} and the e_g electrons, thereby increasing the tendency of the electrons to become localized. Trapped carriers reduce the conductivity, subsequently reducing the Curie temperature.

Whilst this dependence of the Curie temperature with strain has been confirmed experimentally for films of LSMO and LCMO (117; 118; 119), Bibes *et al.* (111; 120) have demonstrated that the thickness of the thin film has more of an effect on the Curie temperature; the thinner the film the lower the Curie temperature. Bibes *et al.* have shown using nuclear-magnetic-resonance measurements that the electronic properties of thin films, especially close to the film/substrate interface, differ from those of the bulk material. The NMR measurements provided evidence that their thin films had an inhomogeneous magnetoelectronic nanostructure with distinguishable regions containing localized charges. These regions were scattered within the films, with a higher density close to interfaces in the case of $La_{2/3}Ca_{1/3}MnO_3$ films on $SrTiO_3$ but more homogeneously distributed for films grown on $NdGaO_3$. Bibes *et al.* argue that since their manganite films were fully strained, the thickness dependence of T_C can neither be related to the strain states nor to dimensional effects.

However, strain and the thickness of the film are not the only factors that can influence

the Curie temperarure. Another factor that has been shown to have an effect is the substrate itself (111). For example, commercially available $SrTiO_3$ substrates generally present two types of terminations, namely SrO or TiO_2 (121). The existence of these two different terminations could promote electron localisation in highly disordered sites as well as the coexistence of a variety of Mn-O distances and Mn-O-Mn bond angles, that could lead to the formation of so called parasitic phases (e.g. antiferromagnetic or paramagnetic regions formed within a nominally ferromagnetic phase) at the substrate/film interface. It is thought (111) that the modification of the carrier density in these parasitic regions (due to localisation) combined with the variety of different bond lengths and angles, is likely to lead to a decrease in the double exchange transfer integral which accounts for the observed reduction of the Curie temperature for the thinnest films.

The effect of strain on the Curie temperature has also been studied in thin films of LBMO on STO by Zhang *et al.* (122). Zhang *et al.* demonstrated that in LBMO thin films, tensile strain enhances ferromagnetism and increases T_C. This is contrary to the predicted results of Millis *et al.* (116) where tensile strain usually reduces T_C, and compressive strain enhances T_C. The phase diagram for LBMO measured by Zhang *et al.* can be seen in Figure 2.13. Zhang *et al.* came to the conclusion that there must be new mechanisms that are responsible for the anomalous strain effect in LBMO thin films. They tried to explain their result in terms of hopping integrals. According to the theory of double-exchange, T_C is proportional to the transfer integral, t, of e_g electrons hopping between Mn^{3+} and Mn^{4+} ions. Tensile strain elongates the in-plane Mn-O bond length, reducing t and thus T_C; in contrast, compressive strain raises T_C. While this is the established understanding of strain in thin films, Zhang *et al.* also believe that a strain-induced modification of e_g electron orbital stability should be considered.

Two orbitals are available for e_g electrons, the in-plane $d_{x^2-y^2}$ orbital and out-of-plane $d_{3z^2-r^2}$ orbital. In bulk LBMO, the electron occupancy in the out-of-plane $d_{3z^2-r^2}$ orbital is higher than that in the in-plane $d_{x^2-y^2}$ orbital, due to a relatively large c/a ratio, which is related to orbital stability and thus the magnetotransport properties. In LBMO thin films, an elongation of in-plane Mn-O distance (decrease in *c*/*a*) due to tensile strain would stabilize the $d_{x^2-y^2}$ orbital, which has a larger transfer intensity than the $d_{3z^2-r^2}$ orbital. This would increase the number of e_g electrons in the $d_{x^2-y^2}$ orbital and increase the effective in-plane carrier density. This would then enhance electron hopping through

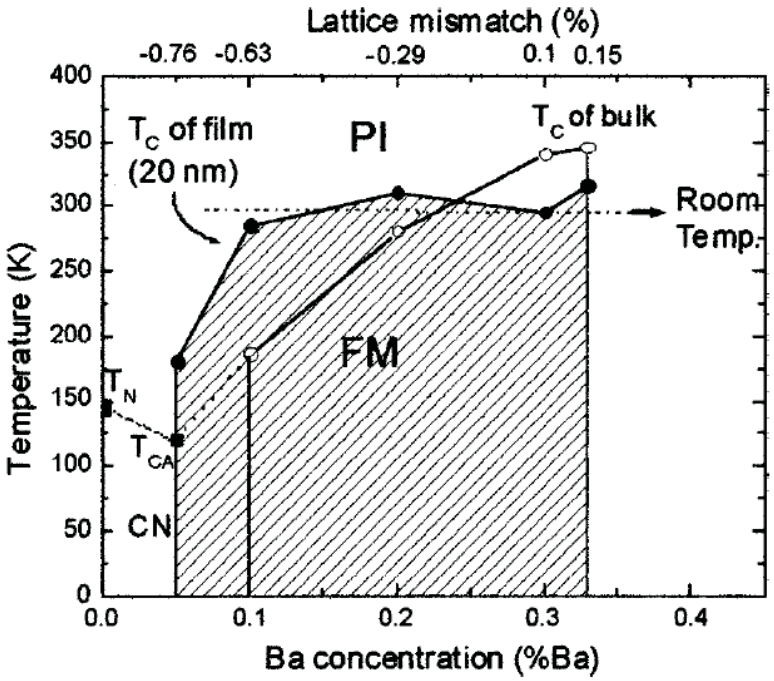

Figure 2.13: Phase diagram and temperature dependent magnetoresistance of tensile strained LBMO on a STO substrate. FM, PI and CNI denote ferromagnetic metallic, paramagnetic insulating and spin canted insulating phases, respectively. Adapted from (122).

double exchange in thin films causing an increase in T_C. In contrast, the compressive strain will suppress ferromagnetism and lead to a decrease in T_C. Zhang *et al.* suppose that the strain-induced modification of the Mn-O bond length and stability of the e_g orbital are competitive processes and that in some manganites the former are dominant. However, Zhang *et al.* believe that in LBMO the latter may be dominant and give rise to the unexpected properties.

Yuan (123), however, disagrees with the orbital-relevant mechanism proposed by Zhang *et al.*. Instead, Yuan believes that while the tensile strain in thin films leads to an elongation of the in-plane lattice parameter, *a*, it does not simply signify an elongation of the (in-plane) Mn-O bond length, *d*. Yuan argues that a possible change of the Mn-O-Mn bond angle ϕ was ignored by Zhang *et al.* and many others (116; 124). The hopping integral *t* between two nearest neighbor Mn sites is ϕ-dependent and reaches a maximum when $\phi = 180°$. Yuan relates the direct dependence of *t* on *d* and ϕ through the following empirical formula:

$$t \propto d^{-3.5} sin\frac{\phi}{2} \tag{2.2}$$

If the angle ϕ in equation 2.2 is assumed to be independent of strain, the elongation of the lattice parameter *a* (and the corresponding *d*) will lead to a reduction of *t* as described by Zhang *et al.*. However, if ϕ is allowed to change, then Yuan argues that it is no longer obvious that tensile strain will elongate *d* and thus reduce T_C. Indeed, Yuan's argument is supported by recent measurements in thin films of $La_{1-x}Ca_xMnO_3$ (x=0.31, 0.39) grown on $SrTiO_3$ and $LaAlO_3$ substrates by Miniotas *et al.* (125), who, after examining extended x-ray absorption fine structure, showed that the bond length *d* is the same as in bulk samples, regardless of whether the films are under tensile or compressive strain or how thick they are. Instead, Miniotas *et al.* found that what is really modified is just the bond angle ϕ. It becomes larger (smaller) under the tensile (compressive) strain, and this is consistent with an elongation (contraction) of *a*.

A similar result was also observed in $La_{0.67}Sr_{0.33}MnO_3$ /$LaAlO_3$ films by Ju *et al.* (89) and in bulk samples of $R_{1-x}A_xMnO_3$ (R = La, Pr, Nd, Y; A = Ca, Sr, Ba with x=0.3, 0.33) by the aforementioned García-Muñoz *et al.* (63). Both showed that changes in the average radius of the ions at (R,A) site (or equivalently the tolerance factor [see section 2.5.2]) only affect the mean Mn-O-Mn bond angle, with the mean Mn-O distance remaining nearly unchanged. Based on all these findings, Yuan argues that it is plausible to believe that for $La_{1-x}Ba_xMnO_3$ thin films, the primary factor modified by strain is the angle ϕ. It is then possible to reach the conclusion that the hopping integral *t* can be enhanced by the tensile strain due to an increase in the bond angle ϕ and in this way, the experimental findings by Zhang *et al.* are not so strange as they claimed. Yuan is convinced that in light of this, the orbital-relevant mechanism proposed by Zhang *et al.*, which is based on the hypothetical elongation of *d*, is no longer valid.

Zhang *et al.* (122) also (partially) studied the effect of strain on the MR in thin films of LBMO on STO. Figure 2.14 shows the temperature dependence of magnetoresistance ratio for LBMO thin films with thickness of 50 nm as measured by Zhang *et al.* in a magnetic field of $H = 0.8T$.

As can be seen in Figure 2.14, there is no obvious relationship between the level of doping, x, and the position of the peak in the MR. One can make the general observation

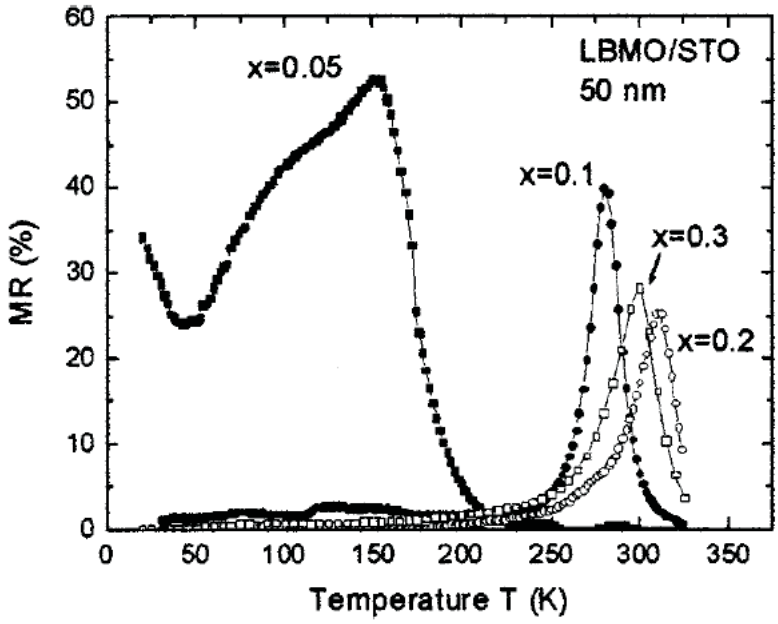

Figure 2.14: Temperature dependence of magnetoresistance ratio for LBMO (x=0.05 to 0.3) thin films with thickness of 50 nm. From (122)

that as x increases, the peak temperature also increases and the MR($\%$) tends to decrease. However, that observation is no longer valid when one looks at the peak temperature and MR of the $x = 0.2$ and 0.3 samples. The MR and peak position for the $x = 0.05$ sample seems out of place compared to the other compositions in the figure. However, if we refer to the phase diagram in Figure 2.13, we can see that at low temperatures, the $x = 0.05$ composition lies on a phase boundary between a ferromagnetic metallic phase and a spin canted insulating phase, which could explain why this sample has such a different MR profile. It comes as no surprise that there is no clear relationship between the temperature at which the peak MR is observed and the level of doping when you consider how dependent the Curie temperature of the sample is on the growth parameters. Even for samples grown in the same laboratory, we can observe a wide range of Curie temperatures for samples grown under nominally the same conditions.

LBMO is of interest from a commercial viewpoint since it has a Curie temperature close to room temperature, so this opens up potential applications that can utilise the change in MR observed at the Curie point. The large MR (40%) observed for the $x = 0.1$ sample is, therefore, very interesting since it occurs at a temperature close to room tem-

perature.

2.7.3 Magnetic domains and grain boundary MR

Like most metallic, magnetic materials, the mixed-valence manganites have magnetic domains, which exist in order to reduce the energy of the system by lowering its demagnetising field. Magnetic domains can be found in both single crystal and polycrystalline samples. Thin film manganite samples are either epitaxial or polycrystalline in nature. In epitaxially films, the sample is grown in such a way that the crystal structure of each deposited layer has the same crystal structure as the previous layer, ensuring that the finished sample behaves like a single crystal. Polycrystalline samples, on the other hand, consist of several smaller crystallites, commonly referred to as grains, with each grain having the same structure as a single crystal. Depending on its size, each grain can contain one or several magnetic domains, again to lower its energy, but there will also be grain boundaries between adjacent grains.

Research into the nature of magnetic domains in the mixed valence manganites has predominantly focussed on thin film samples. In addition, most of the work has concentrated on two temperature regimes. The first of these temperature regimes is at low temperature ($T \ll T_C$), where a high MR has been observed in polycrystalline samples compared to epitaxially grown films. The second temperature regime of interest is at, or around, the metal-insulator transition temperature (T_{M-I}). In this section I will review the research that has been carried out for these two temperature regimes.

2.7.3.1 Magnetic domains at low temperature

A large low-field MR component has been observed in polycrystalline thin film and bulk manganite samples (126; 91) at low temperatures. To investigate the cause of this large MR, Li *et al.* (127) have studied polycrystalline thin film samples of $La_{0.67}Sr_{0.33}MnO_3$ and $La_{0.67}Ca_{0.33}MnO_3$ deposited on single crystal and polycrystalline $SrTiO_3$ substrates. The polycrystalline $SrTiO_3$ substrates were obtained by cutting and optically polishing sintered pellets of the material. The time and temperature of sintering were varied to obtain samples with three different average grain sizes: 24, 14, and 3 μm.

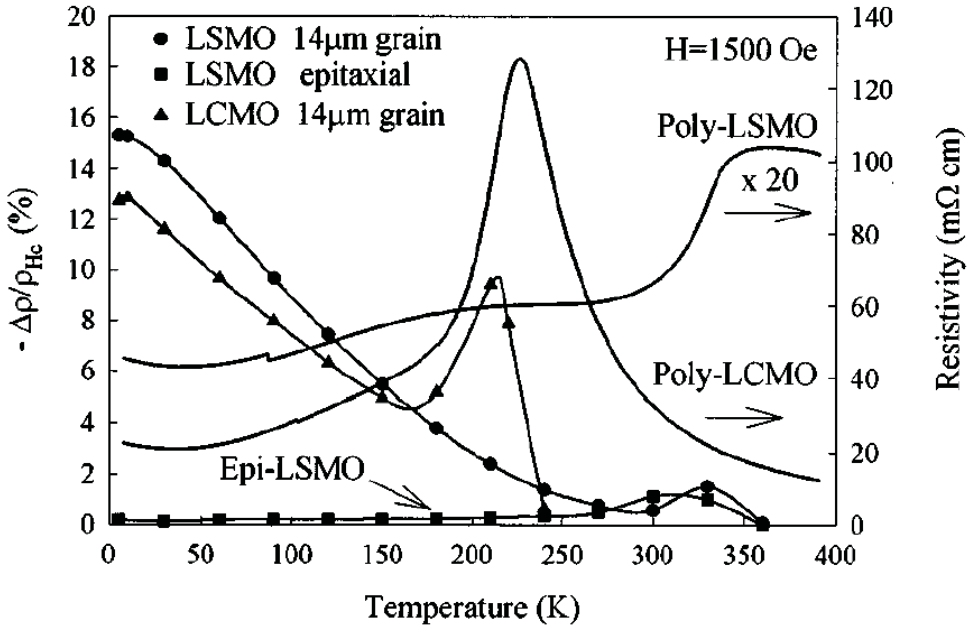

Figure 2.15: Resistivity and MR as a function of temperature for polycrystalline (average grain size of 14 μm) LCMO and LSMO films. The MR measured for an epitaxial LSMO film as a function of temperature is also shown for comparison. Taken from (127).

Figure 2.15 shows the temperature dependence of the MR (H=1500 Oe) and the zero-field resistivity for the polycrystalline LCMO and LSMO films as measured by Li *et al.*. Li *et al.* noted that the peak in the resistivity curves, at 230 and 350 K for LCMO and LSMO, respectively, occur close to the Curie temperature (T_C) of these materials. The MR in both systems show a steady decline with increasing temperature, interrupted by an increase near T_C , before finally dropping to zero above the respective transition temperatures. Note that the low-temperature MR is somewhat higher in LSMO than LCMO. Nonetheless, the subsequent peak occurring close to the T_C is of significantly higher magnitude for the latter, which has the lower ferromagnetic transition temperature. Li *et al.* identified the MR peak near T_C as arising from the colossal magnetoresistance component inside the grains. They argue that this is confirmed from the MR behavior of the epitaxial LSMO film which peaks near the Curie temperature but is negligible at low temperatures. Li *et al.* (127) observed an MR of 13-15 $\%$ in the polycrystalline thin film samples compared to a MR of 0.3 $\%$ measured for an epitaxially grown film under the same conditions.

There is some controversy over the exact cause of the high MR observed in the poly-

crystalline samples at low temperature, but there are essentially two competing theories: the first theory is based on scattering at the grain boundaries and the second is based upon spin-polarized tunnelling between the grains in the polycrystalline samples.

Li *et al.* suggest that the data in Figure 2.15 support the presence of two MR components in polycrystalline thin films: one near T_C from the regular CMR mechanism inside the grains, and the other, most important at low T, from magnetic scattering at grain boundaries, and this is a view shared by Gupta *et al.* (126), Ju *et al.* (89) and Schiffer *et al.* (90). Simply put, the conduction in these materials through the double exchange mechanism requires the spins of the conduction electrons on the Mn^{3+} and Mn^{4+} ions to be in a parallel alignment. Inside any particular magnetic domain the conduction electrons are almost completely polarized due to the strong Hund coupling between the t_{2g} and e_g electrons, and therefore electrons are easily transferred between pairs of Mn^{3+} and Mn^{4+} ions. If the conduction electrons need to travel between different magnetic domains, or across a grain boundary, then the fact that the spins on each side of the boundary have a different alignment will hinder the conduction process, and, if the misalignment of the spins is too severe, it will result in the conduction electron being scattered at the boundary since there are no available states for it to occupy. This will lead to a high zero-field resistivity. Application of a moderately low field can readily align the magnetic domains into a parallel configuration causing the ρ to drop substantially.

Gupta *et al.* have directly imaged the magnetic structure at room temperature in a 100 nm polycrystalline film of LSMO using a wide-field Kerr microscope (126). They found that the magnetic domains, which are defined by the grains in the sample, are decoupled and orientate progressively in a magnetic field.

Figure 2.16 shows a Kerr M-H loop of a 14 μm grain-size polycrystalline film and three corresponding Kerr images. Image (a) displays the nearly uniform magnetic state of the sample at remanence. On moving close to the coercive point, half of the grains switch orientation as seen in image (b). Finally, in image (c) most of the grains have switched as the loop nears saturation. Individual grains can be observed to switch at different fields, and the loop data is an average over the many grains contained in the images. Some of the grains are also observed to switch by wall motion. For example, in the top right corner of (b), a wall can be seen to cross a grain boundary. Gupta *et al.* also observed that

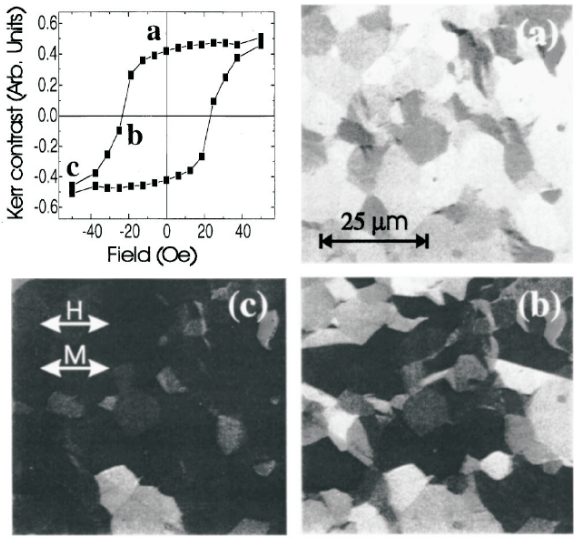

Figure 2.16: Kerr hysteresis loop of a polycrystalline LSMO film sample averaged over a number of grains. The three Kerr images correspond to the points a, b, and c marked in the hysteresis loop. The external field has been applied horizontally, as indicated in the image, and swept between plus and minus 200 Oe. The Kerr signal is sensitive to changes in the horizontal component of the magnetization. Taken from (126)

wall motion was impeded by surface defects such as scratches. Preliminary experiments by the group on epitaxial LSMO films show that, unlike in the polycrystalline samples, magnetization occurs by rotation and domain-wall movement over large areas.

It is thought by Gupta *et al.* that the high-field, low T, MR effect in the polycrystalline samples is most likely related to alignment of spins in a magnetically disordered region near the grain boundaries. The spins are canted in this region and are aligned with increasing magnetic field. This is consistent with the fact that the magnetization continues to increase slowly with field in the polycrystalline samples. On application of a large magnetic field, the increasing alignment of the neighboring spins in the canted region leads to a reduction in the resistivity.

Schiffer *et al.* (90) and De Teresa *et al.* (92) have also studied the conduction properties of polycrystalline samples of $La_{1-x}Ca_xMnO_3$. Schiffer *et al.* analyzed the low temperature resistivity curves of $La_{0.75}Ca_{0.25}MnO_3$ and found for T$<$0.5 T_C the empirical expression $\rho(T) = \rho_0 + \rho_1 T^{2.5}$ gave a good fit to their data. The term ρ_0 is the resistivity due to domain and grain boundaries and other temperature-independent scattering

mechanisms (presumably chemical or nonstoichiometric defects), and the $\rho_1 T^{2.5}$ term is an empirical fit to the data which represents a combination of electron-electron, electron-phonon, and electron-magnon scattering, all of which are expected to be significant in this system.

De Teresa *et al.* have also tried to fit their low-temperature results with different exponents for the term $\rho_1 T^{\nu}$ and $\nu = 2.5$ was also found to give the best fit for all the magnetic fields. It was found that a field of 1 T strongly affects the temperature-independent term ρ_0, whereas it has less influence on the temperature-dependent term $\rho_1 T^{2.5}$. De Teresa *et al.* concluded that it is likely that the main mechanism responsible for the magnetoresistance at low temperatures and low fields is the influence of the magnetic field on the magnetic domains. As low magnetic fields increase the size of the magnetic domains (due to neighbouring grains becoming aligned in the field), the scattering of the electrons due to domain boundaries decreases and the magnetization becomes larger. Fields greater than 1 T were observed to affect both mechanisms (the temperature-dependent and the temperature-independent scattering) to a similar degree.

The alternative theory which explains the large low-temperature MR in terms of spin polarized tunnelling between grains has less support in the literature. The main supporters of this theory are Hwang *et al.* (91) who argue that their results are consistent with a spin polarized tunnelling mechanism between grains. The main reason Hwang *et al.* are convinced that spin polarized tunnelling is responsible for the high MR is that the manganites have 'a high degree of spin polarization' (91), i.e. the e_g electrons find it energetically favourable to align due to the strong Hund's coupling. In a typical itinerant ferromagnet such as nickel, a very wide conduction band ($\approx$ 4.5 eV) is split into minority and majority carrier bands offset by a small exchange energy ($\approx$ 0.6 eV), leading to a partial polarization of the electrons ($\approx 11\%$) (128; 129). In manganites, however, a relatively narrow majority carrier conduction band ($\approx$ 1.5eV) is completely separated from the minority band by a large Hunds energy, as well as an exchange energy ($\approx$ 2.5 eV), leading to a nearly complete polarization of the electrons (25; 130). This is shown diagrammatically in Figure 2.17.

When the electron spin is conserved in the tunneling process, there is an additional magnetic coupling energy when the magnetic moments of the neighboring grains are not

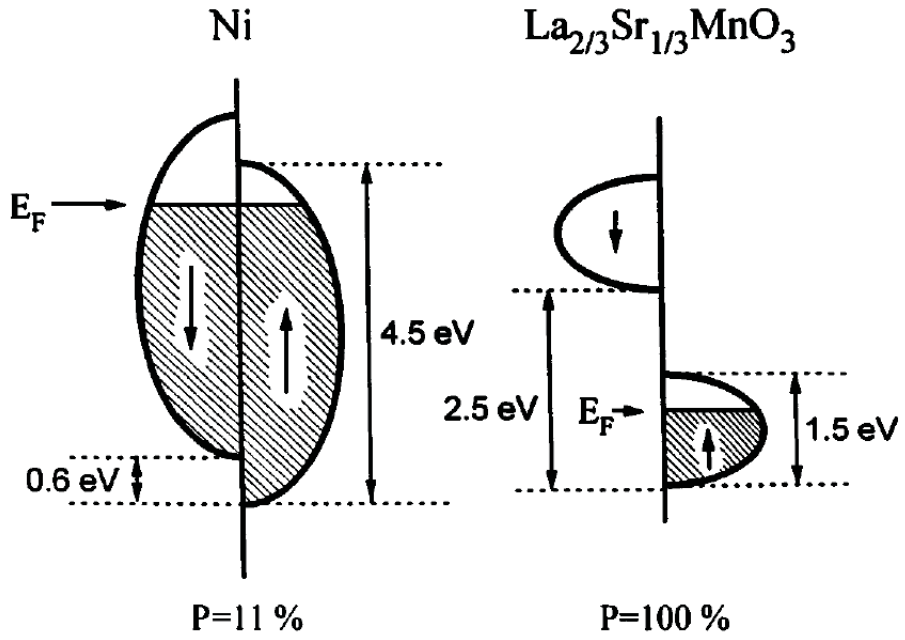

Figure 2.17: Energy level diagram comparing the conduction band of Ni with $La_{2/3}Sr_{1/3}MnO_3$. After (91).

parallel. By considering the magnetic field dependence of this intergrain coupling energy, the first term in the high temperature expansion of the MR is given by:

$$\frac{\Delta\rho}{\rho} = -\frac{JP}{4k_BT}[m^2(H,T) - m^2(0,T)] \tag{2.3}$$

where J is the intergrain exchange constant, P is the electron polarization, and m is the magnetization normalized to the saturation value. When Hwang *et al.* considered the MR in their polycrystalline $La_{2/3}Sr_{1/3}MnO_3$ thin film samples in this framework, they found that, consistent with the m^2 dependence of the MR, there was a sharp drop in resistance that could be associated with the sharp increase in magnetization. Hwang *et al.* found a negative MR which corresponds to J being positive, indicating an antiferromagnetic intergrain interaction. Thus the ferromagnetic alignment of the grains by an applied field gives rise to increased electron tunnelling.

Hwang *et al.* have received some support from Ziese *et al.* (131) who measured the domain-wall width in various LCMO thin films. Ziese *et al.* found that at low temperatures the Bloch-wall width was of the order of 10 to 30 nm. This corresponds to between 25 and

75 lattice spacings and according to the results of Yamanaka and Nagaosa (132), walls of this width do not give a significant contribution to the magnetoresistance. Ziese *et al.* also found that the domain wall width was independent of the microstructure for the epitaxial and polycrystalline LCMO films made from the same target, which again suggested that the large, low field magnetoresistance seen in the polycrystalline film compared to the epitaxial films is not due to magnetic domain-wall scattering.

However, Li *et al.* (127) have measured the current-voltage (I-V) curves at 5 K for their epitaxial and polycrystalline films. They argue that for tunnelling to be the dominant conduction mechanism across the grain boundaries, one would expect strong non-Ohmic I-V characteristics at high bias voltages. To test their hypothesis they measured films with grain sizes of 3 and 14 μm that they patterned to a small (50 μm x 50 μm) square . There are only 3-4 grains along the current path for the sample with 14 μm grain size, and about 17 grains for the 3 μm grain size. If tunnelling is at play, one would expect the I-V curves to be very different for these samples, because the voltage drop across successive grains would be different. A small decrease in the dynamic resistance (dV/dI) of about 5$\%$ at a bias voltage of 0.5 V was observed for the epitaxial films and somewhat higher for the polycrystalline films. Li *et al.* were able to measure the polycrystalline films up to a high bias of 3 V, which only resulted in a modest 35 $\%$ decrease in dV/dI, independent of the grain size. Li *et al.* argue that the lack of grain size dependence and the similarity in the behavior of epitaxial and polycrystalline films are strong evidence excluding tunnelling between the grains as the dominant conduction mechanism.

2.7.3.2 Magnetic domains near the Curie temperature

Yeong-Ah Soh *et al.* (133) have studied temperature dependent phenomena in thin films of LSMO using magnetic force microscopy (MFM). They studied epitaxial $La_{1-x}Sr_xMnO_3$ films (with $x = 0.23$ and 0.3) grown on single and bicrystal $SrTiO_3$ (001) substrates. The bicrystal substrates allow the formation of an 'artificial' grain boundary (GB). It is 'artificial' in the sense that it has been deliberately engineered to form a boundary at this position. Three films were studied: sample A had a composition of $x = 0.3$ and thickness of 200 nm and was deposited on a single crystal. Samples B and C were 60 nm thick with compositions x=0.3 and 0.23, respectively, and were grown on bicrystal substrates with 45° misalignment. Due to the lattice mismatch between $La_{1-x}Sr_xMnO_3$ and the $SrTiO_3$

substrate, these films are known to have a tensile strain resulting in a suppression of T_C compared to the bulk, and a magnetization vector lying in the plane of the film (134).

Yeong-Ah Soh *et al.* imaged magnetic domain structures for their films for zero applied field using MFM. The magnetic tips were magnetized along the tip axis, perpendicular to the film plane, which Yeong-Ah Soh *et al.* refer to as the z-direction. Figure 2.18(a) shows the topography as well as the magnetic domain structure of sample C near the artificial grain boundary at room temperature.

In the left image, we see the artificial GB. The corresponding magnetic image shows the formation of a magnetic domain wall (DW) at the artificial GB. A notable observation is the difference in orientation of the magnetic DWs on opposite sides of the artificial GB. On the left side of the GB, a magnetic DW forms at 45° with respect to the GB, whereas on the right side the DW is at 90° with respect to the GB. This is due to the different crystal orientation of the underlying $SrTiO_3$ bicrystal substrate. On one side of the GB the (100) axis is parallel to the GB. On the other side the (100) axis is rotated by 45°. Since the magnetization vector is coupled to the crystal axis, the magnetization vector rotates at the GB by 45° resulting in the formation of a magnetic DW.

The sizes of the magnetic domains are several tens of microns. Within these large magnetic domains, magnetic patterns with features of submicron length scale are observed (Figure 2.18(b)) (135). Since no correlation exists between the topography and magnetic image, Yeong-Ah Soh *et al.* believe that this texture is magnetic in origin and that the magnetic texture arises from small spatial fluctuations of the magnetization vector within a magnetic domain. The orientation of the magnetic texture is rotated by 45° on opposite sides of the artificial GB, indicating that it is related to the crystal orientation.

Yeong-Ah Soh *et al.* then studied the evolution of magnetic patterns in these films as a function of T by introducing a variable T sample stage. The results obtained for $T<T_C$ showed no appreciable change in the magnetic pattern except for a decrease in the magnetic contrast as T was raised toward T_C . However, at $T\approx T_C$, changes were observed in the magnetic image. As T is increased above T_C to 355 K, this becomes clearer for we see the emergence of a new magnetic pattern (see Figure 2.19) which is uncorrelated with the magnetic pattern observed below T_C.

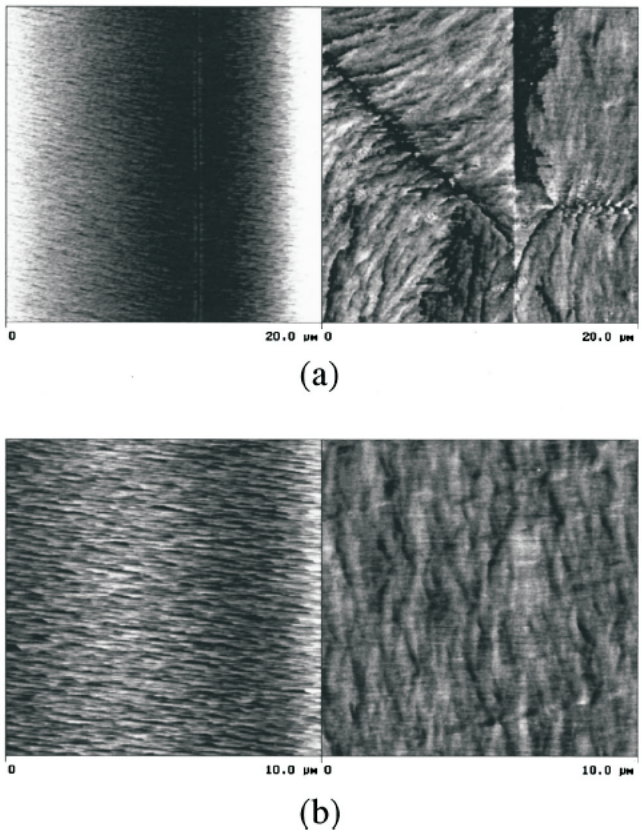

Figure 2.18: (a) Left image shows the topography of the $La_{0.77}Sr_{0.23}MnO_3$ film grown on a bicrystal $SrTiO_3$ substrate around the artificial grain boundary at room temperature. The MFM image on the right shows the formation of a magnetic domain wall at the artificial grain boundary. (b) Typical topography and MFM image of a 10 μm scan region within the magnetic domains described in (a). The magnetic inhomogeneity observed in the right image is not due to topography as can be clearly seen by the difference in orientation compared with the features observed in the left image. Taken from (133)

On top of a uniform background (represented by grey), we observe local mesoscopic regions (represented by black) strongly attracted to the magnetic tip. A vertical stripe forms at the artificial GB and has a width of the order of a micron, which is much larger than the physical width of the GB. These mesoscopic regions were observed up to 370 K, where they eventually disappear. Yeong-Ah Soh *et al.* believe that the local mesoscopic regions are ferromagnetic and the rest of the film is paramagnetic in the range 350K$<$T$<$370 K, giving rise to a large magnetic contrast. The ferromagnetic regions are attracted to the magnetised tip of the MFM. When both this region and the bulk part of the film are ferromagnetic (for T$<$T$_C$) such a contrast is not observable. As the ferromagnetism of the bulk part of the film diminishes when T$\geqslant$T$_C$, the magnetic contrast between the meso-

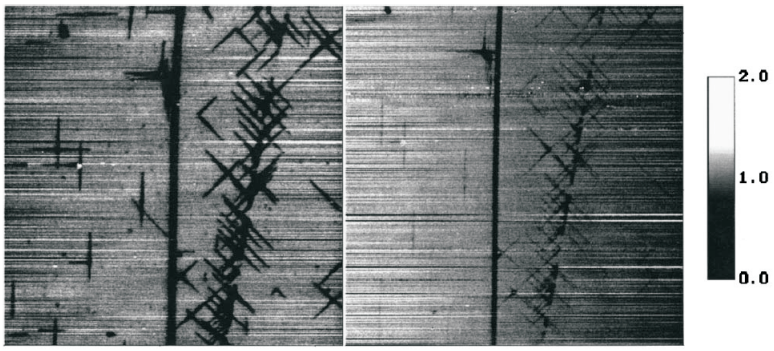

Figure 2.19: MFM images of a 60-nm-thick $La_{0.77}Sr_{0.3}MnO_3$ film at (a) 355 K and (b) 360 K. The scan size is 54.3 μm. A common z scale (in degrees) was used to compare the images. Above 350 K, which is the transition temperature measured by SQUID magnetometry, the magnetic image shows the emergence of new features not observed at temperatures well below T_C . Local ferromagnetic regions (represented by black) are observed, which are distinct from the magnetic pattern observed at $T<T_C$. The new ferromagnetic regions have a higher local T_C compared to the rest of the film. The size of the local ferromagnetic regions varies with temperature and the nature of the underlying defect. Taken from (133).

scopic region and the rest of the sample develops as shown in Figure 2.19. Eventually, the contrast decreases and vanishes as the ferromagnetism of the mesoscopic region vanishes. Yeong-Ah Soh *et al.* believe that a modulation of T_C on a local scale occurs due to strain relief around defects (in this case GBs). These data tie in very nicely with the concept of magnetic polarons and the observed formation of small ferromagnetic clusters in the paramagnetic phase we discussed in section 2.5.4.3. This leads us to the conclusion that magnetic polarons are synonymous with magnetic domains since conceptually they are the same.

2.7.4 Optical properties

The effect of substrate-induced strain on IR optical spectra of thin films of LCMO has been reported by Boris *et al.* (24). They compared the optical conductivity spectra for LCMO deposited on three different substrates: $SrTiO_3$, $LaAlO_3$ and $YAlO_3$, the results of which can be seen in Figure 2.20.

Strain induced by the lattice mismatch between the film and the substrate was found to

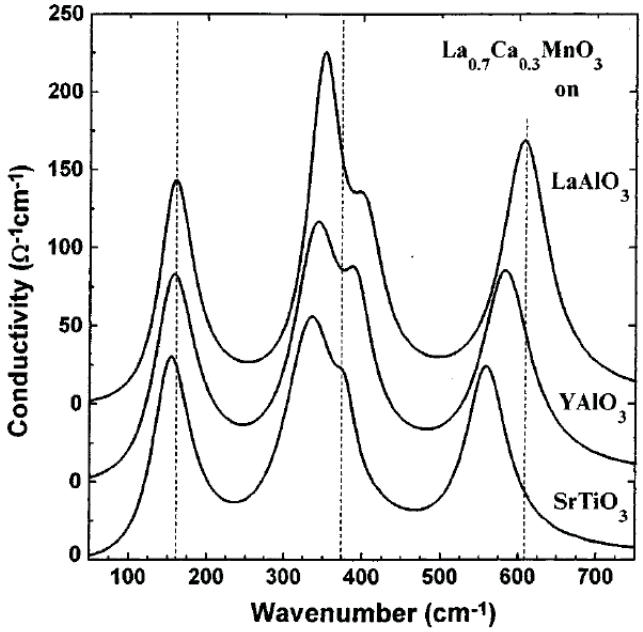

Figure 2.20: Optical conductivity spectra for LCMO prepared on $SrTiO_3$, $LaAlO_3$ and $YAlO_3$. After Boris *et al.* (24).

shift the bending mode (at 330 cm^{-1}) and stretching phonon mode (at 580 cm^{-1}) by up to 22 cm^{-1}. The larger the strain, the larger the observed shift. Boris *et al.* observed that the shift was toward lower frequencies for tensile stress and was toward higher frequencies for compressive stress. However, they also observed that the external mode at 170 cm^{-1} was hardly shifted at all. They concluded that their results provide evidence for a strong dependence of the Mn-O-Mn bending and Mn-O stretching phonon mode parameters on the lattice distortion induced by the substrates.

2.8 Conclusions

The extensive literature on these materials reflects the interesting features they possess. What is clear is that the influence CMR, polarons, electron-phonon coupling and the crystal structure has on conduction in these materials is not fully understood.

These materials have a complicated magnetic phase structure that depends on the temperature and level of doping. In order to understand the influence these factors have on the transport properties of these materials it will be necessary to probe how the resistance of

the materials change as a function of temperature and applied field. This has traditionally been done using four–point probe measurements.

The optical properties of these materials are also extremely interesting. Spectral information is vital since it allows us to determine how the phonon modes respond to external stimuli. This thesis exploits a new magneto-optical experimental technique, the Magnetorefractive Effect, which probes both the spectral and magnetotransport properties of these materials as a function of applied field and temperature. The next chapter will focus on modelling the Magnetorefractive Effect in the mixed-valence manganites.

Chapter 3

The Magnetorefractive Effect

3.1 Introduction

In 1995, Jacquet and Valet (18) discovered a new magneto-optical effect. They showed theoretically that the change in the optical conductivity of magnetic metallic multilayers under the application of a magnetic field, will generally be associated with a significant change in the refractive index. Hence, they called this new magneto-optical effect the magnetorefractive effect (MRE). Jacquet and Valet then made optical transmission measurements under an applied magnetic field through [$Ni_{80}Fe_{20}$/Cu/Co/Cu] multilayers, in the IR region between 2 and 20 μm. These measurements clearly demonstrated the existence of the predicted effect in reasonable agreement with their theoretical calculations.

Since 1995, the effect has been observed in many other materials that exhibit a large magnetoresistance. These include multilayers, like those Jacquet and Valet studied, all-metallic granular alloys of Co-Ag (48) and metal-insulator nanogranular alloys of Co-(Al-O) (21) and CoFe(Al-O) (22). More recently, Granovsky *et al.* have demonstrated the effect in nanocomposites of CoFe-MgF (19) and (CoFeZr)-SiO_n (20) and this thesis demonstrated that this effect can also be observed in the metallic compositions of perovskite samples (47).

The MRE($\%$) is defined as:

$$MRE(\%) = 100 \times \frac{R_0 - R_H}{R_H} \tag{3.1}$$

where R_0 is the IR reflectivity measured in zero applied field and R_H is the IR reflectivity measured in an applied field.

My research into the mixed-valence manganites began with MRE measurements of bulk, polycrystalline LSMO samples. Since these initial experiments, the emphasis has shifted towards studies of thin film samples of LBMO, LCMO and LSMO. Unlike traditional four-point probe measurements, which show how the resistance of the sample changes in an applied magnetic field, the MRE provides additional spectral information, such as IR absorption and phonon resonance features.

The focus of this chapter is the modelling of the MRE in the mixed valence manganites. However, rather than attempting to model a specific system at this stage, instead we shall model the MRE in a generic manganite system. The advantage of using a generic system is that it allows us to explore what happens when the parameters in the model are changed and thus answer the question: 'What happens if I change this?'

3.2 Modelling the Magnetorefractive Effect

The simplest system to model is a bulk sample. Thin film samples are complicated by the fact that the layer of interest must be deposited onto a substrate, and although the substrate is non-magnetic and insulating, it can still influence the results. This chapter will therefore begin by establishing a suitable model for the MRE in bulk samples of a generic manganite sample before introducing the added complexity of a substrate.

For the purpose of this model, it shall be assumed that the generic manganite system is metallic. This is plausible since for low values of doping, x, all of the manganites we have studied are in a ferromagnetic and metallic phase below their Curie temperatures. Since it is the dopant that provides the free carriers required for conduction by the double exchange process, low values of x limits the number of free carriers available, meaning that although the system is metallic, it is not a very good metal.

The MRE is an optical effect and the optical properties of a material are determined by its complex dielectric function, $\varepsilon(\omega)$. Hence, we shall start our modelling by determining the form of the complex dielectric function for our generic bulk manganite system.

3.3 The complex dielectric function

3.3.1 The Drude term and the plasma frequency

If it is assumed that the generic system is metallic, then $\varepsilon(\omega)$ has a linear dependence with the frequency-dependent conductivity, $\sigma(\omega)$ through the Drude relation (see, for example, Ashcroft and Mermin, 'Solid State Physics' (136)):

$$\varepsilon_{Drude}(\omega) = \varepsilon_\infty + \frac{\imath\sigma(\omega)}{\omega\varepsilon_0} \tag{3.2}$$

where ω is the frequency of the incident radiation and ε_0 is the permittivity of free space. ε_∞ is the high frequency response ($\omega = \infty$) of the dielectric function to optical excitation of frequency ω and its value is material specific.

Doped lanthanum manganites with the perovskite structure are ionic systems with the form $A_{1-x}B_xMnO_3$, where A is a trivalent rare earth cation and B is a divalent alkaline earth cation. As formulated by both Boris *et al.* (24) and Kim *et al.* (26), equation 3.2 can also be expressed in terms of the plasma frequency, ω_p:

$$\varepsilon_{Drude}(\omega) = \varepsilon_\infty + \frac{\imath\sigma(\omega)}{\omega\varepsilon_0} = \varepsilon_\infty - \frac{\omega_p^2}{\omega^2 + \imath\gamma\omega} \tag{3.3}$$

where γ is a damping term.

In order to derive this expression we need to start from the frequency dependent conductivity, $\sigma(\omega)$. $\sigma(\omega)$ is defined as (136):

$$\sigma(\omega) = \frac{\sigma_0}{1 - \imath\omega\Gamma}, \sigma_0 = \frac{Ne^2\Gamma}{m} \tag{3.4}$$

where Γ is a relaxation time, N is the number of carriers per unit volume, e is the charge of the free carriers and m is their mass.

Substituting this expression for $\sigma(\omega)$ in equation 3.2, then:

$$\varepsilon(\omega) = \varepsilon_\infty + \frac{\imath\sigma(\omega)}{\varepsilon_0\omega} = \varepsilon_\infty + \frac{\imath\sigma_0}{\varepsilon_0\omega(1 - \imath\omega\Gamma)} \tag{3.5}$$

Equation 3.5 can be re-expressed if we substitute for σ_0 from equation 3.4 such that:

$$\varepsilon_\omega = \varepsilon_\infty + \frac{\imath N e^2 \Gamma}{\varepsilon_0 m\omega(1 - \imath\omega\Gamma)} \tag{3.6}$$

or, equivalently:

$$\varepsilon_\omega = \varepsilon_\infty - \frac{N e^2 \Gamma}{\imath\varepsilon_0 m\omega(1 - \imath\omega\Gamma)} = \varepsilon_\infty - \frac{N e^2 \Gamma}{\imath\varepsilon_0 m(\omega - \imath\omega^2\Gamma)} \tag{3.7}$$

Using the fact that Γ=$1/\gamma$ (where γ is a damping term) and defining the plasma frequency, ω_p such that:

$$\omega_p^2 = \frac{N e^2}{\varepsilon_0 m} \tag{3.8}$$

We can simplify equation 3.7 such that:

$$\varepsilon_{Drude}(\omega) = \varepsilon_\infty - \frac{\omega_p^2}{\omega^2 + \imath\gamma\omega} \tag{3.9}$$

This is the equivalent of the expression given by equation 3.3 that has been used by Boris *et al.* (24) and Kim *et al.* (26).

The plasma frequency, ω_p, is very important. It is the natural frequency of oscillation of electrons in a plasma displaced relative to the ion background. In materials where the effective mass (m_e^*) of the carriers is not necessarily that of a free electron, we can re-express the plasma frequency :

$$\omega_p = \sqrt{\frac{N e^2}{m_e^* \varepsilon_0}} \tag{3.10}$$

The plasma frequency also determines whether or not waves can propagate in the medium. If $\omega < \omega_p$ then waves cannot propagate and incident waves of lower frequency than the plasma frequency will be reflected. The manganites have a low number of free carriers compared to a normal metal and hence have a relatively low plasma frequency. This means

that visible light will propagate in these materials with very little being reflected, giving the manganites their black appearance. IR light has a frequency lower than the plasma frequency, however, and so it is reflected. This forms the basis of the MRE experiments which use IR light to probe the changes in the reflectivity of the sample when a magnetic field is applied.

3.3.2 The Resonance term

One of the reasons that IR light is used in spectroscopy is that many materials have spectral features that are sensitive to light of this wavelength since vibrational modes in many atoms and molecules are resonant at these wavelengths. The mixed-valence manganites also have spectral features that are sensitive to IR light. In particular, there are phonon modes that can be associated with the stretching and bending modes of the Mn-O bonds. These spectral features manifest themselves as resonances in the system since the phonon modes are resonant for certain frequencies of the incident light. Since these resonances are part of the system's response to an optical stimulus they need to be incorporated into the material's dielectric function. Indeed, all of the systems transverse and longitudinal phonon modes need to be considered. This is done by treating the j resonances of the system as the sum of a series of simple harmonic oscillators. Hence the following term is added to the dielectric function (see, for example, Boris *et al.* (24):

$$\sum_{j=1}^{n} \frac{S_j^2}{k_j^2 - k^2 - \imath\gamma_j k} \tag{3.11}$$

Here, k_j is the wavenumber of the j^{th} resonance, k is the wavenumber of the incident light, γ_j is a damping term for the resonance and S_j is the oscillator strength. Spectroscopy is usually the domain of chemists who use units of wavenumber in cm^{-1} for spectral features. This practice is continued here since it is the established convention for spectroscopic results. To convert to frequency simply remember that $\omega \propto ck$. Adding this term to the Drude term gives the following form for the complex dielectric function:

$$\varepsilon(\omega) = \varepsilon_\infty - \frac{\omega_p^2}{\omega^2 + \imath\gamma\omega} + \sum_{j=1}^{n} \frac{S_j^2}{k_j^2 - k^2 - \imath\gamma_j k} \tag{3.12}$$

3.3.3 Magnetic field dependence

The complex dielectric function given by equation 3.12 has no magnetic field dependence. The magnetic field dependence is incorporated by adding a term to the Drude part of the dielectric function such that:

$$\varepsilon(\omega) = \varepsilon_\infty - \frac{\omega_p^2}{\omega^2 + \imath\gamma\omega}(1 + \eta m^2) + \sum_{j=1}^{n} \frac{S_j^2}{k_j^2 - k^2 - \imath\gamma_j k} \tag{3.13}$$

In equation 3.13, m is a field dependent term (with values $0 < m < 1$) which gives a measure of the magnetization of the sample ($m \propto M/M_S$, i.e the ratio of the magnetization, M to the magnetization at saturation, M_S). This term is squared since the MRE is symmetric for positive and negative applied fields and so the field dependence must be an even function of the applied field. The η is simply a scaling parameter for the strength of the magnetization.

When deciding on how to incorporate the magnetic field dependence into the model, there were arguments for making the resonance term field dependent as well. The experimental data were ambiguous as to whether the change in the MRE with applied field came solely from the Drude term or if the resonances were themselves field dependent, which could be the case if magnetic polarons were forming. In the end it was decided that it does not really matter if the resonance term has its own field dependence since this can be accounted for simply by increasing/decreasing the oscillator strength, S_j, though of course, this does not account for the fact that S_j could scale as a function of the applied field.

What is clear experimentally, however (see Chapters 5 and 6), is that electrical conduction in these materials increases in a magnetic field. The Drude term in the dielectric function is directly proportional to the number of free carriers in the system and by extension to the conductivity of the sample. Hence it was decided that the magnetic field should increase the weighting of the Drude term in the dielectric function to represent the increased conductivity in an applied field.

3.4 Reflection coefficients

The link between the complex dielectric function and the MRE is through the Fresnel equations. Once the form of the dielectric function in zero field and in an applied field is known, the Fresnel equations can be used to calculate reflection coefficients for our generic manganite system. Once the reflection coefficients have been determined, calculating the reflectivity, and hence the MRE, is very straightforward.

The Fresnel equations can be used to calculate the reflection coefficients for both s- and p-polarized incident light and take the following form (see, for example, page 124 of Hecht's 'Optics' (Third Edition) (137)):

$$r_{S0} = \frac{\cos\theta - \sqrt{\varepsilon_{m=0} - \sin^2\theta}}{\cos\theta + \sqrt{\varepsilon_{m=0} - \sin^2\theta}} \tag{3.14}$$

$$r_{P0} = \frac{\cos\theta \cdot \varepsilon_{m=0} - \sqrt{\varepsilon_{m=0} - \sin^2\theta}}{\cos\theta \cdot \varepsilon_{m=0} + \sqrt{\varepsilon_{m=0} - \sin^2\theta}} \tag{3.15}$$

$$r_S = \frac{\cos\theta - \sqrt{\varepsilon_{m\neq0} - \sin^2\theta}}{\cos\theta + \sqrt{\varepsilon_{m\neq0} - \sin^2\theta}} \tag{3.16}$$

$$r_P = \frac{\cos\theta \cdot \varepsilon_{m\neq0} - \sqrt{\varepsilon_{m\neq0} - \sin^2\theta}}{\cos\theta \cdot \varepsilon_{m\neq0} + \sqrt{\varepsilon_{m\neq0} - \sin^2\theta}} \tag{3.17}$$

r_{S0} and r_{P0} are the reflection coefficients for s- and p-polarized light in zero applied magnetic field ($m = 0$) and r_S and r_P are the same reflection coefficients in an applied magnetic field ($m \neq 0$). The $\varepsilon_{m=0}$ and $\varepsilon_{m\neq0}$ terms are the complex dielectric functions from equation 3.13 for zero field ($m = 0$) and for an applied field ($m \neq 0$), respectively. The reflection coefficients depend upon the angle of incidence to the plane of the normal to the surface of the sample, θ. Our experimental setup had a fixed angle of incidence of $\theta \backsimeq 65^\circ$ and this value was used in the modelling.

The reflectivities, R_{S0}, R_{P0}, R_S and R_P can be calculated by squaring the modulus of the reflection coefficients, e.g. $R_{S0} = |r_{S0}|^2$, etc.. These reflectivities are then used to calculate the MRE(%)

3.5 Calculating the MRE(%)

The MRE(%) was defined in equation 3.1. However, accounting for the polarization of the incident light, for randomly polarized incident light equation 3.1 becomes:

$$MRE(\%) = 100 \times \frac{(R_{S0} + R_{P0}) - (R_S + R_P)}{(R_S + R_P)} \tag{3.18}$$

where R_{S0} and R_{P0} are the reflectivities measured for S and P-polarized incident light in zero applied magnetic field, and R_S and R_P are those measured in an applied field.

We are now in a position to model IR and MRE spectra for a generic bulk manganite sample.

3.6 Modelling results for a bulk manganite sample

In this section we shall examine the results of modelling the IR and MRE spectra in a generic bulk manganite system using the form of the dielectric function given by equation 3.13. Once we have established the basic result, we shall then explore the consequences that changing the model parameters has on the spectra. The spectra were all modelled using MathCAD, and a copy of the MathCAD code can be found on the CD that accompanies this thesis. A brief description of each of the MathCAD programs used in the modelling can be found in Appendix A.1.

3.6.1 Model parameters

The parameters that have been used in the initial modelling of a bulk manganite sample are shown in Table 3.1.

The initial parameters chosen for the model require some justification. First, let us consider the resonance parameters:

The k-values for the resonance parameters are based upon those for a bulk LSMO sample (25). Since the experimental data will focus on bulk LSMO samples, this seemed

Resonance parameters	j=1	j=2	j=3
k_j (cm^{-1}); λ (μm)	161.6; 61.9	323.2; 30.9	635.3; 15.7
γ_j (cm)	50	50	50
S_j (cm^{-1})	600	600	600
Other parameters			
N	$1.0 \times 10^{26}/m^3$		
ε_∞	9.0		
γ	$1 \times 10^{15} Hz$		
m_e^*	9.11 $\times$ 10^{-31} kg		
η	0.25		

Table 3.1: The parameters used in the modelling of a bulk manganite sample

like a sensible place to begin our modelling. The γ_j and S_j values are completely arbitrary at this point and we shall examine what happens when we change these values later.

The starting values for the other parameters used in the model have been chosen based upon educated estimates of their values. For example, in a normal metal, the number of free carriers, N, is of the order of 10^{28} /m^3. In the manganites, the free carriers are introduced by doping the sample, and hence N will be at least an order of magnitude lower, perhaps more once the restrictions of the double exchange conduction mechanism are enforced. The ε_∞ value was chosen based upon values given by Boris *et al.* (24) for similar materials. Initially, the effective mass of the free carriers, m_e^*, has been chosen to be the mass of an electron. The consequence of changing the effective mass of the free carriers will be considered below. The choice of the value for γ is not quite so arbitrary, however. For a metallic system, we require that $\omega^2 < \imath\omega\gamma$. For IR light, $\omega \simeq 2 \times 10^{14}$ Hz at $\lambda = 10\mu$m, and hence, γ must be larger than 2×10^{14} Hz.

3.6.2 Modelled IR spectra

In Figure 3.1 we see the modelled IR reflection spectra for randomly, s- and p-polarized incident light based on the model parameters given in Table 3.1.

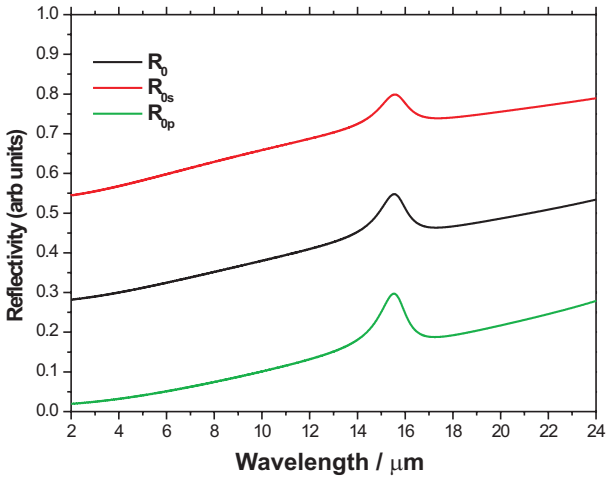

Figure 3.1: Modelled IR spectra for a generic bulk manganite sample as determined by the parameters given in Table 3.1 and equation 3.13. (Original in colour)

In Figure 3.1, we see that the reflectivity increases as the wavelength increases. This trend is expected since more light will be reflected the further we move away from the plasma edge. The resonance feature at 15.7 μm (635.3 cm^{-1}) is very prominent, and we observe a greatly enhanced reflectivity at this position. We also observe that for an angle of incidence of 65°, the s-component of the reflectivity is much larger than for p-polarized light, and the randomly polarized component is given by equation 3.18.

3.6.3 Modelled MRE spectra

The modelled IR spectra shown in Figure 3.2 can used to determine the MRE spectra for our generic sample by substitution in equations 3.1 and 3.18.

Figures 3.2a-c show the modelled MRE spectra for p-, s- and randomly polarized light respectively. Whilst the IR spectra showed the largest reflectivity for s-polarized light, the largest MRE(%) is observed for p-polarized incident light. Each of the lines in the plots

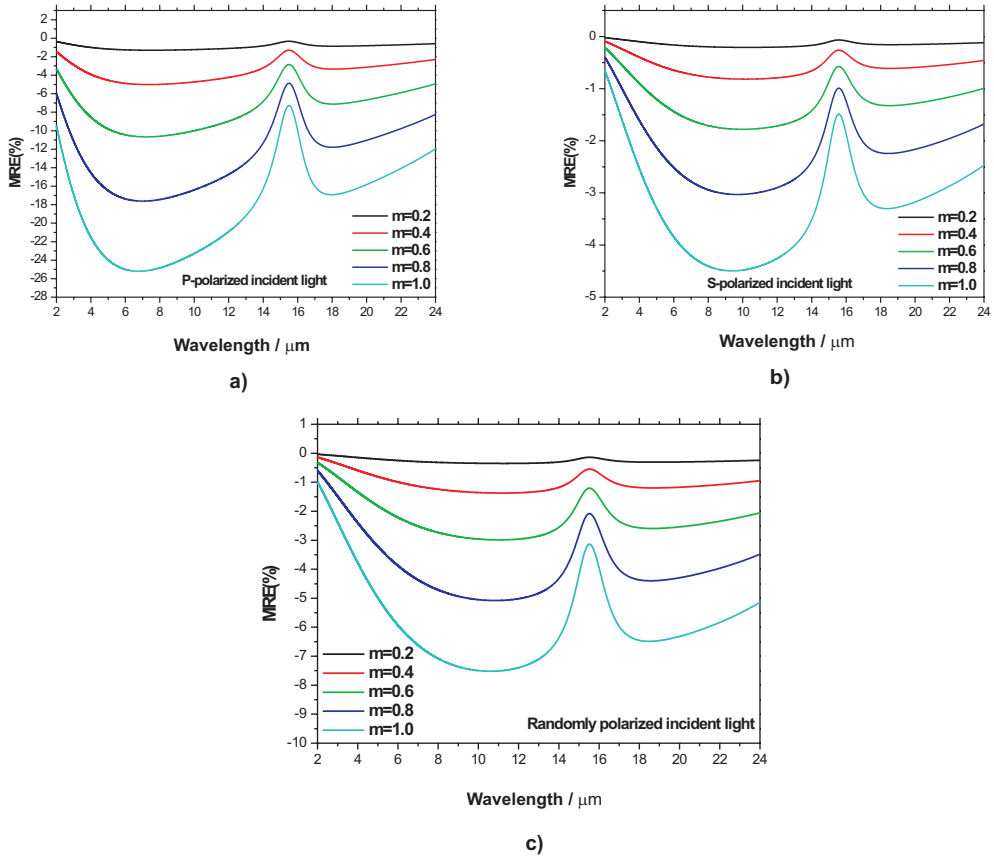

Figure 3.2: Modelled MRE spectra for a generic bulk manganite sample using a) p-polarized, b) s-polarized and c) randomly polarized incident light. The model parameters are given in Table 3.1. (Original in colour)

corresponds to a different value of m in equation 3.13.

As m increases, the Drude-like term in the dielectric function becomes increasingly important and this is reflected in the MRE plots. Interestingly, increasing m also causes the resonance feature to scale with the applied field. It would appear that the resonance feature *is* magnetic field dependent, albeit indirectly, and is sensitive to the change in the balance between the terms in the complex dielectric function caused by increasing the weighting of the Drude-like term.

3.6.4 The consequences of changing parameter values on the IR and MRE spectra

Now we have established the basic form of the modelled spectra, we can examine the consequences of changing the values of the parameters used in the model. In particular, we can see the effect changing the plasma frequency, ω_p, the oscillator strengths, S_j, the damping factors, γ and γ_j, and the frequency of the resonance in equation 3.13 have on the modelled spectra.

3.6.4.1 Changing the plasma frequency

The magnitude of the plasma frequency is very important since it determines the contribution to the dielectric function from the Drude term and consequently the magnetic field dependence as setup in this model. The plasma frequency scales as the ratio of the number of free carriers, N, to their effective mass, m_e^*. Experimentally we cannot distinguish between these two parameters and hence, it does not matter which is changing in the model. Thus we shall model the effect of increasing the effective mass of the carriers (this has the same effect as reducing N and lowering ω_p).

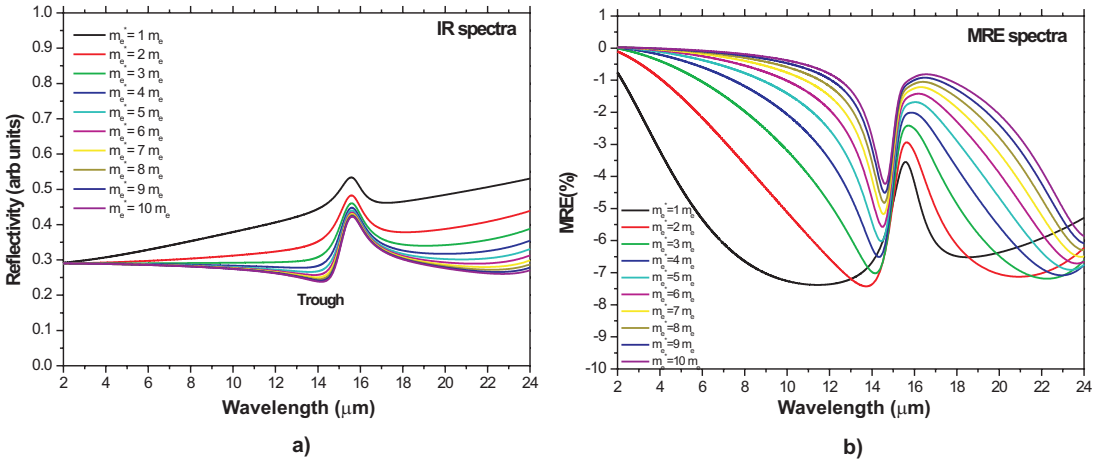

Figure 3.3: The effect of changing the effective carrier mass on a) the modelled IR spectra and b) the modelled MRE spectra for a generic bulk perovskite sample. Increasing the effective mass of the carriers is directly proportional to a reduction in the plasma frequency. (Original in colour)

In Figures 3.3a and b, we see the effect changing the effective mass of the free carriers has on the IR and MRE spectra of our generic bulk perovskite sample. In the figures, only the effective mass of the carriers (m_e^*) in the term for the plasma frequency (equation 3.10) has been changed, all of the other parameters are as given in Table 3.1. The value of m in equation 3.13 is taken to be $m = 1$, i.e, the sample is at magnetic saturation and, hence, the MRE($\%$) values in Figure 3.3b represent the MRE for the maximum applied field. Let us first consider the effect ω_p has had on the IR spectra:

Increasing the effective mass of the carriers reduces the plasma frequency of the sample. As the plasma frequency is lowered, the weighting of the Drude term in the dielectric function also becomes less significant and we therefore expect to see a drop in the reflectivity of the sample. This is what is observed in Figure 3.3a. As the effective mass of the carriers increases (and ω_p decreases) the plasma edge shifts to longer wavelengths and so more of the incident IR light will be transmitted instead of reflected.

Figure 3.3a also shows an effect that is not easily predicted: As the effective mass of the carriers increases we observe the formation of a trough in the reflectivity at around 14-15μm. The origin of this trough is not clear. Most likely it occurs due to the increased weighting of the resonance term in equation 3.13 as the Drude-like term decreases.

A similar effect is observed for the MRE spectra in Figure 3.3b. A reduction in the plasma frequency, brought about by increasing the effective mass of the free carriers, totally changes the shape of the MRE spectra. As the plasma frequency drops, the Drude-like term in the dielectric function is no longer the dominating term and this results in a change in the curvature of the spectra at low to mid-IR wavelengths (2-10μm) as the sample becomes less conducting and less reflective at these wavelengths. The trough observed in the IR spectra begins to form for effective masses greater than 2m$_e$. The position of the trough shifts to higher wavelength as the effective mass is increased, and it also becomes smaller in magnitude and narrower.

3.6.4.2 Changing the Oscillator strength

The oscillator strength was adjusted by multiplying the oscillator strength (S$_j$) for each resonance by an appropriate scaling factor. This scaling factor took the form, since it

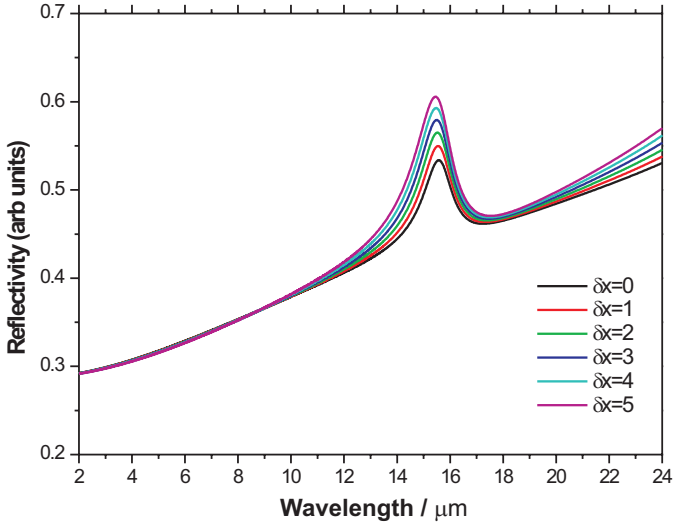

Figure 3.4: The effect of changing the oscillator strength on the IR spectra of a generic bulk perovskite sample. (Original in colour)

allowed me to easily scale the oscillator strength in a linear fashion:

$$A_x = 1 + 0.2\delta x \tag{3.19}$$

Such that:

$$\varepsilon(\omega) = \varepsilon_\infty - \frac{\omega_p^2}{\omega^2 + \imath\gamma\omega} + \sum_{j=1}^{n} \frac{A_x \cdot S_j^2}{k_j^2 - k^2 - \imath\gamma_j k} \tag{3.20}$$

The δx term in equation 3.19 has integer values between 0 and 5. This basically means that S_j is scaled from its original value to twice its original value in increments of 0.2.

The dielectric function used in equation 3.20 has no magnetic field dependence. This is to prevent confusion between effects caused by scaling the field, and those caused by scaling S_j. The results of scaling S_j using this method can be seen in Figure 3.4:

From the figure, we observe that the resonance feature is asymmetric. We can also see that as well as increasing in magnitude, the position of the peak in the reflectivity shifts slightly to lower wavelength as the magnitude of the oscillator strength is increased. The

magnitude of the resonance feature doubles in size as the strength is doubled in magnitude, but it also gets broader too in proportion.

At short wavelengths, well away from the resonance, the magnitude of the oscillator strength has no impact on the IR spectra. However, after the first resonance, the spectra appears to fan out. This is due to the influence of the next resonance peak at 30.9μm, which is not shown in the figure.

3.6.4.3 Changing the damping factor

There are two damping factors that appear in the zero field dielectric function, γ in the Drude-like term, and γ_j in the resonance term. Let us consider the effect of changing these parameters in turn, starting with the γ in the Drude-like term.

As described above, the magnitude of γ is somewhat constrained by the assumption that the sample is metallic. For a metallic system, we require that $\omega^2 < \imath\omega\gamma$. For IR light, $\omega \simeq 2 \times 10^{14}$ Hz at $\lambda = 10\mu$m, and hence, γ must be larger than 2×10^{14} Hz. However, we are now in a position to ascertain what happens if we ignore this restriction. In Figure 3.5 we see the effect of scaling γ from 1×10^{10} to 1×10^{20} Hz. Again, this is done for the zero field dielectric function given by equation 3.12.

When γ is very small (10^{10}-10^{12}Hz) the $\imath\gamma\omega$ term becomes insignificant compared to the ω^2 term in the denominator and hence can be ignored. This means that the Drude term has no imaginary part. However, the imaginary part of the Drude term is directly proportional to the conductivity of the sample, so as this term becomes insignificant, the sample is no longer metallic and electromagnetic waves cannot propagate. This leads to the 100$\%$ reflection observed in the figure at these frequencies.

As γ increases in magnitude the reflectivity drops and the resonance feature becomes apparent again. Interestingly as γ goes beyond our original value of 10^{15}Hz we see the formation of the same trough in the reflectivity as was observed when we reduced the plasma frequency. This makes sense since as we increase γ by several orders of magnitude, the $\imath\gamma\omega$ will become increasingly dominant, and will eventually be such that $\imath\gamma\omega >> \omega_p^2$. Hence, the Drude-like term will again assume a lesser weighting in the complex dielectric function, resulting in exactly the same effect as was observed when we lowered the plasma

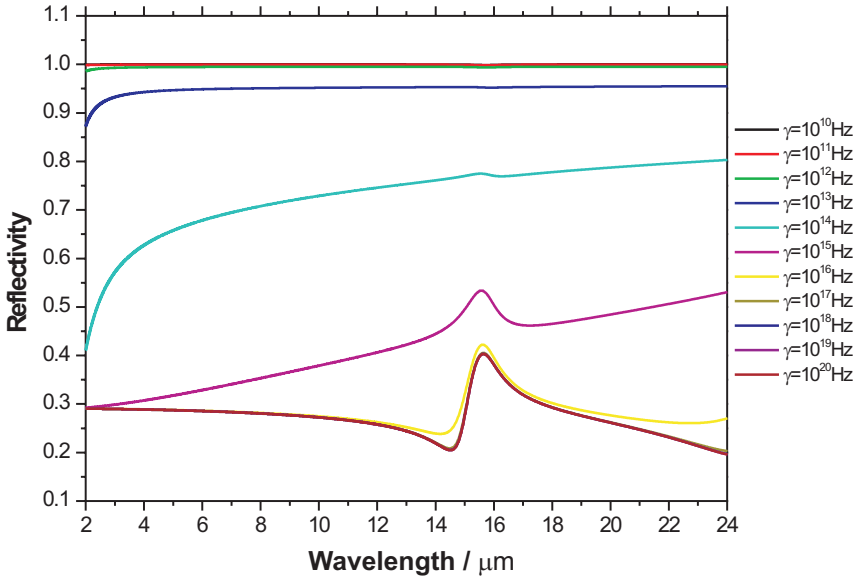

Figure 3.5: The effect of changing the damping factor γ in the Drude-like term of the complex dielectric function on the IR spectra of a generic perovskite sample. (Original in colour)

frequency.

The second damping term, γ_j, appears in the resonance term. We can modify this term using a similar method to that which we used to scale the oscillator strength. Assuming again that we have no magnetic field dependence, the dielectric function will then take the following form:

$$\varepsilon(\omega) = \varepsilon_\infty - \frac{\omega_p^2}{\omega^2 + \imath\gamma\omega} + \sum_{j=1}^{n} \frac{S_j^2}{k_j^2 - k^2 - \imath A_x \gamma_j k} \tag{3.21}$$

The A_x term has the same form as in equation 3.19. As Figure 3.6 demonstrates, increasing the damping factor broadens the width of the resonance feature. The resonance feature remains asymmetric and again we see a slight shift to lower wavelength as the γ_j term is increased.

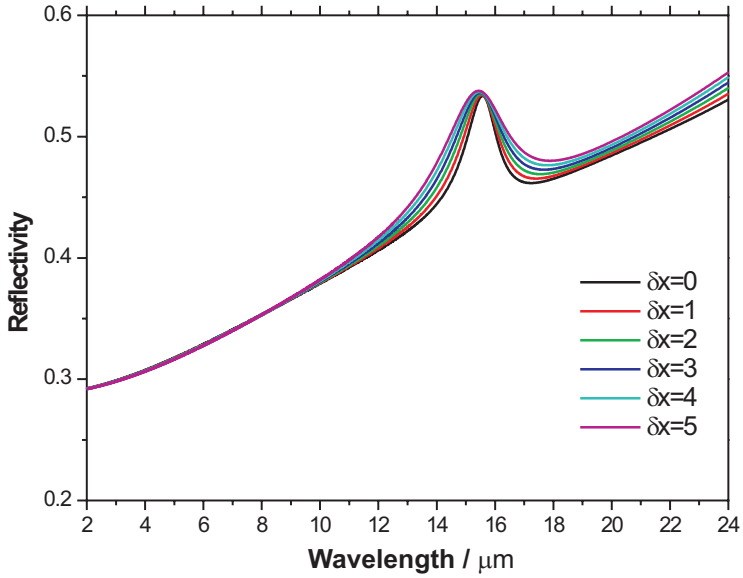

Figure 3.6: The effect of changing the damping factor γ_j in the resonance term of the complex dielectric function on the IR spectra of a generic perovskite sample. (Original in colour)

3.6.4.4 Changing the resonance position

The position of the resonance can also be shifted using a similar method. The dielectric function will thus take the following form:

$$\varepsilon(\omega) = \varepsilon_\infty - \frac{\omega_p^2}{\omega^2 + \imath\gamma\omega} + \sum_{j=1}^{n} \frac{S_j^2}{A_x k_j^2 - k^2 - \imath\gamma_j k} \tag{3.22}$$

The results of shifting the resonance position are shown in Figure 3.7. The position of the resonance feature can, therefore, be tuned to whichever frequency is required, though the reflectivity at the peak of the resonance will decrease by an amount dependent on the position of the plasma edge.

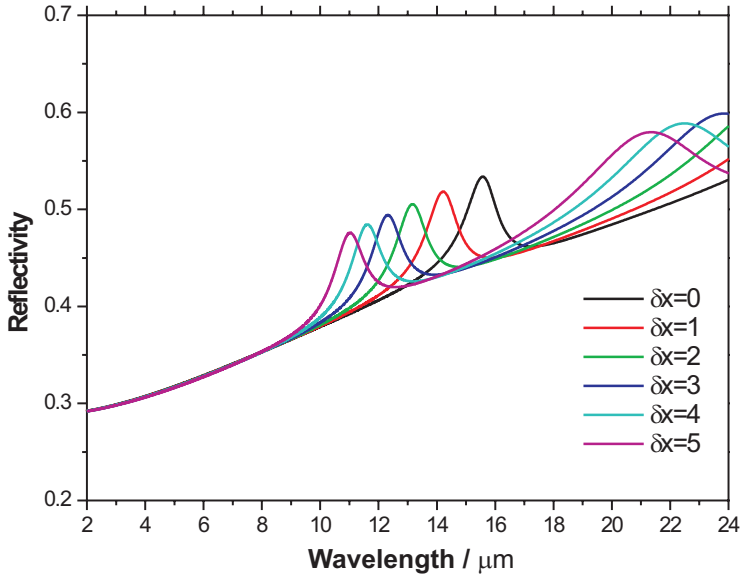

Figure 3.7: The effect of shifting the resonance position on the modelled IR spectra of a generic bulk perovskite sample. (Original in colour)

3.7 Modelling the MRE in a thin film sample

In this section we shall turn our attention to the modelling of the MRE in the more complex thin film manganite samples. To begin, we shall consider the form of the dielectric function for an $SrTiO_3$ substrate. Then we shall consider the form of the dielectric function for the film itself and then finally for the film-substrate system. This will then allow us to model the MRE in such a system.

3.7.1 Modelling an $SrTiO_3$ substrate

To model the $SrTiO_3$ (STO) substrate, two different approaches have been considered. The first is a classical model which models the dielectric function of the substrate (ε_{sub}) as a sum of the high frequency response ($\varepsilon_{sub\infty}$) and a sum of damped harmonic oscillators. This is similar to the form of the dielectric function used to model the bulk manganite sample, the main difference being that, since the substrate is insulating, it does not have a Drude-like term in its dielectric function. This is a three parameter model since you

can only parameterize the wavenumber of the transverse phonon mode resonance (k_{T_j}), its damping term (γ_{T_j}) and the strength of the oscillator (S_j). This three parameter model has the following form, which is equivalent to equation 3.12 with the Drude-like term removed:

$$\varepsilon_{sub}(k) = \varepsilon_{sub\infty} + \sum_{j=1}^{n} \frac{S_j^2}{k_{T_j}^2 - k^2 - \imath\gamma_{T_j}k} \tag{3.23}$$

The second approach is to use a four parameter model to describe the form of the dielectric function in the substrate. This model has been used by Boris *et al.* (24) and Gervais (138) to successfully fit the IR reflectivity spectra of several oxide based perovskites. This model uses a factorized form of the dielectric function and takes the form:

$$\varepsilon_{sub}(k) = \varepsilon_{sub\infty} \cdot \prod_{j=1}^{n} \frac{k_{L_j}^2 - k^2 - \imath\gamma_{L_j}k}{k_{T_j}^2 - k^2 - \imath\gamma_{T_j}k} \tag{3.24}$$

The factorized form of the dielectric function used in the four parameter model can be derived from Maxwell's equations and it assumes that the transverse optical (TO) phonon modes are the poles, while the longitudinal optical (LO) phonon modes are the zeroes, of the dielectric response (23). If these poles and zeroes are complex, then factorization gives the result of equation 3.24 . The four parameter model is itself an extension of the Lydanne-Sachs-Teller relation which states that at zero frequency:

$$\varepsilon_{\omega=0} = \varepsilon_{\infty} \cdot \frac{\omega_L}{\omega_T} \tag{3.25}$$

The adjustable parameters for the j^{th} complex pole p and complex zero z in equation 3.24 uniquely determines four phonon mode parameters for the j^{th} TO-LO pair: the wavenumbers k_{T_j}, k_{L_j} and the damping terms, γ_{T_j}, γ_{L_j}. The assumption of different parameters for the TO and LO modes is necessary when the TO and LO modes have different decay channels and different damping rates (24). Boris *et al.* used a Kramers-Kroning analysis to get a first approximation of the values for the $\varepsilon_{sub\infty}$ and the phonon terms in an STO substrate. These values provided a starting point for a least squares fit of the reflectivity spectra to equation 3.24. The values they obtained are listed in Table 3.2 and it is these values that we too shall use in our model.

The two forms for the substrate's dielectric function were then used in the Fresnel equations to obtain reflection coefficients, and hence the reflectivity, for s and p-polarized incident light. The modelled IR spectra obtained from the three and four parameter models can be seen in Figure 3.8.

Figure 3.8 clearly shows that the two models for the STO substrate's dielectric function produce very different results. The three parameter model shows no difference for s- and p-polarized light, whereas the four-parameter model exhibits a clear polarization dependence. However, the main difference between the two models is the shape of the spectra at low wavenumber. The three parameter model features many more peaks and troughs than is observed for the four parameter model. Each of the transverse optical phonons is represented as a peak in the reflectivity in the three parameter model, whereas for the four parameter model, the peaks merge together.

The reason for this can be seen in Table 3.2. A closer inspection of the k_{T_j} and k_{L_j} values shows that for some of the resonances, the wavenumbers for the TO and LO phonons are very close (e.g. $j = 3$ and $j = 6$), but in some cases the resonant wavenumber for the LO mode is at a higher wavenumber than the next TO mode (e.g. $j = 2$ and $j = 4$). This means that the TO and LO phonon modes of adjacent pairs in the non-conducting substrate have some overlap that is not considered in the three parameter model. The three parameter model works better in metallic systems where the TO and LO modes are close together, and no such overlap is observed.

Figure 3.9 shows an IR spectrum that was measured experimentally for an STO substrate. The experimentally measured spectrum closely resembles the spectrum modelled using the four parameter model. All of the features seen in the modelled spectrum can be seen in the experimental spectrum. The sharp spike seen in Figure 3.9 at approximately 660 cm^{-1} is caused by CO_2 absorption of the IR light and is a contaminant that should be ignored.

The minima at approximately 500 cm^{-1} and 870 cm^{-1} are also well represented by the model, as is the width of the peak between these minima. As we shall see later, the position of the latter minimum becomes very important when we model the MRE.

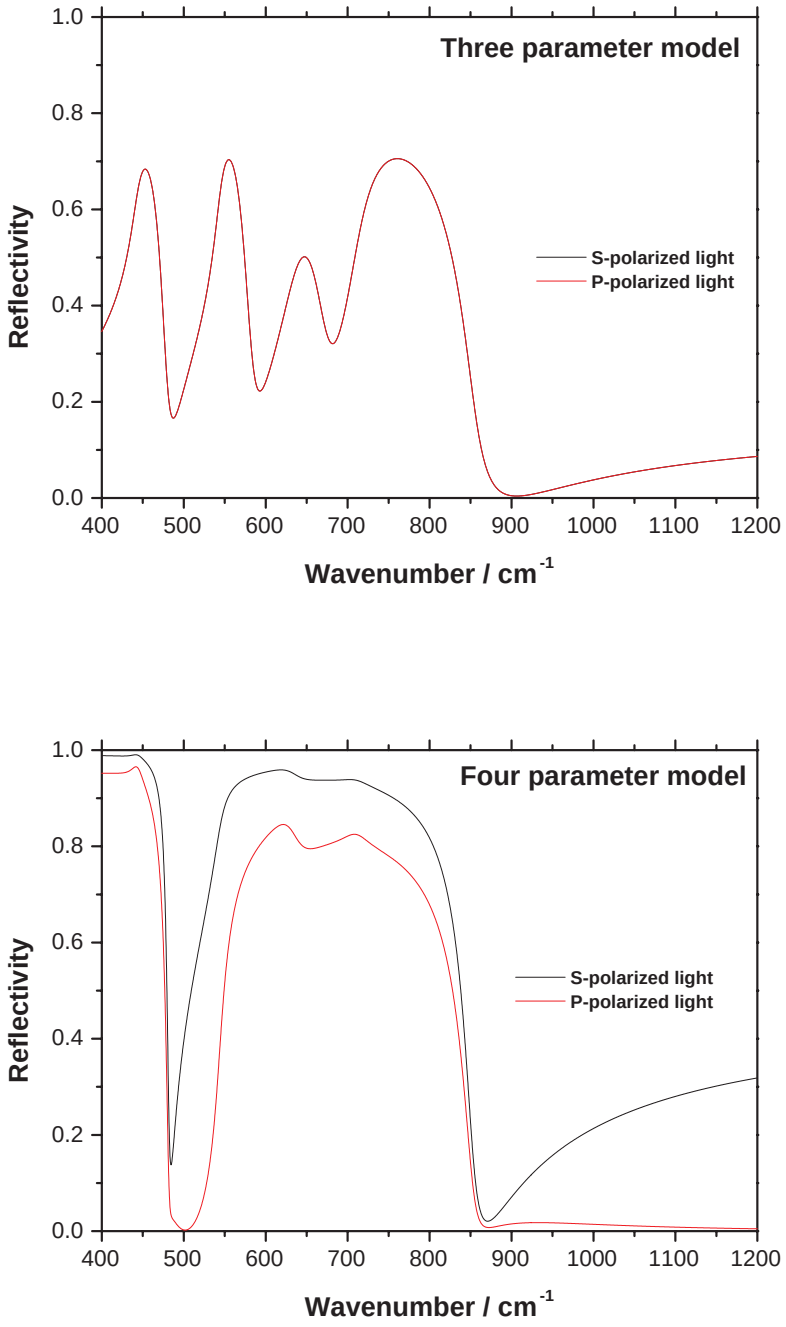

Figure 3.8: Modelled IR spectra using the three parameter model (top) and the four parameter model (bottom) of the STO dielectric function for s- and p-polarized incident light. The parameters used in the model are given in Table 3.2. (Original in colour)

STO	$\varepsilon_{sub\infty} = 5.2$					
Three parameter model						
Resonance parameters	j=1	j=2	j=3	j=4	j=5	j=6
k_{T_j} (cm^{-1})	92	175	443.5	544	635.1	710.1
γ_{T_j} (cm)	16	6.2	18.6	17	43	41
$S_j^{\dagger}$ (cm^{-1})	600	600	600	600	600	600
Four parameter model						
k_{T_j} (cm^{-1})	92	175	443.5	544	635.1	710.1
k_{L_j} (cm^{-1})	171	476	443.8	793	635.2	710.8
γ_{T_j} (cm)	16	6.2	18.6	17	43	41
γ_{L_j} (cm)	3.8	5.3	18.6	24	40	41

† The arbitrary value of 600 cm^{-1} was chosen for each of the oscillator strengths.

Table 3.2: A summary of the parameters used in the three and four parameter models for an STO substrate. All values are as given by Boris *et al.*(24)

The overall shape of the experimental spectrum closely resembles that modelled for s-polarized incident light. The geometry of the experimental setup (see Chapter 4) gives an angle of incidence of approximately 65° which favours reflection for s-polarized light. Hence, randomly polarized light will have a larger s-component in our reflectivity spectra.

3.7.2 Modelling the thin film

The thin film is modelled using a dielectric function that has the same form as that used for the bulk sample. Hence, the dielectric function in zero field (ε_{film0}) takes the form:

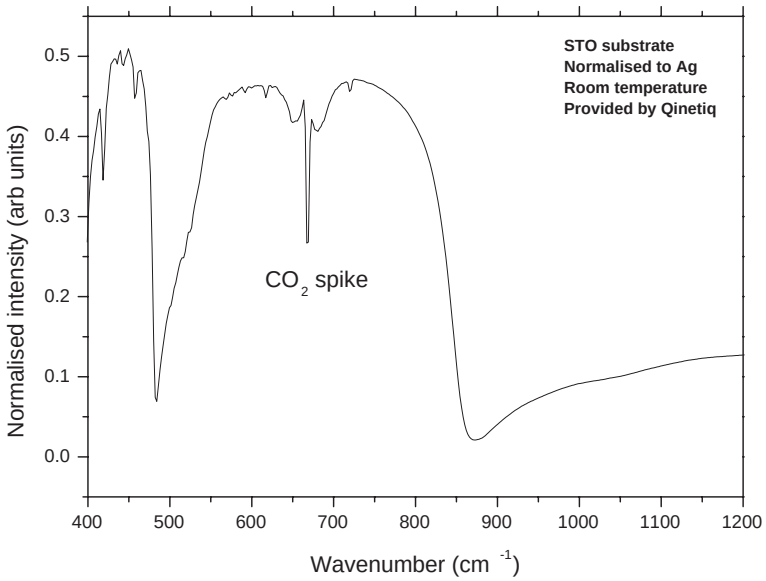

Figure 3.9: Normalized experimental IR spectrum for an $SrTiO_3$ substrate for randomly polarized incident light.

$$\varepsilon_{film0}(\omega) = \varepsilon_{film\infty} - \frac{\omega_p^2}{\omega^2 + \imath\gamma\omega} + \sum_{j=1}^{n} \frac{S_j^2}{k_j^2 - k^2 - \imath\gamma_j k} \tag{3.26}$$

In an applied field , the dielectric function (ε_{film}) becomes:

$$\varepsilon_{film}(\omega) = \varepsilon_{film\infty} - \frac{\omega_p^2}{\omega^2 + \imath\gamma\omega}(1 + \eta m^2) + \sum_{j=1}^{n} \frac{S_j^2}{k_j^2 - k^2 - \imath\gamma_j k} \tag{3.27}$$

$\varepsilon_{film\infty}$ is the high frequency response of the film's dielectric function. The remaining parameters were determined using the data in Table 3.3. The k, γ_j and S_j values are taken from Boris *et al.* (24) which they fitted for an LCMO thin film sample.

Using these parameters in the dielectric function produces the IR spectra shown in Figure 3.10. There are three main phonon modes in the spectra: the Mn-O stretching mode observed around 580 cm^{-1}, the Mn-O-Mn bending mode around 350 cm^{-1} and an external mode located around 160 cm^{-1} (24).

Resonance parameters	j=1	j=2	j=3	j=4
k_j (cm^{-1})	154	335	379	559
γ_j (cm)	59	23	25	35
S_j (cm^{-1})	671	854	259	569
Other parameters				
N	$2.0 \times 10^{25}/m^3$			
$\varepsilon_{film\infty}$	8.6			
γ	$1 \times 10^{15} Hz$			
m_e^*	9.11×10^{-31} kg			
η	0.55			

Table 3.3: Parameters used in the modelling of a thin film manganite sample.

3.7.3 Modelling the thin film-substrate system

The film-substrate system combines the dielectric functions of the film and the substrate to produce a single film-substrate dielectric function. This combined dielectric function has two forms, the first of which is the zero field dielectric function:

$$\varepsilon_{total0} = \varepsilon_{film0} + \varepsilon_{sub} \tag{3.28}$$

or

$$\varepsilon_{total0} = \varepsilon_{film\infty} - \frac{\omega_p^2}{\omega^2 + \imath\gamma\omega} + \sum_{j=1}^{n} \frac{S_j^2}{k_j^2 - k^2 - \imath\gamma_j k} + \varepsilon_{sub\infty} \cdot \prod_{j=1}^{n} \frac{k_{L_j}^2 - k^2 - \imath\gamma_{L_j} k}{k_{T_j}^2 - k^2 - \imath\gamma_{T_j} k} \tag{3.29}$$

The second form of the dielectric function is used when a magnetic field is applied:

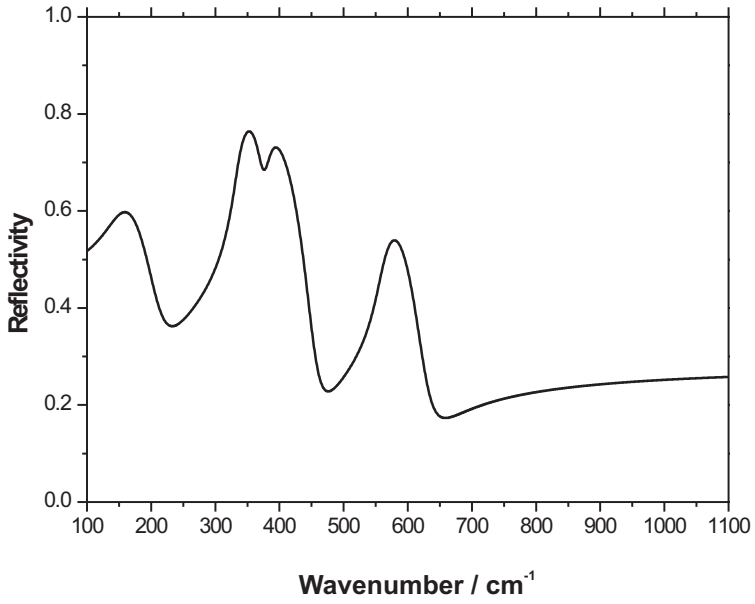

Figure 3.10: Modelled IR spectrum for a thin film perovskite

$$\varepsilon_{total} = \varepsilon_{film} + \varepsilon_{sub} \tag{3.30}$$

or

$$\varepsilon_{total} = \varepsilon_{film\infty} - \frac{\omega_p^2}{\omega^2 + \imath\gamma\omega}(1 + \eta m^2) + \sum_{j=1}^{n} \frac{S_j^2}{k_j^2 - k^2 - \imath\gamma_j k}$$
$$+\varepsilon_{sub\infty} \cdot \prod_{j=1}^{n} \frac{k_{L_j}^2 - k^2 - \imath\gamma_{L_j} k}{k_{T_j}^2 - k^2 - \imath\gamma_{T_j} k} \tag{3.31}$$

The modelled IR spectra for the film-substrate system can be seen in Figure 3.11. The spectra in Figure 3.11a shows the three main phonon modes observed in these materials: the stretching, bending and external modes. The bending and stretching modes cannot be accessed experimentally using our MRE setup. The stretching mode, however, can be studied and a close up of this feature is shown in Figure 3.11b. Each of the curves in the figure correspond to different values of m in equation 3.31.

It is clear from the figure that the application of a magnetic field changes the IR spectra. In particular, we observe the most change at or near positions where the reflectivity is at

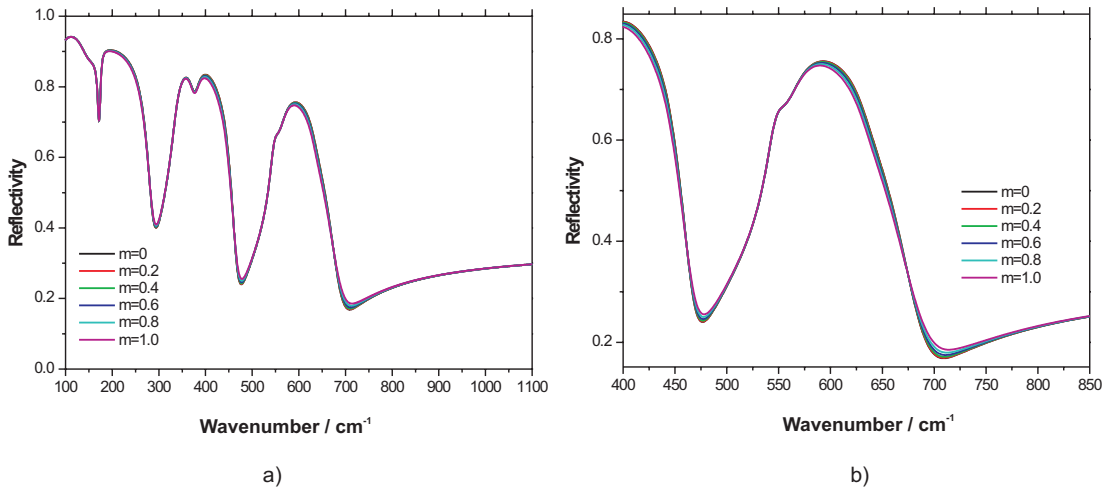

Figure 3.11: Modelled IR spectra for the film-substrate system for a) the stretching, bending and external phonon modes and b) the wavenumber range that can be observed experimentally. (Original in colour)

maxima or minima. The maxima correspond to phonon modes within the sample. However, the minimum at approximately 700 cm^{-1}, is not associated directly with phonon modes of the sample. The position of this minimum is sensitive to changes in the weighting of the Drude-like term in the dielectric function since it shifts to higher wavenumber as the field is scaled via the m parameter. In fact, the position of this minimum is determined by the delicate balance of all three terms in the dielectric function: ε_∞, the Drude-like term and the resonance term. Changing the weighting of any of these terms in the complex dielectric function will cause its position to change. This will become apparent when we examine the consequences of changing the parameter values used to model the IR spectra below. What is interesting to consider for the moment is the influence this minimum will have on the modelled MRE spectra for our generic thin film perovskite sample.

3.7.4 Modelled MRE spectra

The MRE spectra are modelled using the same technique as was demonstrated for the bulk sample. Using equation 3.18 we obtain the MRE spectra shown in Figure 3.12 for randomly polarized incident light. In Figure 3.12a we see the MRE plotted as a function of wavelength and in Figure 3.12b we see the same MRE spectra plotted as a function of

wavenumber. Again, each of the curves seen in the figures corresponds to a different value of m in equation 3.31.

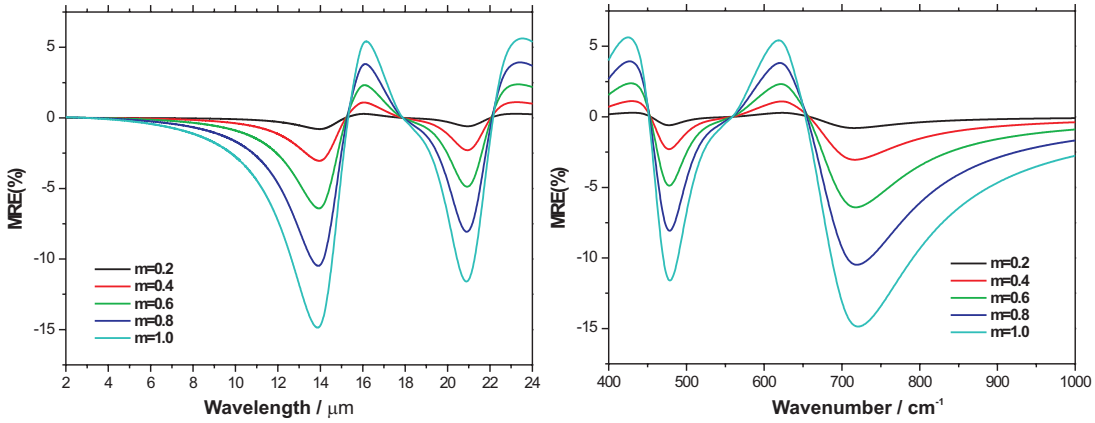

Figure 3.12: Modelled MRE spectra for a thin film perovskite sample plotted a) as a function of wavelength, b) as a function of wavenumber. (Original in colour)

If we compare Figures 3.11b and 3.12b, we can directly see how the field induced changes in the IR spectra manifest themselves in the MRE spectra.

As one would expect from the definition of the MRE, we observe that wherever the reflectivity changes in the IR spectra in an applied field, there is a corresponding change in the MRE spectra. The most obvious of these changes is the large negative MRE observed at around 700 cm^{-1} in Figure 3.12b. The reason this feature is so prominent is linked to the reflectivity at this wavenumber. As the MRE is proportional to $\Delta R/R$, if R is very small, as it is at the minimum in the reflectivity at 700 cm^{-1}, then $\Delta R/R$ can become quite large giving an enhanced MRE at these positions. A similar effect is observed for the other minimum at 477 cm^{-1}. The changes in the reflectivity at the maxima are still evident in the MRE spectra, but since ΔR is not as large compared to R at these positions, the change in the MRE spectra is less pronounced.

3.7.5 The consequences of changing parameter values on the IR spectra

As for the bulk sample, we will now examine what happens when we change the values of the parameters used to model the IR spectra in the thin film sample.

3.7.5.1 Changing the plasma frequency

Using the same method as was used for the bulk sample, we can observe the effect changing the plasma frequency has on the modelled IR spectra. Figure 3.13 shows what happens to the IR spectra as the effective mass of the free carriers is increased from 1 electron mass to 5 electron masses.

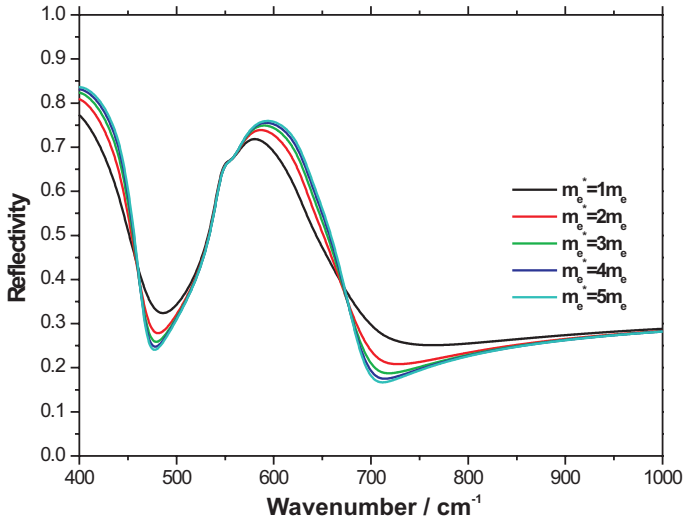

Figure 3.13: The effect of changing the effective carrier mass from 1 to 5 electron masses on the modelled IR spectra for a generic thin film perovskite sample. (Original in colour)

The main observation one can make is that the minima become much more pronounced as the effective mass of the carriers is increased. As the plasma frequency decreases the plasma edge moves too. This allows light of shorter wavelength to be transmitted instead of reflected, and hence the reflectivity of the sample decreases. The Drude-like term in the dielectric function is directly linked to the conductivity of the sample, and hence any

reduction in the relative strength of this term will result in poorer conductivity and reflectivity.

3.7.5.2 Changing the ratio of the film to the substrate

Until now, the model has considered that the substrate and the film have an equal weighting in the combined system's dielectric function. In this section, we shall consider how the IR spectra are influenced by the ratio of the film to the substrate in the dielectric function. In order to achieve this, the dielectric function for the zero field scenario (equation 3.28) is modified to allow us to change the relative weighting of film to substrate, thus:

$$\varepsilon_{total0} = 0.2x\varepsilon_{film0} + (1 - 0.2x)\varepsilon_{sub} \tag{3.32}$$

In equation 3.32, x is an integer that has values from 0 to 5. This allows us to vary the dielectric function from a pure substrate ($x = 0$) to a pure film ($x = 5$) in increments of 20%. The result of this modification to the IR spectra for two different values of effective mass can be seen in Figure 3.14.

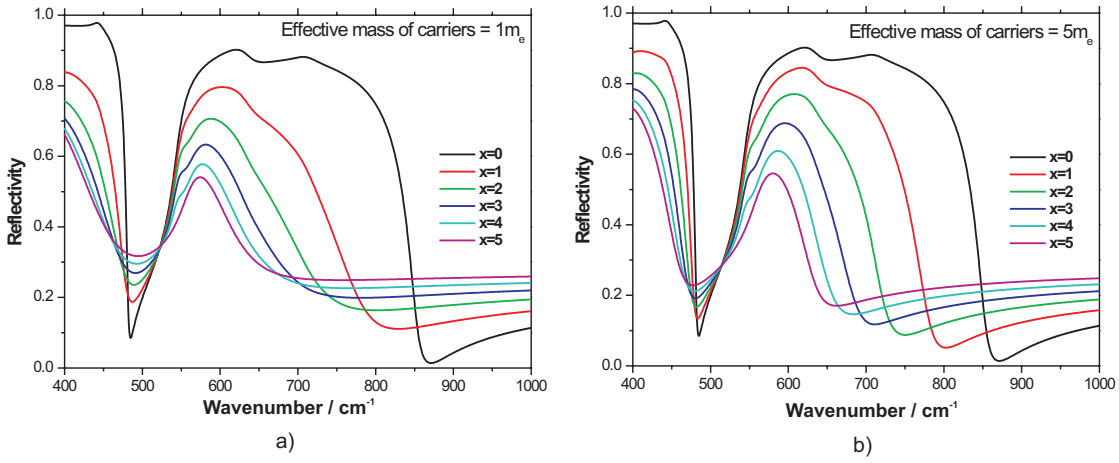

Figure 3.14: The effect changing the weighting of the substrate to film ratio in the dielectric function of a thin film sample has on the IR spectra for free carriers of effective mass a) 1 m_e and b) 5 m_e. (Original in colour)

The effective mass of the free carriers clearly influences the IR spectra. In Figure 3.14a the free carriers have a the mass of a single electron, whereas in Figure 3.14b this

has been increased to 5 electron masses. The difference between these two figures shows the influence the substrate has on the spectra. In Figure 3.14b, the reduced contribution from the Drude-like term in the dielectric function, due to the high effective mass, gives the substrate much more influence over the shape of the spectra, especially for the x=1 case. This results in the phonon mode associated with the stretching mode (at 600 cm^{-1}) being broader. Again we observe that the minima in the reflectivity are much more pronounced for the heavier free carriers, though it should also be noted that the maxima are slightly enhanced too. A key point to note is how much the position of the minimum at 700 cm^{-1} can shift as the effective mass of the carriers changes.

3.7.5.3 Changing the Oscillator strength

The oscillator strength can also be adjusted using a similar method to that which was used for the bulk sample. Figures 3.15a and b show the result of scaling the oscillator strength for free carriers of mass 1 m_e and 5 m_e, respectively.

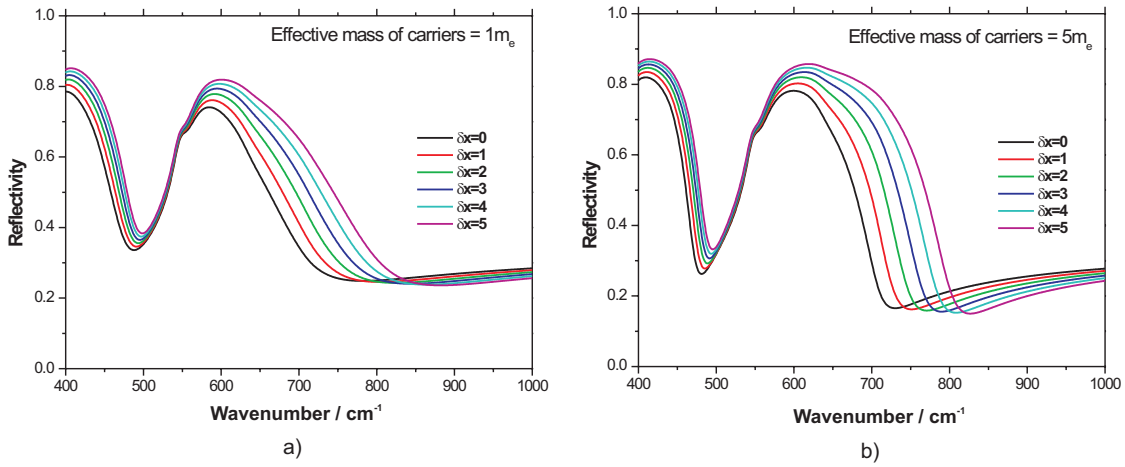

Figure 3.15: The effect changing the oscillator strength in the dielectric function of a thin film sample has on the IR spectra for free carriers of effective mass a) 1 m_e and b) 5 m_e. (Original in colour)

In the figures, we observe again that the effective mass of the carriers changes the shape of the modelled IR spectra. Again, the larger the effective mass, the more influence the substrate has on the result. The position of the minimum at 700 cm^{-1} shifts to higher wavenumber (lower wavelength) as the oscillator strength is increased. We can

observe from the figures that its position is determined by both the changing weighting of the Drude-like term as the effective mass increases and the changing weighting of the resonance term in the dielectric function as the oscillator strength is increased.

3.7.5.4 Changing the damping factors

As for the bulk sample, two damping terms appear in the complex dielectric function for the thin film sample: γ and γ_j. To begin, let us consider what happens to the IR spectra as we change the damping term in the Drude term, γ.

As before, γ was allowed to take values between 10^{10} and 10^{20} Hz. In Figures 3.16a and b we plot the modelled IR spectra using these γ values:

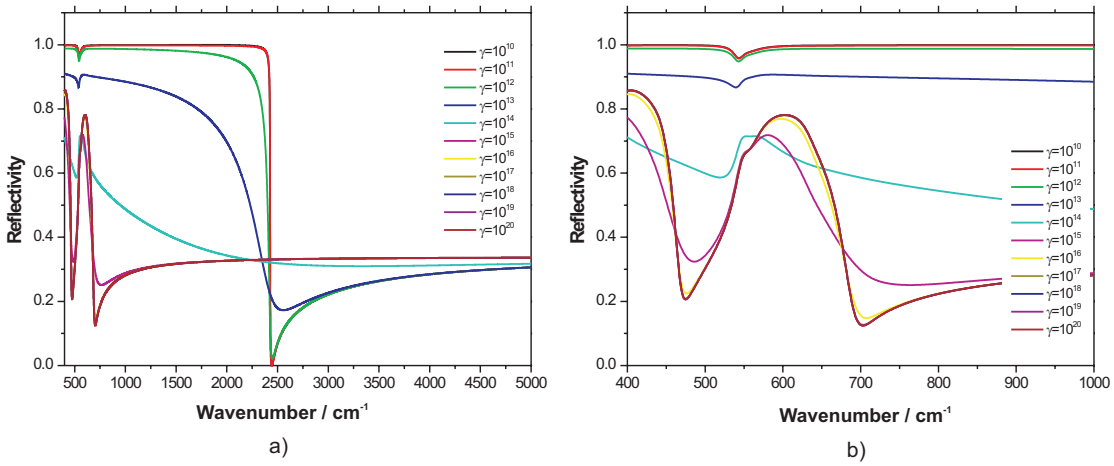

Figure 3.16: The effect changing γ in the Drude term of the dielectric function of a thin film sample has on the IR spectra. In a) we see the spectra corresponding to the wavelength range 2-25 μm and in b) we see a close up of the stretching phonon mode. (Original in colour)

For very low values of γ, the phonon modes are washed out. As for the bulk sample, the reflectivity becomes very high for low γ values; as the complex part of the Drude term (and hence the conduction) becomes negligible, electromagnetic waves can no longer propagate in the medium. For $\gamma = 10^{10}$ to 10^{12} Hz, the reflectivity drops very sharply at approximately 2400 cm^{-1} (4 μm) to form a minimum in the reflectivity. This minimum is the same one as was observed at approximately 700 cm^{-1} in the previous figures. It has just been greatly shifted in wavenumber due to the large change in the weighting of the

Drude term in the dielectric function.

For very high values of γ, we observe a similar spectral shape as was observed when we increased the effective mass of the carriers i.e. the minima are enhanced. This can be explained using the same argument as was made for the bulk sample: i.e. as we increase γ by several orders of magnitude, the $\imath\gamma\omega$ term will become increasingly dominant, and will eventually be such that $\imath\gamma\omega > \omega_p^2$. This reduces the importance of the Drude term in the dielectric function, resulting in exactly the same effect as was observed when we lowered the plasma frequency.

The γ_j parameter in the resonance term of the dielectric function can also be adjusted using the same method as was used in the bulk sample. In Figures 3.17a and b, we can see how this affects the IR spectra for free carriers with effective masses of 1 m_e and 5 m_e, respectively.

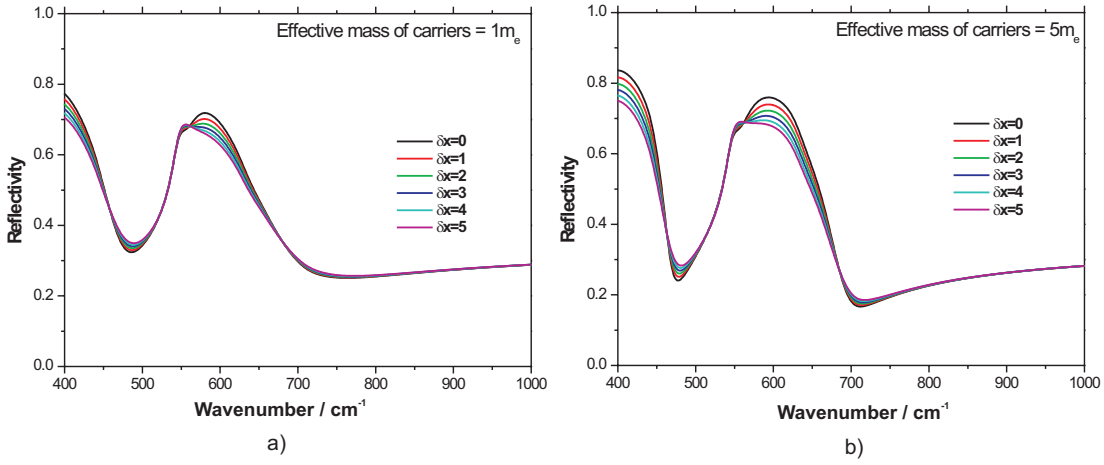

Figure 3.17: The effect changing γ_j in the resonance term of the dielectric function of a thin film sample has on the IR spectra for free carriers of effective mass a) 1 m_e and b) 5 m_e. (Original in colour)

The larger effective mass of the free carriers in Figure 3.17b enhances the resonance feature at 600 cm^{-1}; it is broader and has a higher reflectivity than the spectra for the lower mass carriers. Increasing γ_j cause the resonance to become squarer in shape and very slightly narrower.

The minimum at 700 cm^{-1} is not greatly affected by changing γ_j, at least for the low

mass carriers in Figure 3.17a. As the effective mass of the carriers is increased, however, the position of the minimum does shift to higher wavenumber, and we also observe slightly increased reflectivity at the minimum.

3.7.5.5 Changing the resonance position

The positions of the resonances can also be adjusted using the same method as for the bulk sample. The spectra, however, become rather messy, as Figure 3.18 demonstrates.

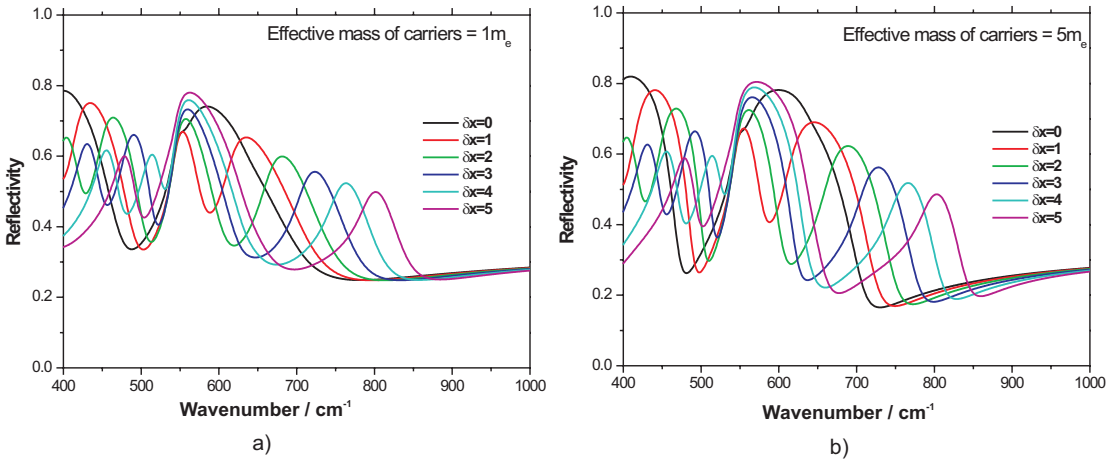

Figure 3.18: The effect changing k_j in the resonance term of the dielectric function of a thin film sample has on the IR spectra for free carriers of effective mass a) 1 m_e and b) 5 m_e. (Original in colour)

In Figure 3.18, we see the formation of additional resonance features in the spectra. The reason for these additional resonances is the complicated way in which the three parameter model used to model the thin film and the four parameter model used to model the substrate are combining into a single dielectric function. In general, the substrate is selected based upon a lattice match between the film and the substrate i.e. the similarity between the minima in the substrate and the minima in the film is not coincidental; they have been selected to provide the best possible match between film and substrate. By moving the position of the resonances in the film, we have severely disrupted this lattice match, and this has produced the additional modes.

3.8 Conclusions

In this chapter I have modelled IR and MRE spectra for a generic bulk perovskite sample and a generic thin film sample on a $SrTiO_3$ substrate. It has been discovered that for both of these systems the weighting of the terms that comprise the complex dielectric function for these media is vital in determining the IR spectra.

In the bulk samples, the model has shown that generally the reflectivity from the sample will increase as we move to longer wavelengths, as we move away from the plasma egde. The resonance feature associated to the stretching phonon mode of the Mn-O bonds is represented in the spectra by an increased reflectivity at the resonant wavelength. We have also found that the shape of the IR spectra are determined by the balance of the terms in the complex dielectric function (equation 3.12). Increasing the weighting of the Drude-like term of equation 3.12 (by increasing the plasma frequency) is observed to cause an additional minimum in the IR spectra to appear.

In the model for the thin film samples we have observed that the added complexity introduced by of the substrate has repercussions on the features observed in the IR spectra. In particular, the substrate produces features that are not observed in the bulk sample, for example the minimum at 700 cm^{-1}. The position of this minimum has been shown to be very sensitive to the balance between the terms of the dielectric function: any adjustments that increase the weighting of one term relative to the others, whether it be due to changing the resonance parameters or changing plasma frequency, will cause this minimum to move. The fact that we observe this minimum in the reflectivity needs to be explained. Essentially, a minimum in the reflectivity will be observed whenever the sum of the terms in the complex dielectric function tends towards one, i.e. $\sqrt{\varepsilon_{total}} \rightarrow 1$. This is because the reflectivity can also be defined in terms of the complex dielectric function such that:

$$R = \left| \frac{\sqrt{\varepsilon_{total}} - 1}{\sqrt{\varepsilon_{total}} + 1} \right|^2 \tag{3.33}$$

Hence, as $\sqrt{\varepsilon_{total}} \rightarrow 1$, R$\rightarrow 0$. This is the reason we observe the minimum at 700 cm^{-1}. Its position changes as we change the weighting of the terms in the dielectric function because equation 3.33 is satisfied for different values of the parameters used in

the model.

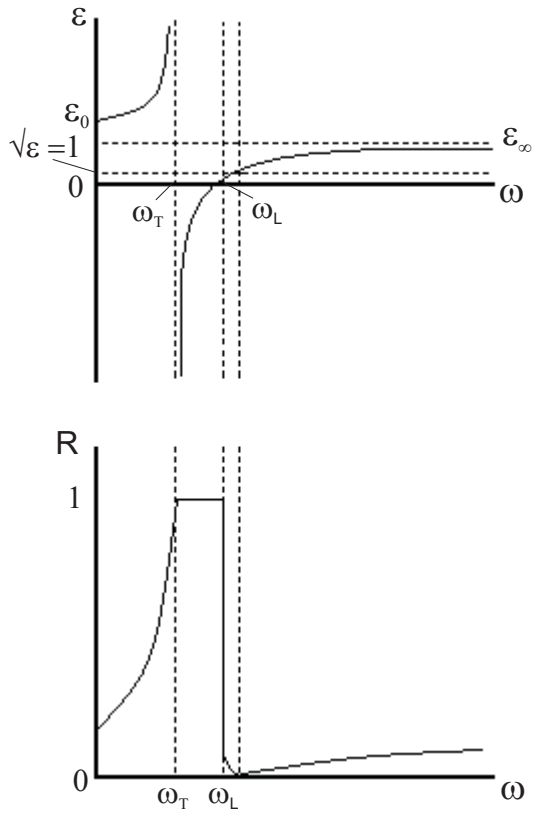

Figure 3.19: The relationship between the reflectivity (R) and the dielectric function (ε) for a lorentzian oscillator.

This is easily shown graphically as Figure 3.19 demonstrates. The value of the dielectric function approaches +∞ at for frequencies slightly below ω_T and -∞ for frequencies slightly above ω_T, while ε approaches zero at ω_L. Between ω_T and ω_L there is 100$\%$ reflection. The proximity in frequency of ω_T to ω_L determines how sharp the peak in the reflectivity is, and for materials like STO, where the transverse and longitudinal frequencies can be well separated, we can observe high reflection over an extended range of frequencies. The reflectivity approaches zero when $\sqrt{\varepsilon} = 1$.

A key observation that can be made from the modelling of the IR and MRE spectra in these materials is that unlike in normal metals, the response of the dielectric function is far more sensitive to changes in the plasma frequency than to changes in the damping factor in equation 3.12. The plasma frequency only has to change slightly to produce noticeable results, whereas γ has to change by orders of magnitude to achieve the same

effect. Since the shape of the modelled IR and MRE spectra are so closely linked to the plasma frequency, experimentally measured IR and MRE spectra should also be very sensitive to changes in the conductivity of the sample. This is a concept that will become evident when I present my experimental results for bulk and thin film samples in Chapters 5 and 6.

This is a key result since the minimum associated with the plasma edge is very dominant in the modelled MRE spectra and amplifies the change in the spectra due to the magnetoresistance. In essence we have a magnetic switch which can made to switch on at a particular frequency, governed by the careful engineering of the sample's dielectric function. The number of free carriers in these materials can be selected through doping and hence the plasma frequency can be tailored to a certain extent. The position of the minimum can also be somewhat determined by the choice of substrate, since the substrate constrains the other parameters in the system, and by changing the thickness of the film layer. This is an important result and has potential commercial value.

In Chapters 5 and 6, I will refer back to the modelling done in this chapter to help explain the results that have been obtained experimentally using the MRE. The model that has been developed in this chapter is quite simple, yet it can provide us with a great deal of information with regard to the magnetotransport in these materials.

Chapter 4

Experimental Techniques

4.1 Introduction

A variety of experimental techniques have been used to characterise the physical properties of a wide range of bulk and thin film LSMO, LBMO and LCMO perovskite samples. Most of the experimental techniques employed will be familiar to readers with a background in magnetism, for example hysteresis measurements made using a Vibrating Sample Magnetometer (VSM), four-point probe measurements of the magnetoresistance and measurements of the surface topography using a Scanning Electron Microscope (SEM).

However, most of the measurements made for this thesis have been measurements of the Magnetorefractive Effect in the mixed-valence manganites, and it is likely that this experimental technique will not be familiar to the reader. This chapter will start by introducing the reader to the basic MRE setup, including a discussion of the geometry used in the alignment. It will then go on to discuss the effect the polarization of the incident IR light on the sample can have on the results.

Since the mixed-valence manganites have such an interesting magnetic phase diagram that depends on the temperature as well as the amount of doping, a lot of time has been spent developing the basic MRE setup to allow us to make temperature controlled MRE measurements. The design considerations and problems associated with these temperature controlled measurements will be discussed.

Once I have outlined the experimental setup for room temperature and temperature

controlled MRE measurements, I will then outline the experimental procedures for making the hysteresis, SEM and four-point probe measurements; the latter as a function of temperature.

4.2 Measuring the magnetorefractive effect

4.2.1 Room temperature measurements

The experimental setup required to make room temperature MRE measurements is relatively simple. In Figure 4.1 we show a schematic top-down of view the experimental setup. The key components are the FTIR spectrometer, the detector, the enclosure, the electromagnet, the goniometer and the optional KRS-5 grid polarizer.

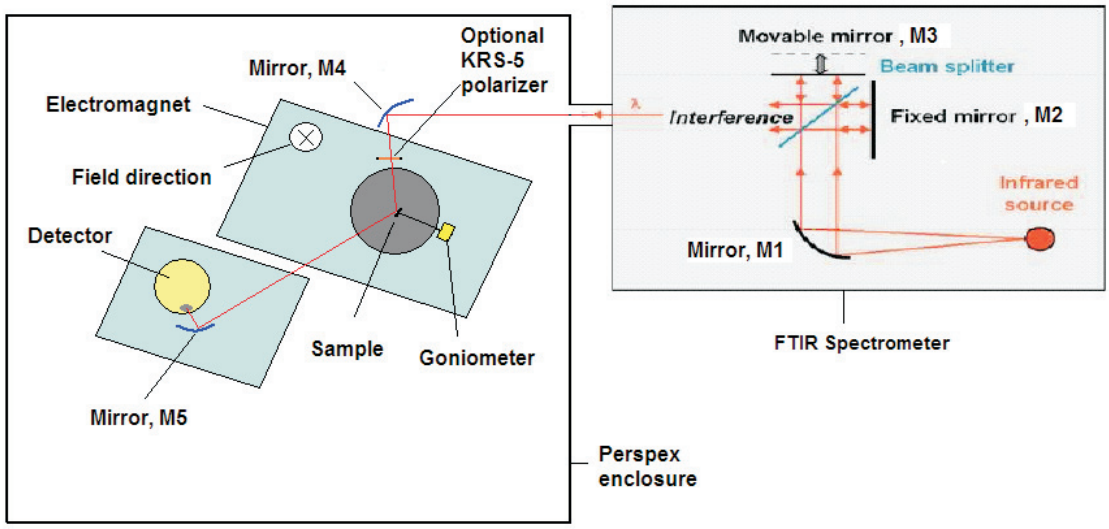

Figure 4.1: Overhead view of the room temperature MRE experimental setup. (Original in colour)

4.2.1.1 The spectrometer, the detector and the enclosure

The infrared spectra are acquired with a Nexus 550 Fourier-Transform spectrometer from NICOLET. The heated infrared light source emits randomly polarized infrared light with a wavelength from 2 to 26 μm. This is deflected off an internal mirror (M1) onto a KBr beam splitter which is part of the optical bench. In addition to the beam splitter the optical bench

contains a stationary mirror (M2) and a movable mirror (M3), whose velocity is controlled by the spectrometer's OMNIC software. As the mirror is moved along the bench the length of the beam path is changed and thus we obtain a different interference pattern for each wavelength. The interfered beam is then deflected off another internal mirror (not shown) and leaves the spectrometer, entering the Perspex enclosure. The beam is then reflected by an aluminium coated external mirror (M4), onto the sample at an angle of incidence of $\approx 65^{\circ}$ to the normal of the sample surface. The reflection from the sample is collected by a second aluminium coated external mirror (M5) and deflected onto a Mercury-Cadmium-Telluride (MCT) detector. The detector records the total intensity of the infrared beam over the time when the mirror (M3) moves, the so called interferogram or scan. From this interferogram the information for each single wavelength, the spectrum, is resolved using Fourier transformation.

The spectrometer includes a visible light HeNe-laser system for self-calibration (laser quadrature calibration). This laser serves a double purpose since it can also be used to aid us to align the IR beam on the sample. This is particularly useful since the IR beam is obviously invisible to the naked eye.

The detector is a photoconductive MCT detector. It is designed to operate at low temperatures and hence needs to be cooled using liquid nitrogen. Since the active area of the detector is very small (1 mm^2) and the thermal radiation of the surroundings is in the same wavelength range, the focussing optics of the setup are very important.

The spectrometer uses its own OMNIC software to control many of the parameters of the experiment. In particular, the OMNIC software allows the user to set the resolution, the number of scans, the gain and also allows the user to include correction algorithms for the spectra. The spectrometer offers resolutions from 0.125 to 32 wavenumbers. Typically for our measurements a resolution of 4 wavenumbers was used. This corresponds to the movable mirror moving in steps of 1.928 cm^{-1} (0.012 μm) between 4000 and 400 wavenumbers (2.5 to 25 μm).

In order to allow a direct comparison between spectra, it was necessary to normalise the spectra to an Ag reference sample. This required that the spectra of the sample and the reference to be taken with the same resolution. This is because the number of scans does not change the number of data points in the spectrum, instead it determines how

many scans are performed and averaged for the whole spectrum. Increasing the number of scans reduces the noise level of the data and for most perovskite samples 150 scans gave satisfying results. A higher signal is also obtained by increasing the gain on the detector. Perovskite samples usually require the highest gain of 8 since they are not very reflective.

The OMNIC software contains several correction algorithms for further corrections to the data. However, as these algorithms might falsify physical effects in the spectra, they were avoided where possible, i.e. the correction for peaks due to atmospheric gases and the zero filling (a smoothing algorithm), were set to zero and for the phase correction the default setting, 'Mertz' correction, was used. Phase correction is often necessary in FTIR spectroscopy to compensate for not taking data exactly at the position where the two beams of the interferometer have zero optical path difference, and for frequency dependent variations caused by the beam splitter and signal amplification. The Mertz correction is a well established phase correction technique that only modifies the phase of the Fourier transform of the interferogram and keeps the magnitude unchanged (139).

Since no correction algorithms were used it was necessary to place the entire experimental setup within a purged, airtight Perspex enclosure. The reason for this is that many atmospheric gases, like carbon dioxide and water vapour, have vibrational and stretching modes in the IR. These modes would be present in the spectra from the sample and thus these contaminants must be kept out of the beam path. To achieve this, the air in the enclosure is dehydrated with silica gel and the entire volume inside the enclosure is cleaned with a purge gas generator (PG28L from Peak Scientific). The purge gas generator removes water vapour and carbon dioxide using pressure swing adsorption with a molecular sieve. The sieve regenerates during the process and so the system is self-sustaining. If needed, the enclosure can additionally be purged with pure nitrogen gas.

4.2.1.2 The magnet, the power supply and the teslameter

The magnet and its power supply were purchased from Bouhnik Sarl. The power supply provides between $\pm$ 70 A at $\pm$ 35 V, which allows a maximum field of 1.3 Tesla parallel to the sample surface. The pole shoes of the magnet had to be reshaped to adapt for the optional cooling system (see below). Prior to this reshaping a maximum field of 1.5 T was achievable so in some of our earlier results this field was used. The magnet and its power

supply are both water-cooled. Despite the water cooling, the temperature between the pole shoes is slightly above the ambient room temperature, typically by a few degrees.

For the calibration of the magnetic field to voltage conversion a Group 3 Technology teslameter (DTM-141) with a miniature Hall probe was used. This teslameter operates in the range from +2.2 to -2.2 T ($\pm 0.03\%$ at 25 °C) and is also capable of making a measurement of the temperature at the probe's position. The calibration results for the field as a function of power supply current and voltage can be found in the Appendix.

4.2.1.3 Experimental procedure

Figure 4.2 shows a photograph of the experimental setup from a side view. The sample is first cleaned with isopropanol and is then attached with blue tac to the (non-magnetic) brass sample holder. The sample holder is then affixed to the goniometer and is positioned as shown in Figure 4.2 between the pole pieces of the magnet. The field direction is from the top of the figure to the bottom. The sample shown is a highly reflective silver sample which is used in the initial alignment of the system. The red dot seen in the centre of the sample is the HeNe calibration laser and is coincident with the IR beam path.

For room temperature measurements the sample is positioned to give the maximum signal possible. The OMNIC software has a 'bench' program that can be used to maximise the signal received by the detector. The position of the sample can be fine tuned by using the goniometer which allows us to move the sample forwards and backwards, up and down, from side to side and can also to rotate the sample in the horizontal plane. The position of the mirror M5 and the height of the optical bench the detector is sitting on can also be altered to fine tune the alignment. Once the maximum signal has been achieved, the system is left to settle for a period of time to reduce the amount of water vapour and CO_2 within the Perspex enclosure. The amount of time required depends on how long the system was open during the alignment procedure and is typically between 30 and 90 minutes. The water vapour and CO_2 spectral features are observable in the IR spectra obtained when scanning with the spectrometer. The easiest method to establish when the atmospheric conditions are stable is to take two zero-field IR spectra a few minutes apart and then subtract one spectrum from the other (the OMNIC software has this functionality built-in). If there are still obvious features once the subtraction is done you need to wait

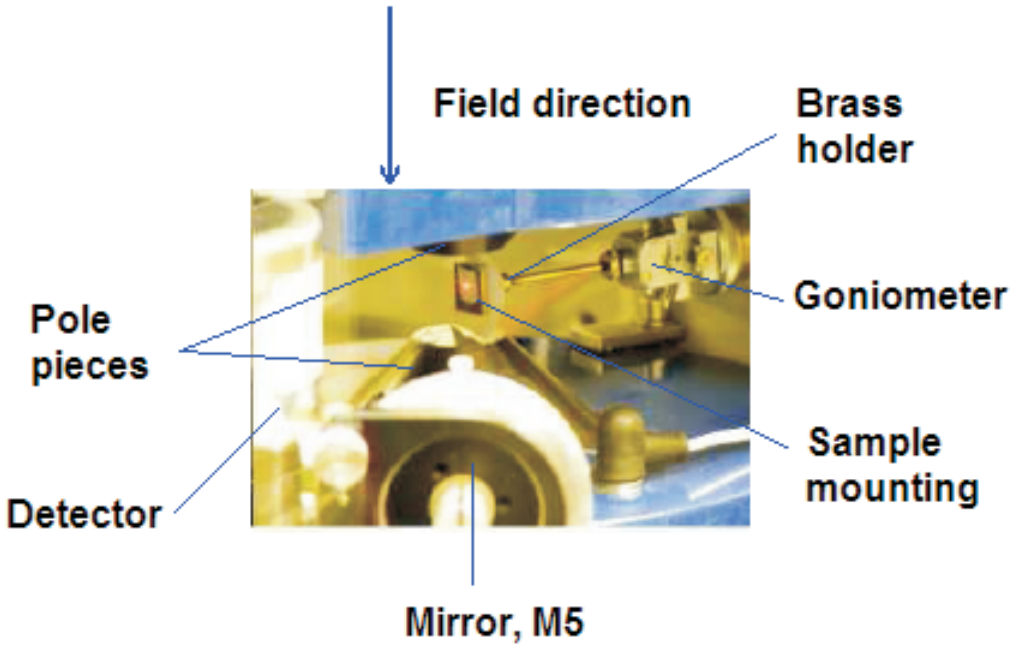

Figure 4.2: A close-up, side-view of the sample position for the room temperature MRE experiments. (Original in colour)

longer for the system to settle, otherwise you may proceed to take the MRE measurements.

The MRE measurement, as described by Vopsaroiu *et al.*(140), requires us to take three reflection spectra: the first (S_1) is taken in zero magnetic field, the second (S_2) is taken in a magnetic field H and the third (S_3) is again taken in zero magnetic field. The zero field spectra are averaged to correct for variations of the magnetic state in the sample and also to take into account any change in the background spectra between the taking of S_1 and S_3 due to, for example, a drift in the detector response and/or a build up of water ice on the detector. The MRE(%), which is the change in the IR spectra in a magnetic field, was then calculated using the equation:

$$MRE(\%) = \frac{0.5 \times (S_1 + S_3) - S_2}{S_2} \times 100 \tag{4.1}$$

which is the equivalent of equation 3.1 in Chapter 3.

The MRE measurements are repeated three to five times depending on the noise level of the spectra and the final MRE(%) spectrum is calculated as an average of the single

MRE measurements. The measurements can be repeated for s- and p-polarized infrared light by placing a KRS-5 grid polarizer between the first external mirror (M4) and the sample as shown in Figure 4.1.

The measured spectra are normalised to an Ag reference spectra. Ag is used since it has a uniform optical response over the 2-26 μm IR wavelength range. Normalisation is achieved by dividing the sample's IR spectrum by the Ag reference spectrum. The normalisation process is necessary since it removes the parts of the sample's spectrum that are not unique to the sample e.g. the spectral characteristics of the source, the detector and the optical path. The IR spectra for the Ag reference sample used to normalise the spectra for randomly, s- and p-polarized light is shown in Figure 4.3.

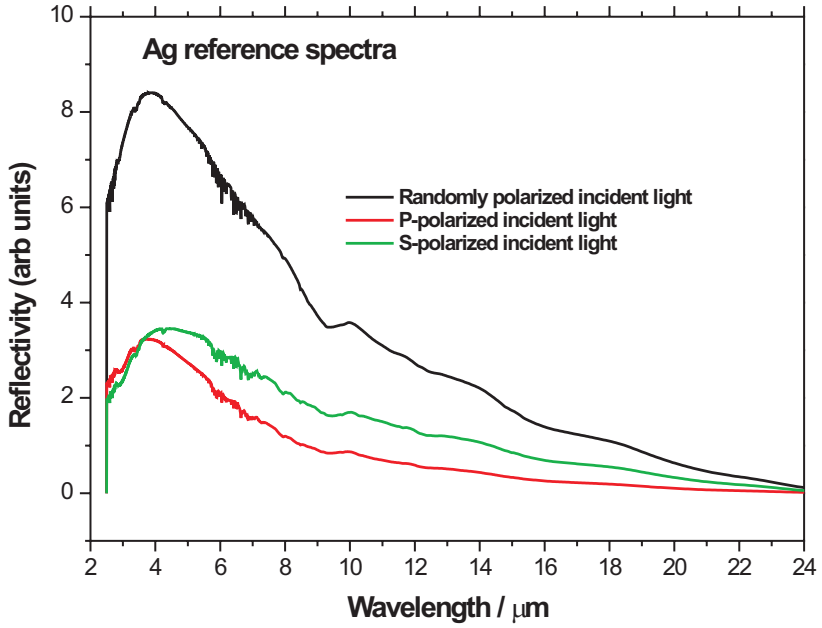

Figure 4.3: IR spectra for a Ag reference sample for randomly, s- and p-polarized incident light. (Original in colour)

4.2.2 The consequences of polarization

The MRE is sensitive to both the polarity and angle of incidence of the of the IR light source due to the fact that the s- and the p-components of the reflectivity have a different angular dependence. If we define s-polarized light as having an electric field vector that is perpendicular to the plane of incidence to the sample and p-polarized light as having an an electric field vector parallel to the plane of incidence to the sample (as shown in Figure 4.4), then we can calculate the reflectivities, R_S and R_P as a function of the angle of incidence, θ_i.

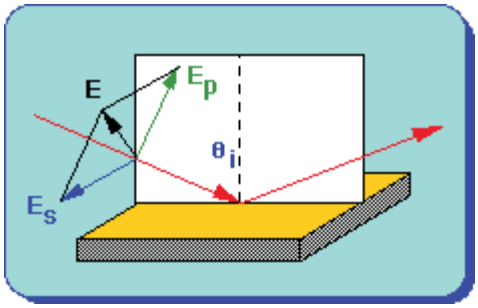

Figure 4.4: Schematic showing the electric field vectors of light in reflection. (Original in colour)

R_S and R_P are given by the equations:

$$R_S = \left(\frac{sin(\theta_i - \theta_t)}{sin(\theta_i + \theta_t)}\right)^2 \tag{4.2}$$

$$R_P = \left(\frac{tan(\theta_i - \theta_t)}{tan(\theta_i + \theta_t)}\right)^2 \tag{4.3}$$

(see, for example Hecht's *Optics* (137)) where θ_i and θ_t are the angle of incidence and the angle of transmittance, respectively. θ_t is calculated using Snell's Law i.e. by rearranging $n_i sin\theta_i = n_t sin\theta_t$ in terms of θ_t. If we assume that the first medium is air ($n_i = 1$) and the second medium has a refractive index $n_t = 2.37$ (this is the refractive index of KRS-5 at 11μm (141)), then we get the results shown in Figure 4.5 (see Appendix A.3).

Granovsky *et al.* (142) have shown that:

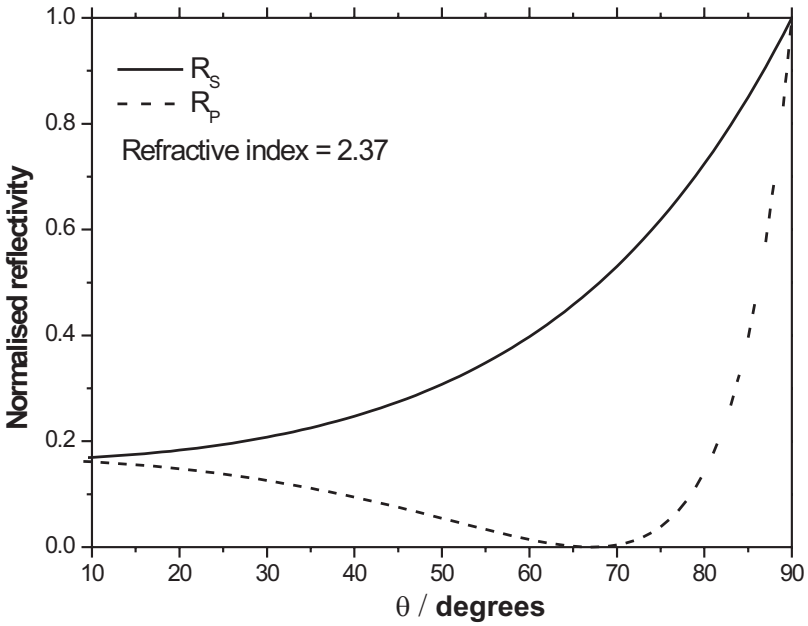

Figure 4.5: Normalised reflectivity as a function of the angle of incidence θ for s- and p-polarized light for KRS-5 at a wavelength of 10 μm.

$$\frac{\Delta R}{R} \propto 1 - R \tag{4.4}$$

The ratio $\frac{\Delta R}{R}$ is essentially the MRE of the sample and since the reflectivity, R, at an angle of 65° is much less for p-polarized light than s-polarized light, from equation 4.4 we would expect that the MRE of the p-polarized light should be a lot larger than is observed for s-polarized light. However, this makes matters harder experimentally since the reflectance of the sample is so small for p-polarized light it makes it much harder to obtain good experimental results due to the poor signal-to-noise ratio. Having said that, for good quality thin film samples this is less of an issue and hence we maintain the 65° angle of incidence since at this angle we can potentially see the largest effect.

A consequence of the geometry used in the experiment is that p-polarized light will exhibit a transverse magneto-optical Kerr effect, where the magnetic field induces a change in reflectivity from the sample's surface for p-polarized light (143). This may have an effect on measurements made using p-polarized light (a slight enhancement), but it is

thought to be a small effect at these IR wavelengths. However, whilst the effect has been considered it has never been quantified.

4.2.3 Temperature controlled MRE measurements

A great deal of time was spent modifying the room temperature MRE setup to allow us to make temperature controlled MRE measurements. Having the ability to make temperature controlled measurements is extremely important since the mixed-valence manganites have magnetotransport properties that are temperature dependent, including the magnetic metal-to-insulator phase transition at the Curie temperature. In this section we will discuss the factors that influenced our solution to the problem of how to make these temperature controlled measurements.

4.2.3.1 Design brief

The design brief for the temperature controlled measurements was fairly straightforward: Incorporate temperature control into the MRE measurements but keep all of the other equipment parameters the same as for the room temperature measurements, i.e. use the same optical alignment and geometry so that we can use the current spectrometer, electromagnet and HgCdTe detector. The solution to this problem would need to fulfil several criteria: Firstly, the design had to be able to cool the sample down to low temperatures but also had to have the capability of heating the sample for those samples whose Curie temperature is above room temperature. Secondly, the design needed to be compact enough to fit between the pole pieces of the magnet. Thirdly, it needed to be magnetically inert since it cannot have any parts that can alter the response of the sample in an applied magnetic field. Fourthly, and perhaps most importantly, it had to allow us optical access for a reflection geometry to the sample in the IR wavelength range of the spectrometer.

4.2.3.2 The solution

The solution to the problem was a micro-miniature refrigeration system from MMR Technologies Inc.. Each of the criteria listed above could be satisfied by such a system. I will now discuss how it satisfied each criterion in more detail:

Cooling and heating

The micro-miniature refrigeration system (MMRS) is a small, cryogenic refrigerator that derives its cooling power from the Joule–Thomson expansion of a high pressure gas. Joule–Thomson cooling occurs when a non-ideal gas expands from high to low pressure at constant enthalpy. The effect can be amplified by using the cooled gas to pre-cool the incoming gas in a heat exchanger. This can be understood by referring to the Temperature vs Entropy diagram for nitrogen shown in the Figure 4.6a. Nitrogen at a pressure of 120 bar passes down a counter-current heat-exchanger from A to B. At B it is allowed to expand through a valve or restricting capillary where it cools by the Joule-Thomson effect. The cold gas then passes back up the exchanger from D to E (144).

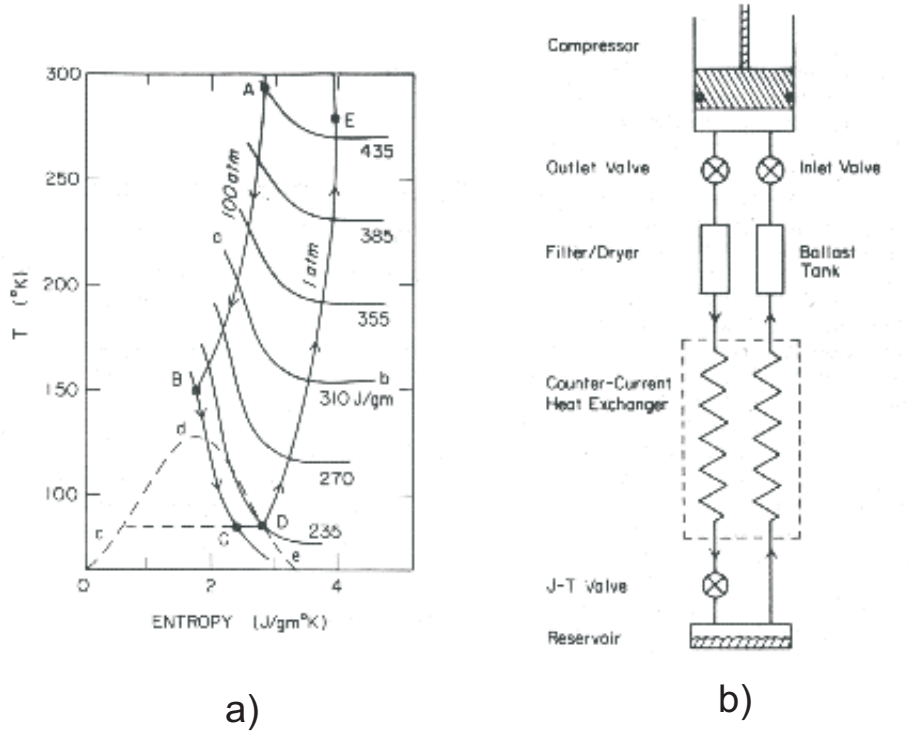

Figure 4.6: The Joule-Thomson effect and its use in a micro-miniature refrigerators. In a) we see how the Joule–Thomson expansion of a non-ideal gas at constant enthalpy reduces the temperature and in b) we see how this effect can be applied to a refrigeration device. Adapted from (144).

This process can be used in refrigeration as shown in Figure 4.6b. Here a compressor compresses the gas to high pressure, forcing it through the filter-dryer, down the counter-current heat exchanger, then through the Joule-Thomson (J–T) valve where it expands and cools. Eventually the gas liquefies and collects in the reservoir. The evaporated vapour

passes back up the heat exchanger, pre-cooling the incoming gas, then returns to the compressor, and the cycle is repeated (144). To achieve very low temperatures it is necessary to evacuate the volume in which the sample is placed. For pressures of 5 mTorr or less it is possible to cool the sample down to 80K. The reverse process can be used to heat the sample to approximately 400K. It takes about 15 minutes for the system to reach its lowest operating temperature and the temperature can be changed in 0.1K intervals using the accompanying K-20 Temperature controller. When operating the MMRS requires a supply of 99.99% pure nitrogen gas at a pressure of 120 bar in order to allow the system to cool to 80K. Once the lowest possible temperature has been reached, the gas pressure can be reduced to 100 bar. The nitrogen gas is prefiltered before entering the MMRS to remove any water vapour or other impurities that could potentially freeze out during the cooling process, clogging the system.

Size

Figure 4.7 shows a schematic of the MMRS including its dimensions. One of the benefits of this system is its small size. The gap between the pole pieces still had to be slightly increased to accommodate the MMRS and this reduced the maximum obtainable field from 1.5 T to 1.3 T.

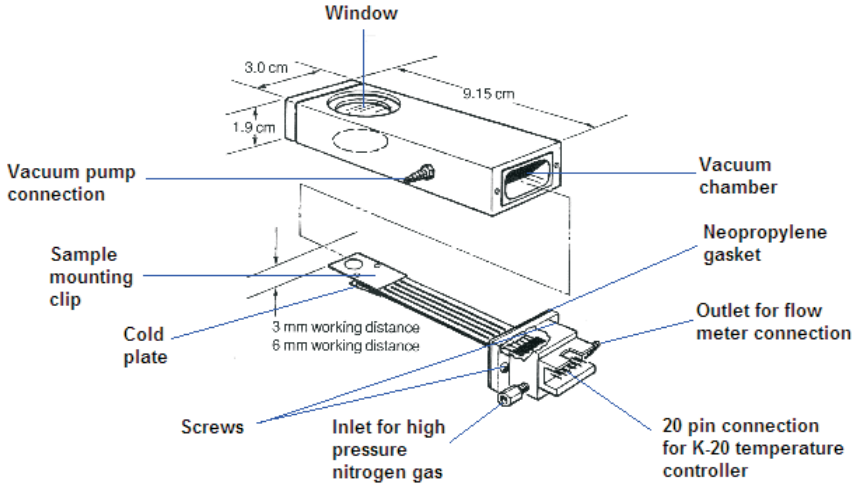

Figure 4.7: Schematic diagram showing the dimensions and connections for vaccuum chamber of the micro-miniature refrigeration system. (144)

Magnetically inert

The MMRS is totally devoid of any parts that can be magnetised. The sample is mounted on a brass clip which attaches to a ceramic plate on the heat exchanger. The heat exchanger itself is made of glass and the protective outer casing is also non magnetic.

The window and optical access in a reflection geometry

The vacuum chamber has a window on the front face that allows optical access to the sample position inside the vacuum chamber. There is also another window on the rear face that allows users to make transmission measurements. However, our samples are too thick to allow transmission and hence we need to use a reflection geometry.

There were two factors that we had to consider for my experiments: Firstly, I had to decide what material to make the window from, and secondly, I had to determine whether or not it would be possible for me to direct the IR beam through the window and onto the sample, and then manage to get the reflected beam back out through the window to the detector given that the window has a diameter of only 25 mm.

In choosing the window material I had to consider both the transmission properties of the material and the wavelength range over which the material would effectively operate. For my experiments the wavelength range is 2-26 μm and this limited the choice of window material to KBr (Potassium Bromide) and KRS-5 (Thallium Bromoiodide). Both of these materials are highly transmissive for IR light in the wavelength range 2-26 μm with KBr transmitting approximately 90 $\%$ and the KRS-5 transmitting approximately 70 $\%$ over this wavelength range (145). Due to its higher transmission, I decided to use KBr for the window material.

The question of whether or not it would be possible to successfully reflect the light from the sample into the detector from inside the vacuum chamber was answered by drawing a scale diagram. The schematic in Figure 4.7 shows that the working distance, i.e. the distance from the sample to the window can either be 3mm or 6mm. Since none of our samples are 3mm thick, the 3mm working distance could be used exclusively. Armed with a knowledge of the thickness of the window (2mm) and the refractive index of KBr at 2 and 26 μm (145), it was a straightforward application of Snell's Law to show that for an angle of incidence of approximately 65° to the normal to the plane of the window (25° to

the plane of the window) it was possible to reflect an IR beam of this wavelength range onto and from the sample.

4.2.3.3 The experimental method

The sample is attached to the brass mounting clip using Dow Corning 340 Heat Sink Compound which is a grease-like silicone material that ensures there is a good thermal contact between the cold plate and the sample. The cooling system is then placed inside the vacuum chamber such that the sample is positioned in the centre of the window.

The screws on the end of the cooler are then tightened until a good seal has been established. The neopropylene (neoprene) rubber gasket ensures that a good vacuum is possible. If necessary the gasket can be coated in a thin layer of vacuum grease to enhance the seal.

Once the vacuum chamber has been sealed it is attached to the goniometer using a modified version of the room temperature sample holder as demonstrated in Figure 4.8. The entire assembly is then placed between the pole pieces of the magnet. The vacuum chamber is positioned so that the sample/window is in the same position as for the room temperature setup (as was shown in Figure 4.2). The field direction and the path the IR light follows is as indicated in Figure 4.8. Before carrying out the fine alignment of the system the high pressure gas line is attached to the gas inlet (see Figure 4.7), the vacuum chamber is attached to the vacuum pump and the K-20 temperature controller is attached via the 20 pin connection on the rear of the cooler.

The vacuum pump used is a two stage turbo pump. Stage 1 is a rotary pump which can achieve a pressure of approximately 20 mTorr in the chamber. The second stage is a turbo molecular pump which can achieve the desired 5mTorr or better pressure required to reach the lowest temperatures.

Once the required vacuum pressure has been reached the fine alignment process can begin. Aligning the sample while it is inside the vacuum chamber is much more difficult than it is for the room temperature setup. For the latter all that is required is that the detector receives the maximum possible signal from the sample. However, when aligning the temperature controlled setup, the largest reflection comes from the front face of the

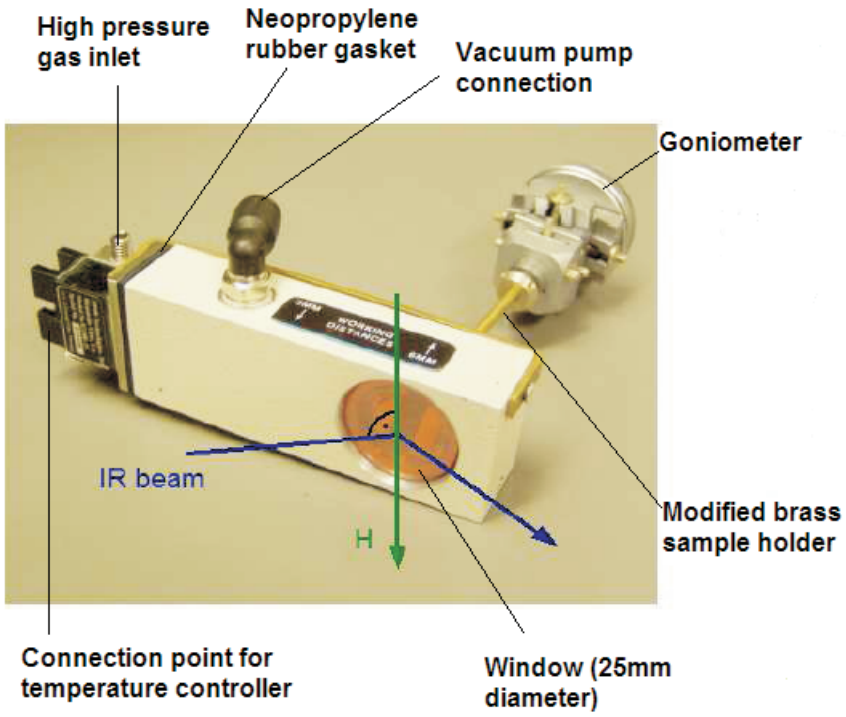

Figure 4.8: Photograph showing the vacuum chamber. (Original in colour)

window and not from the sample. To ensure that the signal detected is indeed from the sample it is best to compare characteristic peaks in the spectra with spectra of the sample taken outside of the chamber. Also it may be necessary to do a 'test' MRE at the maximum field. Since the cooling system has no magnetic field dependence if you see a noticeable difference in the spectra taken in the field compared to those at zero field, then you are receiving the signal from the sample.

After the sample has been aligned at 'room temperature' inside the vacuum chamber the entire setup is left to settle so that the atmosphere in the Perspex enclosure can be purged of impurities as was discussed above. The high pressure gas can then be turned on and the temperature can be set using the K-20 temperature controller. The cold plate has a platinum resistance thermocouple so that the user can monitor the temperature externally using a handset attached to the K-20 controller.

Once the desired temperature has been reached the experimental procedure and the analysis is identical to the room temperature procedure. At each new temperature, however, the system was left for 10-15 minutes to allow the temperature to stabilise before the

measurements were made. It was established that it was best to start at the lowest temperature and increase the temperature as required. This was because after extended periods the system could clog and the lowest temperatures could no longer be reached.

4.2.3.4 Initial successes and failures

The first sample that I successfully managed to obtain a signal from inside the vacuum chamber was not a manganite but a highly reflective spin-valve sample with the designation BSV_2b provided by Seagate. This sample was chosen for its high reflectivity and also because it has a distinctive response to the applied field. The first tests were all performed at room temperature so that we could compare the spectra taken inside the chamber with those taken outside.

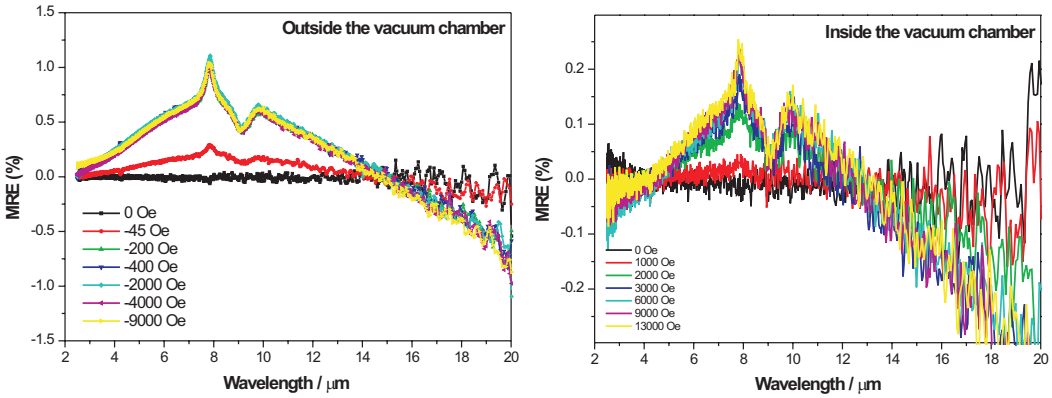

Figure 4.9: Initial testing of the alignment was done using a highly reflective spin valve sample. The spectra measured outside of the vacuum chamber, shown on the left, are similar to those on the right measured inside the vacuum chamber at room temperature, though the magnitude of the MRE is reduced inside the chamber. The spin valve consists of a layered structure containing two CoFe layers separated by a thin Ru spacer layer, topped off by layers of Cu, NiFe/Fe and a PtMn cap. (Original in colour)

As can be seen in Figure 4.9, which shows the results for the measurements outside the chamber alongside those taken inside the chamber, the shape of the MRE spectra are remarkably similar. The main difference is in the amplitude of the MRE. The MRE(%) measured inside the chamber is approximately one-quarter of that measured outside the chamber, which can be attributed to the low signal strength reaching the detector.

Bolstered by my successful trial of the new equipment I then tried to see if I could get similar results from one of the manganite samples. For the first test I used a thin-film LSMO ($x = 0.3$) sample. The reflectivity of this manganite sample is poor compared to the spin valve so the alignment process was very difficult in comparison. Figure 4.10 shows a comparison of the the MRE(%) measured for inside and outside of the vacuum chamber for the $x = 0.3$ sample. It is clear from Figure 4.10 that the MRE measured inside the vacuum chamber is the same as measured externally.

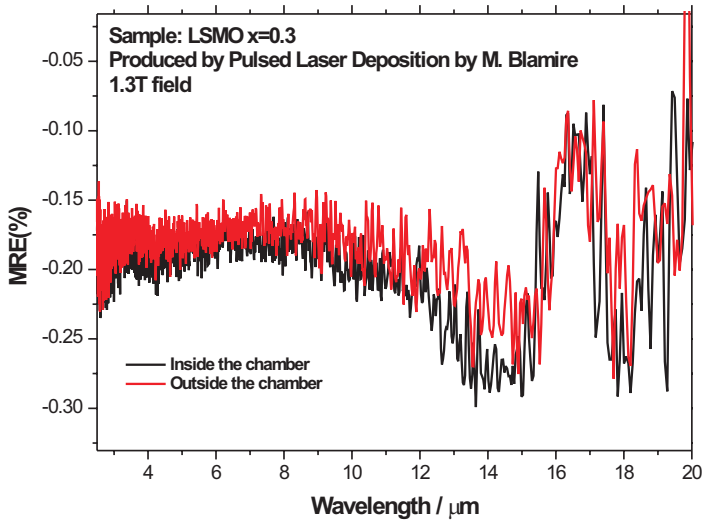

Figure 4.10: MRE spectra measured for a thin film $La_{0.7}Sr_{0.3}MnO_3$ sample. (Original in colour)

The initial results were very promising. However, I started to encounter problems after a short time since I started to observe inexplicable peaks in the MRE spectra that did not represent any known modes in the manganites. An example of this is shown in Figure 4.11 for a bulk LSMO ($x = 0.2$) sample. The two MRE spectra shown in Figure 4.11 were measured in a magnetic field of 1.3 T.

Eventually the cause for these extra peaks was determined. One of the properties of KBr is that it is very hygroscopic, meaning that it readily absorbs water. This makes the normally clear KBr become very cloudy and it was this that caused the problem. It was known that the KBr was sensitive to water, but it was thought that storing the chamber inside the Perspex enclosure would be sufficient since the air inside the chamber is very

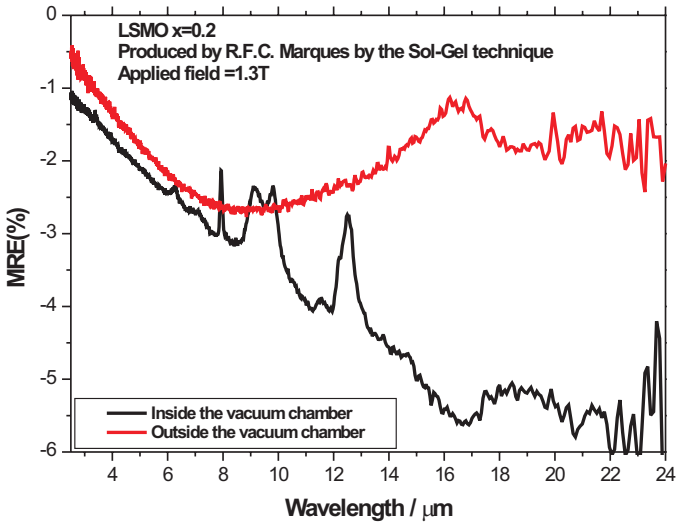

Figure 4.11: MRE(%) spectra measured inside and outside of the vacuum chamber for a bulk $La_{0.8}Sr_{0.2}MnO_3$ sample. (Original in colour)

dry. Unfortunately, the exposure of the window to the atmosphere when changing the sample proved sufficient to contaminate it.

Ultimately the decision was made to replace the KBr window with a more resilient material. Fortunately, the next best alternative, KRS-5, is non-hygroscopic so this material was used instead. The window shown in Figure 4.8 is made from KRS-5, hence its distinctive orange colour. The drawback is that the KRS-5 transmits less of the IR light, thus making the alignment more difficult, particularly for the poorly reflecting manganite samples. An additional, unforeseen drawback, is that the KRS-5 window actually p-polarizes the IR light. As was discussed above, the MRE is larger for p-polarized light, but the reflectivity is much lower. This makes an already difficult alignment procedure that much more difficult. However, despite these setbacks I still managed to acquire temperature controlled MRE spectra for a number of manganite samples, the results of which shall be discussed in Chapter 6.

4.3 Additional experiments

4.3.1 Vibrating sample magnetometer measurements

Hysteresis measurements were made for a small selection of samples using a Vibrating Sample Magnetometer (VSM).

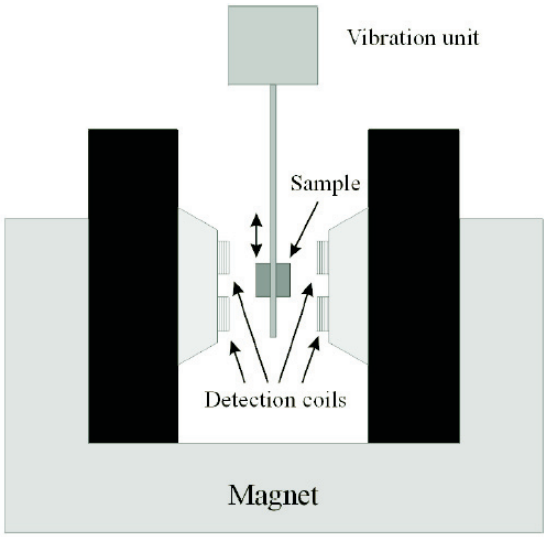

Figure 4.12: Schematic of the setup for a Vibrating Sample Magnetometer

The use of a VSM to make such measurements is a well established technique. The VSM, shown schematically in Figure 4.12, employs an electromagnet to provide a uniform (DC) magnetizing field. When a magnetic material is placed within a uniform magnetic field and is made to undergo sinusoidal motion (i.e. mechanically vibrated), there is some magnetic flux change. This induces a current in the detection coils, which is proportional to the magnetic moment of the sample. The field is swept in a loop from zero field to the maximum positive field, to the maximum negative field and back to the maximum positive field.

4.3.2 Four-point probe measurements of CMR

The four point probe is the traditional technique used to measure the magnetoresistance of a sample. The four-point probe setup is shown schematically in Figure 4.13.

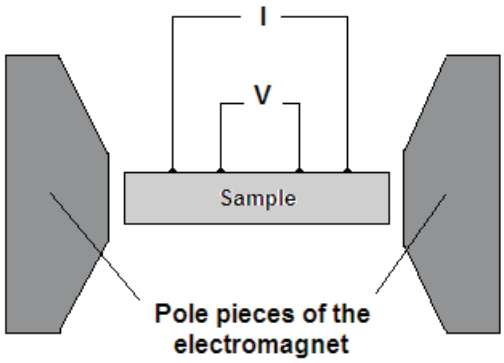

Figure 4.13: Schematic of the Four point probe experimental setup

A constant current I (of 2mA) is passed down one of the outer probes, through the sample and back out through the other outer probe. The voltage V across the sample is then measured as the magnetic field is changed. The magnetoresistance can then be found by using Ohm's Law to calculate the resistance as a function of the magnetic field. The maximum field we could achieve with our magnet was ± 0.9 T. For a sufficiently large sample area, the probes can be held in contact with the sample by spring loading the tips of the probes and applying a slight pressure. For the smaller samples it is necessary to affix the probes (usually very thin copper wires) with silver paint or a silver-loaded conducting epoxy.

4.3.3 Temperature controlled CMR measurements

Figure 4.14 shows a schematic of the setup for the temperature controlled four-point probe measurements of the CMR.

The sample is placed inside the cryostat, between the pole pieces of the magnet. The cooling is generated by the cryogen (in this case liquid nitrogen) flowing under the cold plate. Since the sample is not placed on the cold plate, an exchange gas is required to cool the sample. Helium is an ideal exchange gas for a liquid nitrogen cryogen since it remains gaseous at 77K. The volume between the inner, He-filled, chamber and the outer jacket of the cryostat is evacuated using a combination of a rotary pump and a diffusion pump. This is to prevent the atmosphere outside the cryostat from heating the sample chamber.

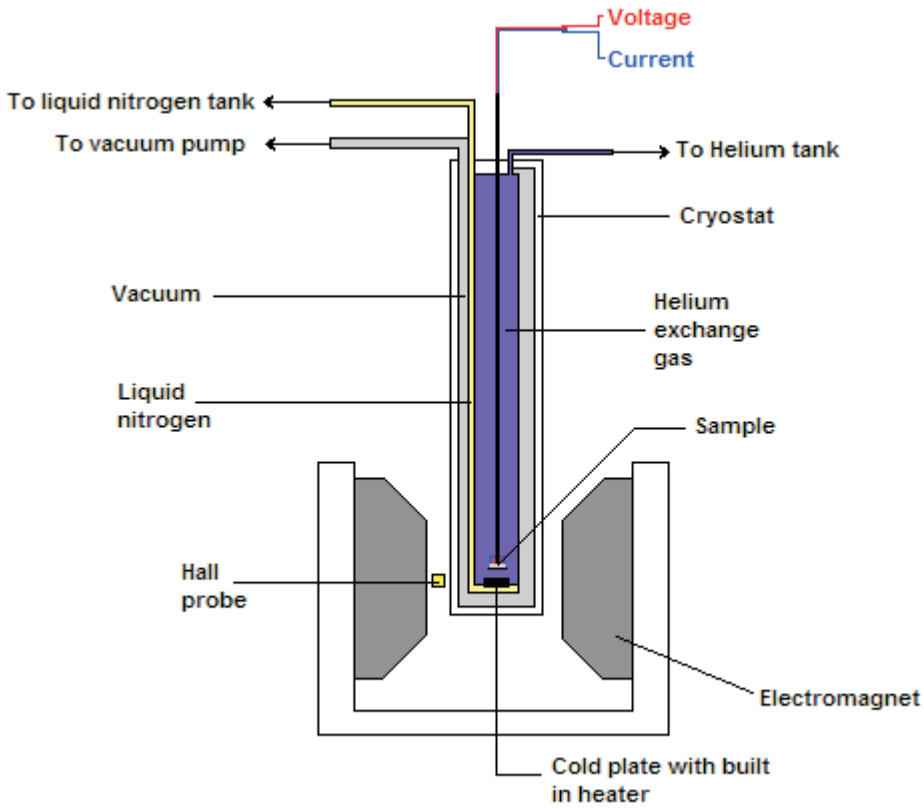

Figure 4.14: Schematic of the temperature controlled CMR experimental setup. (Original in colour)

The temperature is controlled by changing the temperature at the cold plate. The plate has an in-built heater that can be turned on to raise the temperature of the plate, and thus the exchange gas and sample. It takes up to 30 minutes for the temperature to stabilise at a given temperature. The temperature is additionally measured by using a calibrated platinum resistor mounted close to the sample position. A proportional-integral-derivative controller (PID controller) was used to set the temperature of the plate. Once the required temperature is reached, the experimental procedure is identical to that for the room temperature four-point probe measurements.

4.3.4 Scanning Electron Microscope measurements

The use of a Scanning Electron Microscope (SEM) to examine the surface of conducting samples is another well established experimental technique. The SEM uses electrons

instead of light to form an image. A beam of electrons is produced at the top of the microscope by heating of a metallic filament. The electron beam follows a vertical path through the column of the microscope. It makes its way through electromagnetic lenses which focus and direct the beam down towards the sample. Once it hits the sample, other electrons (backscattered or secondary) are ejected from the sample. Detectors collect the secondary or backscattered electrons, and convert them to a signal that is sent to a viewing screen producing an image. For my measurements on bulk LSMO samples I used an FEI Sirion FEG SEM which has an accelerating voltage from 200eV – 30keV. A 15keV electron beam was used for my measurements. The detector was set to collect secondary electrons (SE).

Chapter 5

Experimental results for bulk samples of $\mathbf{La_{1-x}Sr_xMnO_3}$

5.1 Introduction

In Chapter 3 we modelled the infrared and MRE spectra of a generic bulk manganite sample. It was found that the IR and MRE spectra could be derived from the complex dielectric function of the sample and that it was the balance between the competing terms in this dielectric function that controlled the features of the spectra. For the bulk samples, the complex dielectric function consisted of three terms, a high frequency term, a Drude-like term and a resonance term, as is reiterated in equation 5.1:

$$\varepsilon(\omega) = \varepsilon_\infty - \frac{\omega_p^2}{\omega^2 + \imath\gamma\omega}(1 + \eta m^2) + \sum_{j=1}^{n} \frac{S_j^2}{k_j^2 - k^2 - \imath\gamma_j k} \tag{5.1}$$

For metallic samples, with a large number of free carriers, the Drude-like term has a higher weighting in the complex dielectric function and this was reflected in the IR and MRE spectra. However, it was also shown that as the plasma frequency was reduced, either by increasing the effective mass or reducing the number of free carriers, the Drude-like term became less significant and the resonance term became increasingly important.

In this chapter I will present the results of a variety of experiments carried out on bulk samples of $La_{1-x}Sr_xMnO_3$ that will help us to characterise their magnetic and magnetotransport properties. I will also examine how well this form of the complex dielectric

function models a real set of bulk manganite samples. The samples were provided by R.F.C. Marques, a visiting student from the Instituto de Química de Araraquara in Brazil, and he also carried out some of the early experiments on the samples during his visit to our group. The analysis and the modelling of the data presented in this chapter, and in Chapter 3, is a continuation of his experimental work on these samples.

This chapter will begin with a brief description of the preparation techniques used to produce the samples before demonstrating with SEM images how the preparation technique influences the surface topography of the samples. After showing magnetization curves, I will then focus on how well the model represents the real IR and MRE spectra obtained from these samples. At the end of the chapter, I will compare the results obtained from traditional four-point probe measurements with those obtained using our MRE technique and I hope to convince the reader that the contactless MRE measurement technique is a viable alternate to the standard four-point probe method of measuring a sample's magnetoresistance.

5.2 The samples

Bulk samples of $La_{1-x}Sr_xMnO_3$ ($x = 0, 0.1, 0.2$ and 0.3) were prepared in Brazil using two different preparation methods: a solid state reaction (SSR) method and a sol-gel (SG) method. The SSR samples were prepared using an in situ solid state oxidation reaction using a stoichiometric mixture of Mn_2O_3, LaO_3 and SrO_2 as oxide reaction agents. The resulting disks were fired at 1300$^\circ C$ for 16 hours. The SG samples were prepared through a homogeneous co-precipitation method using urea as a precipitant agent. The resulting powders were pressed at 2.5 x 10^3 kg cm^{-2} into disks of diameter 8mm, thickness 1mm, and were calcined for 18 hours at 1100$^\circ C$. A more detailed description of these preparation techniques is published elsewhere (146; 147).

The bulk LSMO samples that were studied are shown in Table 5.1. The first column in the table is the chemical composition of the sample and the second column shows a shorthand designation that is used for each sample.

Sol-Gel	
Composition	**Sample code**
$LaMnO_3$	LSMO_ SG_ 00
$La_{0.9}Sr_{0.1}MnO_3$	LSMO_ SG_ 01
$La_{0.8}Sr_{0.2}MnO_3$	LSMO_ SG_ 02
$La_{0.7}Sr_{0.3}MnO_3$	LSMO_ SG_ 03
Solid State Reaction	
Composition	**Sample code**
$LaMnO_3$	LSMO_ SSR_ 00
$La_{0.9}Sr_{0.1}MnO_3$	LSMO_ SSR_ 01
$La_{0.8}Sr_{0.2}MnO_3$	LSMO_ SSR_ 02
$La_{0.7}Sr_{0.3}MnO_3$	LSMO_ SSR_ 03

Table 5.1: The bulk LSMO samples that were studied. The first column in the table is the chemical composition of the sample and the second column shows a shorthand designation that is used for each sample.

5.3 Surface topography

The MRE relies on the infrared light from the spectrometer being reflected from the surface of the sample. It was observed that the SSR samples were much less reflective than their SG counterparts. In order to understand why this should be the case, SEM images of the surface topography were taken. Figure 5.1 clearly illustrates the fundamental difference between the surface topography of the SG and the SSR samples, using as an example the $x = 0.2$ sample.

The SG samples (as demonstrated for the $x = 0.2$ SG sample in Figure 5.1a) were characterized by large flat areas typically larger than 40μm, whereas for the SSR samples, smaller particles varying in size from a few μm to 40μm were observed (Figure 5.1b). The topography of the samples is important because we are observing surface features for the SSR samples that are similar in size to the wavelength of the incident IR light from the

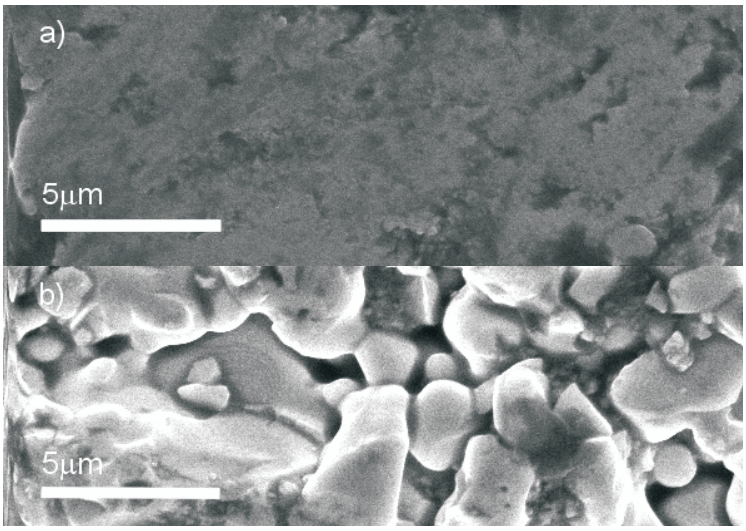

Figure 5.1: Scanning electron micrograph of $La_{0.8}Sr_{0.2}MnO_3$ prepared by a) the sol-gel technique and b) the solid state reaction method. Reproduced from (47).

spectrometer. This will result in increased scattering and possibly increased absorption of the incident light, particularly for shorter wavelengths. This results in a lower reflected signal being detected than for the SG samples. Since the reflected signal from the SSR samples was so inferior compared to the SG samples, the majority of the measurements made for these samples has focussed on the SG samples. (Further images can be found on the accompanying CD - see Appendix A.2 for details.)

5.4 Magnetization measurements

The magnetization curves of the samples were measured by R.F.C. Marques at room temperature using a vibrating sample magnetometer. Figure 5.2 shows the normalised magnetization curves of the SG $La_{1-x}Sr_xMnO_3$ ($x = 0, 0.1, 0.2$ and 0.3) samples. In agreement with Urushibara et al (54), $LaMnO_3$ and $La_{0.9}Sr_{0.1}MnO_3$ are both paramagnetic at room temperature. By contrast, $La_{0.8}Sr_{0.2}MnO_3$ and $La_{0.7}Sr_{0.3}MnO_3$ are both ferromagnetic and metallic at ambient temperatures. The ferromagnetic samples exhibit a very weak hysteresis, but no remanence, as illustrated in the bottom figure of 5.2 for the $x = 0.3$ sample.

The $x = 0.2$ and 0.3 samples both exhibit rapid magnetization as the applied field is increased with the magnetization becoming linear with applied field at around 0.4 T for

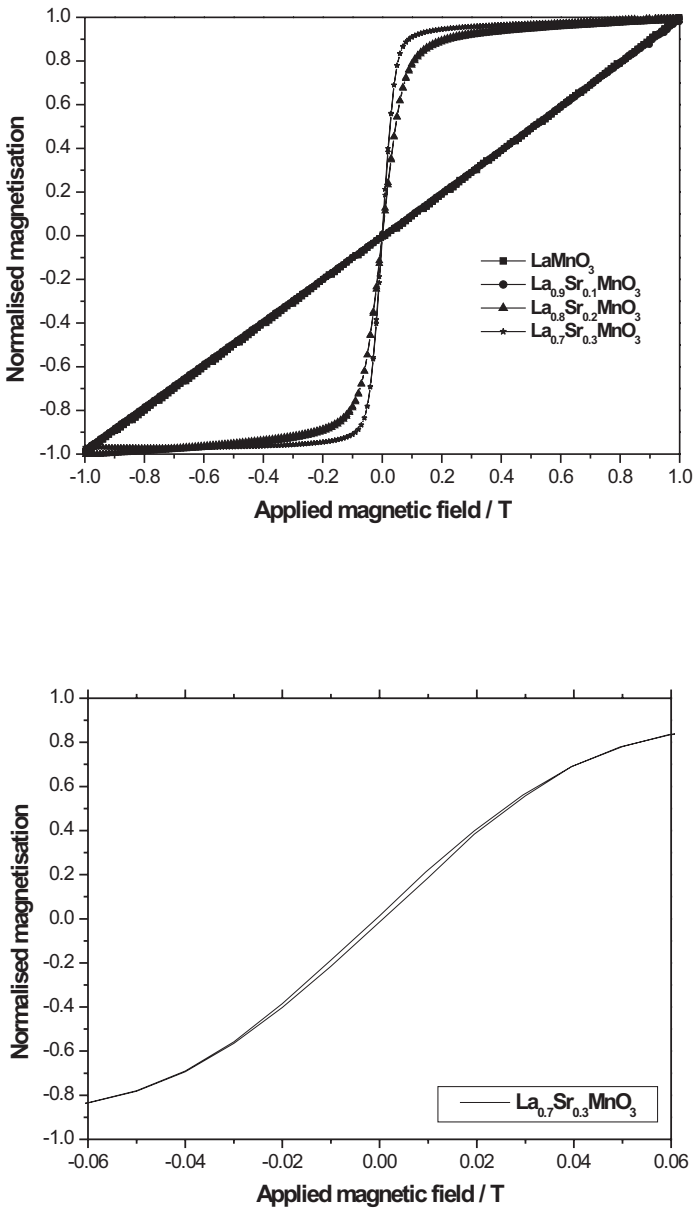

Figure 5.2: Top: Room temperature normalised magnetization curves for $La_{1-x}Sr_xMnO_3$ ($x = 0, 0.1, 0.2$ and 0.3) as measured by R.F.C. Marques. The magnetization curves for $x = 0$ and $x = 0.1$ overlay each other. Bottom: Close up view at low fields for the $x = 0.3$ sample showing the very weak hysteresis in the sample at room temperature.

the $x = 0.3$ sample and 0.5 T for the $x = 0.2$ sample. The magnetization continues to increase linearly with applied field, typical of paramagnetic behaviour. As these are bulk samples, it is likely that there will be regions of inhomogeneity within the sample where the doping concentration is lower than the nominal value, leading to paramagnetic regions within the ferromagnetic phase.

The fact that the ferromagnetic samples do not saturate in high field may be important when we consider the magnetic field dependence of the MRE spectra. This will be discussed in section 5.5.4.

The VSM data demonstrates that the magnetic domains in the ferromagnetic samples will very readily align with the applied field. This comes as no surprise since the strong Hund coupling between the t_{2g} and e_g electrons in these materials favours alignment of the electron spins to minimise the energy of the system. Indeed, the small hysteresis observed in these samples reflects the fact that the ferromagnetic domains are already well aligned in this phase.

5.5 IR and MRE spectra

5.5.1 Room temperature measurements

Figure 5.3 shows the infrared spectra from the $La_{1-x}Sr_xMnO_3$ sol-gel samples ($x = 0, 0.1, 0.2$ and 0.3) in randomly polarized light in zero applied magnetic field. Figure 5.3a shows the raw spectra, as measured directly by the spectrometer for the $La_{1-x}Sr_xMnO_3$ sol-gel samples ($x = 0, 0.1, 0.2$ and 0.3). These spectra also contain the signatures of water and CO_2 absorption. The figure shows the IR spectrum of the Ag reference sample (from Figure 4.3) for easy comparison. Figure 5.3b shows the same IR spectra for the $La_{1-x}Sr_xMnO_3$ sol-gel samples after normalisation using the Ag reference spectra.

The Curie temperature is important in these materials since it marks the boundary between competing paramagnetic insulating and ferromagnetic metallic phases and is strongly dependent upon the level of doping, x (54). As indicated in Figure 5.2, $LaMnO_3$ and $La_{0.9}Sr_{0.1}MnO_3$ are paramagnetic at ambient room temperatures (RT), whereas the $La_{0.8}Sr_{0.2}MnO_3$ and $La_{0.7}Sr_{0.3}MnO_3$ are ferromagnetic. The $x = 0.2$ sample has a $T_C \sim$

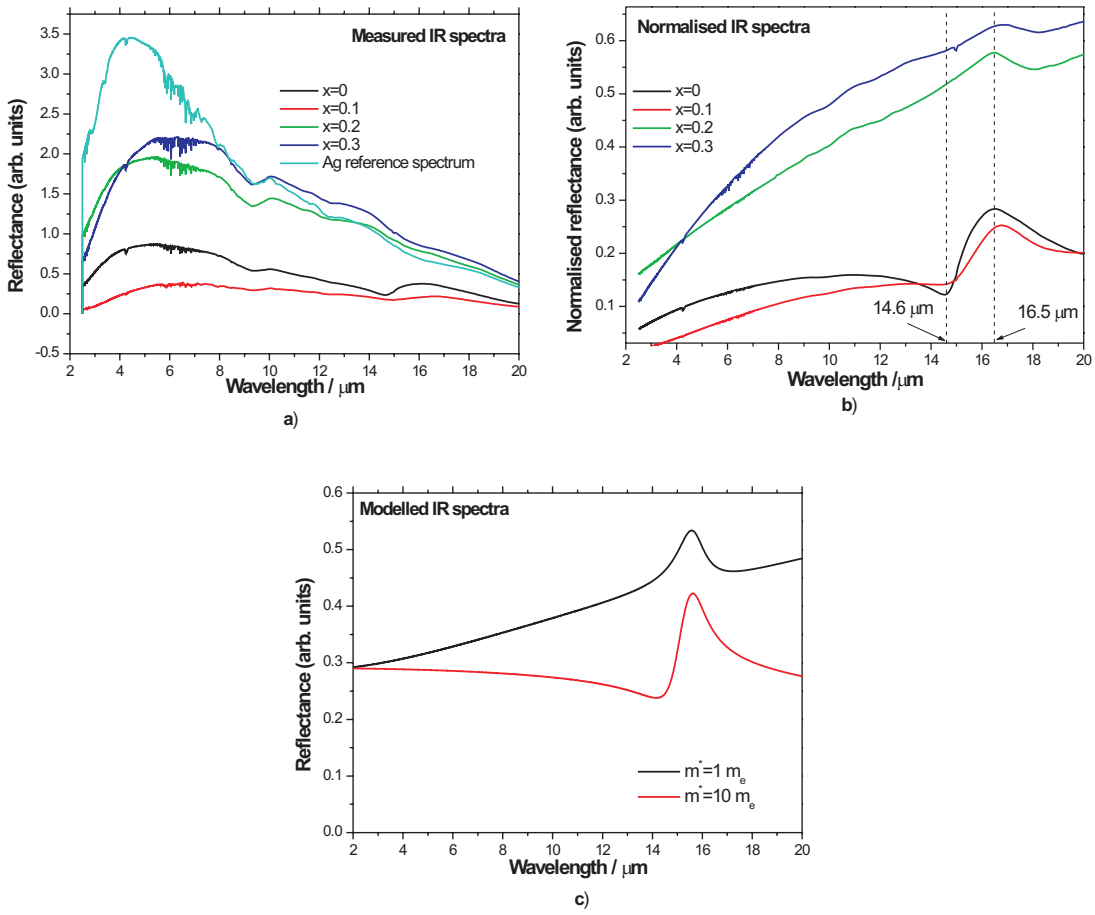

Figure 5.3: a) IR spectra (as measured) in randomly polarized light for $La_{1-x}Sr_xMnO_3$, $x = 0, 0.1, 0.2$ and 0.3 and a Ag reference sample in zero applied magnetic field at room temperature. b) Normalised IR spectra in randomly polarized light for $La_{1-x}Sr_xMnO_3$, $x = 0, 0.1, 0.2$ and 0.3 in zero applied magnetic field at room temperature. c) Modelled IR spectra for a bulk manganite sample using the numerical values in Table 3.1 with η =0.07. The figure shows the effect of changing the effective mass in the plasma frequency of the Drude-like term from 1 electron mass to 10 electron masses. (Original in colour)

305K, though of course the value will depend on the stoichiometry of the sample. This is very close to room temperature, placing the sample near the boundary between metallic and insulating behaviour. The $x = 0.3$ sample has a Curie temperature of $\sim$ 370K and this sample is well within a ferromagnetic and metallic phase at room temperature. A high reflectivity is associated with a higher conductivity in the sample. Figures 5.3a and b illustrate this point since the conductivity and hence reflectivity in the paramagnetic insulating samples is markedly lower than that observed in the ferromagnetic metallic samples. The infrared spectra for the samples with T>T$_C$ at room temperature ($x = 0$ and 0.1 in Figure 5.3b) exhibit an additional feature located at 14.6 μm (as shown). The peak located between 16–17 μm is attributed to the stretching vibrational mode of the Mn–O bonds (25) and is marked by an increase in the reflectance and hence an increase in the conductivity.

The IR spectra for the $x = 0.2$ and $x = 0.3$ samples are very similar in shape to those predicted by the model for these samples as is shown in Figure 5.3c. The main difference between the experimental result and the model is that the experimental reflectivity is markedly lower at shorter wavelengths than was predicted by the model. The model is an idealised situation, however, and does not account for scatter caused by surface irregularities, or absorption at shorter wavelengths.

The fact that the modelled spectra seem to converge at the value 0.3 at short wavelengths is intriguing. This is likely to be a limitation of the model at short wavelengths. Simply put, at short wavelengths, the ε_∞ term becomes dominant over the Drude and resonance terms. The ε_∞ term, however, is wavelength independent in this model and hence has a fixed value - a value that the modelled spectra will tend to converge upon. Hence, at short wavelengths, it may be that the model is unsuitable to describe the real situation. Therefore, it may not just be diffuse scattering or absorption at short wavelengths that gives the markedly lower experimental reflectivities, it may be that the model breaks down at these wavelengths.

The peak at 16–17 μm is much more pronounced in the $x = 0$ and $x = 0.1$ samples. These samples have a low free carrier concentration compared to the $x = 0.2$ and $x = 0.3$ samples so it is most likely that the free carriers are screening the effect of the stretching mode in the latter. This can be understood in terms of the complex dielectric function for the samples as given by equation 5.1. As the number of free carriers drops, the Drude

term in the dielectric function becomes less significant, meaning that the weighting of the phonon term becomes more important. Hence, in the $x = 0.2$ and $x = 0.3$ samples where there are more free carriers, the Drude term in equation 5.1 becomes more significant than in the $x = 0$ and $x = 0.1$ samples and, hence, the balance of the dielectric function changes, thus lowering the contribution from the phonon term in the dielectric function and hence reducing its contribution in the IR spectra. In summary then, at short wavelengths the surface roughness may change the apparaent reflectivity in all of the samples. At intermediate wavelengths, a reduction in the plasma frequency for the low doped samples will lower the reflectivity.

The spectral feature observed at 14.6 μm is an interesting characteristic of the paramagnetic samples. As Figure 3.3 (p.61) demonstrates, we can reproduce this spectral feature in the model if we allow a reduction in the plasma frequency, which is modelled in the figure by increasing the effective mass of the free carriers from 1 electron mass to 10 electron masses. As predicted by the model, we observe that a reduction in the plasma frequency lowers the weighting of the Drude term in the dielectric function thus reducing the reflectivity of the sample. The $x = 0$ and $x = 0.1$ samples are much less reflective at all wavelengths than the $x = 0.2$ and $x = 0.3$ samples since they have fewer free carriers. The lower value of ω_p in the $x = 0$ and $x = 0.1$ samples shifts the plasma edge shifts to longer wavelengths and so more of the incident IR light will be transmitted instead of reflected, resulting in a lower reflectivity from these samples compared to the $x = 0.2$ and $x = 0.3$ compositions. Again, the model is not in agreement with the experimental data at short wavelengths, but this will again be because the model does not account for scatter caused by surface irregularities, or absorption at shorter wavelengths.

Alternatively, we also saw that the feature at 14.6 μm could be replicated in the model by increasing the frequency of the damping term, γ, by several orders of magnitude in the Drude-like term of the dielectric function in equation 5.1. This was shown in Figure 3.5. However, this is less realistic than changing the plasma frequency, since in effect, increasing the magnitude of the damping term serves to make the $\imath\gamma\omega$ in equation 5.1 increasingly dominant such that eventually $\imath\gamma\omega > \omega_p^2$. Hence, the Drude-like term will again assume a lesser weighting in the complex dielectric function, resulting in exactly the same effect as was observed when we lowered the plasma frequency.

Resonance parameters	j=1	j=2	j=3
k_j (cm^{-1}); λ (μm)	161.6; 61.9	323.2; 30.9	600.3; 16.6
γ_j (cm)	50	50	50
S_j (cm^{-1})	600	600	600
Other parameters			
N	$1.0 \times 10^{26}/m^3$		
ε_∞	9.0		
γ	$1 \times 10^{15} Hz$		
m_e^*	9.11 $\times$ 10^{-31} kg		
η	0.05		

Table 5.2: The parameters used in the modelling of bulk LSMO samples.

The $x = 0$ and $x = 0.1$ samples are in a paramagnetic phase, hence it makes more physical sense that the feature at 14.6 μm is due to either a decrease in the number of free carriers or a change in their effective mass, or both, rather than an change in the damping factor of several orders of magnitude. As we saw in Chapter 2, the formation of polarons in the paramagnetic phase has been suggested to explain the conduction in this phase. It is certainly true that a polaron has a larger effective mass than a free electron and it is possible that the feature we are seeing at 14.6 μm in the IR spectra is caused by polaron formation. In addition, the formation of polarons traps the free carriers, thus reducing their number. Hence, whether it is an increase in the effective mass of the carriers or a reduction in their number, both are consistent with the formation of polarons in the paramagnetic phase but cannot prove their existence.

In Figure 5.4, I have plotted the modelled and experimental IR spectra of the $x = 0.1$ (top), $x = 0.2$ (middle) and $x = 0.3$ (bottom) samples. The parameters used to model the IR spectra in Figure 5.4 are given in Table 5.2. For the $x = 0.1$ sample, it was necessary to increase the effective mass of the free carriers from 1 to 3 electron masses.

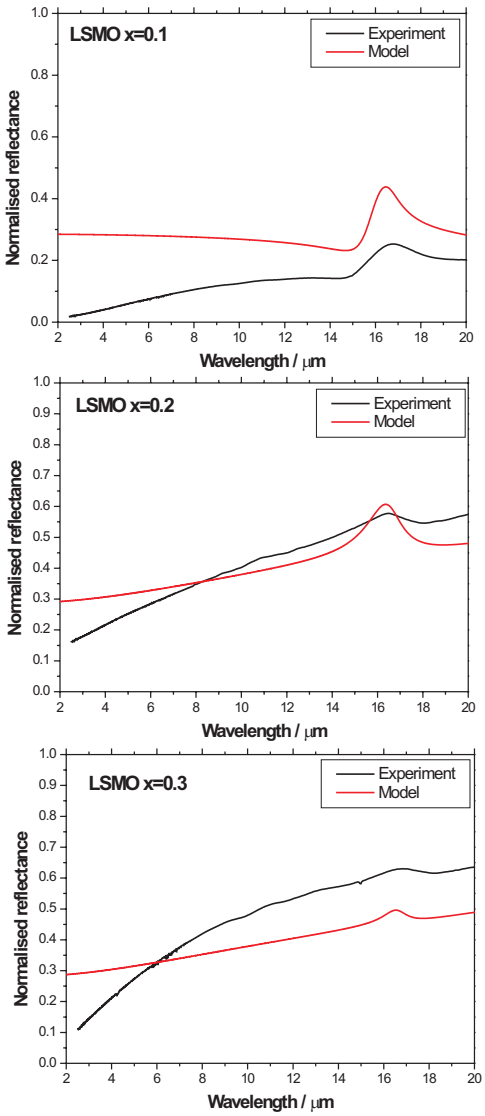

Figure 5.4: From top to bottom: Modelled and experimental IR spectra for $La_{0.9}Sr_{0.1}MnO_3$, $La_{0.8}Sr_{0.2}MnO_3$ and $La_{0.7}Sr_{0.3}MnO_3$. All measurements were made using randomly polarized incident light at ambient room temperature. The modelled spectra were based on parameters given in Table 5.2. Please refer to the main text for changes in the parameters given in the table. (Original in colour)

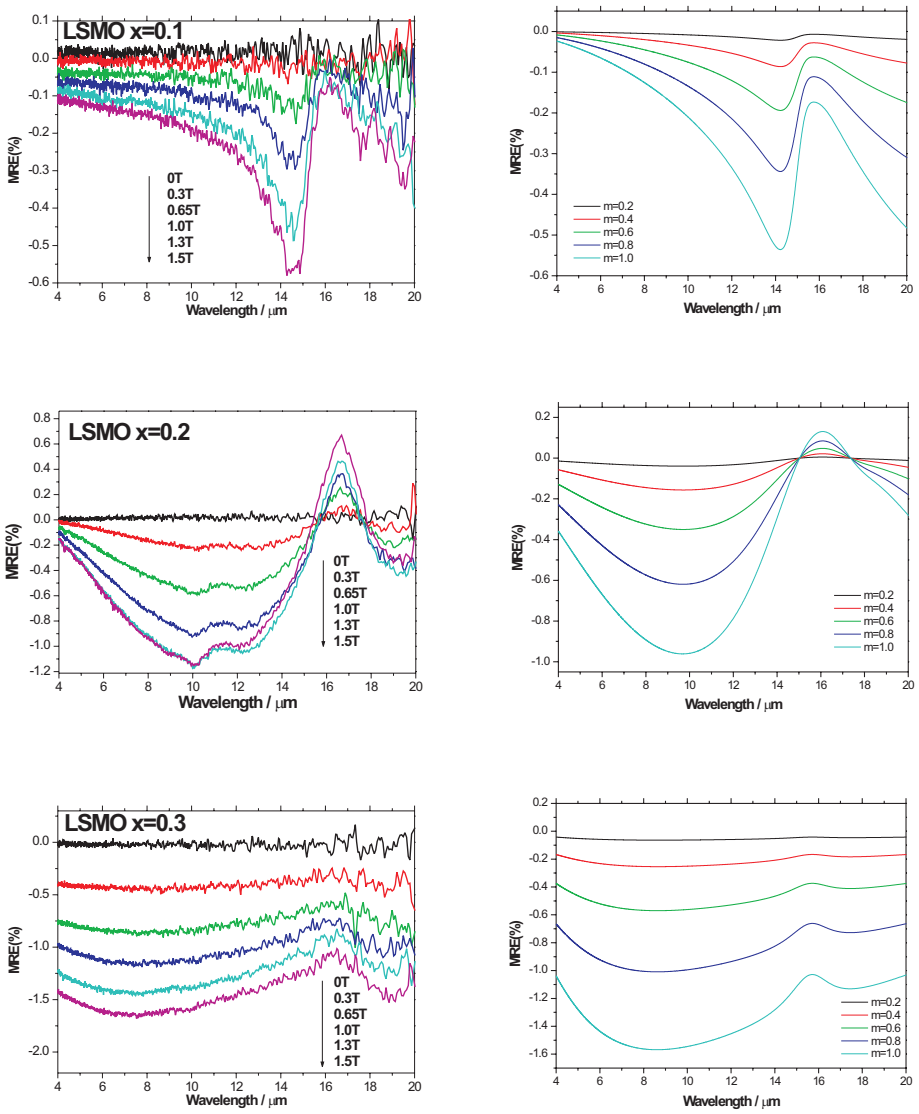

Figure 5.5: Left: From top to bottom, MRE (%) spectra for $La_{0.9}Sr_{0.1}MnO_3$, $La_{0.8}Sr_{0.2}MnO_3$ and $La_{0.7}Sr_{0.3}MnO_3$. All measurements were made using randomly polarized incident light at ambient room temperature. The applied magnetic field ranges from 0 to 1.5 T as indicated. Right: Modelled MRE(%) spectra. The modelled spectra were based on parameters given in Table 5.2. Please refer to the main text for changes in the parameters given in the table. (Original in colour)

For the $x = 0.2$ sample it was necessary to increase the oscillator strength of the 3^{rd} phonon mode from 600 to 1500 cm^{-1}, and for the $x = 0.3$ sample it was necessary to reduce the oscillator strength to 250 cm^{-1}. The modelled spectra are not exact fits to the experimental spectra, but they are in reasonable agreement. Generally the modelled spectra have a lower reflectivity that those measured experimentally at all wavelengths. However, minimal changes had to be made between the different compositions to produce the modelled spectra. Are these parameter changes sensible? The increase in effective mass for the $x = 0.1$ sample from 1 to 3 electron masses is reasonable since the $x = 0.1$ sample is in the paramagnetic phase where the free carriers are more likely to be localised in polarons. It is not clear, howver, why the oscillator strength should vary so much between the $x = 0.2$ and $x = 0.3$ samples. It could simply be due to the tolerance factor as was discussed in Chapter 2. The mismatch in size between the La and Sr ions in the unit cell is likely to change the resonance frequency of the stretching mode. It could, therefore, be that doping in the $x = 0.2$ sample enhances the resonance, whereas the increased doping prevalent in the $x = 0.3$ sample serves to dampen the resonance feature. This is all conjecture, but it would perhaps explain the observed results.

In Figure 5.5, I have plotted the corresponding MRE spectra for these data. The MRE spectra also depend on the sample composition. In the left hand panels of Figure 5.5, I show from top to bottom the experimentally measured MRE spectra for the sol-gel $x = 0.1, 0.2$ and 0.3 samples, respectively. In the right hand panels of the figure I show modelled MRE spectra. The parameters used to model the MRE spectra in Figure 5.5 are given in Table 5.2. It is clear from Figures 5.4 and 5.5 that if one can find the correct values for the parameters in the complex dielectric function, then the model can successfully reproduce all of the spectral features observed experimentally.

5.5.2 Temperature induced effects

Due to the poor reflectivity of the bulk samples in p-polarized incident light, it was not possible to use the micro-miniature refrigeration system to measure the IR and MRE spectra as a function of temperature. The $x = 0.2$ sample has a Curie temperature of 305K. This means that room temperature measurements are made in close proximity to the boundary between the ferromagnetic metallic-paramagnetic insulating phase transition. Hence, if

the ambient room temperature were to increase it would then be possible to observe how the metal-insulator transition influences the IR and MRE spectra.

Figures 5.6a and 5.6b present the infrared spectra for the same $x = 0.2$ sample after normalisation to the Ag reference spectrum at different ambient room temperatures, it being approximately 10K warmer for the data in Figure 5.6b.

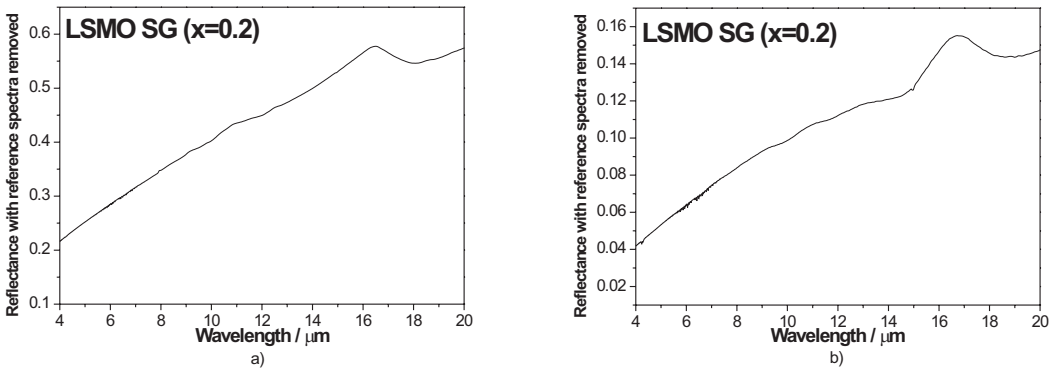

Figure 5.6: Infrared spectra for $La_{0.8}Sr_{0.2}MnO_3$ taken on two separate occasions using randomly polarized incident light. The ambient room temperature in b) is 10K higher than that in a), which is as in Figure 5.3.

As the ambient temperature increases there are signs of an additional dip forming at around 14.6 μm and in addition, the reflectance, and hence the conductivity, drops considerably in Figure 5.6b indicating a change to more insulating behaviour. It is apparent that the increase in the ambient room temperature has had an effect on the conduction properties of the sample due to the proximity of the metal-insulator transition. This clearly demonstrates that the magnetic phase of the sample is very important in determining the conductive properties of the sample. The modelled data in Figure 5.3 demonstrates that the spectral feature at 14.6 μm is created by reducing the weighting of the Drude-like term in equation 5.1. It is still not clear from these experiments, however, whether it is the number of free carriers or their effective mass that has changed as the sample enters the paramagnetic phase.

Figures 5.7a and 5.7b show the MRE (%) results for different applied fields for the same set of data as shown in Figures 5.6a and 5.6b. The shape of the two MRE data sets is clearly very different and confirms the presence of the additional dip at 14.6 μm when

the ambient temperature has increased.

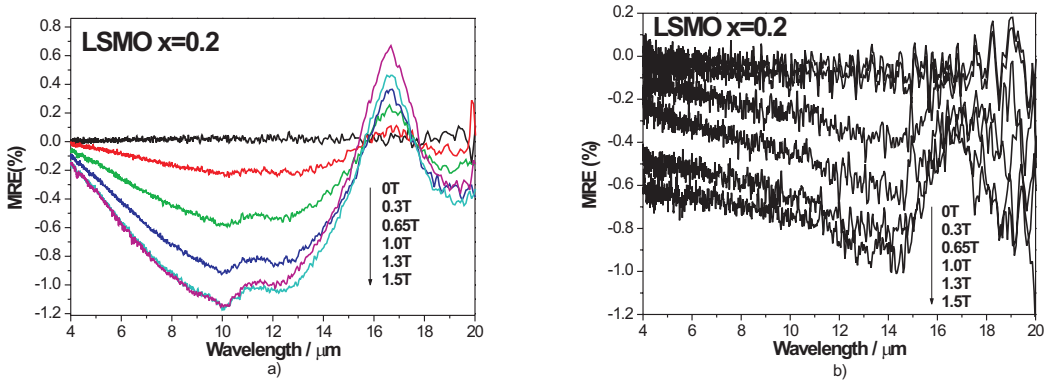

Figure 5.7: MRE(%) spectra for $La_{0.8}Sr_{0.2}MnO_3$ taken on two separate occasions using randomly polarized incident light. The ambient room temperature in b) is 10K higher than that in a), thus making the sample enter the metal-insulator transition. (Original in colour)

As has been argued above, the change in shape in the MRE spectra can be modelled by increasing the effective mass of the free carriers, or more correctly by reducing the plasma frequency in the Drude-like term in the dielectric function. As the plasma frequency drops, the Drude-like term in the dielectric function is no longer the dominating term and this results in a change in the curvature of the spectra at low to mid-IR wavelengths (2-10μm) as the sample becomes less conducting and less reflective at these wavelengths.

5.5.3 Polarization dependence

In section 4.2.2 of Chapter 4, it was predicted that for an angle of incidence of 65°, the reflectivity would tend toward zero, thus producing a large MRE since the MRE is proportional to $\Delta R/R$. This was also predicted by the modelling in Chapter 3 where I showed in Figure 3.2a that the MRE is largest for p-polarized light. The magnitude of the MRE was also shown to be polarization dependent experimentally as Figure 5.8 shows. The maximum MRE for p-polarized light is approximately 7% at 7μm. This compares to a maximum value of 1.1% at 10μm for the same sample in randomly polarized incident light (as shown in Figure 5.7a)

In Figure 5.8, I also compare the shape of the modelled MRE spectra for p-polarized

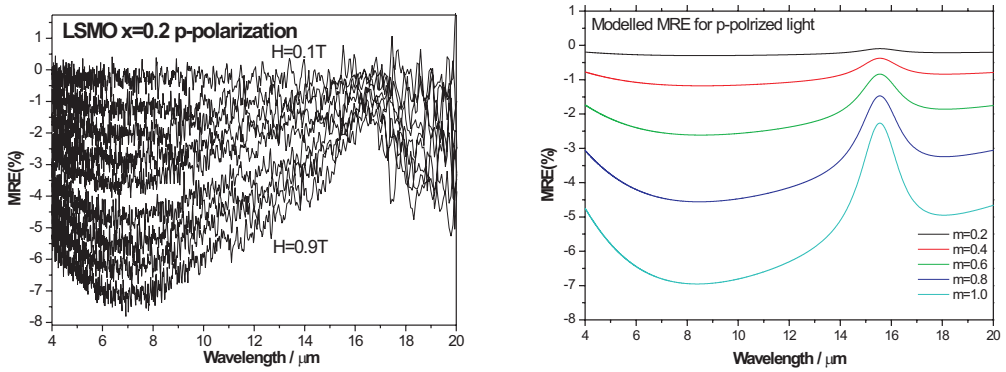

Figure 5.8: Left: MRE(%) as a function of wavelength for $La_{0.8}Sr_{0.2}MnO_3$ using p-polarized incident light at room temperature. The applied magnetic field was varied in 0.1 T intervals between 0.1 and 0.9 T. Right: Modelled MRE(%) for p-polarized light using the parameters given in Table 5.2 with the exception of η=0.06, S_1=671 cm^{-1}, S_2=559 cm^{-1} and S_3=559 cm^{-1}. (Original in colour)

light with the experimental result. The model is fairly successful at reproducing the spectral features that are observed experimentally. The curvature at low wavelengths is not quite correct, but it should be possible to fine tune the parameter values in order to make the fit better.

5.5.4 Magnetization dependence

In section 5.4 we observed from the VSM measurements that the the $x = 0$ and $x = 0.1$ samples had a linear field dependence, typical of samples exhibiting paramagnetic behaviour. However, the magnetization of the ferromagnetic and metallic samples was observed to be non-linear with the applied magnetic field. The question is, how does this magnetization dependence manifest itself in the MRE spectra?

If we compare the MRE values at 10μm in the MRE spectra for the paramagnetic $x = 0.1$ with the ferromagnetic $x = 0.2$ and 0.3 samples, we observe the magnetization dependence shown in Figure 5.9:

The paramagnetic $x = 0.1$ sample exhibits a linear variation in the MRE(%) with magnetization. The ferromagnetic samples behave differently, however. The $x = 0.2$

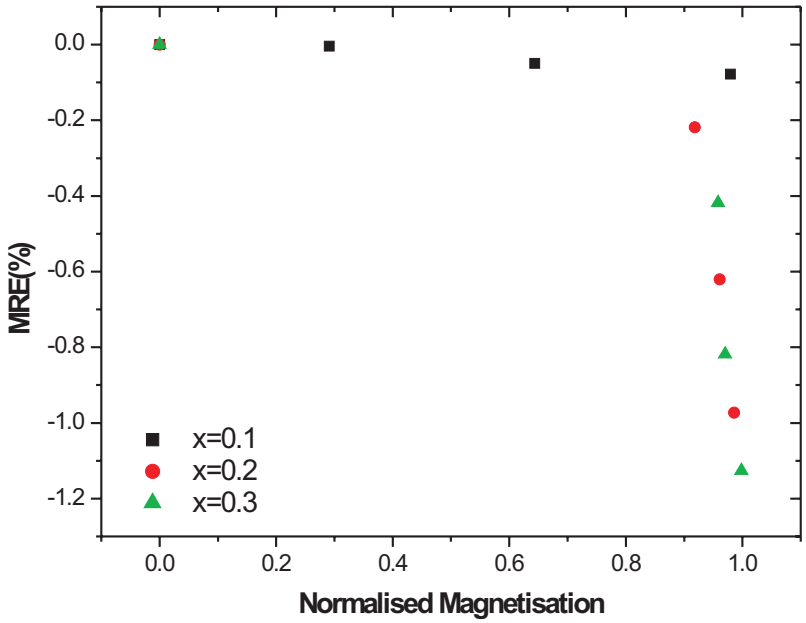

Figure 5.9: Magnetization dependence of the MRE(%) at 10 μm for the LSMO samples. The MRE values for the paramagnetic $x = 0.1$ sample has a linear magnetization dependence. The $x = 0.2$ and 0.3 samples also exhibit a linear magnetization dependence for fields above 0.3T. (Original in colour)

and 0.3 samples only exhibit a linear magnetization dependence for fields above 0.3 T. This is in accordance with the VSM data which showed that the $x = 0.2$ and 0.3 samples both exhibited rapid magnetization as the applied field is increased with the magnetization becoming linear with applied field at around 0.4 T for the $x = 0.3$ sample and 0.5 T for the $x = 0.2$ sample. Hence, the magnitude of the MRE for a given field is related to the magnetization of the sample. We could expect the MRE to vary with the square of the magnetization (i.e. m^2) if the intergrain tunnelling asserted by Hwang *et al.* (91) is true, particularly in the $x = 0.1$ sample. There is, however, insufficient data at low fields to determine the relationship between the MRE(%) and the magnetization for fields between 0 and 0.3T for all of the samples. By 0.3T we are already starting to enter a regime where the MRE(%) has a linear dependence with the magnetization for all of the

sample compositions, and the MRE(%) clearly varies linearly with the magnetization for the $x = 0.1$ sample in any case. Further MRE measurements at low fields would be required to determine whether a m^2 relationship is observed in any of the samples.

It is important to notice that despite the fact that the $x = 0.1$ sample is in an insulating phase we still observe field dependent conduction in the MRE spectra. From the way the MRE has been defined, a negative MRE(%) indicates that the reflectivity, and hence the conductivity, has increased. This is a surprising result in particular because the sample is well above T_C at room temperature. The fact that the increase in the conductivity is field dependent (a larger field produces a larger negative MRE) suggests that the field is responsible for this increased conductivity. A possible explanation for this increased conductivity in an applied field is based upon the concept of the magnetic polaron that was discussed in Chapter 2. If one allows that small ferromagnetic clusters can exist within the paramagnetic phase, then one should observe limited conductivity between adjacent clusters through the double exchange mechanism. If however one applies an external magnetic field, then more of the randomly orientated ferromagnetic clusters will tend to align with the applied field, thus facilitating the double exchange process, enhancing the conductivity of the sample in this phase.

5.6 A comparison between four-point probe and MRE measurements of the magnetoresistance

Traditionally, the dc four-point probe technique has been used to measure the magnetoresistance of a material. However, this technique requires contact to be made with the sample's surface, which could potentially damage it. An advantage of the MRE technique is that it requires no surface contacts and it lends itself to measurements with spatial resolution. In order to explore the correlation of the MRE technique with the four-point probe technique the CMR results were compared with the MRE values for p-polarized incident light at a wavelength of 7 μm for the $La_{0.8}Sr_{0.2}MnO_3$ SG sample, as depicted in Figure 5.8. All MRE and four point probe measurements were taken at ambient room temperature, the results of which are shown in Figure 5.10.

Let me clarify why I chose to use the MRE values at 7μm for p-polarized light. The

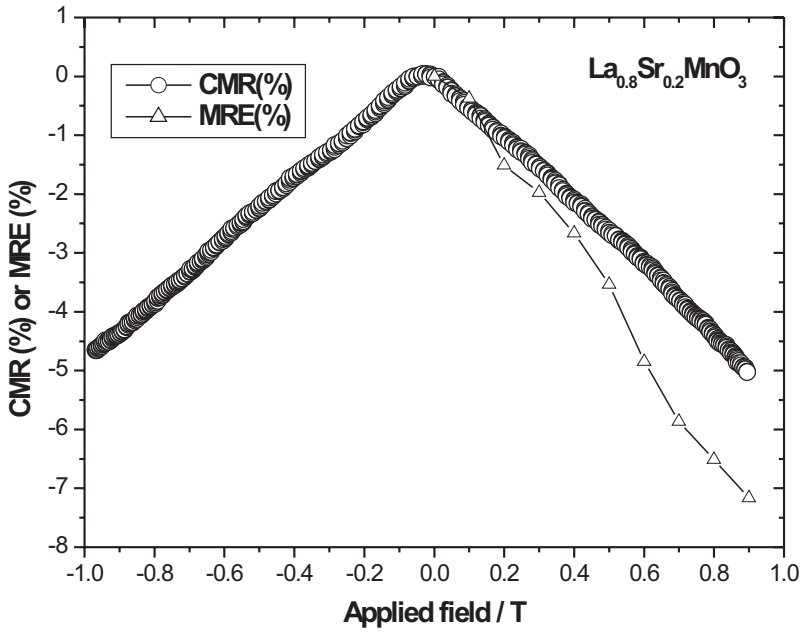

Figure 5.10: Electrically measured magnetoresistance in the $La_{0.8}Sr_{0.2}MnO_3$ sample taken at ambient room temperature (–o–) together with the MRE values at a wavelength of 7 μm for p-polarized light (black points). The line connecting the black points is shown to guide the eye.

four point probe measurements are only sensitive to the 'Drude-like' term in the complex dielectric function of equation 5.1 since this term is the only one that is proportional to the conductivity. The MRE values for p-polarized incident IR light at 7 μm were used since these represented the maximum MRE values for each field and were in the 'Drude' dominated regime far removed from the resonance feature at 16 μm.

As Figure 5.10 demonstrates, the MRE and the CMR measurements show a good correlation up to an applied field of about 0.4 T, with both sets of data changing linearly with the applied field. Beyond 0.4T, the two sets of data begin to demonstrate a slightly different response to the applied field. The CMR measurements are related to the dc resistivity whereas the MRE measurements are related to the ac, high frequency response of the sample to IR light. The difference between the two sets of data, therefore, could well be indicative of different conduction processes within the sample. As discussed in Chap-

ter 2, the dc resistivity will depend on grain boundaries and magnetic domains within the sample. The ac MRE measurements, on the other hand, could provide quantative information of how polarons respond to changes in the applied field for light of this frequency (148). Further study will be required to ascertain what additional information the MRE measurements contain, however.

This is an important result; it demonstrates that the MRE measurement technique is a viable alternative to the traditional four-point probe method of determining a samples magnetoresistance. As highlighted above, the most obvious benefit from a commercial viewpoint is that the MRE measurements can be made in situ without having to make potentially damaging contacts to the sample's surface. Of course an added benefit of the MRE technique is that it not only allows us to study the conductivity of the sample, it also allows us to investigate many more of the sample's properties, such as the behaviour of the phonon modes and to obtain further spectral information. Furthermore, the MRE experimental technique will also work for samples where it is not possible to attach contacts to the sample, e.g. samples in powdered form, though they do of course need to reflect infrared light.

5.7 Conclusions

In this chapter I have presented the results of experimental measurements on bulk samples of $La_{1-x}Sr_xMnO_3$ ($x = 0, 0.1, 0.2$ and 0.3) produced using the sol-gel method. I have shown that a model of IR and MRE spectra using the form of the complex dielectric function given by equation 5.1 successfully reproduces all of the spectral features observed experimentally for these bulk samples.

The model has helped us to appreciate the balance and competition between the terms in the complex dielectric function. Prior to the modelling, there was no explanation for the appearance of the spectral feature at 14.6 μm. This feature has been shown to exist in samples that have a low number of free carriers, e.g. the $x = 0.1$ sample, and has also been observed in the FM $x = 0.2$ sample as it approaches the M-I transition. Based upon the model, the most likely explanation for this feature is that ω_p has a lower value in the insulating sample/phase, which means that either the effective mass of the free carriers has

increased, and/or the number of free carriers has decreased. With regard to the $x = 0.2$ sample, this means that the free carriers must become trapped as the sample approaches T_C, since there is no other way of reducing the number of free carriers in the system. The field dependent increase in the conductivity observed in the MRE spectra is consistent with magnetic polarons being responsible for the conduction above T_C in the PM phase.

In this chapter I have shown that the MRE experimental technique is well suited for investigating the magnetotransport properties of bulk samples of LSMO. The technique has advantages over the traditional four-point probe method because it also provides spectral information that is not available to the latter.

In the next chapter I shall present the results of MRE experiments on thin film samples of LBMO and LCMO.

Chapter 6

Experimental results for thin film manganite samples

6.1 Introduction

In the last chapter it was shown that it is possible to successfully model the IR and MRE spectral features of bulk samples of LSMO using a simple form of the complex dielectric function for these samples. In Chapter 3 an extension to this simple model was proposed that would allow the modelling of the IR and MRE spectra of thin film manganite samples. As illustrated in Chapter 3, the modelling of the thin film samples is complicated by the fact that the film needs to be deposited on a substrate and we proposed a complex dielectric function of the form:

$$\varepsilon_{total0} = \varepsilon_{film0} + \varepsilon_{sub} \tag{6.1}$$

such that, in zero applied field:

$$\varepsilon_{total0} = \varepsilon_{film\infty} - \frac{\omega_p^2}{\omega^2 + \imath\gamma\omega} + \sum_{j=1}^{n} \frac{S_j^2}{k_j^2 - k^2 - \imath\gamma_j k}$$
$$+\varepsilon_{sub\infty} \cdot \prod_{j=1}^{n} \frac{k_{L_j}^2 - k^2 - \imath\gamma_{L_j} k}{k_{T_j}^2 - k^2 - \imath\gamma_{T_j} k} \tag{6.2}$$

In an applied field, the complex dielectric function was changed to allow for a field dependent term:

$$\varepsilon_{total} = \varepsilon_{film} + \varepsilon_{sub} \tag{6.3}$$

such that:

$$\varepsilon_{total} = \varepsilon_{film\infty} - \frac{\omega_p^2}{\omega^2 + \imath\gamma\omega}(1 + \eta m^2) + \sum_{j=1}^{n} \frac{S_j^2}{k_j^2 - k^2 - \imath\gamma_j k}$$
$$+\varepsilon_{sub\infty} \cdot \prod_{j=1}^{n} \frac{k_{L_j}^2 - k^2 - \imath\gamma_{L_j} k}{k_{T_j}^2 - k^2 - \imath\gamma_{T_j} k} \tag{6.4}$$

In this chapter I will present the experimental IR and MRE spectra for a variety of thin film manganite samples to determine how successful such a model is at reproducing the experimental data. The chapter will begin with a brief description of the sample preparation techniques used to prepare the thin film samples before examining the IR spectra of the substrates. I will then present the IR and MRE spectra for a selection of our thin film samples, and observe how the substrate and the film's thickness influences the results. Towards the end of the chapter I will present the results of temperature controlled MRE experiments on thin film samples of LBMO. The results of these temperature controlled experiments will then be compared to temperature controlled four-point probe measurements of the magnetoresistance. By the end of the chapter I will demonstrate that, just as for the bulk samples, it is the balance of the terms in the complex dielectric function that determines the spectral features of these samples.

6.2 The samples

The majority of the thin film samples were provided by P. Wright from QinetiQ Ltd. Malvern. Additional samples were provided by the University of Sheffield (Professor Gehring's group) and the Leibniz-Institut für Festkörper- und Werkstoffforschung in Dresden (K. Dörr's group). The thin films were epitaxially grown by pulsed laser deposition (PLD) or Chemical Vapour Deposition (CVD) on commercially available substrates of $SrTiO_3$ (100), $NdGaO_3$ (110) and $LaAlO_3$ (100).

In PLD a highly intense UV laser beam is focused onto a target of the desired film material. The target is usually a stoichiometric ceramic target grown by a solid state reaction. During rf laser pulses, the target is ablated due to the high energy density of 1.5 to 2 W/cm^2. The ablated material forms a plasma which is deposited on a substrate opposite to the target. The film quality depends on the deposition conditions such as the deposition temperature, the deposition rate and the ambient gas.

Chemical vapour deposition is a generic name for a group of processes that involve depositing a solid material from a gaseous phase. Precursor gases (often diluted in carrier gases) are delivered into the reaction chamber at approximately ambient temperatures. As they pass over or come into contact with a heated substrate, they react or decompose forming a solid phase which is deposited onto the substrate.

Table 6.1 summarises the samples that were studied. The table includes the preparation method, the thickness, composition, substrate and 'sample code' for each of the samples. For example, LBMO_1154_STO refers to the $La_{0.7}Ba_{0.3}MnO_3$ sample deposited on $SrTiO_3$. The '1154' and similar terms in the sample code was the designation given to the sample by QinetiQ.

The majority of the research on the thin film samples in this thesis has focussed on the LBMO samples from QinetiQ and the University of Sheffield. The LBMO samples listed in Table 6.1 cover a wide range of substrates and compositions, which helps to determine the influence of the substrate and the composition on the IR and MRE spectra. In order to determine the influence of the substrates it is first necessary to measure their IR spectra. Pure substrates of STO, LAO and NGO were provided by QinetiQ and a LAO substrate from the University of Sheffield for this purpose.

6.3 The substrates $SrTiO_3$, $LaAlO_3$ and $NdGaO_3$

The substrates are very influential in all our IR optical experiments on manganite thin films due to the large skin depth of the manganites. The skin depth of $La_{0.7}Ca_{0.3}MnO_3$, for example, is 270 to 940 nm at 277.5 K (paramagnetic phase) and 40 to 135 nm at 4.2 K

LBMO

Composition	Sample code	Thickness	Substrate	Preparation method
$La_{0.86}Ba_{0.14}MnO_3{}^q$	LBMO_1155_STO	100 nm	STO	CVD
$La_{0.76}Ba_{0.24}MnO_3{}^q$	LBMO_ 1191a_NGO	50 nm	NGO	CVD
$La_{0.76}Ba_{0.24}MnO_3{}^q$	LBMO_ 1191b_STO	50 nm	STO	CVD
$La_{0.76}Ba_{0.24}MnO_3{}^q$	LBMO_ 1191c_LAO	50 nm	LAO	CVD
$La_{0.7}Ba_{0.3}MnO_3{}^s$	LBMO_Shef_STO	Unknown	STO	PLD
$La_{0.7}Ba_{0.3}MnO_3{}^q$	LBMO_1154_STO	105 nm	STO	CVD
$La_{0.66}Ba_{0.34}MnO_3{}^q$	LBMO_ 1207_STO	230 nm	STO	CVD

LCMO

Composition	Sample code	Thickness	Substrate	Preparation method
$La_{0.7}Ca_{0.3}MnO_3{}^q$	LCMO_ 1109_NGO	50 nm	NGO	CVD
$La_{0.7}Ca_{0.3}MnO_3{}^q$	LCMO_ 1109_LAO	50 nm	LAO	CVD
$La_{0.7}Ca_{0.3}MnO_3{}^q$	LCMO_ 1148_NGO	80 nm	NGO	CVD
$La_{0.7}Ca_{0.3}MnO_3{}^q$	LCMO_ 1148_LAO	80 nm	LAO	CVD
$La_{0.7}Ca_{0.3}MnO_3{}^s$	LCMO_ 03A_LAO	Unknown	LAO	PLD

Table 6.1: The thin film perovskite samples. Those provided by QinetiQ Ltd. are designated with the superscript q and those from The University of Sheffield with the superscript s.

(ferromagnetic phase) for the near infrared range from 2 to 24 μm (149).

Room temperature measurements were made by J. Linke, a MSc. student in our research group, as part of her MSc research on 'The Magnetorefractive Effect in Doped Lanthanum Manganite Thin Films' (150), for all of the substrates that were available: STO, LAO and NGO substrates from QinetiQ , a LAO substrate from Sheffield and a STO and LAO substrate from the CSIC in Barcelona. Her results are reproduced here because it is crucial to understand exactly how the phonon spectra of the pure substrates behave in order to see their influence on the spectra of the thin films.

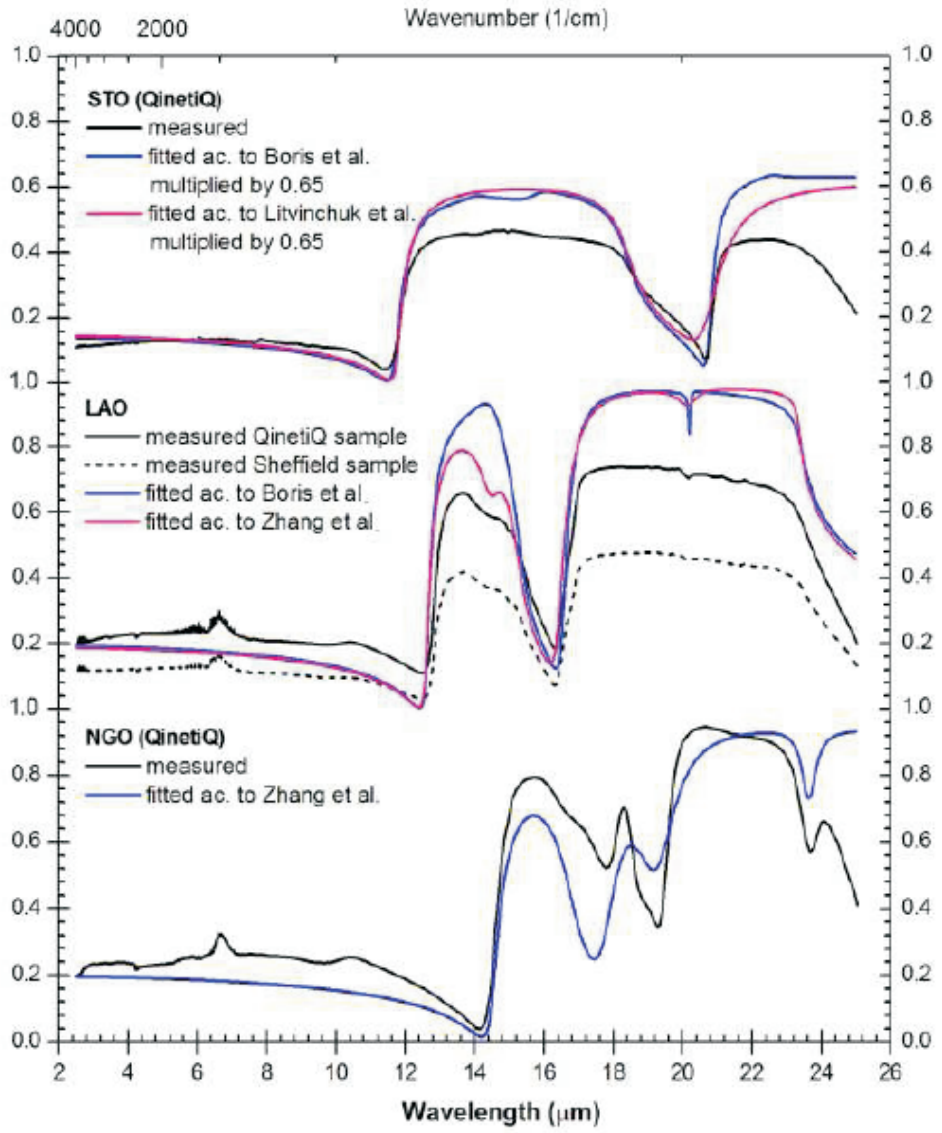

Figure 6.1: Normalised infrared reflection spectra of the pure substrates $SrTiO_3$ (STO), $LaAlO_3$ (LAO) and $NdGaO_3$ (NGO) at room temperature and random polarization of the IR light, and their fits according to models by Litvinchuk *et al.* (151), Boris *et al.* (24) and Zhang *et al.* (152). Reproduced from (150). (Original in colour)

6.3.1 Reflection spectra at room temperature

The normalised infrared spectra are shown as black lines in Figure 6.1 together with simulated data modelled from phonon parameters given by Litvinchuk *et al.*, Boris *et al.* and Zhang *et al.* for a temperature of 300 K (151; 24; 152).

The STO spectra shown in the top of Figure 6.1 were simulated with phonon parame-

ters given by Litvinchuk *et al.* and Boris *et al.*. The model of Litvinchuk *et al.* is based on a sum of Lorentz oscillators, such that the complex dielectric function is given by:

$$\varepsilon_{Litvinchuk}(\omega) = \varepsilon_\infty - \frac{\omega_p^2}{\omega^2 + \imath\omega\Gamma} + \sum_{j=1}^{n} \frac{S_j k_j^2}{k_j^2 - k^2 - \imath\gamma_j k} \tag{6.5}$$

where ω_p and Γ are the unscreened plasma frequency and scattering rate, and the sum accounts for phonons with a frequency k_j, damping γ_j and oscillator strength S_j. This model seems a little peculiar since it includes a term for the free carriers via the plasma frequency which makes little sense for a sample with no free carriers. However, Litvinchuk *et al.* provide three sets of phonon parameters for STO, which unfortunately do not fit the feature at 20.7μm (483 cm^{-1}) very well. The model of Boris *et al.* is based on the factorised expression for the dielectric function, after Gervais (138), as was described in Chapter 3 for the STO substrate in equation 3.24. Boris *et al.* provide six sets of phonon parameters, which fit the shape of the spectrum reasonably well, if the whole spectrum is attenuated by a factor of at least 0.65. Both models predict a much higher reflectance than is measured, so it must be assumed that the surface texture of the sample is not ideal.

The comparison of the measured spectra for LAO with the simulated spectra from the parameters of Boris *et al.* and Zhang *et al.* (middle of Figure 6.1) reveals a similar phonon response to the QinetiQ sample, but the spectrum from the Sheffield sample is much less intense. This might be due to differences in the alignment of the samples in the IR beam or in the surface texture of the samples (150), or indeed differences in the sample's surface area.

The model of Zhang *et al.* again uses a sum of Lorentz oscillators to model the complex dielectric function such that:

$$\varepsilon_{Zhang}(\omega) = \varepsilon_\infty + \sum_{j=1}^{n} \frac{S_j k_j^2}{k_j^2 - k^2 - 2\imath\gamma_j k} \tag{6.6}$$

The original paper contained a typographical error since it omitted an $\imath$ from the $2\gamma_j k$ term. This meant that the expression was always real and that the oscillators had no complex component. Adding the $\imath$ term as shown in equation 6.6 allowed the reproducuction of the plots given in the original paper.

In the simulations for LAO, neither the factorised form by Boris *et al.* nor the model based on a sum of Lorentz oscillators by Zhang *et al.*, fit the spectral shape between 15.6 and 13.0 μm (640 and 770 cm^{-1}) exactly. The feature at 14 μm (715 cm^{-1}) is better described by the model of Zhang *et al.*, however, but the dip at 20.2 μm (495 cm^{-1}) is pronounced more strongly than in the measurement, whereas the peak at 6.7 μm (1500 cm^{-1}) is not produced at all (150).

For NGO there was only one set of parameters available, based on the work of Zhang *et al.* (bottom of Figure 6.1). The reflection minima are reproduced at the correct frequency but the overall shape of the spectrum is not a very good fit, which means that the damping parameters and oscillator strengths are not the same as in the sample. In addition the peak at 6.7 μm (1500 cm^{-1}) does not appear in the simulated spectra. It is interesting to note that this feature at 6.7 μm is observed in both the LAO and NGO substrates but is not observed for STO.

The measured spectra of STO, LAO and NGO show the plasma edges of the reststrahlen spectrum at 11.44, 12.45 and 14.14 μm (874, 803 and 707 cm^{-1}) respectively. The features at 6.7 μm (1500 cm^{-1}) in LAO and NGO are beyond the plasma edge, therefore they can not be assigned to phonon modes. They are very likely to be caused by contaminants in the substrates (150). The comparison to the reflectivity measured in an applied external magnetic field has shown that the substrates do not exhibit a magnetorefractive effect.

The minima at 20.7 μm (483 cm^{-1}) in STO and 16.3 μm (612 cm^{-1}) in LAO correspond to longitudinal resonance frequencies of the stretching mode of the oxygen octahedron (153; 154; 155; 156; 157). The orthorhombic crystal structure of NGO is more complex (158; 159) than the simple cubic structure of STO or pseudocubic structure of LAO (100), and it is thought by Linke (150) that this is responsible for the additional features that are observed in its spectrum.

Linke discovered that the additional phonon features in the spectrum of NGO were strongly dependent on the orientation of the substrate sample in the infrared beam, as shown in figure 6.2. If the NGO substrate is rotated by 90° around its normal, the features at 19.5 and 18.3 μm (512 and 545 cm^{-1}) become masked by the highly reflective part of the spectrum, which is broadened from 19.3 to 17.2 μm (517 to 581 cm^{-1}). In p-polarized

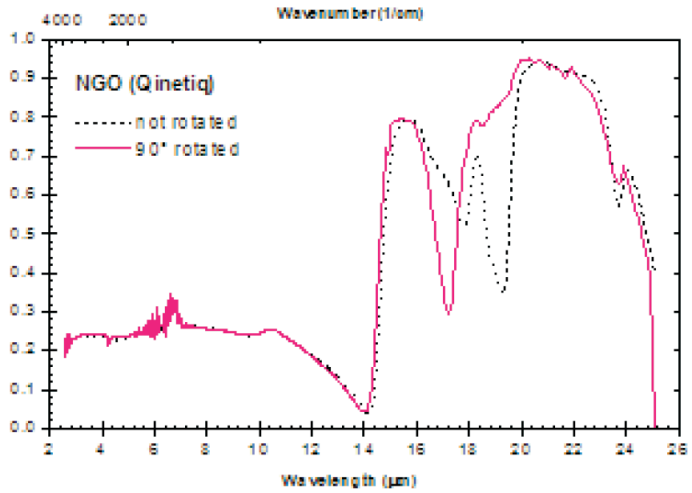

Figure 6.2: Randomly polarized IR spectra for a NGO substrate for different rotations around the normal of the substrate surface. Reproduced from (150)

light the feature at 19.3 μm (517 cm^{-1}) was observed to shift significantly to higher frequencies, distinguishing it from the LO modes in the other substrates; in STO or LAO neither rotating the sample in the randomly polarized light nor changing the polarization of the incident IR light affects the frequency of the phonon modes as shown in Figure 6.3.

The spectra for p-polarized light are observed to be less intense than that for s-polarized light in agreement with the Fresnel equations (equations 3.8–3.11). The phonon modes are broader in the p-polarized spectra, because light polarized parallel to the film is absorbed more strongly by the longitudinal modes (160). The reflection minima at 11.44, 12.45 and 14.14 μm (874, 803 and 707 cm^{-1}) are not broadened in p-polarized light, because they are not caused by phonon modes but by the plasma edge.

In Chapter 3, I modelled the polarization dependence of the STO substrate using a four parameter model based on the phonon parameters given by Boris *et al.*. In Figure 3.8 the reflectance was plotted as a function of wavenumber, but in Figure 6.4, I plot the same data as a function of wavelength.

The modelled spectra shows the same broadening of the LO phonon mode at 20.7μm (483 cm^{-1}) as was observed experimentally in the top panel of Figure 6.3, though as stated above the reflectance from the experimental data is significantly lower than that predicted by the model. The modelled spectra also show the same minima in the reflectance at the

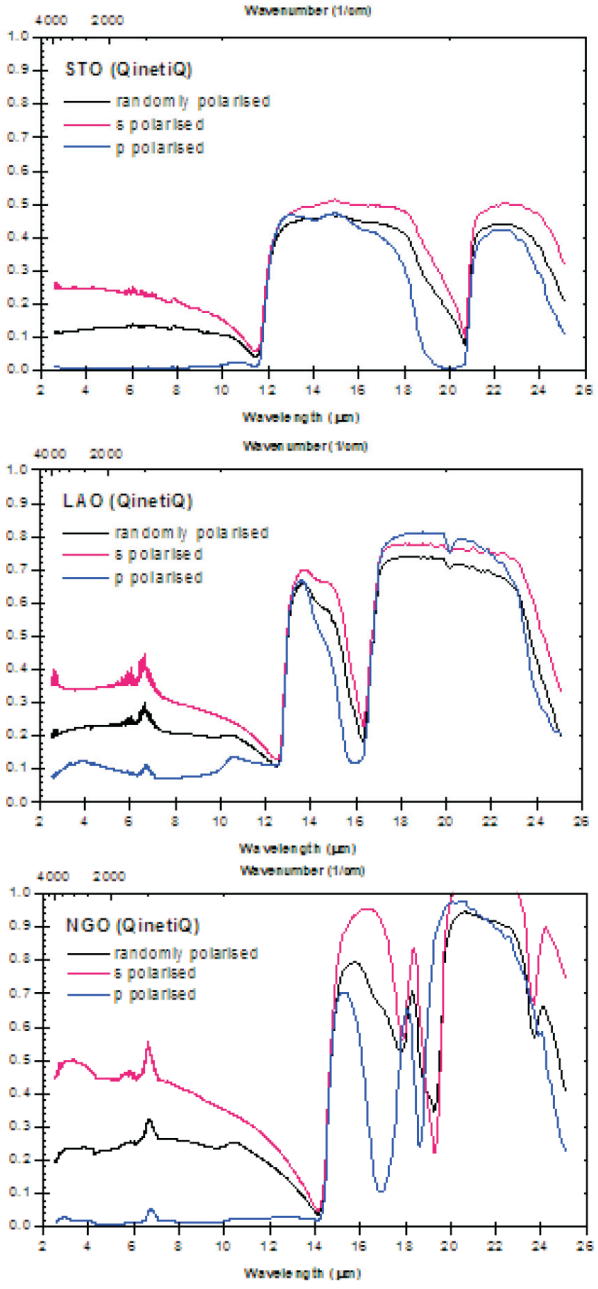

Figure 6.3: Normalised reflection spectra of the substrates at room temperature in perpendicular (s) and parallel (p) polarized light. Top: STO, middle: LAO, bottom: NGO. Reproduced from (150). (Original in colour)

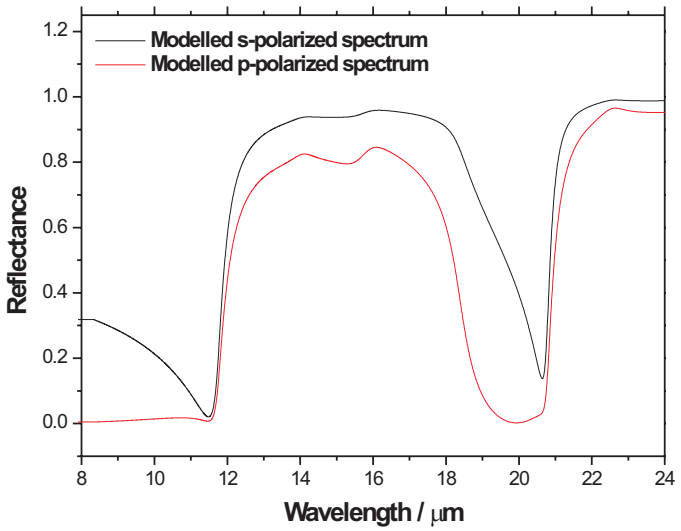

Figure 6.4: Modelled IR spectra using the four parameter model of the STO dielectric function for s- and p-polarized incident light. The parameters used in the model are given in Table 3.2. (Original in colour)

plasma edge as was observed experimentally. Hence, despite the fact that the experimental data were of lower amplitude than predicted by the model, the four parameter model we have used to simulate the STO substrate in Chapter 3 produces a better fit to all of the spectral features of the STO substrate than the model suggested by Litvinchuk *et al.*. Since the majority of the LBMO samples I have studied are on STO substrates I will continue to use the four parameter model to model the STO substrates.

6.3.2 Reflection spectra below room temperature

J. Linke also investigated the temperature dependence of the reflection spectra of the STO and LAO substrates provided by the CSIC group from Barcelona. The substrates were placed inside the Joule-Thomson cooler and cooled to a minimum temperature of 100K in zero applied field. The temperature dependence of IR spectra for LAO and STO is shown in Figure 6.5.

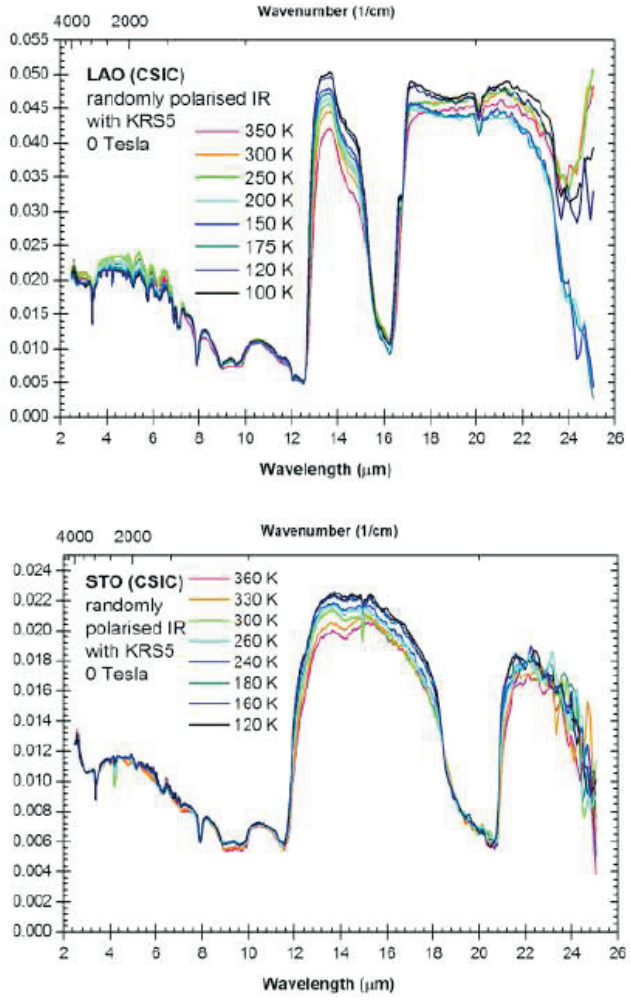

Figure 6.5: Temperature dependence of the normalised reflection spectra of the substrates in randomly polarised IR light in zero applied field. Top: LAO, bottom: STO. Reproduced from (150). (Original in colour)

As was discussed in Chapter 4, the KRS-5 window of the MMRS p-polarizes the IR light which will therefore tend to broaden the phonon modes at 20.7 and 16.3 μm (482 and 615 cm^{-1}) for STO and LAO, respectively, as shown in Figure 6.5. The mode at 20.2 μm (495 cm^{-1}) in LAO is also more pronounced and for STO a mode at 14.9 μm (670 cm^{-1}) appears. Besides the change to p-polarization, the window also introduces a pattern of dips and peaks between 11.8 and 3.8 μm (850 and 2660 cm^{-1}), as shown in Figure 6.5. These lie outside of the range where the MRE occurs and do not disturb the measurements.

Upon decreasing the temperature the reflectance of the spectra at 14.3 μm (700 cm^{-1}) increases by $\approx$14% for STO at 120 K and $\approx$24% for LAO at 100 K (compared to $\approx$ 30%

at 78 K observed by Zhang *et al.* (152)). The overall shape of the spectrum is unchanged upon cooling, the phonon mode in LAO at 16.8 μm (595 cm $^{-1}$) develops a sharp edge for lower temperature, which does not have an equivalent in the STO spectrum. The four parameter model does not account for any changes in the substrate's complex dielectric function with temperature. It is known, however, that STO undergoes a phase transition at 110K (161) where a soft phonon mode at the [111] zone boundary turns this zone boundary into a superlattice point, enlarging the unit cell. Furthermore, the dielectric constant (ε_0) can increase dramatically for very low temperatures (T$<$32K). It is possible that this is responsible for the observed change in reflectance with temperature for the STO substrate.

6.4 IR and MRE spectra of thin manganite films

6.4.1 Samples of $\mathbf{La_{1-x}Ba_xMnO_3}$

6.4.1.1 The influence of the substrate

The influence the substrate has on the IR spectra of a thin film of LBMO is clearly demonstrated in Figure 6.6, which shows the IR and MRE spectra of the LBMO_1191_STO samples in an applied field of 1.3T.

This set of LBMO samples were grown simultaneously in the same deposition run and only the substrate differs between the samples. All measurements were made at room temperature using randomly polarized incident light. These samples are only 50nm thick and it is clear from the figure that the substrate is dominant in the IR and MRE spectra. The position of the plasma edge in the IR spectra is shifted slightly from the pure substrate values: from 11.44 to 11.76μm for the LBMO sample on STO, from 12.45 to 12.65 μm for the LBMO sample on LAO and from 14.14 to 14.32 μm for the LBMO sample on NGO. According to Boris *et al.* (45), this shift is introduced by compressive stress due to the lattice mismatch between the film and the substrate and these results are in agreement with a shift of 22 cm^{-1} reported by Boris et al..

However, it is not just the position of the plasma edge that shifts from the values observed in the pure substrates. All of the spectral features observed in the substrate spectra are reproduced in all three film/substrate systems, and all are shifted by a uniform amount.

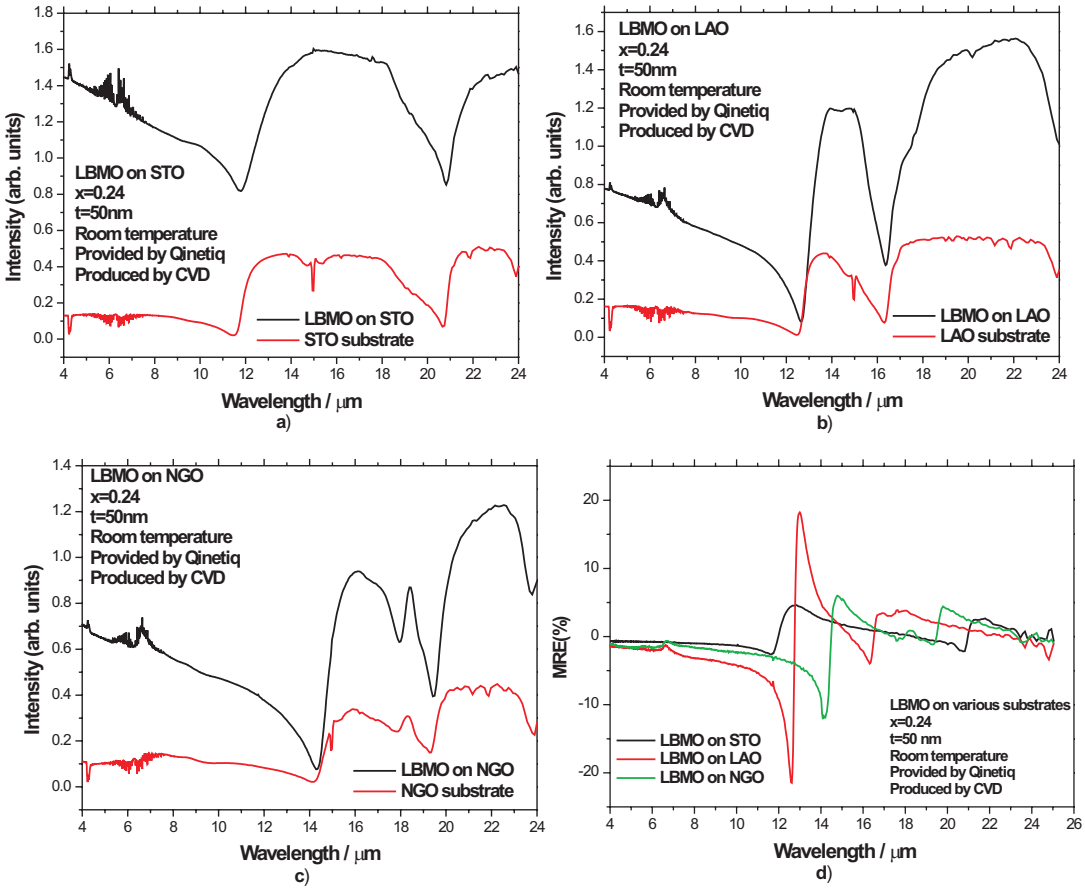

Figure 6.6: IR spectra for LBMO_1191 on a) STO, b) LAO and c) NGO. The pure substrate spectra are also shown for comparison. In d), the MRE spectra for the LBMO_1191 a-c samples are shown for a 1.3T applied field. The samples are $x = 0.24$ and are 50nm thick. All the samples were deposited on the STO, LAO and NGO substrates in the same run. (Original in colour)

This suggests that rather than the shift being caused by strain between the substrate and film layer, since one would expect that the various substrates would introduce different degrees of strain, the uniform shift can be attributed to the enhanced conductivity introduced by the deposition of the thin film layer.

The feature observed in the IR spectra at 6.7 μm is also evident in the MRE spectra for the LAO and NGO based samples. The substrates themselves exhibit no magnetic field dependence at this wavelength, but the deposition of the thin film appears to introduce a field dependence at this wavelength. This feature was also observed in LCMO samples

deposited on LAO and NGO (150) and will be discussed in more detail below. It should be noted at this stage that the model can supply us with no information about this spectral feature. This is because the feature occurs below the plasma edge, a wavelength regime that only depends upon ε_∞ and the Drude-like term in the complex dielectric function. This is a smooth function that contains no resonance features at all.

6.4.1.2 Thickness dependence

The thickness dependence of the LBMO_1154 (105 nm), LBMO_Sheffield (150+ nm) and LBMO_1207 (230 nm) samples is shown in Figure 6.7. The IR spectra were measured in zero field and the MRE spectra are for the maximum magnetic field of 1.3T.

All three of the samples shown in the figure were grown on STO and have the same composition within experimental error (taken as 10% in the PLD and CVD preparation process). While the thickness of the Sheffield sample is not known exactly, it is known to be $\geq$ 150 nm thick (162).

The experimental results show a large, thickness dependent shift of the plasma edge to higher wavelengths as the sample thickness increases. The plasma edge moves from 11.54 μm for the 105nm thick sample to 13.24 μm for the 230 nm thick sample. The stretching phonon mode is also observed to shift to higher wavelength but not by as large an amount as the change in the plasma edge wavelength, increasing from 20.72 μm for the 105 nm sample to 21.28 μm for the 230 nm sample. In Chapter 3 we examined the effect of changing the weighting of the film to substrate ratio in the complex dielectric function, the results of which are shown in Figures 3.14a and b. These figures show that as the contribution from the film becomes more significant the position of the plasma edge shifts to longer wavelength. A change to the weighting of the film/substrate ratio can be linked to a change in the sample's thickness via the skin depth. Since the IR light interacts with a volume that contains both the film and the substrate, if the film layer is thicker, then the volume penetrated by the IR light will contain more free carriers and hence will have a higher conductivity. This increased conductivity reduces the skin depth in the thicker samples, which will lead to a change in the film/substrate ratio, with the substrate making a smaller contribution in the thicker samples.

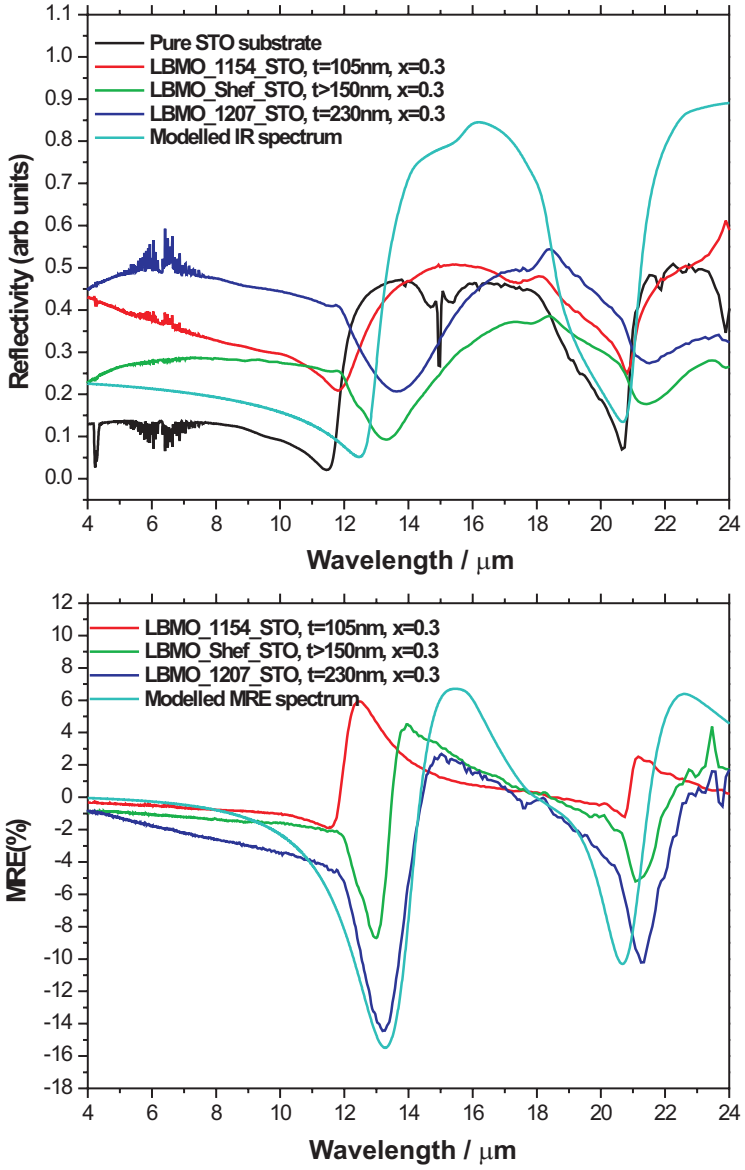

Figure 6.7: Top: IR and bottom: MRE spectra showing the thickness dependence for LBMO (x=0.3) for randomly polarized incident light. The modelled IR and MRE spectra shown in the figures were calculated using the parameters in Table 3.3. with $\varepsilon = 7.2$. (Original in colour)

In Chapter 3 we changed the film/substrate ratio quite substantially: from pure substrate to pure film in steps of 20%. According to Coey (1), $La_{0.7}Ba_{0.3}MnO_3$ has a resistivity of approximately 5×10^{-5} Ωm at room temperature. For IR light with a wavelength of 10 μm, this gives a skin depth of approximately 900 nm, or about 9 times the film's thickness. The skin depth scales with the conductivity as $1/\sqrt{\sigma}$. Strain in thin films is very important, and the properties of very thin films depend a great deal on the substrate/film interface. In such thin films, the strain at the interface can cause carriers to become localised, thus reducing the number of free carriers per unit volume, N (148). This could be related to the biaxial strain proposed by Millis *et al.* (116) in Chapter 2, whereby the Jahn-Teller splitting between the t_{2g} and the e_g orbitals is increased thereby increasing the tendency for electrons to become localised. For arguments sake, let us consider what would happen if the number of free carriers is doubled when the film thickness is doubled. Since σ is directly proportional to N, doubling the thickness of the film will therefore scale the skin depth by a factor of $1/\sqrt{2}$, hence changing the substrate:film ratio from 9:1 to 6.4:1. This is equivalent to changing the film's contribution from 11.1% of the total skin depth to 15.6%. This change can be modelled and the results are shown in Figure 6.8.

In the figure we consider two samples: one has N carriers per unit volume (where N=2x10^{25}m^{-3}) and its complex dielectric function consists of $\varepsilon = 0.889\varepsilon_{substrate}+0.111\varepsilon_{film}$. The second sample has 2N carriers per unit volume and $\varepsilon = 0.844\varepsilon_{substrate} + 0.156\varepsilon_{film}$. Experimentally, the plasma edge moves from 11.54 μm for the 105nm thick 1154 sample to 13.24 μm for the 230 nm thick 1207 sample. Figure 6.8 clearly demonstrates that if we use a simple model, based solely on considerations of sample thickness, then we cannot produce the shift in wavelength observed experimentally. However, it is also clear from the figure that while the simple model may not tell the whole story, it certainly makes a contribution to the observed shift. The model cannot be used to determine how many free carriers would actually be required to achieve the observed shift; it would require changing N by several orders of magnitude. This results in the contribution from the substrate being completely screened out by the free carriers, leaving us with the same shape of spectrum as was observed for a bulk, conducting sample. It is likely that the localisation of carriers in the thinner films at the substrate/film interface plays at significant role in these samples.

The modelled IR and MRE spectra in Figure 6.7 were calculated using the model parameters given in Table 3.3 (except with $\varepsilon = 7.2$) and highlight both the strengths and

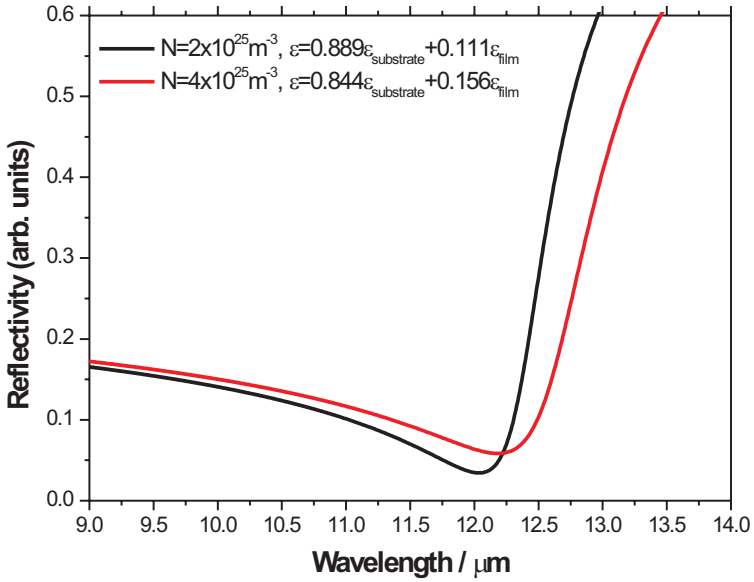

Figure 6.8: Modelled IR spectra that shows the effect changing the number of free carriers and the film/substrate contribution has on the position of the plasma edge. (Original in colour)

the weaknesses of the model. If we first consider the IR spectra shown in the top panel of Figure 6.7, we see that the modelled spectrum is not actually a very good fit to any of the other spectra. This is not actually too surprising, however, when you observe how varied the experimental spectra are for these samples. Since the substrate is clearly so influential and the effects of strain are hard to predict and model, it is not clear which parameters ought to be changed to provide a better fit. This is a clear weakness of the model, yet from another point of view it is also one of its strengths. The modelled IR spectrum is representative of *all* of the other spectra shown in the figure since all of the experimentally observed spectral features are evident in the modelled spectra from the minimum associated to the plasma edge to the minimum associated with the stretching phonon mode. The model even reproduces the double-humped shape observed in the experimental spectra between these two minima, albeit not quite at the wavelength this feature is observed at experimentally. In conclusion, therefore, one can say that the model is good at reproducing the generic features observed experimentally, but it is rather bad at

reproducing all of the details observed in a specific experimental spectrum.

If we now consider the modelled MRE spectrum in the lower panel of Figure 6.7 we notice that the model is very good at reproducing the MRE spectrum of a specific LBMO sample. In this case the model parameters were tailored for the LBMO_1207 sample ($m = 1$) and the fit is remarkable considering how poor a fit the IR spectrum was for this sample. There is a good overlap between the modelled and experimental spectra for most wavelengths. Indeed, the minimum associated with the plasma edge is in the same place in both the modelled and experimental spectra. However, although the minimum associated with the stretching phonon mode is reproduced in the model with the correct amplitude, it occurs at a lower wavelength than was observed experimentally, and it is here that the model deviates the most from experiment. A quirk of the model is that while it is possible to fit the position of the plasma edge or the stretching mode accurately, for some reason it is not possible to fit both accurately simultaneously. A possible explanation for this can be found in Figure 3.17b in Chapter 3, where it was observed that if the damping term (γ_j) of the resonance is changed, it is possible to change the position of the stretching mode without changing the position of the plasma edge. It is therefore likely that some form of strain is changing the damping factor of the resonance such that the position of the resonance is changing, but the position of the plasma edge is not.

There are a few other details the model cannot reproduce. One such detail is the kink observed experimentally in the MRE spectra at 11.8 μm. This feature lies beyond the plasma edge, and is not a substrate feature, so it cannot be reproduced in the model. The model also underestimates the MRE at low wavelengths, but this could be due in some part to the kink in the spectra. In addition the positive MRE signal observed between 14 and 18 μm is too large compared to the experimental spectra, though the MRE is positive over the same wavelength range. A possible explanation for this will be discussed below.

Overall, the model is successful at reproducing the spectral features we observe experimentally. While it may not be very good at modelling a specific sample 100% accurately, the model is very useful since it allows us to study trends in a set of samples, such as the thickness dependence, or the consequences changing the doping has on the conductivity. Hence, the model is a useful aid to furthering our understanding of these materials.

6.4.1.3 The magnetorefractive effect in LBMO: a comparison between model and experiment

In Figure 6.7 we observed that the MRE spectrum for the LBMO_1207 sample in the maximum field of 1.3T could be well represented by the model proposed in Chapter 3. A question we should ask now is: Does the model show the same trends in the MRE spectra as were observed experimentally as a function of applied field? This question is answered in Figure 6.9.

The parameters used to model the LBMO_1207 thin film sample and substrate are given in Table 6.2.

STO substrate parameters	j=1	j=2	j=3	j=4	j=5	j=6
k_{T_j} (cm^{-1})	92	175	443.5	544	635.1	710.1
k_{L_j} (cm^{-1})	171	476	443.8	793	635.2	710.8
γ_{T_j} (cm)	16	6.2	18.6	17	43	41
γ_{L_j} (cm)	3.8	5.3	18.6	24	40	41
Resonance parameters	j=1	j=2	j=3	j=4		
k_j (cm^{-1})	154	335	379	559		
γ_j (cm)	59	23	25	35		
S_j (cm^{-1})	671	854	259	569		
Other parameters						
N	$2.0 \times 10^{25}/m^3$					
$\varepsilon_{film\infty}$	7.2					
γ	$1 \times 10^{15} Hz$					
m_e^*	9.11×10^{-31} kg					
η	0.55					

Table 6.2: Parameters used in the modelling of LBMO_1207 on STO.

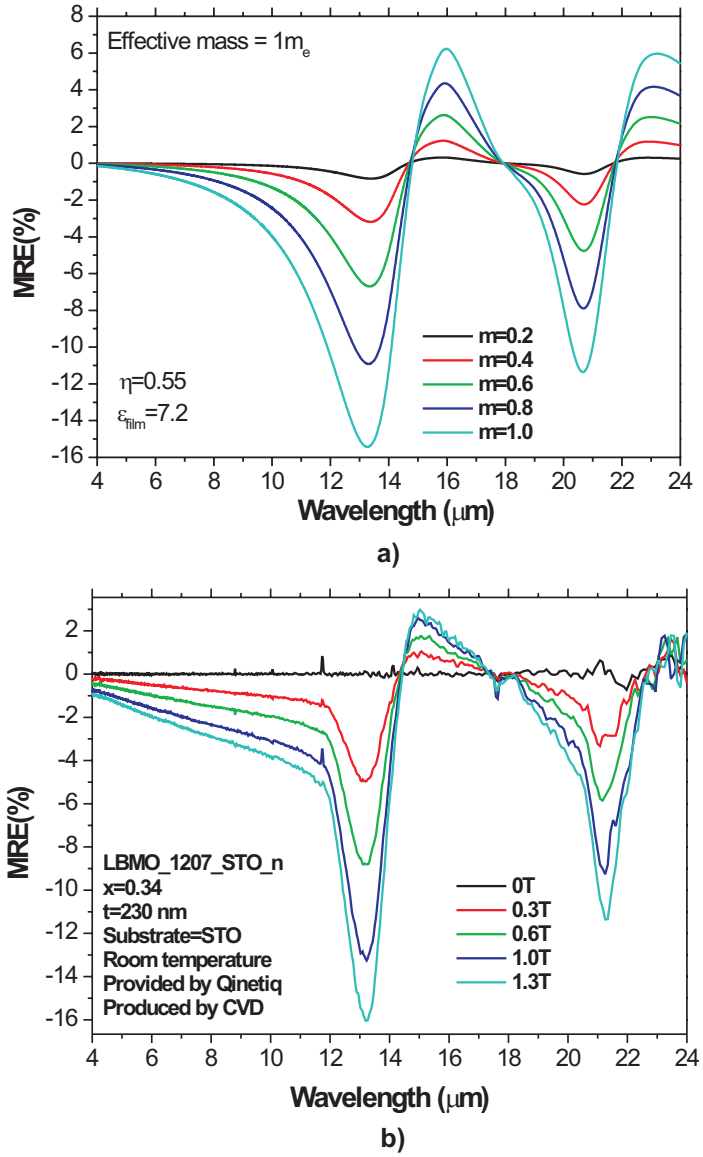

Figure 6.9: A comparison between a) the MRE spectra predicted by our model and b) the MRE spectra measured experimentally for LBMO_1207_STO. The parameters used in the modelled spectra are given in Table 6.2 (Original in colour)

As shown in Figure 6.9, the overall shape of the modelled spectra compare extremely well with those observed experimentally. In particular we see that as the magnetic field increases, the position of the plasma edge minima and the position of the phonon mode shifts very slightly to a lower wavelength. This is consistent with an increase in the reflectivity, and by extension the conductivity, as the field increases. The crossover points from negative MRE values to positive MRE values occur at the same wavelengths in both the model and experiment, but again the position of the phonon mode is slightly lower in the model than was observed experimentally. However, the amplitude of the minima are in the same proportion in both the model and experiment.

The part of the spectra where the MRE is positive (λ = 14-18 μm) is over estimated by the model. The reason for this may in fact be due to the substrate. In Figure 6.5 we saw that the reflectivity of the STO substrate spectra decreased as the temperature increased over the same wavelength range (14-18 μm). Since the reflectivity is related to the conductivity, this means that the substrate becomes less conducting for this range of wavelengths as the temperature increases. As we will see later, changes in the conductivity achieved by changing the temperature are akin to those caused by applying a magnetic field to these samples. The skin depth for these samples for IR radiation is of the order of μm, but any change in the conductivity will result in changes to the skin depth, which will change the film/substrate weighting. Hence, for films that are 100 nm thick, the conductivity of the substrate at a given wavelength will be extremely important in determining the MRE observed from the film. The model does not account for field/temperature induced changes in the substrate's conductivity at a particular wavelength. For any further work on these samples it would be useful to model changes in the film/substrate weighting as a function of field.

6.4.2 Samples of $\mathbf{La_{1-x}Ca_xMnO_3}$

The MRE in thin films of LCMO on LAO and NGO was studied extensively by J. Linke in our group (150). She found that although the model I have described above works very well for LBMO on the cubic STO substrate, it fails to accurately model LCMO on the more complicated LAO and NGO substrates.

This is clearly illustrated in Figure 6.10 where I plot the experimental results for

LCMO_03A_LAO together with a modelled spectra using parameters for the thin film/substrate system as given in Table 6.3. The substrate parameters for LAO are as given by Boris *et al.* (24).

LAO substrate parameters	j=1	j=2	j=3	j=4	j=5
k_{T_j} (cm^{-1})	183	427	494.7	651	680
k_{L_j} (cm^{-1})	277	596	494.5	743	687
γ_{T_j} (cm)	3.9	6.4	1.7	22	65
γ_{L_j} (cm)	4.3	9.9	1.6	10	70
Resonance parameters for film layer	j=1	j=2	j=3	j=4	
k_j (cm^{-1})	160	351	405	607	
γ_j (cm)	53	51	52	71	
S_j (cm^{-1})	670	792	511	832	
Other parameters					
N	$2.0 \times 10^{25}/m^3$				
$\varepsilon_{film\infty}$	7.2				
γ	$1 \times 10^{15} Hz$				
m_e^*	9.11×10^{-31} kg				
η	0.12				

Table 6.3: Parameters used in the modelling of LCMO_03A on LAO.

The model manages to reproduce the large MRE caused by the low reflectivity at the plasma edge but completely fails to model the phonon mode correctly, despite the fact that the parameters in the paper by Boris *et al.* are optimised for such a sample. The model also fails to produce the large positive MRE at 14 μm. Clearly there is something wrong with the parameterisation for this particular film/substrate combination. It is likely that the strain caused by the lattice mismatch between the substrate and film is creating the disparity between the modelled and measured spectra.

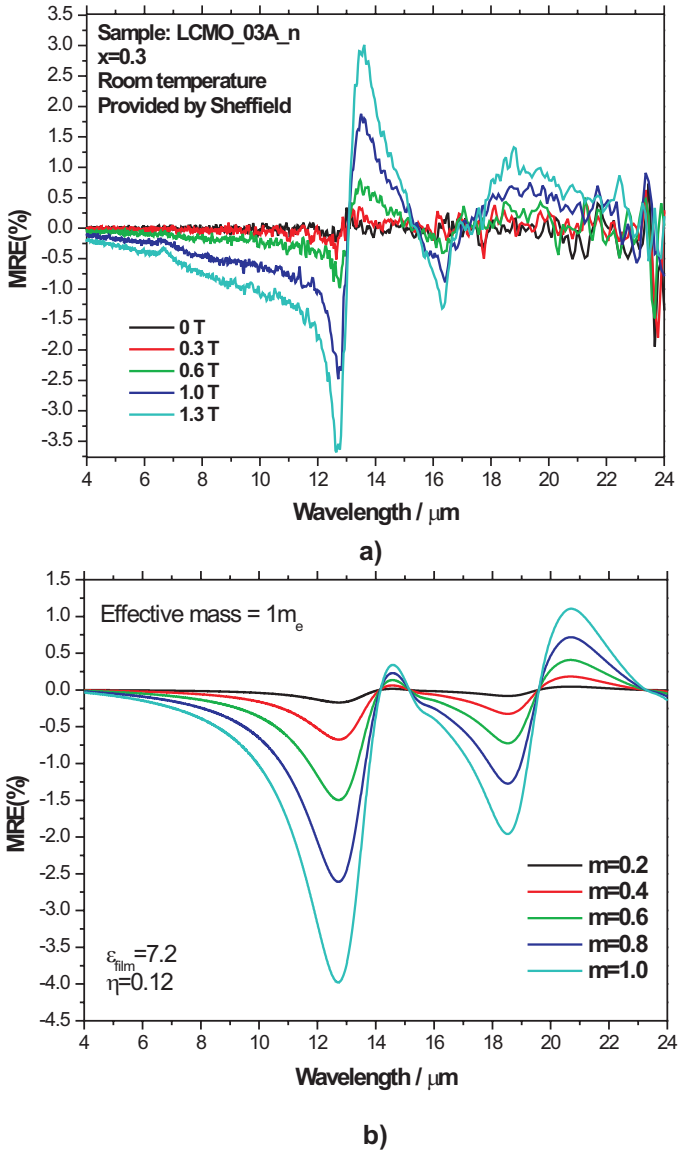

Figure 6.10: A comparison between a) the MRE spectra measured experimentally and b) the MRE spectra predicted by our model for LCMO_03A_LAO. The parameters used in the model are given in Table 6.3. (Original in colour)

The spectral feature at 6.7 μm observed in Figure 6.6 for the LAO and NGO substrates is also evident in Figure 6.10. It is possible that this spectral feature is an indication of phase separation. As mentioned above, the spectral feature cannot be assigned to a phonon mode of the substrate or the film as it lies well below their plasma edge. To uncover the origin of this feature, J. Linke measured reflection spectra from the substrate side of the LBMO_1191c_LAO and LCMO_03A_LAO samples, and, intriguingly, the feature at 6.7 μm was observed to increases in intensity as the applied magnetic field is increased. It was concluded (150) that the feature may be due to contamination or phase separation at the interface between the substrate and film. The LAO and NGO substrate already showed a change in the reflectivity at around 6.7 μm, which was previously explained as contamination. However, the 'contamination' is observed in two samples produced by two different preparation methods by different facilities. It is probable that the lattice mismatch between the film and substrate produces a strain that leads to a inhomogeneous nucleation during the deposition. This results in a second phase being formed close to the film surface which has a weak magnetic field dependence in the MRE spectra.

Towards the end of Chapter 2 we discussed how, for example, commercially available $SrTiO_3$ substrates generally present two types of terminations, namely SrO or TiO_2 (121). The existence of these two different terminations could promote electron localisation in highly disordered sites as well as the coexistence of a variety of Mn-O distances and Mn-O-Mn bond angles, that could lead to the formation of so called parasitic phases (e.g. antiferromagnetic or paramagnetic regions formed within a nominally ferromagnetic phase) at the substrate/film interface. It is possible that this is what is being observing in the MRE spectra.

6.5 Temperature controlled experiments

Temperature controlled experiments were performed on two samples with different compositions, but similar thicknesses: LBMO_1154_STO and LBMO_1155_STO samples; composition $x = 0.3$ and $x = 0.14$ and thickness 105 nm and 100 nm thick, respectively. These samples were also as we had already studied the temperature dependence of these samples on a visit to FELIX, the free electron laser facility based at the FOM Institute in Holland, the results of which are presented in Appendix B.

In Chapter 2 we observed that the Curie temperatures in strained films of LBMO on STO could be substantially changed from their bulk values, and according to Figure 2.14 on p.38 both of the LBMO samples I have studied are close to the transition between the ferromagnetic and metallic phase below T_C and the paramagnetic insulating phase above T_C at room temperature. In the previous chapter, we observed in the bulk samples that small increases in temperature near T_C could radically change the measured MRE. Hence, a study of how the CMR varies as a function of temperature should be of interest.

Traditionally, the magnetoresistance as a function of temperature has been measured using a temperature controlled four-point probe technique, as was discussed in Chapter 4. This section will begin by presenting the results of such four-point probe measurements of the CMR before presenting the equivalent temperature controlled MRE data. I will then compare the results from these two different methods of measuring the temperature dependence of the magnetoresistance.

6.5.1 Temperature controlled four-point probe measurements for LBMO_1155_STO and LBMO_1154_STO

In Figure 6.11a, the CMR(%) versus applied magnetic field for the LBMO_1154 sample is plotted. Figures 6.11b shows the CMR(%) versus applied magnetic field for LBMO_1155 sample for T$\leq$240K. These two figures clearly demonstrate the different characteristics of the two samples.

The CMR(%) is directly proportional to the applied field for the $x = 0.3$ sample at all measured temperatures. In Figure 6.11b we see that unlike the $x = 0.3$ sample, the $x = 0.14$ sample exhibits a sharp, temperature dependent change in the magnetoresistance at low fields, as indicated by the sharp peak around zero applied field. This sharp peak diminishes with temperature, and disappears completely above T=240K whereupon the CMR(%) versus applied field becomes linear for all fields. According to Dörr (163) and Gross *et al.* (164), such behaviour is indicative of spin-dependent tunnelling between grains across grain boundaries (GBs) in low fields. Figure 6.11c shows the results of Gröss *et al.* for an $La_{2/3}Ca_{1/3}MnO_3$ sample prepared with and without grain boundaries. The shape of the plot for the sample with grain boundaries is in very good agreement with the experimental results observed in the LBMO_1155 sample at low temperatures and Figure

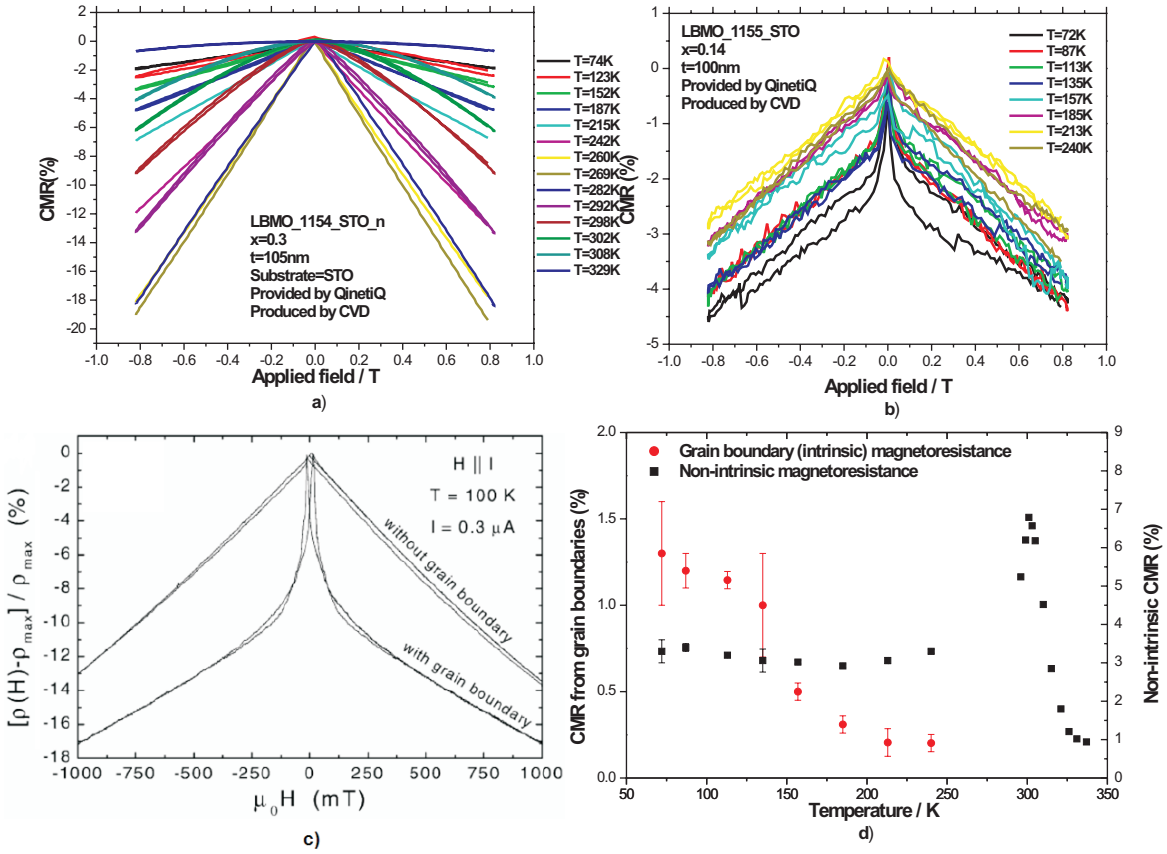

Figure 6.11: Plot of CMR(%) versus applied field for a) LBMO_1154_STO and b) LBMO_1155_STO at T$\leq$240K as measured using the four-point probe method. c) Low-field magnetoresistance of $La_{2/3}Ca_{1/3}MnO_3$ with and without grain boundaries, showing the characteristic steep resistance drop in low magnetic fields from spin-dependent transport between grains as measured by Gröss *et al.*.(164) d) A plot showing the intrinsic, grain boundary contribution and non-intrinsic contribution to the CMR for the LBMO_1155_STO sample. The applied magnetic field in a), b) and d) was 0.9T. (Original in colour)

6.11b suggests that the influence of the grain boundaries diminishes as the temperature increases and spin dependent transport between grains becomes less significant than conduction by double exchange. In Chapter 2 (section 2.7.3) I discussed the fact that GBs are the origin of an additional resistance observed in low magnetic fields; the so called low field MR (LFMR). This resistance is particularly large in polycrystalline thin films manganites since polycrystalline samples have inherently more GBs than an epitaxial film. In Figure 6.11d the GB and non-GB contribution to the CMR(%) is shown. The linear CMR at high fields was extrapolated to zero field to determine the contribution from the GBs at low fields. At low temperatures the GBs contribute almost 50% of the observed magnetoresistance for this sample and are responsible for the enhanced CMR observed at low temperatures. This contribution drops to just 5% of the total CMR by 240K and is not observable at higher temperatures.

In Figures 6.12a and b, I have plotted the resistance versus the temperature for both samples. Although both samples had approximately the same contact area with the probes, and approximately the same thickness, the resistance is 3 times higher ($\approx$9kΩ compared to $\approx$3kΩ) in the $x = 0.14$ sample, and this confirms that the conduction in this sample is more restricted. The peak resistance in the $x = 0.3$ and $x = 0.14$ samples occurs at 295K and 320K, respectively. The LBMO_1155 measurements were made by Andrew Vick, a project student in our research group and he found that the measurements on the $x = 0.14$ sample were not repeatable over the whole temperature range. The initial measurements had a lower resistance at low temperature than subsequent measurements. The most probable explanation for this is that ice built up on the surface of the sample at low temperatures and effectively reduced the resistance between the contacts or provided an alternative current path.

In Figures 6.13a and b I have plotted the CMR(%) versus temperature for the two samples. The CMR(%) was taken to be the difference between the resistance in zero field and the resistance in the maximum applied field, hence for the LBMO_1155 sample at low temperatures, this has incorporated the sharp peak associated with the low-field grain boundary MR into the results. The magnitude of the CMR in Figure 6.13b is comparable to that shown in Figure 6.11d since the grain boundaries do not contribute at all at this temperature.

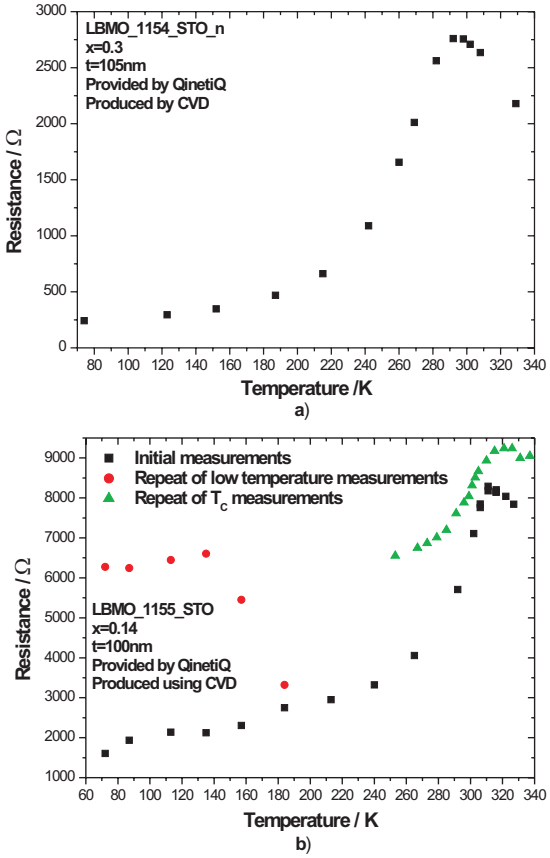

Figure 6.12: A plot of resistance versus temperature for a) LBMO_1154_STO and b) LBMO_1155_STO as measured using the four-point probe method in zero applied magnetic field. The resistance for the $x = 0.14$ sample incorporates the combined contribution from both the CMR and the grain boundaries. (Original in colour)

We observe that the magnetoresistance is much larger in the more conductive sample, since the CMR(%) in the $x = 0.3$ sample (figure 6.13a) peaks at almost 20% whereas in the $x = 0.14$ sample (Figure 6.13b), the CMR(%) reaches a maximum value of 7%. The magnetoresistance also peaks at a lower temperature than observed for the dc resistance for both samples. In each case the peak in the CMR occurs about 20K lower than the dc resistance, with the CMR peak in the $x = 0.3$ sample occurring at ≈275K and in the $x = 0.14$ sample at ≈300K, compared to 295K and 320K for the dc resistance. The peak in the CMR is related to the Curie temperature of the sample where the magnetic phase of the sample changes from ferromagnetic to paramagnetic. The peak in the dc resistance

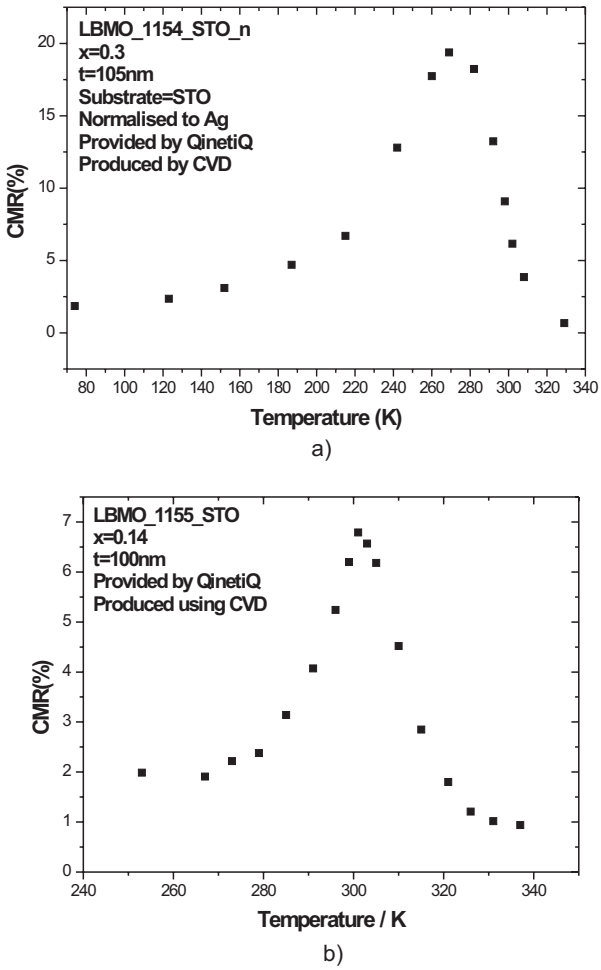

Figure 6.13: A plot of CMR(%) versus temperature for a) LBMO_1154_STO and b) LBMO_1155_STO.

is related to the metal to insulator transition temperature (T_{M-I}) and usually happens at a different temperature to the magnetic phase change (43). T_{M-I}<T_C occurs in polycrystalline or granular samples or in films where the metallic conduction is hindered because of carrier scattering at grain boundaries and/or because of poor connectivity between grains (86), i.e., extrinsic effects. T_{M-I}>T_C is observed in single crystals, well sintered pellets and epitaxial thin films (87). It is interesting to see that despite the fact that the electrical conductivity of the $x = 0.14$ is comparatively lower than in the $x = 0.3$ sample and despite the fact that there is likely to be tunnelling between grains in low fields, the T_{M-I} is still above T_C.

6.5.2 Temperature controlled MRE measurements for LBMO_1155_STO and LBMO_1154_STO

6.5.2.1 Temperature dependence of the infrared spectra of LBMO on STO

The infrared spectra of a sample as a function of temperature is shown in Figure 6.14 for the LBMO_1154_STO sample. I have also plotted the normalised STO substrate spectrum measured at 300K for comparison. The shape of the substrate's spectrum is very similar to that of the film+substrate's spectra for all temperatures. The presence of the film enhances the reflectivity over the entire wavelength range at all temperatures.

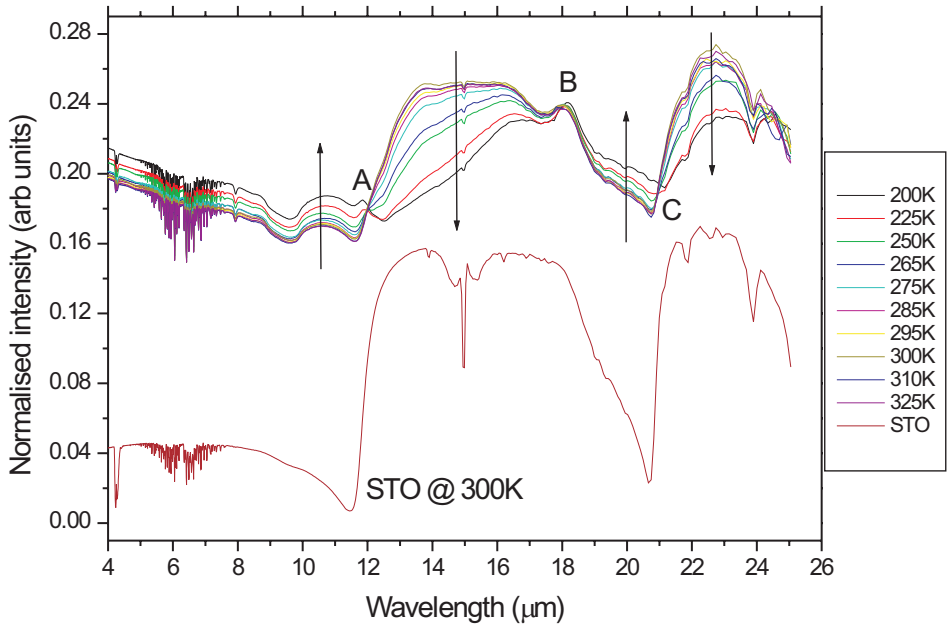

Figure 6.14: Temperature dependence of the infrared spectra for LBMO_1154_STO. The arrows indicate the the direction the spectra move as the temperature is *decreased*. (Original in colour)

It is noticeable in the figure that there are distinct regions where the spectra are temperature dependent. I have indicated with arrows in the figure the direction the spectra move as the temperature is *decreased*.

The points marked A, B and C are crossover points and appear as nodes in the spectra. For short wavelengths prior to point A, the sample becomes more reflective as the temperature decreases whereas between points A and B the sample becomes less reflective as the temperature decreases. This pattern alternates as we pass each node: between B and C the sample is more reflective as the temperature decreases and above C the sample is less reflective again. The IR spectra of the STO substrate has some temperature dependence as shown in Figure 6.5, but if one looks closely you notice that the response of the film/substrate spectra is the complete opposite of the substrate by itself. For example, between points A and B for the pure substrate, the substrate becomes more reflective as the temperature decreases whereas for the film/substrate, one observes a reduction in the reflectivity over this wavelength range. The observed shift in the substrate's reflectivity over this range is less than 10% of that observed in the film/substrate system and the reason that the substrate responds in the opposite sense to the combined system is due to the fact that the substrate is an insulator whereas the combined system is metallic and conducting.

A potential explanation for this response has been suggested by Prof. Cohen from Imperial College, London (148). Prof. Cohen suggests that we may be observing the response of polarons to changes in the frequency of the incident radiation. The hypothesis is that at certain frequencies the polarons find it either easier or harder to respond to the driving frequency of the incident radiation, thus producing the observed effect. Obviously, it would be necessary to test the validity of this hypothesis further before we can make any definitive statement regarding these spectral features.

6.5.2.2 MRE spectra as a function of wavelength for LBMO_1155_STO and LBMO_1154_STO

Figures 6.15a and 6.15b show the temperature dependent MRE spectra measured for a 1.3T field as a function of wavelength.

The alternation of increased and decreased reflectivity in the IR spectra gives the MRE spectra their characteristic appearance. If the reflectivity is increasing with temperature or applied field one observes a negative MRE, but if the reflectivity is decreasing with temperature or applied field one observes a positive MRE. Hence, in the MRE spectra one observes that between the points A and B of Figure 6.15a, which are the equivalent

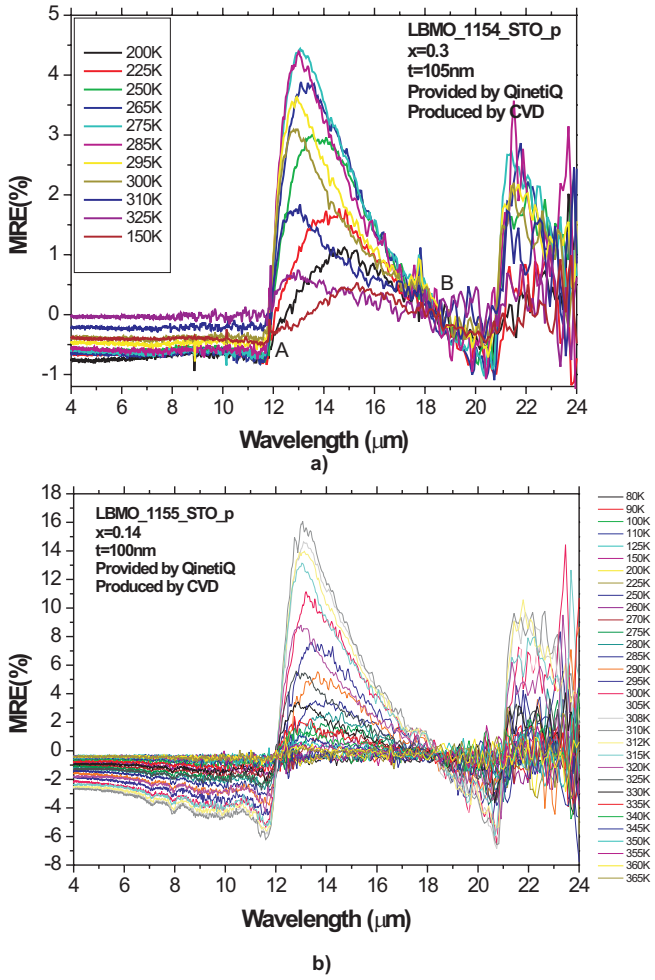

Figure 6.15: A plot of MRE(%) versus wavelength for a) LBMO_1154_STO and b) LBMO_1155_STO for a range of temperatures in an applied field of 1.3T. (Original in colour)

of points A and B in Figure 6.14, the amplitude of the positive MRE decreases as the temperature decreases.

Figures 6.16a-c show that changing the temperature can produce a similar effect to changing the applied magnetic field. In Figure 6.16a I have plotted the temperature equivalent of the MRE versus wavelength. The y-axis in this figure shows the result of subtracting the IR spectrum obtained at a given temperature, T, from the IR spectrum obtained at 295K, normalised to the spectrum at T=295K, i.e. [(T(295K)-T)/T(295K)], and is then multiplied by 100 to give the percentage change. The results in the figure were all taken

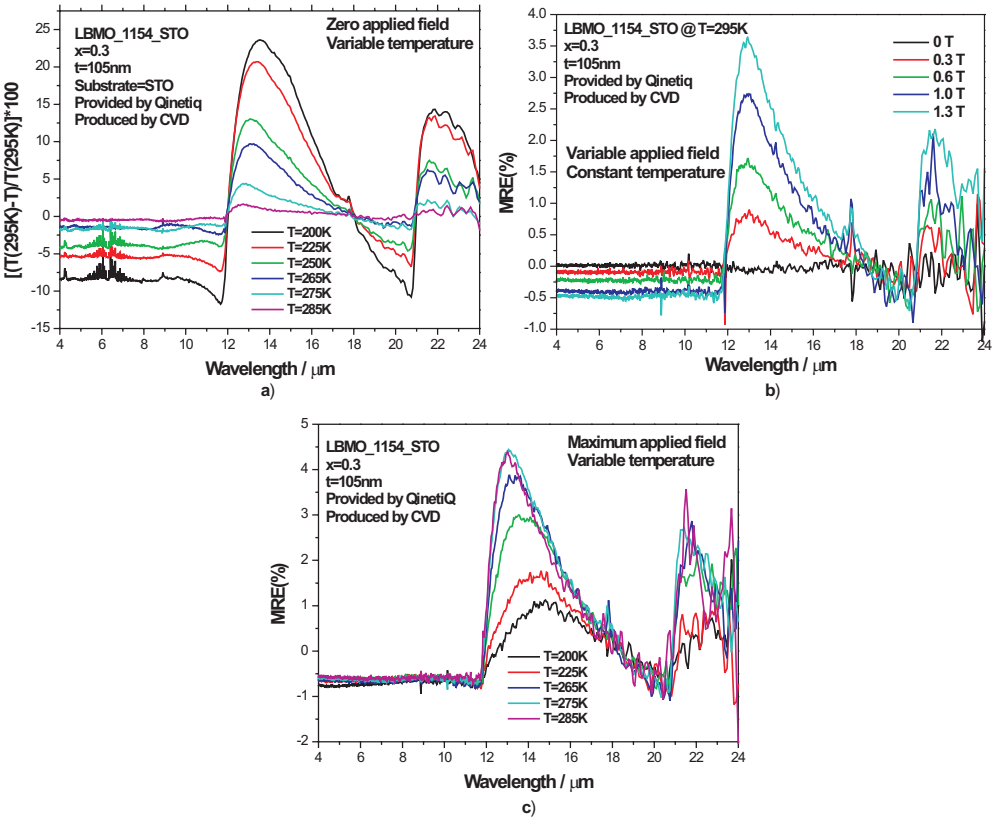

Figure 6.16: A comparison between a) temperature induced and b) magnetic field induced changes in the IR spectra for LBMO_1154. The figures show that changing the temperature in zero field has the same effect as changing the applied magnetic field at a constant temperature. In c) we see what happens when we allow the temperature to change while the sample is in a field of 1.3T. (Original in colour)

with zero applied magnetic field. In Figure 6.16b, I show the MRE spectra as a function of field (as measured inside the MMRS) for the same sample at a constant temperature of 295K. The two figures show similar changes as a function of field and temperature, particularly regarding the shape and the direction that the peak in the positive signal between 12-18 μm shifts as a function of temperature and field, which clearly indicates that changing the temperature in zero magnetic field is the equivalent of changing the magnetic field at a constant temperature.

Figure 6.16c shows the result of changing the temperature while a 1.3T magnetic field

is applied to the sample. While the profile is similar to that observed in Figure 6.16b, the position of the positive peak between 12-18 μm is observed to move in the opposite direction with temperature than was observed in Figure 6.16b. This is interesting because it demonstrates that while changing either the field or the temperature separately produces one trend, changing both together can produce a different trend. However, it is to be expected since it clear from Figure 6.16a that the change in amplitude of the positive peak is non-linear with changes in temperature. We should, therefore, expect a non-trivial convolution when we allow both the temperature and the applied field to change simultaneously.

6.5.2.3 A comparison between the CMR and MRE results

Figures 6.17a-d show a comparison between a) the CMR(%) and MRE(%) versus temperature results for LBMO_1154_STO b) the IR reflectivity and the electrical resistance for LBMO_1154_STO as a function of temperature, c) the CMR(%) and MRE(%) versus temperature results for LBMO_1155_STO and d) the IR reflectivity and the electrical resistance for LBMO_1155_STO as a function of temperature.

In Figures 6.17a and c I have plotted the absolute amplitude of the positive MRE as a function of temperature where I have defined the absolute MRE(%) as the difference between the minimum and maximum MRE(%) for each temperature in an applied field of 1.3T. The profile of the temperature dependence of the MRE is markedly different for the $x = 0.3$ sample compared to the $x = 0.14$ sample. Both profiles have a peak at the Curie temperature, but the former is characterised by a broad, asymmetric curve whereas the profile of the latter is sharper and is much more symmetric around T_C. The shapes of the profiles agree very well with those observed by Zhang *et al.* (122) as shown in Figure 2.14, though the peak in the MRE occurs at a different temperature. However, this can be easily explained since the samples Zhang *et al.* studied were only 50 nm thick compared to the 100+ nm of these samples. This means that the strain in these samples will be different to the ones Zhang *et al.* studied and hence, as was discussed in Chapter 2, the Curie temperature can be very different since it is so dependent on the growth conditions of the sample.

There is a clear correlation between the CMR and MRE data in Figures 6.17a and c for both samples. The profiles as a function of temperature for the CMR and MRE

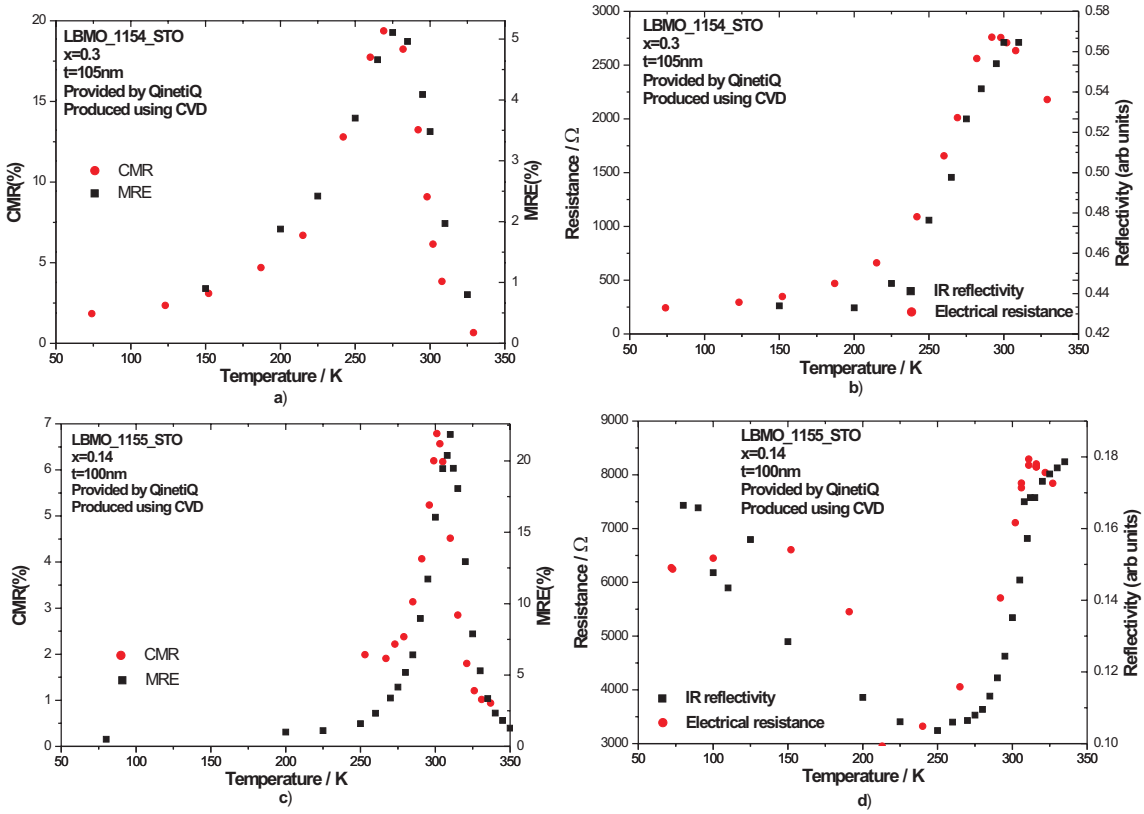

Figure 6.17: a) A comparison between changes in the CMR(%) and absolute MRE(%) versus temperature for LBMO_1154_STO. b) A plot comparing changes in IR spectra to changes in the electrical resistance as a function of temperature for LBMO_1154_STO. c) A comparison between changes in the CMR(%) and absolute MRE(%) versus temperature LBMO_1155_STO. d) A plot comparing changes in IR spectra to changes in the electrical resistance as a function of temperature for LBMO_1155_STO. in an applied field of 1.3T Changes in the IR reflectivity are related in the same way to changes in the electrical resistance as changes in the MRE are related to changes in the CMR. All MRE measurements were made using an applied field of 1.3T. The CMR measurements were made using an applied field of 0.9T. (Original in colour)

measurements very similar, with the only obvious difference being that the peak MRE(%) does not coincide exactly with the four-point probe measurement, with the entire profile being shifted by approximately +10K for both samples.

Figures 6.17b and d show that the changes in the IR spectra as a function of temperature are related to changes in the electrical resistance of the sample in the same way that changes in the MRE are related to changes in the CMR. Since the MRE spectra are derived from the IR spectra in the same way as the CMR data are derived from the resistance measurements this is consistent. The IR reflectivity data were taken at a wavelength of 11.7 μm for the $x = 0.3$ sample and at 13.3μm for the $x = 0.14$ sample. We observe the same +10K shift between the two sets of data in all of the figures.

As was highlighted above, this shift could be due to a systematic error in the measurement process. The temperature controlled CMR and MRE experiments are both expected to have some error in the temperature measurements. For the CMR measurements the error in the temperature arises from the fact that the sample position is slightly displaced from the position of the Pt resistor that is used to calibrate the PID, hence it is possible that the temperature is actually slightly different at the sample position than indicated by the PID. A similar problem occurs in the MRE measurements; the temperature is measured at the cold plate of the MMRS using a Pt resistor. However, this relies on there being a good thermal contact between the cold plate and the sample. The substrates used for the thin films are insulating and it may be that the temperature recorded for the film is not entirely accurate as a result of the poor thermal conductivity between the thin film layer and the cold plate. In both cases, care was taken to ensure that any thermal lag would be minimised, but such systematic errors could well explain the shift observed in the data. However, while there is a systematic error that can explain the shift between the CMR and MRE or the resistance and reflectivity measurements, this does not explain why the peak temperature is different, for example, in the MRE and reflectivity data. This could be due to a random source of error that has not been accounted for.

6.5.2.4 Peak wavelength as a function of temperature for LBMO_1155_STO and LBMO_1154_STO

On first inspection, the MRE spectra shown in Figures 6.15a and 6.15b seem quite random, especially between points A and B on the figure. As mentioned above, the wavelength where the peak amplitude of the the positive MRE occurs changes with temperature.

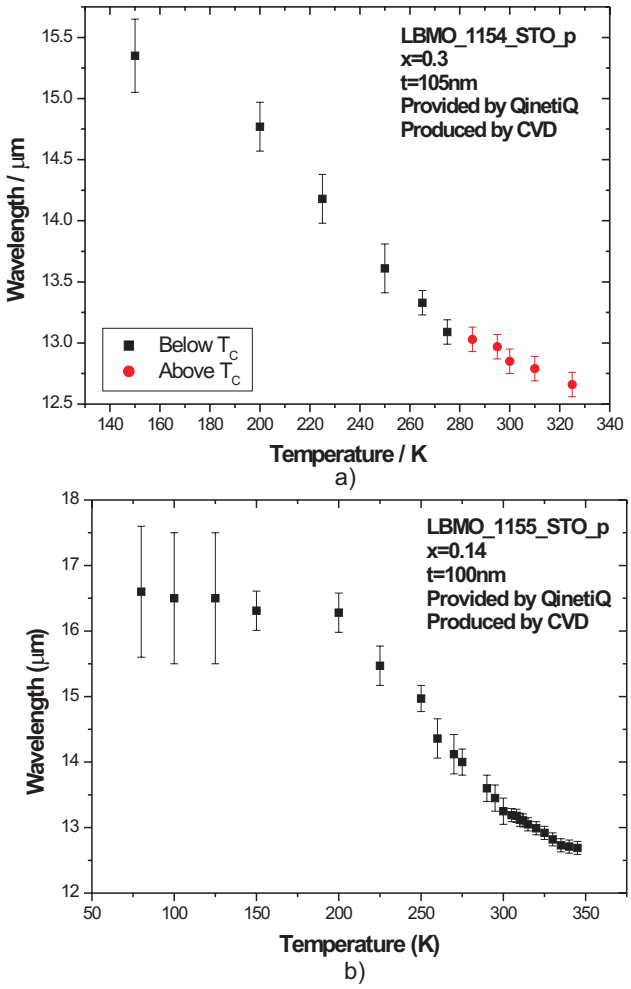

Figure 6.18: A plot of the wavelength of the maximum positive MRE versus temperature for a) LBMO_1154_STO and b) LBMO_1155_STO. (Original in colour)

Figures 6.18a and 6.18b show how the position of the peak amplitude varies with temperature for the LBMO_1154 and LBMO_1155 samples. The figures demonstrate that the

wavelength of the maximum positive MRE actually varies systematically with temperature. The position of the peak of the positive MRE is observed to shift towards longer wavelength as the temperature decreases. However, there appear to be three temperature regimes: T>T_C, 200K<T<T_C and T<200K. Above T_C the change in wavelength with temperature is non-linear, as is shown clearly in Figure 6.18a. In the temperature range 200K<T<T_C, the change in wavelength with temperature is linear and below 200K the position of the peak in the positive MRE assumes a fixed value. Unfortunately no data were available for the LBMO_1154 sample below 150K so it was not possible to see if this trend was the same for both samples. The explanation for this temperature dependence is most likely linked to the behaviour of the substrate as a function of temperature. If we refer to Figure 6.5b, we see that the pure STO substrate spectra are temperature dependent between 12 and 18 μm. As was discussed above with reference to Figures 6.16a-c, the convolution of the effect caused by applying the field with that caused by changing the temperature is expected to be non-trivial. It is most likely that this convolution is producing the wavelength dependence identified in Figure 6.18.

6.6 Conclusions

In this chapter I have presented the results of room temperature and temperature controlled experiments performed on a variety of LBMO and LCMO thin film samples. These experiments have clearly demonstrated that thin film manganite samples contain a lot of interesting physics and a key observation is that the substrate dominates the IR spectra of the thin films and can be used to enhance the detection of the film's properties.

The experimental results have shown that the transport properties of these materials are sensitive to changes induced by applying a magnetic field, by changing the temperature of the sample or by changing the polarization of the incident IR radiation. This is evident in the IR spectra where we see a wavelength dependent response to these external stimuli. Every thin film sample that has been studied to date has displayed similar characteristics in their IR and MRE spectra. One characteristic is the presence of nodes in the IR spectra. All the samples have at least two nodes in their spectra (as depicted by points A and B in Figures 6.14 and 6.15a). These nodes relate to specific wavelengths where the spectra are seemingly independent of the applied field and/or temperature changes and give the

MRE spectra their characteristic negative-positive-negative appearance as a function of wavelength. Prior to the first such node, which always occurs after the plasma edge, the reflectivity (and hence the conductivity) of the sample always increases in an applied field, whereas beyond this node the reflectivity decreases. A second node always occurs before we reach the wavelength of the stretching phonon mode since this mode always exhibits an increase in reflectivity with field or temperature.

Another key experimental observation in the MRE spectra of such thin films is that there is always a large negative MRE observed between 10 and 14 μm. The magnitude and position of this large negative MRE has been shown experimentally to depend upon the thickness and the doping of the thin film and indeed upon the polarity of the incident IR radiation. The latter is especially obvious in the temperature controlled MRE experiments where the negative MRE prior to point A in Figure 6.15a is heavily suppressed when the IR radiation is p-polarized. As was identified towards the end of Chapter 3, unlike in normal metals, these materials are very sensitive to changes in their plasma frequency. The dependence on sample thickness and doping arises from the fact that the plasma frequency is directly proportional to changes in the number of free carriers, which is directly proportional to changes in the sample's thickness or the level of doping.

The temperature controlled measurements presented towards the end of this chapter further demonstrate that the MRE is an ideal alternative to the traditional four-point probe technique of characterizing the magnetotransport in a sample. The fact that changes in the conductivity as a function of field are mirrored so accurately by changes in the amount of IR light reflected from the sample is very important for any potential applications. Of course, the additional benefit of obtaining spectral information as a function of temperature and field cannot be understated, since this provides more information on the magnetotransport in these materials than can be inferred from CMR measurements alone.

In order to understand the experimental results it has been necessary to develop a model that would explain the observed spectral features. It has been shown in this chapter that a model of the IR and MRE spectra using the form of the complex dielectric function given by:

$$\begin{aligned}\varepsilon_{total} &= \varepsilon_{film\infty} - \frac{\omega_p^2}{\omega^2 + \imath\gamma\omega}(1+\eta m^2) + \sum_{j=1}^{n} \frac{S_j^2}{k_j^2 - k^2 - \imath\gamma_j k} \\ &\quad + \varepsilon_{sub\infty} \cdot \prod_{j=1}^{n} \frac{k_{L_j}^2 - k^2 - \imath\gamma_{L_j} k}{k_{T_j}^2 - k^2 - \imath\gamma_{T_j} k} \end{aligned} \tag{6.7}$$

can successful reproduce all of the spectral features observed experimentally for thin film samples deposited upon an STO substrate, but fails to provide an adequate solution for an LAO substrate.

Prior to developing the model, there was no explanation for the large negative MRE observed experimentally in these samples at what we now know to be the plasma edge. The model has helped us to understand that all of the experimental observations can be understood in terms of changing the relative weighting of the terms in this complex dielectric function and that the position of the minimum associated with the plasma edge is determined by the point where $\sqrt{\varepsilon}_{total} = 1$.

However, it has also been shown that whilst the model is particularly good at reproducing the key features of the MRE spectra, it is less successful at reproducing the fine detail of individual IR spectra. In theory it should be possible to fine tune the parameters in Table 3.3 to produce a slightly better fit to the experimental data. In practice, however, this is not as simple as it would first appear since the model contains a large number of inter-related variables and, especially when one considers the overlap between some of the transverse and longitudinal phonon modes in the substrate, it is non trivial to predict the outcome of changes to a particular parameter. Despite numerous attempts, it has not yet been possible to exactly fit any of the experimentally obtained IR spectra using the model in its current form. The most likely reason for this is that strain introduced during the growth process e.g. from the lattice mismatch between film and substrate, is not being incorporated properly into the model, since the effect of strain on the magnetotransport is unpredictable at best. That said, the model presented in this thesis provides a good starting point for someone who wishes to develop a more advanced model of the magnetotransport in these materials. Future development could include a more material specific dielectric function that would allow us to fit a specific sample better, and any future model should also incorporate temperature dependence into the dielectric function.

A potential application for these materials could be developed if we could manipulate their complex dielectric function to our advantage. In all of the thin film samples that have been studied, the largest MRE has always been observed at the plasma edge and even modest fields produce a large MRE at this point because the reflectivity is tending towards zero, and therefore $\Delta R/R$ is large. As has been demonstrated, the position of the plasma edge is very sensitive to changes in the balance between the terms in the dielectric function. If the position of the plasma edge could be reliably controlled, through doping with impurities for example, then it should be possible to produce a contactless, magnetic switch that could be operated with radiation of a particular wavelength. Basically, applying a small field at the position of the plasma edge would result in a large change in the reflectivity from the material. This would clearly be beneficial in certain applications and the development of such a switch should be explored in future work on these materials.

Chapter 7

Conclusions and future work

Throughout this thesis a recurring theme has been one of conductivity in the manganite perovskites. The experimental results have shown that in these materials the conductivity is sensitive to changes that are induced by either applying a magnetic field or by changing the temperature of the sample (or both). This was first observed in the bulk LSMO samples, where we saw that applying an external magnetic field increased the conductivity, and thus increased the reflectivity, and that increasing the temperature could introduce new spectral features into the IR and MRE spectra. These new spectral features were later shown through simulations to be related to a lowering of the plasma frequency as the temperature increased. Similar observations were later made in thin film manganite samples and understanding these results has been the subject of this thesis.

A second theme throughout this thesis has been the use of the MRE measurement technique to study the magnetotransport properties of the mixed-valence manganites. As discussed in Chapter 1, this measurement technique had been successfully used to measure the properties of other materials prior to this work, but its applicability to these materials was not yet established. We have seen, however, that the MRE measurement technique has been very important in developing our understanding of the magneto-optical properties of these materials.

The field dependence in the bulk samples was explained in Chapter 5, where it was concluded that the application of an external magnetic field would tend to align the spins in neighbouring domains, thus facilitating conduction by double-exchange. The temperature dependence is more subtle. In Chapter 5, I discussed how that above T_C the free carriers

are likely to become trapped as a result of the increased spin disorder effectively preventing double-exchange from occurring, thereby lowering the conductivity. It was also pointed out that there was no way to be certain whether the plasma frequency was dropping as a result of a reduction in the number of free carriers (N) or an increase in their effective mass (m_e^*), or a combination of these effects. The $x = 0.2$ bulk LSMO sample provided us with some insight into this question. The number of free carriers (N) is determined by x, and is fixed. However, the modelling showed us that in order to create the spectral feature at 14.6μm, it was necessary for ω_P to drop, and hence N or m_e^* must change i.e. the carriers must become bound as the temperature increases, resulting in the formation of polarons.

The trapped free carriers simply do not have sufficient energy to escape their bounds. Of course, as the temperature of the sample increases further, conduction will again increase as more and more of the free carriers will manage to escape their bounds and we will likely see the variable range hopping proposed by Viret *et al.* (82; 79) as was discussed in Chapter 2. My MRE experiments clearly demonstrate that the conductivity above T_C in the bulk samples is field dependent; the larger the applied field, the larger the conductivity. The explanation is remarkably simple: the external field will tend to align the domains in the sample above T_C thus allowing double-exchange to occur in a similar way to that usually seen below T_C. Depending on the degree of spin disorder, the external field may not be strong enough to align all of the spins, hence we may again observe variable range hopping. Although the experiments cannot prove it directly, one can infer that the field dependence suggests the presence of magnetic polarons: locally FM regions trapped in the PI phase. The results of de Teresa *et al.*(76), for example, suggest that this hypothesis has merit. Clearly though, it would be a good idea to obtain experimental confirmation of the formation of magnetic polarons in these samples, and neutron diffraction data would be welcomed. Additionally, it would be instructive to see how the conductivity of samples with different compositions or dopants would compare to bulk LSMO, e.g bulk LCMO or LBMO samples, .

I was able to successfully simulate the IR and MRE spectra of bulk LSMO samples based on a model that considered the complex dielectric function, ε of these materials. A sensible choice of parameters was shown to produce all of the spectral features that were observed experimentally, and indeed, the model provided crucial insight into the origin of the additional spectral feature observed at 14.6μm. It is safe to say that without such a

simulation, this spectral feature would still be unexplained. It is now very clear that the samples are extremely sensitive to changes in their plasma frequency, a fact first alluded to in Chapter 3 where I showed that the response of the dielectric function was orders of magnitude more sensitive to changes in ω_P than changes in the damping term, γ.

The importance of the plasma frequency was further emphasized when I started to measure the MRE of thin film LBMO sample. Just as for the bulk samples, the IR and MRE spectra could only be understood after the spectra had been simulated. The actual model was a simple extension of the model previously used in the bulk samples; it just added terms that allowed us to model the contribution of the substrate to the complex dielectric function of the sample. However, the substrate has been shown to dominate the IR and MRE spectra, making the spectra very different to those observed in the bulk samples. Every thin film sample that has been studied to date has displayed similar characteristics in their IR and MRE spectra. One characteristic is the presence of nodes in the IR spectra with all the samples having at least two nodes in their spectra. These nodes relate to specific wavelengths where the spectra are seemingly independent of the applied field and/or temperature changes and give the MRE spectra their characteristic negative-positive-negative appearance as a function of wavelength. Prior to the first such node, which always occurs after the plasma edge, the reflectivity (and hence the conductivity) of the sample always increases in an applied field, whereas beyond this node the reflectivity decreases. A second node always occurs before we reach the wavelength of the stretching phonon mode since this mode always exhibits an increase in reflectivity with field or temperature.

Another key experimental observation that was discussed in Chapter 6, is that there is always a large negative MRE observed in the MRE spectra of the thin films between 10 and 14 μm. The magnitude and position of this large negative MRE has been shown experimentally to depend upon the thickness and the doping of the thin film and indeed upon the polarity of the incident IR radiation. As discussed above, and towards the end of Chapter 3, unlike in normal metals, whose conductivity is primarily determined by scattering processes, these materials are very sensitive to changes in their plasma frequency. The dependence on sample thickness and doping arises from the fact that the plasma frequency is directly proportional to changes in the number of free carriers, which is directly proportional to changes in the sample's thickness or the level of doping.

To a certain extent the modelling of the thin film samples was not quite as robust as that for the bulk samples. While a dielectric function of the form:

$$\begin{aligned}\varepsilon_{total} &= \varepsilon_{film\infty} - \frac{\omega_p^2}{\omega^2 + \imath\gamma\omega}(1+\eta m^2) + \sum_{j=1}^{n} \frac{S_j^2}{k_j^2 - k^2 - \imath\gamma_j k} \\ &\quad + \varepsilon_{sub\infty} \cdot \prod_{j=1}^{n} \frac{k_{L_j}^2 - k^2 - \imath\gamma_{L_j} k}{k_{T_j}^2 - k^2 - \imath\gamma_{T_j} k} \end{aligned} \tag{7.1}$$

allows us to model the response of a generic thin film manganite sample, it was concluded that the model was less well equipped to allow us to fit the experimental IR and MRE spectra of a specific sample. As was discussed in Chapter 6, the reasons for this are numerous. The principle reason is that the model contains a large number of inter-related variables and especially when one considers the overlap between some of the transverse and longitudinal phonon modes in the substrate, it is non-trivial to predict the outcome of changes to a particular parameter. Another possible reason that was discussed is strain. There is likely to be strain introduced to the sample during the growth process e.g. from the lattice mismatch between film and substrate and this is not incorporated properly into the model.

The model was certainly invaluable when it came to developing an understanding of the origin of the large negative MRE observed between 10-14μm since, prior to developing the model, there was no explanation for this feature at all. Indeed, the model has helped me to appreciate that all of the experimental observations can be understood in terms of changing the relative weighting of the terms in the sample's complex dielectric function and that the position of the minimum associated with the plasma edge, that is responsible for the large MRE, is determined by the point where $\sqrt{\varepsilon}_{total} = 1$

As was discussed towards the end of Chapter 6, a potential application for these materials could be developed if we could manipulate their complex dielectric function to our advantage. In all of the thin film samples that have been studied, the largest MRE has always been observed at the plasma edge and even modest fields produce a large MRE at this point because the reflectivity is tending towards zero, and therefore ΔR/R is large. As has been demonstrated, the position of the plasma edge is very sensitive to changes in the balance between the terms in the dielectric function. If the position of the plasma edge

could be reliably controlled, through doping with impurities for example, then it should be possible to produce a contactless, magnetic switch that could be operated with radiation of a particular wavelength. This would clearly be beneficial in certain applications and the development of such a switch should be explored in future work on these materials.

Another key observation that has been made for both the bulk and the thin films samples is the strong correlation between the CMR and MRE measurements. This correlation was first observed in the bulk LSMO samples at room temperature and later in two thin film LBMO samples on STO. I have shown conclusively that the MRE is an ideal alternative to the traditional four-point probe technique of characterizing the magnetotransport in a sample. The fact that changes in the conductivity as a function of field are mirrored so accurately by changes in the amount of IR light reflected from the sample is very important for any potential applications. Of course, the additional benefit of obtaining spectral information as a function of temperature and field cannot be understated, since this provides more information on the magnetotransport in these materials than can be inferred from CMR measurements alone. Potentially, therefore, the MRE could be used instead of traditional CMR measurements as an instrument for industrial quality control testing of future CMR devices, particularly in devices where making contact with the sample is either difficult or damaging.

There are a number of ways of extending the work presented in this thesis in the future. The main work that needs to be performed is a better characterisation of my samples. I have been limited primarily to IR reflectivity measurements, both at room temperature and as a function of temperature. However, in order to fully understand these materials it would be necessary to perform further measurements. In particular I would have liked to have made VSM measurements as a function of temperature for both the bulk and thin film samples, so that I could examine how the magnetization of the samples changed with temperature. In addition, it would be a good idea to measure the resistivity of the samples directly rather than relying on values from the literature. Furthermore, I would have like to have studied the samples using neutron and/or X-ray diffraction techniques. This would have allowed me to determine the structure of the samples and, potentially, to observe polarons in the PI phase. Atomic force microscope measurements of the sample surface would also help, particularly with regard to determining the roughness of the surface, and its potential influence on the IR reflectivity spectra.

In addition to the improved characterisation of the samples, it would also be desirable to be able to produce my own samples. One of the main limitations of modelling and understanding the properties of these materials has been the diverse nature of the samples I have had to use in my experiments. For the bulk samples, I would like to be able to compare the results I obtained for the bulk LSMO samples with those from similarly doped bulk LCMO and LBMO compositions. I think a comparison between different compositions would help to re-enforce the work presented here. Likewise, the thin film samples were too diverse in nature to allow a systematic approach to making my measurements. I would like to have access to several complete sets of samples. For example, I would like to have a set of samples that have the same thickness but different levels of doping. Conversely, I would also like to have a set of samples that have the same doping but different thicknesses. This would allow me to look for trends in the data, which would obviously help with the modelling of the IR and MRE spectra. This was not possible with the sample sets I currently possess since the samples all had either different thicknesses, levels of doping or substrates.

The modelling could also be developed further in the future. The form of the complex dielectric function used to model the bulk and thin film samples is very simplistic, but the fact it can reproduce all of the spectral features observed experimental is an achievement. This simplistic model could provide an excellent starting point for a more detailed model of the magnetotransport in these materials. For the bulk samples, I would like to investigate how we could achieve a better fit to the experimental data. In particular I would like to more realistically model the short wavelength IR spectra. In the current model, the short wavelength values all tend towards a fixed value (as shown in Figure 5.3b). This was discussed in Chapter 5 in terms of the model not accounting for diffuse scattering or absorption at these wavelengths, hence making the model predict higher reflectivities than was observed experimentally. However, the fact that the ε_∞ term is frequency independent in this model also contributes to this fixed value at short wavelengths since this term is becoming dominant in the dielectric function at these wavelengths. In light of the experimental results, I think it is likely that, at these wavelengths, the ε_∞ term has a frequency dependence. Future models should test this hypothesis.

In the thin film samples, the model really needs to include interface effects between the thin film layer and the substrate. To do this properly, however, it would be necessary to

know more about the structural changes to the sample when they become strained. This, of course, brings us back to the need for a better characterisation of the properties of the samples. Future development could also include a more material specific dielectric function that would allow us to fit a specific sample better, and any future model should also incorporate temperature dependence, of both the film and the substrate into the dielectric function.

In Chapter 4, I mentioned that the geometry of the MRE setup would result in a transverse magneto-optical Kerr effect for p-polarized incident light. This is something we have been aware of but have never quantified. I think it would be sensible to make a measure of this effect so as to quantify how it could potentially influence the experimental results, not only those presented in this thesis, but for all experiments carried out on this equipment.

In Appendix B of this thesis, I present the results of pump-probe, ultrafast experiments carried out on several thin film LBMO/STO samples at FELIX (the Free Electron Laser for Infrared eXperiments), an international free-electron laser facility based at the FOM Institute, located just outside Nieuwegein in The Netherlands. The work presented in Appendix B was done in collaboration with Professor G. Gehring's research group at the University of Sheffield, and the experimental results are still being interpreted. The work carried out at FELIX was not considered to be sufficiently developed to be included in the main body of this thesis, but it is included in the Appendix so that there is some record of the work that I have carried out. The experimental results obtained from FELIX are very interesting and provide information about the carrier dynamics in the thin film LBMO samples. Understanding the results that we obtained at FELIX, and developing further experiments and models that can be performed and tested there, should hopefully increase our understanding of the carrier dynamics of these materials and will form a large body of our potential future work on these materials.

The main aims of this thesis were to understand the IR and MRE spectra of the bulk and thin films samples and to incorporate temperature control into our MRE measurements. These aims have been realised contributing to a much better understanding of the transport properties of these materials than at the start of this project. The MRE technique has been shown to be an excellent tool for studying the magnetotransport properties of the mixed-valence perovskites. The spectral information provided by the technique has proved to be

invaluable in increasing our understanding of the magnetotransport of these materials.

Appendix A

A.1 Modelling IR and MRE spectra using MathCAD

The modelling of the IR and MRE spectra discussed in Chapter 3 was done using MathCAD 2001 Professional. The MathCAD code used to model the bulk and thin film manganite samples can be found on the accompanying CD. In this section I will briefly review the contents of the CD, describing the function of each of the MathCAD programs contained therein.

The root directory on the CD contains two folders: 'Bulk samples' and 'Thin film samples'. In the following description, bold text refers to a folder and itallic text is used for the individual files.

Bulk samples → LSMO

LSMO_bulk.mcd

This file shows the complete model for the IR and MRE spectra for bulk LSMO samples.

LSMObulk_gammachange.mcd

This file shows the complete model for the IR and MRE spectra for bulk LSMO samples but allows the user to easily vary the value of γ_j in equation 3.13.

LSMObulk_kchange.mcd

This file shows the complete model for the IR and MRE spectra for bulk LSMO sam-

ples but allows the user to easily vary the wavenumber of the transverse phonon modes, k_j, in equation 3.13.

LSMObulk_masschange.mcd

This file shows the complete model for the IR and MRE spectra for bulk LSMO samples but allows the user to easily vary the effective mass of the free carriers, m_e^*, which is used to determine the plasma frequency.

LSMObulk_oscilchange.mcd

This file shows the complete model for the IR and MRE spectra for bulk LSMO samples but allows the user to easily vary the oscillator strength of the transverse phonon modes, S_j , in equation 3.13.

Thin film samples → LBMO

LBMO_STO.mcd

This file models the IR and MRE spectra of LBMO on a STO substrate.

LBMO_STO_masschange.mcd

This file models the IR and MRE spectra of LBMO on a STO substrate but allows the user to easily change the effective mass of the free carriers in the Drude-like term of equation 6.7.

LBMO_STO_gammachange.mcd

This file models the IR and MRE spectra of LBMO on a STO substrate but allows the user to easily change the value of the γ in the Drude-like term of equation 6.7.

LBMO_STO_gammaharmonic.mcd

This file models the IR and MRE spectra of LBMO on a STO substrate but allows the user to easily change the value of the γ_j in the harmonic oscillator term of equation 6.7.

LBMO_STO_oscillatorharmonic.mcd

This file models the IR and MRE spectra of LBMO on a STO substrate but allows the

user to easily change the value of the oscillator strength, S_j, in the harmonic oscillator term of equation 6.7.

LBMO_STO_kharmonic.mcd

This file models the IR and MRE spectra of LBMO on a STO substrate but allows the user to easily change the value of the wavenumber of the j^{th} phonon mode in the harmonic oscillator term of equation 6.7.

LBMO_STO_substrate.mcd

This file models the IR and MRE spectra of LBMO on a STO substrate but allows the user to easily change the film to substrate ratio in equation 6.7.

LBMO_STO_substratefixedvalue.mcd

This file models the IR and MRE spectra of LBMO on a STO substrate but sets a fixed film to substrate ratio in equation 6.7. This program was used to calculate the shift in the plasma edge when the film thickness was alloed to change as was discussed in Chapter 6 with regard to Figure 6.8.

Thin film samples → LCMO

LCMO_LAO.mcd

This file models the IR and MRE spectra of LCMO on a LAO substrate.

Thin film samples → Substrates

GervaisLAO.mcd

Modelled $LaAlO_3$ substrate spectra using a four parameter model.

GervaisSTO.mcd

Modelled $SrTiO_3$ substrate spectra using a four parameter model.

LAO_Classical.mcd

Modelled $LaAlO_3$ substrate spectra using a three parameter model.

STO_Classical.mcd

Modelled $SrTiO_3$ substrate spectra using a three parameter model.

A.2 SEM images

As discussed in Chapter 5, further examples of the SEM images for the bulk LSMO samples can be found on the accompanying CD. The images can be found at:

Bulk samples → SEM images

The naming convention for the files is simple: SG and SSR refer to the sample preparation method, Sol-Gel and Solid State Reaction, respectively. The numbers 1, 2 and 3 refer to sample's composition i.e. $x = 0.1$, $x = 0.2$ and $x = 0.3$, respectively.

A.3 Polarization dependence

The polarization dependence shown in Figure 4.5 was calculated using the MathCAD software. The program can be found on the accompanying CD at:

Bulk samples → Polarization dependence

Polarization Dependence.mcd

This file contains a program that simulates the polarization dependence of the incident IR light with respect to the angle of incidence, as was shown in Figure 4.5.

A.4 Modelling the response of FELIX

The MathCAD program used to model the response of the samples to FELIX can be found on the accompanying CD at:

Thin film samples → FELIX model

FELIXmodel.mcd

This file contains a basic simulation of the response of the sample to FELIX, as given by equation B.5 in Chapter 7.

A.5 Skin depth

A question often asked is: 'What is the skin depth of the infrared light?' This is particularly important for the thin film samples where the substrate can influence the results.

The skin depth is calculated using the formula:

$$\delta = \frac{2}{\sqrt{\omega \mu_0 \sigma}} \tag{A.1}$$

or:

$$\delta = \frac{2}{\sqrt{\omega \mu_0 \frac{1}{\rho}}} \tag{A.2}$$

Where ω is the frequency of the light, μ_0 is the permittivity of free space and ρ is the resistivity. For infrared light with a wavelength of 10μm, $\omega \approx 2x10^{14}$ Hz. A typical value for ρ for an LSMO ($x = 0.2$) manganite sample at room temperature is 5x10^{-3} Ωm (54). This results in a skin depth, δ, of approximately 9 μm.

In LBMO, the resistivity of an $x = 0.3$ sample is 5x10^{-5} Ωm (68). Using the same values for the other parameters in equation A.2, this gives a value for δ of approximately 900 nm. Hence, the skin depth can vary widely between different samples. However, in every sample, the skin depth is much greater than the film thickness and therefore the substrate is very important in all of our measurements.

A.6 Calibration of the magnet and power supply

The magnetic field recorded by the probe attached to the Gaussmeter seems to depend greatly upon the position of the probe with respect to the pole pieces of the electromagnet (EM). This is as expected, but it means that the sample may not be exposed to the same magnetic field as is recorded by the probe. To account for this, the probe was placed as close to the position the sample occupies as possible and the magnetic field as a function of current (I) and voltage (V) on the power supply was recorded.

These are tabulated in Table A.1 and plotted in the top and middle panels of Figure A.1 below. Also included in the bottom panel of Figure A.1 is a plot of V against I, i.e. the resistance of the power supply.

Figure A.1 shows that the current and voltage required to generate a field is fairly linear up to about 1.0 T. After that it requires an increasing amount of current or voltage to generate the larger fields. This is because the coils in the EM get hotter as more current is applied. The figure also shows us that the power supply maintains a constant resistance. i.e as the current required to produce the field increases, the voltage required increases at the same rate.

Magnetic field (B) / T ($\pm 0.000005 T$)	**Voltage (V) / V** ($\pm 0.05 V$)	**Current (I) / A** ($\pm 0.05 A$)
0.00845	0	0
0.05000	1.8	0.5
0.10000	3.9	1.2
0.15000	5.9	1.7
0.20000	8.0	2.3
0.25000	10.0	2.9
0.30000	12.0	3.5
0.35000	13.9	4.1
0.40000	15.9	4.7
0.45000	17.9	5.3
0.50000	19.9	5.8
0.55000	21.9	6.4
0.60000	24.0	7.0
0.65000	26.0	7.6
0.70000	28.0	8.2
0.75000	30.1	8.8
0.80000	32.2	9.5
0.85000	34.2	10.0
0.90000	36.4	10.7
0.95000	38.6	11.3
1.00000	40.9	12.0
1.05000	43.3	12.7
1.10000	45.7	13.5
1.15000	48.4	14.3
1.20000	51.2	15.1
1.25000	54.3	16.1
1.30000	57.6	17.1
1.35000	61.2	18.2
1.40000	65.4	19.5

Table A.1: Calibration data for the power supply of the electromagnetic

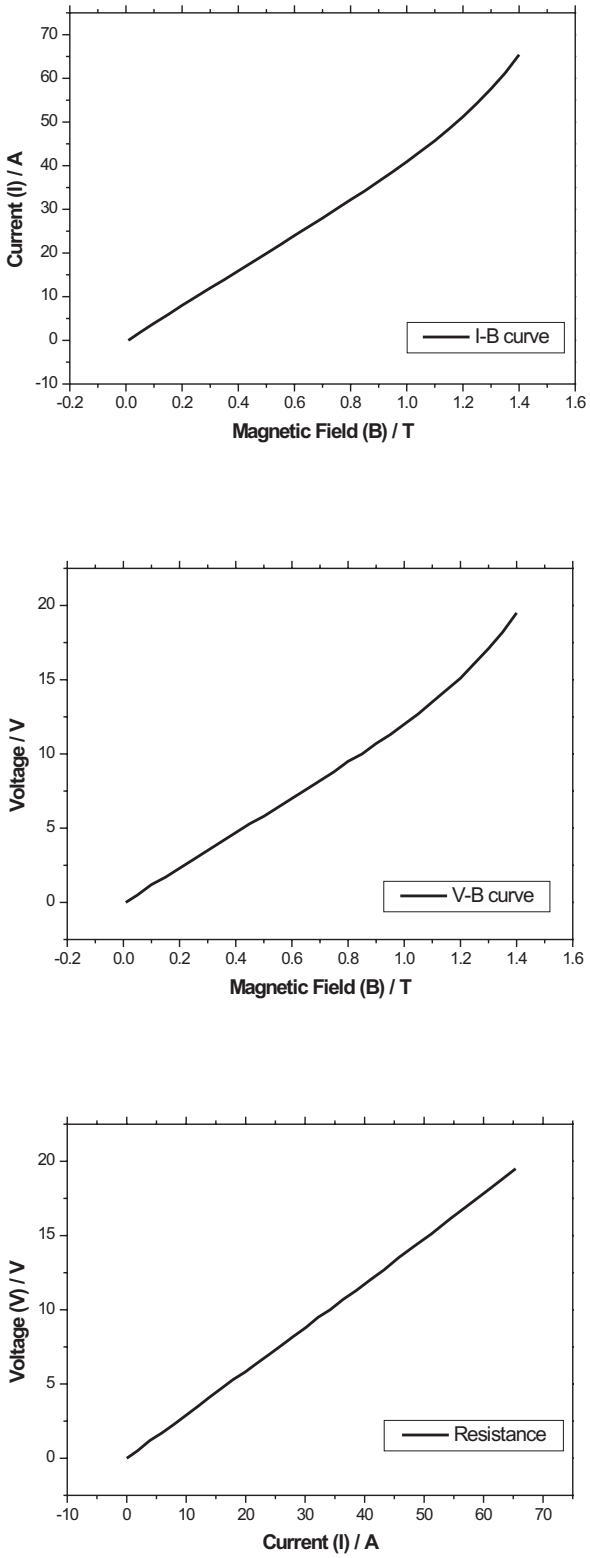

Figure A.1: Current and voltage versus magnetic field characteristics of the electromagnet's power supply. The top panel of the figure shows how the current varies with field, the middle panel shows how the voltage varies with field, and the bottom panel shows the resistance of the power supply.

Appendix B

Electron-lattice interactions: a study of carrier dynamics at FELIX

B.1 Introduction

The work presented in this Appendix was not considered to be developed enough to include in the main body of this thesis. It is included here as a reference for anyone who should happen to continue this work in the future. In this Appendix, I will present the results of pump-probe, ultrafast experiments carried out on several thin film LBMO/STO samples at FELIX (the Free Electron Laser for Infrared eXperiments), an international free-electron laser facility based at the FOM Institute, located just outside Nieuwegein in The Netherlands. The work presented in this chapter was done in collaboration with Professor G. Gehring's research group at the University of Sheffield. It should be noted that this research is work-in-progress and that the interpretation of our experimental results is still on-going. The models presented towards the end of this appendix represent our current hypothesis for the experimental results we obtained at FELIX.

This Appendix will begin with a very brief review of how FELIX operates before discussing our experimental setup for pump-probe measurements in a reflection geometry. I will then present the results of power, wavelength, temperature and magnetic field dependent measurements for several LBMO/STO thin film samples. The chapter will conclude with our current explanation for the observed results.

B.2 Experimental setup

B.2.1 A brief overview of FELIX

FELIX is an rf-linac based free electron laser operating in the Compton regime. A relativistic beam of electrons is injected into a resonator, consisting of two high-reflectivity mirrors, around an undulator. The magnetic field of the undulator is perpendicular to the direction of the electron beam and periodically changes polarity a (large) number of times along its length. This will cause a periodic deflection of the electrons while traversing the undulator. The transverse motion is quite analogous to the oscillatory motion of electrons in a stationary dipole antenna and hence will result in the emission of radiation with a frequency equal to the oscillation frequency (165). This radiation, referred to as spontaneous emission, is usually very weak though. This is a consequence of the fact that the electrons are typically spread out over an interval that is much larger than the radiation wavelength and will therefore not emit coherently. But on successive roundtrips in the resonator, this weak radiation will be amplified by fresh electrons, until saturation sets in at a power level which is typically 10 million to 100 million times that of the spontaneous emission.

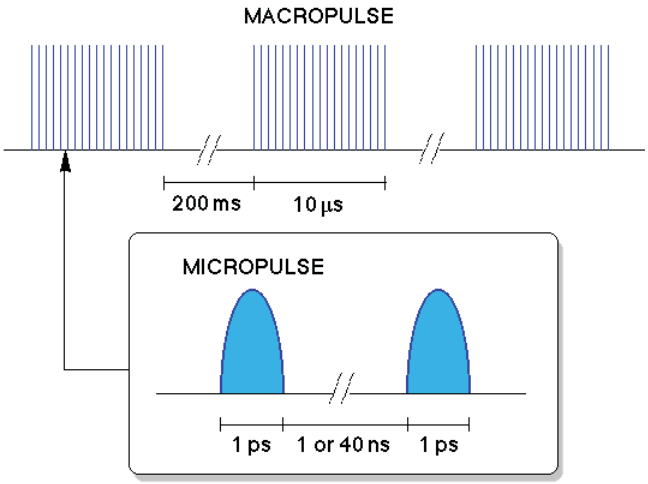

Figure B.1: Schematic illustrating the time structure of the FELIX electron beam. Taken from (165).

Due to the temporal structure of the electron beam, FELIX has an optical pulse structure consisting of a macropulse which is $\sim$6 μs long having a repetition rate of either 5

or 10 Hz. The macropulse itself, consists of ∼300 micropulses and have a pulse length which is variable between 300 fs and ∼5 ps. This is illustrated in Figure B.1.

B.2.2 Pump-probe in a reflection geometry

Our experiments were made using a standard pump-probe technique whereby the sample is excited by a large pump signal from the FELIX and then the response of the sample to the pump is probed by a much weaker, delayed signal of the same frequency. Typically, pump-probe measurements at FELIX have been done in a transmission geometry and such a setup is shown schematically in Figure B.2.

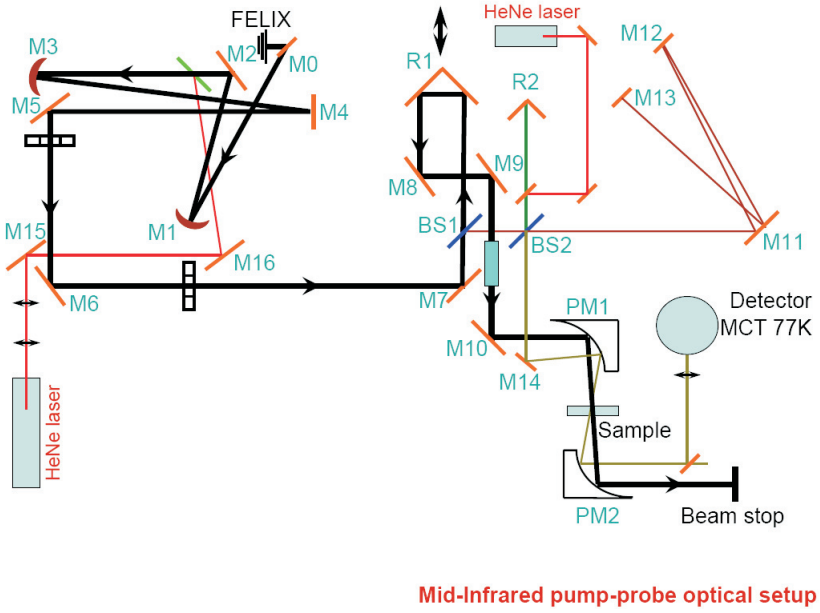

Figure B.2: A schematic showing a typical pump-probe experimental setup at FELIX for a transmission geometry. The thick black line shows the beam path of FELIX. The prefixes M, PM, BS and R corresponds to Mirrors, Parabolic Mirrors, Beam Splitters and Right-angled mirrors, respectively. Original figure was designed by N.Q. Vinh at FELIX. (Original in colour)

Our setup was identical to this except that instead of transmitting through the sample, we instead reflected from the sample into the MCT detector. We wanted a reflection geometry since this would allow a direct comparison to results from the MRE experiments, and also because transmission through the substrates is low.

The optical setup illustrated in Figure B.2 is much simpler than it first appears. The

thick black line in the figure shows the beam path of FELIX. The initial optics consists of several parabolic mirrors and pinholes, designed to focus the beam and to ensure that it is at the correct position. The HeNe laser is used to aid the alignment process since IR light is not visible to the naked eye. Between mirrors M7 and R1, the beam from FELIX is split by beam-splitter BS1. The majority of the signal (95%) passes through BS1 and is reflected from R1. R1 is positioned on a movable, computer controlled microstage that allows us to change the delay time between the pump and the probe signal with high precision. This signal, which acts as the pump, is then reflected onto the sample.

The other 5% of the signal from BS1 is then split again by BS2. The beam directed at R2 is used as the probe signal. Like the pump beam, it has a HeNe laser aligned along the same optical path to aid alignment. The part of the beam directed at mirror M11 is used for a reference signal. The optical distance between BS2 to M11, M12, M13 and back to BS2 is such that it takes light exactly 20ns to traverse it. This means that the reference signal will always occur between the micropulses.

For the pump-probe method to work it is important that there is an overlap between the pump and the probe beams on the sample and it is also very important to find the position of t=0 i.e the position where the pump and the probe signals both reach the sample at the same time. Since the pump and the probe are in phase, we can determine both the overlap and the t=0 position using interferometry. Basically, the microstage is moved until we get an interference pattern that shows the two beams are overlapping. The position where the maximum signal for constructive interference is observed is then set to t=0.

The sample is cooled in a microstat to 4K using liquid helium. As we will see later, it is necessary to cool the sample since at higher temperatures the signal amplitude received from the sample is indistinguishable from its thermal noise.

The signal received by the MCT detector is processed using a band pass filter. A boxcar is ‘gated’ around the signal so that the electronics are sensitive to changes in the signal over the same 6μs time period as the pulse and allows the signal to be averaged to reduce noise. The signal from the detector is balanced to the reference signal after any change in the attenuation or temperature to ensure that the boxcar doesn’t become saturated by the new signal.

B.2.3 Corrections for attenuation

A typical power output from FELIX is 1 mJ / macropulse, though the power output is in fact wavelength dependent. Each macropulse contains approximately 300 micropulses, and hence each micropulse has an energy of approximately 3.3 μJ. The diameter of the spot size on the sample was measured to be 450 μm ($\pm 50\mu$m). The measurement was made using a 100 μm diameter pinhole (the smallest available), which we placed in the beam path. The diameter of the beam was inferred from the signal amplitude detected on an oscilloscope as the pinhole was moved across the beam. The amplitude of the signal was obviously largest in the centre of the beam, but dropped off sharply as the pinhole was moved away from the centre. From this, we were able to determine that the beam had a diameter of about 450 μm, but obviously the error is quite large since the pinhole is of similar dimensions. In order to preserve the sample it is necessary to attenuate the signal from FELIX. It was possible to apply attenuation to the beam from FELIX: using a computer, it was possible to 'flip' four switches with attenuations of 3dB, 5dB, 5dB and 5dB. These switches could be flipped in any combination to provide attenuations of 3, 5, 8, 10....18dB.

The liquid nitrogen cooled MCT detector, used to detect the reflected signal from the sample, could also become saturated if the probe signal was too large. This signal could also be attenuated manually using the same attenuation system as was used for the main beam.

In order to directly compare results that have been attenuated to varying degrees, it is necessary to make a correction for the attenuation. For the dB system, the attenuation, A is given by:

$$A = 10 \log_{10} \left(\frac{P_d}{P_s} \right) \tag{B.1}$$

where P_d is the detected power and P_s is the source power. Rearranging equation B.1 in terms of the source power we see that:

$$P_s = P_d \cdot 10^{\frac{A}{10}} \tag{B.2}$$

Hence, in order to correct for the attenuation, it is necessary to multiply the attenuated values at the detector by $10^{\frac{A}{10}}$.

B.2.4 Samples

All of the samples we have studied at FELIX have been thin film LBMO samples on STO substrates. Our first visit (of four) to FELIX took place before the modelling of the previous chapter was started. At that time we did not know the origin of the large negative MRE signal observed in the MRE spectra of the thin film LBMO samples at their plasma edge, nor indeed did we even know that we were at the plasma edge. This was only discovered after the successful modelling of LBMO on STO that we discussed in Chapter 6 (see Figure 6.9). We were therefore curious to discover if FELIX could provide us with some additional information that would help us to characterise the properties of this feature, and hence all our measurements were made at, or around, this wavelength.

On our first visit to FELIX we focussed almost entirely on the LBMO_Sheffield sample. This sample has $x = 0.3$. On our subsequent visits we measured the power, temperature and wavelength dependencies for other LBMO samples. By the time of our later visits, I had measured the temperature-dependent MRE data for the LBMO_1154 and LBMO_1155 samples and it was therefore desirable to use FELIX to study these samples in more detail. These samples have $x = 0.3$ and $x = 0.14$, respectively, so it is possible to see the influence doping has on the results. To complete the doping series, we also studied the $x = 0.24$, LBMO_1191a sample. The magnetic field dependence of two of the samples (LBMO_Sheffield and LBMO_1154) was also measured.

B.3 Experimental results

B.3.1 Power dependence

Figures B.3a-d shows the power dependence of the LBMO_1155 ($x = 0.14$), LBMO_1191a ($x = 0.24$), LBMO_1154 ($x = 0.3$) and LBMO_Sheffield ($x = 0.3$) samples, respectively. The figures are corrected for the attenuation on FELIX and the detector.

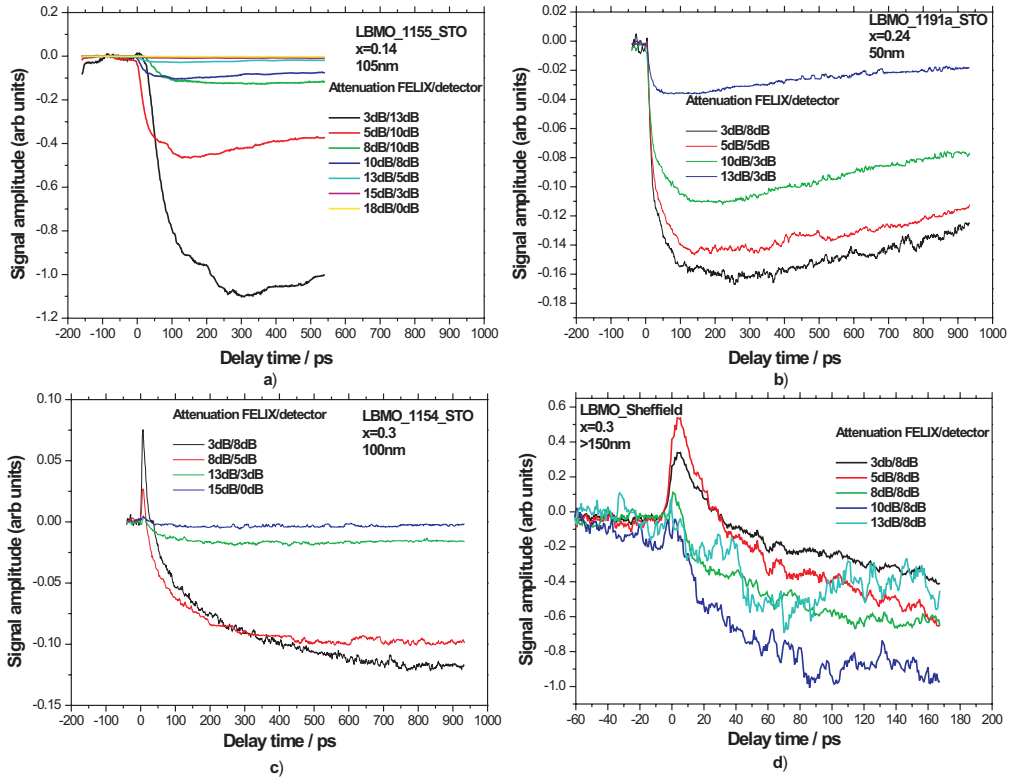

Figure B.3: Power dependent measurements at 4K for a) LBMO_1155, b) LBMO_1191a, c) LBMO_1154 and d) LBMO_Sheffield. The figures are corrected for the attenuation the detector. (Original in colour)

The response from the samples to FELIX is very different and is strongly dependent on both power and the sample composition. The $x = 0.3$ samples (Figures B.3c and d) exhibit a large, power dependent positive signal shortly after the t=0 position. This positive signal is much diminished in the $x = 0.24$ sample (Figure B.3b) and is not observed at all in the $x = 0.14$ sample (Figure B.3a). Since the doping of the samples changes the number of free carriers in the sample, it appears that a positive peak is only observed in the more conducting samples. Another interesting observation is that the positive peak does not occur precisely at t=0. There is always a delay of typically 8–12 ps before the maximum positive signal is reached. Such a 'long' delay time is not observed in optical (1.5eV, λ=825nm) pump-probe measurements made by Taylor *et al.* (166) in thin film LCMO and LSMO samples, where the typical rise time is sub-picosecond (as shown in

Figure B.4).

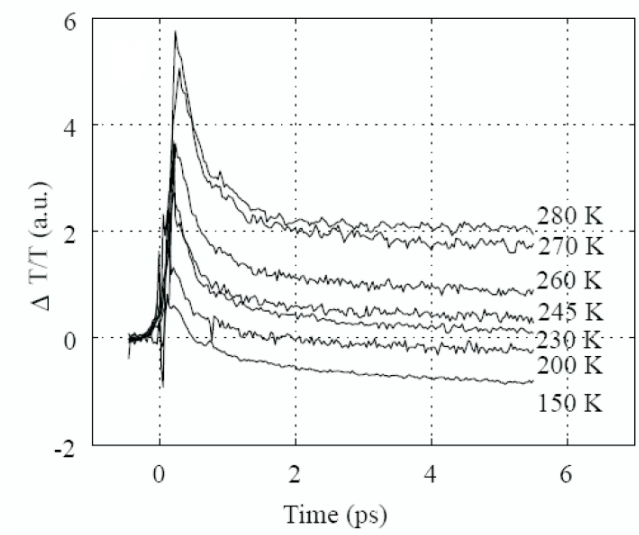

Figure B.4: Change in transmission as a function of temperature for $La_{0.7}Ca_{0.3}MnO_3$ close to T_C at 1.5 eV (λ=825nm). Taken from (166).

A negative signal amplitude is observed for all four samples, yet its behaviour is also sample dependent: in the $x = 0.3$ samples the negative sample reaches a minimum value and has not recovered by the end of the measurement. For the less conducting samples, however, the negative signal shows signs of recovery on longer (300ps+) timescales. The positive and negative signal both respond in a similar way to increasing power. Both the positive and the negative signal amplitude generally become larger as the power increases. This is clearly demonstrated in Figure B.5 where I plot the amplitude of the positive and the negative signals corrected for attenuation on the detector for LBMO_1154. The decay constant for the negative signal is approximately half that observed for the positive peak.

It is possible to fit exponential decay curves to the initial drop in the amplitude of the negative signal. Typically the time constant is of the order of 20–30 ps but the fits are usually unsatisfactory since they are heavily dependent on the start and end points used in the plot.

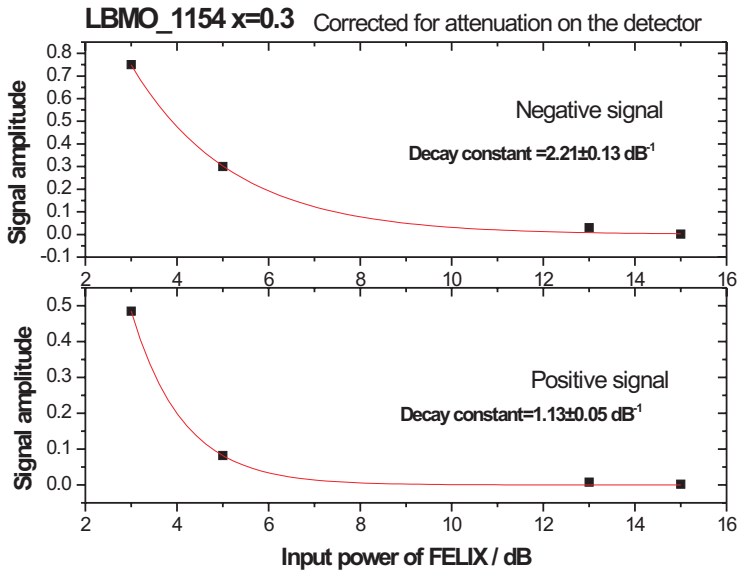

Figure B.5: Power dependence of the negative and positive signal for LBMO_1154. The decay constant for the negative signal is approximately double that observed for the positive signal in this sample as a function of power.

B.3.2 Wavelength dependence

Both the positive and the negative peaks invert when we cross from the regime in the IR spectra where we observe a decrease in the reflectivity as the conductivity increases to the regime where the reflectivity increases as the conductivity increases. This is shown clearly in Figures B.6a-d.

Figure B.6a shows the wavelength dependence of the LBMO_1191a (x=0.24) sample measured at a temperature of T=240K at FELIX. Figure B.6b shows a close up of the t=0 region, and Figure B.6c shows the normalised IR spectra for this sample at room temperature. In Figures B.6a and B.6b we observe that at wavelengths below 12.5 μm we have the familiar positive peak followed by the negative signal. However, at wavelengths above 12.5 μm the whole plot becomes inverted; the positive peak becomes a sharp negative peak and over longer time periods the negative signal becomes positive instead.

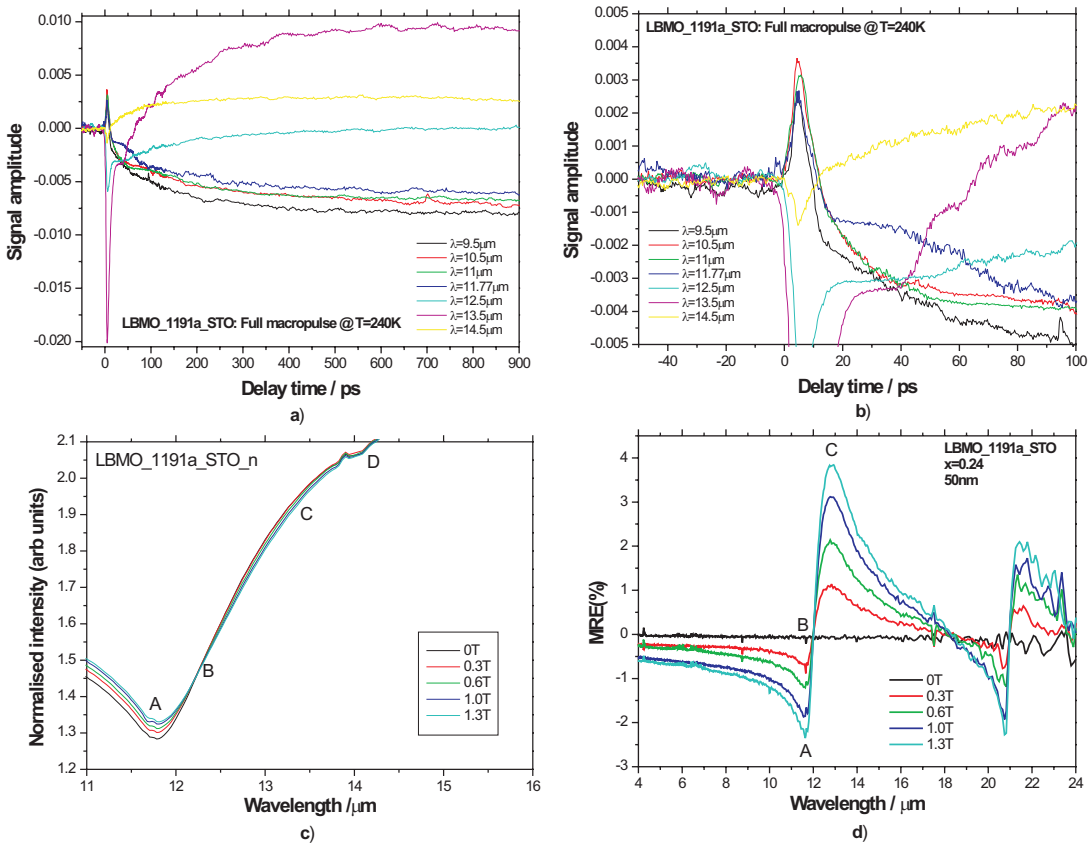

Figure B.6: Wavelength dependent measurements for LBMO_1191a taken at T=240K. In a) we plot the data as measured by FELIX for all delay times. In b) we show a close up of the t=0 region. In c) we show the normalised IR spectra at room temperature and in d) we show the MRE spectra. The points A, B, C and D are referred to in the main text. (Original in colour)

An explanation for this behaviour can be found by examining the normalised IR spectra (taken at room temperature) for this sample as shown in Figure B.6c and has already been discussed in section 6.5.2.1 of Chapter 6. As highlighted in the figure, the IR spectrum contains 4 main features which have been marked as points A, B, C and D.

At point A we observe the maximum increase in reflectivity as the applied field is increased and we also observe the largest positive peak in the FELIX data. Points B and D correspond to nodes where the reflectivity is independent of the applied field. The reflectivity either side of a node behaves differently. Prior to point B we see that the reflectivity increases with field and also see a positive peak at FELIX. At wavelengths longer than

point B, the reflectivity decreases as the applied field is increased. At such wavelengths we observe a negative peak at t=0 at FELIX. The maximum negative initial peak is observed at point C which corresponds to the wavelength where the maximum decrease in reflectivity with applied field is seen. In the last chapter we saw that changes in the reflectivity (R) of the spectra (induced by applying a magnetic field [R(B)] or by changing the temperature [R(T)]) were as a result of changes in the conductivity (σ) of the sample. It would seem, therefore, that the wavelength dependence observed at FELIX is strongly dependent on how the reflectivity of the sample responds at that particular wavelength in the IR spectra to induced changes in the conductivity of the sample, i.e. R(σ). This is made particularly clear in the MRE spectra for this sample, shown in Figure B.6d. The point A, B and C correspond to those shown in the IR spectra. Point A corresponds to the point where we observe the maximum negative MRE and point C corresponds to the point where we observe the maximum positive MRE. Point B is a null point where no MRE is observed.

The wavelength dependence of the LBMO_1155 sample is shown in Figures B.7a and b. The signal amplitude as a function of delay time is plotted for each wavelength in Figure B.7a. In Figure B.7b, I show the maximum signal amplitude that was measured at each wavelength. The amplitude of the signal appears to peak at around λ = 13.3 μm, clearly demonstrating how sensitive the response of the sample is to changes in wavelength.

It should be made clear that referring to the signals as either positive or negative is actually misleading since the signal can be either positive or negative depending upon how R varies as a function of σ at any given wavelength. As I will discuss below, we should really refer to the signals as ‘fast’ and ‘slow’, since in reality the signal is comprised of a fast response to the pump, which is associated with an increase in the ‘conductivity’, followed by a slower relaxation process, or rather processes. However, at this stage I will still refer to the positive and negative signal and positive and negative peaks, as this is what is observed experimentally. It is only when we start to interpret these experimental features that we encounter difficulties with this nomenclature.

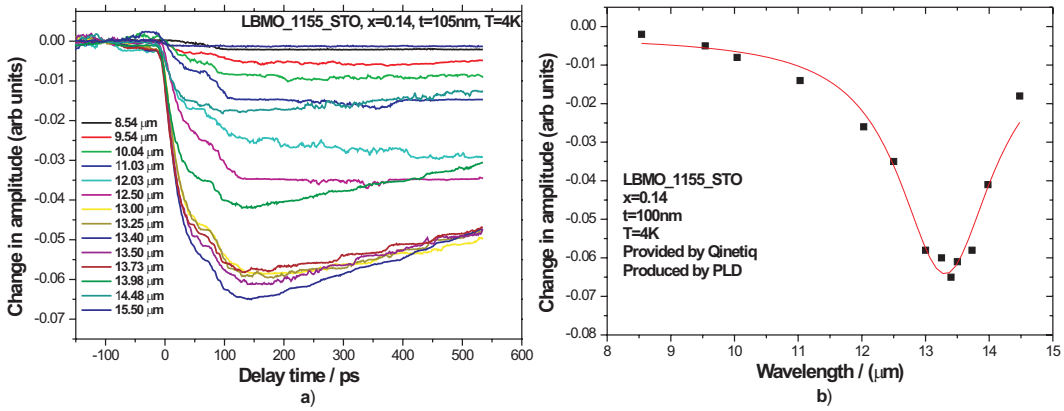

Figure B.7: a) Plot of signal amplitude as a function of delay time for the LBMO_1155 sample for a variety of wavelengths. b) Plot showing how the maximum signal amplitude varies with wavelength. (Original in colour)

B.3.3 Temperature dependence

We have studied the temperature dependence of three samples at FELIX: LBMO_1155, LBMO_1191a and LBMO_1154. Each sample exhibited a different response to changes in temperature. We shall consider each sample in turn.

B.3.3.1 LBMO_1155, x=0.14

The LBMO_1155 sample has $x = 0.14$, is 105 nm thick and is nominally weakly ferromagnetic and metallic at low temperatures (according to Figure 2.14). The Curie temperature varies between 200 K (for bulk) and 300 K (for 20nm thin films as measured by Zhang *et al.* (122)). Figure B.8a shows the experimental results obtained when we measured the temperature dependence of the signal from the LBMO_1155_STO sample at a wavelength of 13.3 μm.

A close up of the $t = 0$ position in Figure B.8b shows that there is no positive peak at any temperature for this particular sample. One can also argue that the shape of the curve changes at 200K. The recovery seems to curve in the opposite sense at T $>$ 200 K

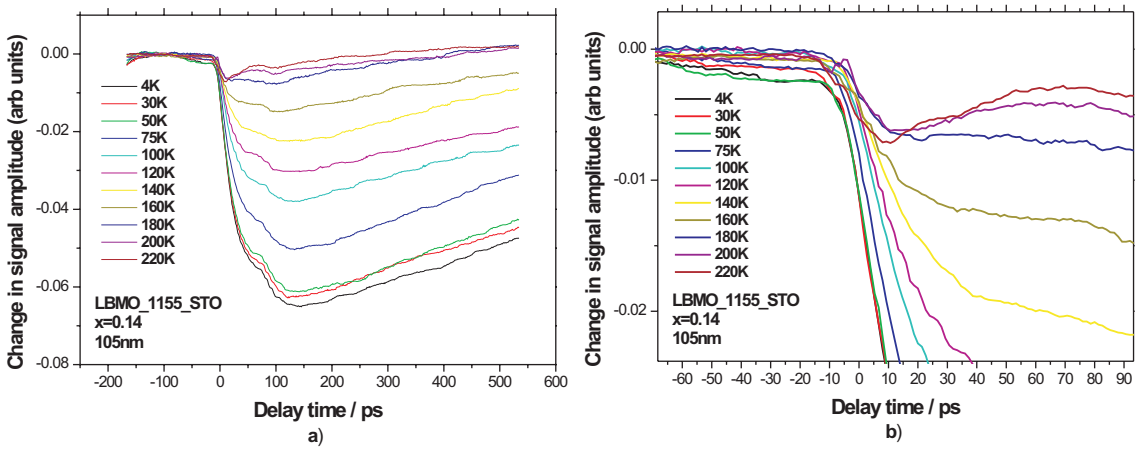

Figure B.8: Temperature dependent measurements for LBMO_1155 taken at λ=13.3 μm at FELIX for a) the complete time interval and b) a close up of the t=0 position. (Original in colour)

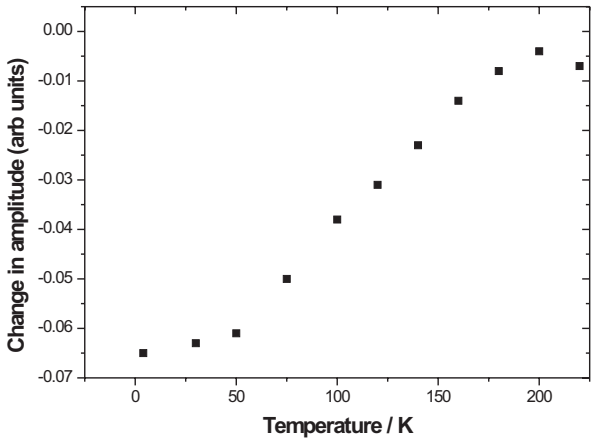

Figure B.9: Amplitude of the negative signal for LBMO_1155 at 13.3 μm

compared to T $<$ 200K. However, the shape of the curve is very similar to those observed above the Curie temperature in the $x = 0.24$ and $x = 0.3$ samples below. The CMR and MRE data for this sample (shown in Figure 6.17c) suggest a Curie temperature of 310K. However, this sample also exhibited a low-field GB magnetoresistance which was observed at all temperatures below T=240K. There is not enough experimental evidence to suggest that the onset of GB magnetoresistance changes the FELIX result, but it could be a potential explanation as to why the sample is behaving differently above and below T=240K.

We can plot the maximum negative amplitude as a function of temperature. This is shown in Figure B.9. The change in signal amplitude as the temperature is increased is clearly non-linear. The maximum negative signal is observed at the lowest temperature (4K). There is only a small change in signal amplitude up to about T=50K, and then the signal starts to decrease very rapidly. However, beyond T=200K, the signal appears to become more negative again, but this could be debated. The amplitude of the negative signal of the more conducting samples behaves differently, as we will see below.

B.3.3.2 LBMO_1191a, x=0.24

Temperature dependent measurements for LBMO_1191a taken at a wavelength of 11.7 μm can be seen in Figures B.10a and b. The sample exhibits a similar temperature dependence as was observed for the $x = 0.14$ LBMO_1155 sample. The negative signal is observed to reduce as the temperature increases and there are signs of recovery for longer delay times.

In Figure B.10b we show a close up of the $t = 0$ region for the LBMO_1191a sample. This sample has $x = 0.24$ and so should be in a ferromagnetic and metallic phase below the Curie temperature. Below T=210K, the positive peak increases in height and broadens as the temperature increases. The peak reaches its maximum height at 210K, though the peak is broader at 240K and 270K. The Curie temperature for this particular sample is not known. If we refer to Figure 2.14 then we can estimate that T_C is around 300K, but of course the Curie temperature can vary considerably between nominally identical samples and depends on the film's thickness. It has not been possible to make low temperature MRE or CMR measurements for this sample, so it is unknown whether it exhibits a GB magnetoresistance.

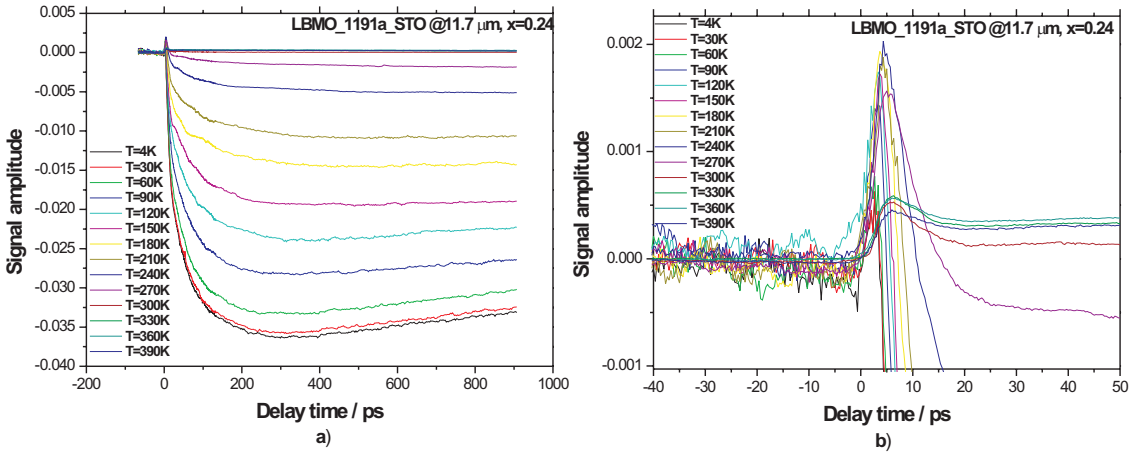

Figure B.10: Temperature dependent measurements for LBMO_1191a taken at λ=11.7 μm at FELIX for a) the complete time interval and b) a close up of the t=0 position. (Original in colour)

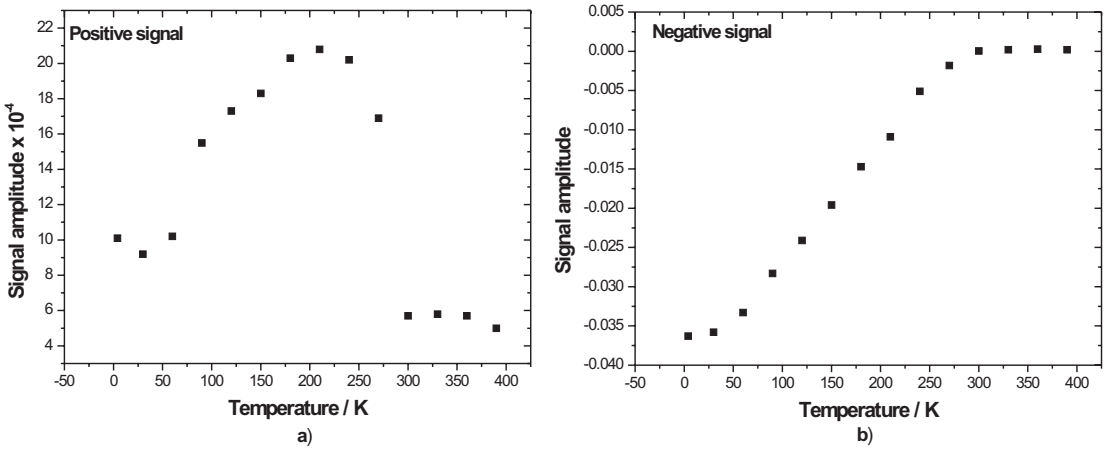

Figure B.11: Amplitude of a) the positive and b) the negative signal as a function of temperature for LBMO_1191a at 11.7 μm.

Since this sample has both a positive and a negative signal amplitude we can compare how both of these signals change with temperature. This is shown in Figures B.11a and b. The figures demonstrate that the amplitudes of the positive and the negative signal

have a very different temperature dependence. The negative signal behaves in a similar way to that observed in the $x = 0.14$ sample. The main difference between this sample and the LBMO_1155 sample is that the negative signal tends to plateau at higher temperatures. However, we see a dramatic drop in the positive signal as the temperature goes above 300K. This could be indicative of a phase change and may suggest that something significant happens when the sample reaches the Curie point.

B.3.3.3 LBMO_1154, x=0.3

Temperature dependent measurements for LBMO_1154 taken at a wavelength of 11.7 μm can be seen in Figures B.12a and b.

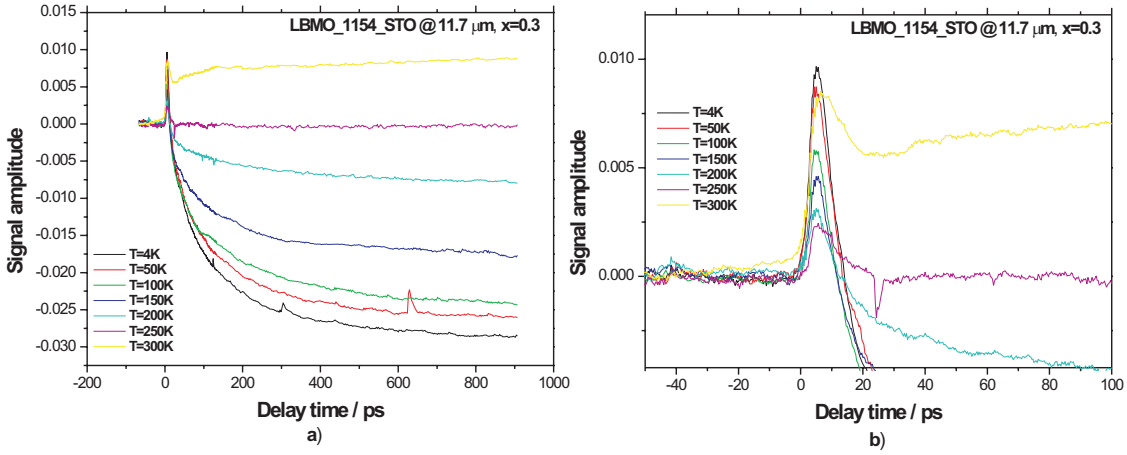

Figure B.12: Temperature dependent measurements for LBMO_1154 taken at λ=11.7 μm at FELIX for a) the complete time interval and b) a close up of the t=0 position. (Original in colour)

As seen in Figure B.12a, a positive peak was observed at all temperatures from 4 to 300K. This positive peak was then followed by followed by the negative signal. The size of the negative signal decreases with temperature as was observed for the 1155 ($x = 0.14$) and the 1191a ($x = 0.24$) samples. Between 250 K and 300 K the signal changes dramatically again. Prior to T=300K, the positive peak gets smaller as the temperature increases. However, at 300 K, the positive peak becomes comparable in magnitude to that measured at 50K. We then observe a slight dip before the signal starts to recover. The

signal is always positive at 300K, and it could be that the large positive peak observed at this temperature is due to the peak being 'dragged up' by the other parts of the curve. An alternative explanation is that polarons are involved. As was discussed in Chapter 2, we expect the free carriers to become trapped in polarons above T_C. However, if the free carriers receive enough energy from FELIX, then they can escape their traps and start to conduct by variable range hopping. This will lead to a noticeable increase in the conductivity above T_C and is, therefore, a possible explanation for the positive signal observed above the Curie temperature.

In the last chapter we discussed the results of MRE and CMR measurements made for this sample from which we estimated that the Curie temperature is approximately 280K. So it is likely that the change observed between 250K and 300K is in some way linked to the phase transition at the Curie temperature.

As for the 1155 and 1191a samples, we can plot the change in signal amplitude for the negative and positive parts of the signal as a function of temperature, as shown in Figures B.13a and b. The results for the negative signal in Figure B.13a are similar to those observed in the other samples, except at high temperatures the signal neither plateaus nor increases in amplitude.

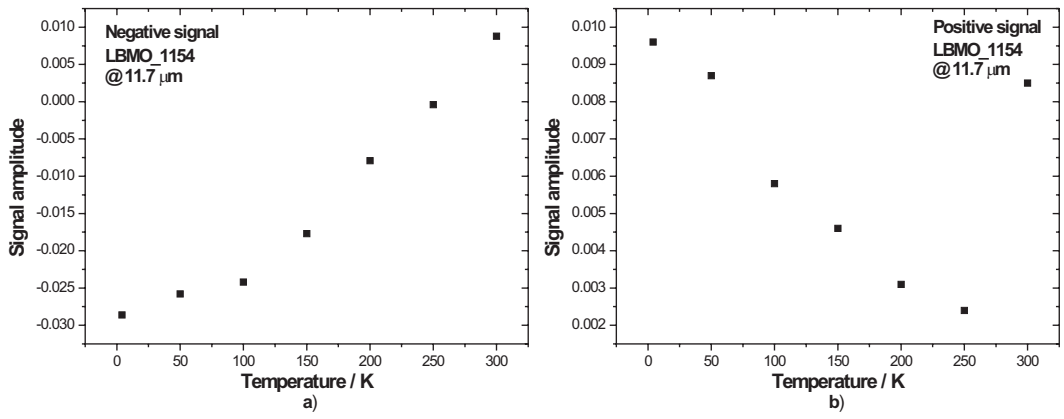

Figure B.13: Amplitude of a) the negative and b) the positive signal as a function of temperature for LBMO_1154 at 11.7 μm.

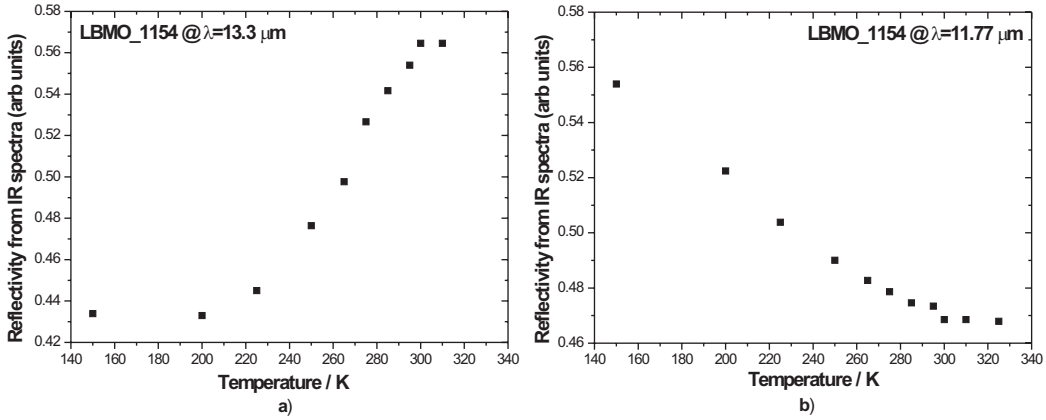

Figure B.14: Normalised IR reflectivity for LBMO_1154 at a) 13.3 μm and b) 11.7 μm as a function of temperature.

On first inspection, the results for the positive signal look rather different than those obtained in the LBMO_1191a sample since the amplitude of the positive signal is actually at a minimum near its Curie temperature rather than at its maximum value. However, a further observation can be made from the R(T) data in the IR spectra measured in the laboratory. As discussed above, the reflectivity from the sample is strongly dependent on the wavelength that the measurements were taken. This is clearly demonstrated in Figure B.14 where I have plotted the change in the equilibrium IR reflectivity with temperature at 11.7 μm and 13.3 μm for the LBMO_1154 sample. At a wavelength of 11.7 μm, the change in reflectivity with temperature has a similar profile to the positive signal in Figure B.13b, whereas at 13.3 μm the reflectivity behaves more like the results for the negative signal in Figure B.13a. In other words, if we move from one wavelength regime to another that causes R(σ) to switch sign, then R(T) will also switch sign. The wavelength that the measurements were taken at is therefore critical and can have a huge impact on the results. The results depend upon strongly on R(T): if we are in the regime where the reflectivity increases with temperature you observe the opposite response to that observed in the regime where the reflectivity decreases with temperature. In either case, we observe a saturation of the response at or near the Curie temperature. Unfortunately, no measurements were made as a function of temperature at FELIX for this sample at 13.3μm, so we cannot be sure that this predicted reversal either side of the node would have been observed experi-

mentally; futhermore we should note that the sign of the response at FELIX is the same for both LBMO_1191a and LBMO_1154 at 11.7 μm, i.e. the initial fast response is positive.

B.3.4 Field dependence

We have studied the in-plane magnetic field dependence of two samples at FELIX: LBMO_1154 and LBMO_Sheffield. The magnetic field was introduced by inserting a NdFeB magnet on either side of the sample mounting stage in the microstat. The magnetic field produced by these magnets was 0.1T. The samples were field-cooled (FC) to 4K.

These two samples are both $x = 0.3$ and were observed to have both a positive and negative component when they were zero field-cooled (ZFC). In Figure B.15, I show a comparison between the ZFC and FC results for these samples.

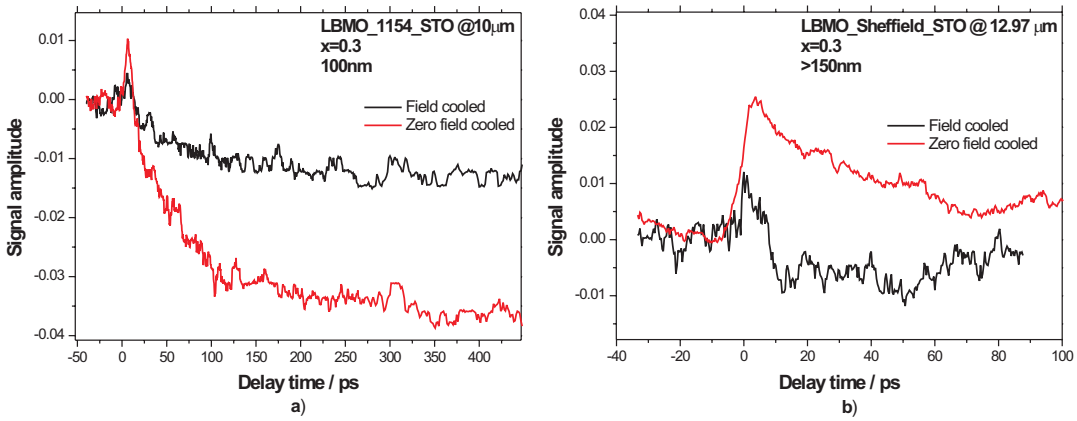

Figure B.15: Signal amplitude versus delay time at 4K for field cooled and zero field cooled samples of a) LBMO_1154 and b) LBMO_Sheffield. (Original in colour)

The field seems to suppress both the positive and the negative parts of the signal. The positive and the negative peaks are suppressed by differing amounts: the FC positive peak is approximately one-half of its ZFC value in Figure B.15a whereas the negative signal is reduced by one-third of its ZFC value. The results of the LBMO_Sheffield sample (Figure B.15b) are much noisier and it is hard to quantify the change in the negative peak.

However, the FC positive peak is again about one-half the magnitude observed in the ZFC sample.

For each sample, the measurements were repeated several times in order to ensure that the alignment had not changed when the magnets were inserted into the sample holder. We were reassured to see that the original ZFC result was repeatable once the magnets had been removed. The fact that we have observed a similar result in two different $x = 0.3$ samples also convinces us that the effect is real.

B.4 Interpreting the FELIX results

How do we interpret the results from FELIX? There are clearly several features that we need to try and explain in order to understand what is happening when we reflect the FELIX beam from the sample. These features include the power dependence of the positive and negative signals, the temperature dependence and the magnetic field dependence.

B.4.1 Understanding the positive and negative signals

A sensible starting point is to refer to the paper by Taylor *et al.* (166) to see how they explained their results in $x = 0.3$ samples of LSMO and LCMO. The results of Taylor *et al.* are shown for an LCMO sample in Figure B.4. Taylor *et al.* made their measurements at 1.5 eV ($\lambda = 825nm$) and from their optical pump-probe measurements, they suggest that the dynamics reveal two components: an ultrafast (< 1 ps) component and a much slower component (>20-200 ps). Our measurements have a similar profile to the results obtained by Taylor *et al.*, but the positive peak is occurring on a much longer timescale than they observed. However, we are operating in a different energy regime (0.1 eV compared to their 1.5 eV), so this difference in timescales could perhaps be attributed to this energy difference.

Based upon the results of Taylor *et al.* and our own observations, we have developed a very simple model of what we think is happening at FELIX:

When a micropulse hits the sample, it excites the free carriers in the sample, producing

hot electrons that are not in thermal equilibrium with their surroundings. However, it is assumed that the spin of these hot electrons will be conserved. This will lead to an increase in the 'conductivity' due to the availability of free carriers. The positive rise in signal amplitude is associated with the increased 'conductivity' provided by these hot, non-equilibrium electrons. This 'positive' signal can be represented by a function of the form:

$$P(t) = +A_P(1 - e^{-\beta t}) \tag{B.3}$$

Having been given energy by FELIX, the hot electrons will seek ways to come into thermal equilibrium with their surroundings, i.e. the system will relax. The first means the electrons will find to lose energy will be to emit phonons (in a scattering process that will thus lower their energy). These hot phonons will in turn start to heat up the lattice. Once the lattice begins to heat up, it will slowly start to heat up the core electrons' spins. This process will tend to disorder the spins and, hence, will lead to a drop in the conductivity of the sample since the spins are required to be aligned in order to facilitate double exchange. These relaxation processes give us the 'negative' signal we observe at FELIX, and can be represented by a function of the form [1]:

$$N(t) = -A_N(1 - e^{-\alpha t}) \tag{B.4}$$

These two 'fast' and 'slow' processes, the ultrafast heating of the electrons followed by the slower relaxation processes, combine together so that we observe a positive rise followed by a negative decay. This combination will produce a peak, followed by a negative signal, to give us the characteristic profile as a function of time (f(t)) that we observe at FELIX. This can be represented by a function of the form:

$$f(t) = P(t) + N(t) = +A_P(1 - e^{-\beta t}) - A_N(1 - e^{-\alpha t}) \tag{B.5}$$

where it is assumed that $A_P < A_N$ and that $\alpha << \beta$. This model was first proposed by Professor Gehring (167) in order to explain why we observe a 'positive peak' in the FELIX

[1] There is likely to be more than one 'time' in equation B.4, corresponding to different relaxation processes, but using a single 't' in the equation simplifies the expression.

data at some finite time, t and in Figure B.16, I show the results of plotting f(t) in equation B.5 for A_P=1, A_N=2, α=0.03 and β=0.3: (see Appendix A.4)

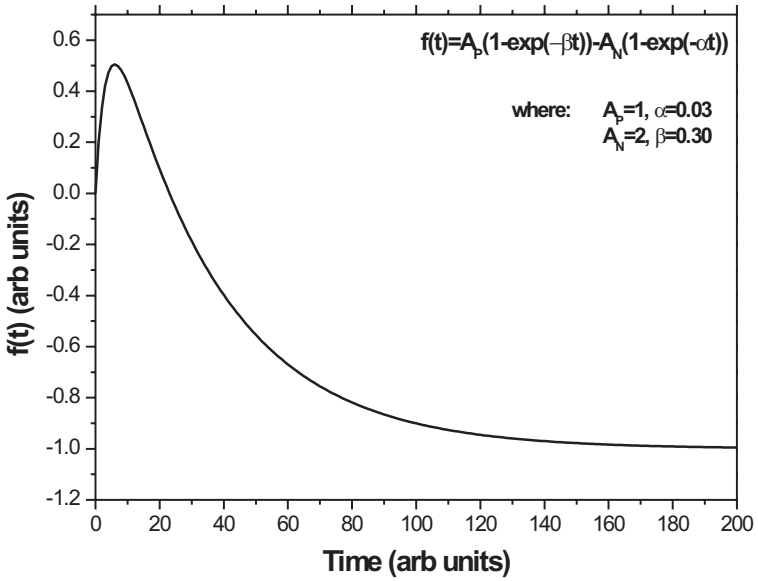

Figure B.16: Modelled profile for f(t) versus time using the parameters: A_P=1, A_N=2, α=0.03 and β=0.3.

The shape of f(t) in Figure B.16 is the same as we have observed experimentally for our LBMO, $x = 0.3$ samples and gives a clear indication that the position of the 'positive peak' is determined by the way that these 'fast' and 'slow' processes combine. Interestingly, if we allow the time axis to have the units ps, the time constant for the negative signal is approximately 34 ps, which is in good agreement with that observed experimentally for a sample with a positive peak occurring at 10ps.

The 'positive peak' occurs when the relaxation processes start to dominate. The size of the positive peak has been shown to be both power and doping dependent. Clearly, if the initial energy input from FELIX is reduced, the hot electrons will not be heated so much, and hence the effect will be reduced. Similarly, if a sample has fewer free carriers to begin with, then the heating from FELIX will have less effect and the initial rise in 'conductivity' will be diminished.

B.4.2 Understanding the temperature dependence

In this section I will try to explain the temperature dependence of the samples at FELIX. Let us start by considering the 'negative' signal, which is representative of the sample reaching thermal equilibrium. Experimental observations show that between 4 and 50K there is very little change in the amplitude of the 'negative' signal (see Figures B.9, B.11b and B.13a). Beyond 50K the signal amplitude drops steadily until it either plateaus or increases again near the Curie temperature.

We know that FELIX is heating the sample, but the obvious question is by how much? We can make a very rough estimation of the equilibrium temperature the sample reaches based upon what we know about the power output of FELIX, the diameter of the spot-size of the beam and estimations of the specific heat capacity of the sample.

The specific heat capacity (C) of a manganite can be treated in a similar way to that of a normal metal (68), as given by the expression:

$$C = \gamma T + \beta T^3 + \text{Magnetic terms} \tag{B.6}$$

Coey *et al.* (68) have measured γ for an LBMO ($x = 0.3$) sample and report a value of 6.1mJmol^{-1}K^{-2}. The value of β is related to the Debye temperature (θ_D) such that (68):

$$\theta_D = \left(\frac{n \times 1944}{\beta}\right)^{1/3} \tag{B.7}$$

where n is the number of atoms per unit cell. For an $x = 0.3$ LBMO sample, Coey *et al.* have reported a Debye temperature of 333K which gives β a value of 2.6×10^{-4}Jmol^{-1}K^{-3}.

In order to proceed we need to know how many moles of material are contained in the heated volume. However, the γ and β require slightly different treatments; the γ term requires us to know how many complete molecules we have in the heated volume (since this term is related electronic contribution), whereas the β term requires us to know how many atoms we have per unit cell (since this term is related to the structure of the lattice). This means that the number of moles is different for γ and β.

The beam from FELIX forms a circular spot on the sample with a diameter of 450 μm. The volume of thin film that is heated is 1.6×10^{-14}m^3. The volume of a unit cell is a_0^3, where a_0 = 0.3885 nm (68). This means that the volume of the film contains 2.73×10^{14} unit cells. For the γ term we assume that each unit cell contains one complete molecule. The β term assumes we have 5 atoms per unit cell (if we refer to the cubic perovskite structure shown in Figure 2.1, we observe that each unit cell has $1/8^{th}$ of an atom from the 8 La/Ba corner atoms, 1/2 of an atom from the 6 O atoms on the cube's faces and 1 atom from the Mn atom, making 5 in total).

We can now calculate γ* and β* where γ*=$\gamma\times$ the number of moles (molecular) and β*=$\beta\times$ the number of moles (atomic). The final temperature, T_2, the sample reaches when it is hit by a micropulse from FELIX when it has an initial temperature, T_1, can then be calculated by solving the following equation:

$$\Delta Q = \int_{T_1}^{T_2} \gamma^* T + \beta^* T^3 \mathrm{d}T \tag{B.8}$$

To proceed, we need to obtain a value for ΔQ. The unattenuated power of FELIX varies, but is generally around 1 mJ per macropulse. Each micropulse lasts approximately 1ps and is separated from the next micropulse by about 20ns, meaning that each macropulse actually contains approximately 300 micropulses, each with an energy of about 3.3 μJ. The depth of penetration of the beam into the sample will be governed by the skin depth. In chapter 6, we calculated the skin depth to be of the order of 900 nm for LBMO samples with an $x = 0.3$ composition, giving a substrate to film ratio of 9:1, meaning that FELIX will go completely through the thin film layer and into the substrate. Hence, we will assume that the thin film layer absorbs approximately $1/10^{th}$ of the energy from each micropulse, thus giving us ΔQ = 0.33 μJ. It should also be noted that this is the minimum energy that the thin film layer can absorb. In the more conducting samples, the thin film layer is likely to absorb more of the incident energy from FELIX up to the maximum value of 3.3 μJ. Also, the absorption is exponential making it likely that the thin film layer will absorb more energy than we have assumed here.

The solution to equation B.8 can be found using an iterative process. In Figure B.17a, I show the change in temperature (T_2-T_1) as a function of initial temperature, T_1. At low temperatures, the energy from FELIX increases the sample temperature substantially.

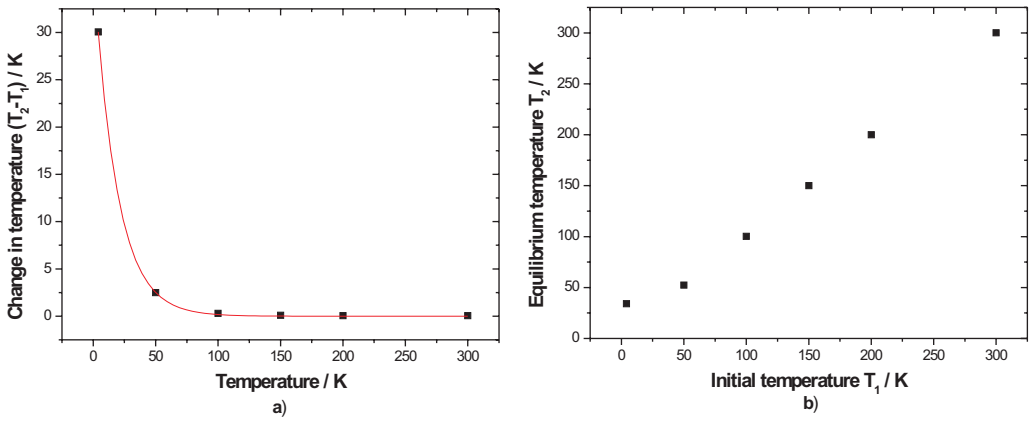

Figure B.17: The change in sample temperature induced by the FELIX micropulse. The plot assumes that ΔQ in equation B.8 is around 2 μJ per micropulse as discussed in the main text.

However, as the initial temperature of the sample increases, the energy from FELIX is a smaller contribution to the overall energy of the system. At 4K FELIX heats the sample by approximately 30K and at 50K, FELIX heats the sample by about 2.5K. This is clearly demonstrated by Figure B.17b, where I have plotted the final, equilibrium temperature T_2 versus the initial temperature, T_1. If the thin film layer actually absorbs more of the energy from the macropulse than was assumed here, then the final equilibrium temperature will obviously be higher, particularly for T_1=4K, than is shown in the figure, and this will tend to flatten the curve in Figure B.17b between 4K and 50K.

An important observation is that at temperatures below 50K, we are in a region where we do have a finite change in temperature when the sample is hit by FELIX. This means that over this temperature range you will also have a finite change in the reflectivity which will give us the signal we observe at FELIX. The system will finally come into thermal equilibrium as the phonons heat up the lattice, which in turn causes spin disorder and reduces the conductivity. The larger the spin disorder, the larger the 'negative' signal.

The disorder is caused by the flipping of the electron spins. There are typically two ways that the spins can flip: firstly, the spins can flip due to spin-orbit coupling (though this is weak in these materials (167)) and secondly, the hot electrons have sufficient energy

to move from a domain with a particular alignment to a domain with a different alignment. These hot electrons can cause flipping as they cross from one domain to another because the hot electrons are strongly coupled to the spin of the manganese core spins of the new domain by the large Hund's exchange energy. The result of the hot electrons travelling to other domains is that the net magnetisation will fall, and as a result the conductivity of the sample will also be reduced, since the maximum conductivity is achieved when all the spins are perfectly aligned. Hence, the initial phonon scattering process can cause disorder which will tend to lower the conductivity. This means that there is an additional process by which the conductivity can be lowered, so although the temperature change induced by FELIX may not be very large above T=50K, perhaps the induced spin disorder is large enough to give us the observed drop in conductivity we observe experimentally as the sample is heated.

This interpretation of the heating at FELIX explains the low temperature effects very well. Of course, as the sample is heated by the microstat, the contribution from FELIX becomes negligible compared to the sample's internal energy due to its temperature. The function that fits the data points in Figure B.17a is an exponential decay, and this reflects the fact that FELIX heats the sample by a considerably lesser amount as the sample's temperature increases. However, a byproduct of the exponential decay is that there is still a small change in a sample's temperature even at 300K, and this could be detectable by the pump-probe measurements.

Of course, this simple model has assumed that equation B.8 is valid at all temperatures. However, this will not be true in reality since the specific heat capacity will change considerably as we approach the Curie temperature. Indeed, we can understand the plateau observed experimentally near T_C in terms of the magnetic phase transition. Any excess energy from FELIX near T_C will be used to change the phase of the sample rather than increase its temperature.

It could also be that we are severely underestimating the energy input from FELIX. The energy from FELIX was calculated per micropulse under the assumption that the heat will have dissipated by the time the next micropulse hits the sample. This may not be true, and we may see an accumulation of energy from several micropulses exciting the hot electrons. We did occasionally see sparking from samples that had been exposed

to the unattenuated beam for extended periods, showing that something serious must be happening within the sample. These sample never really recovered from such exposure and often their properties had changed as a result. For example, repeat MRE measurements on the LBMO_Sheffield sample, after the trip to FELIX, showed a much reduced MRE(%), indicating a degradation in sample quality.

The temperature dependence of the 'positive peak' is related to the relaxation processes. We expect that the electrons are in thermal non-equilibrium with their surroundings and that they will rapidly achieve thermal equilibrium through the relaxation processes identified above. This means that the 'positive peak' is controlled by the negative 'decay'. As discussed above, near the Curie temperature, a large proportion of the energy absorbed by the sample will be used to change its magnetic phase. This will also provide an additional means for the sample to relax, and therefore we would expect that the relaxation processes will dominate, causing the 'positive peak' to rapidly drop in amplitude. This type of behaviour is evident in Figures B.11a and B.13b near T_C.

Another interesting observation is that the 'positive' and 'negative' signals can behave differently depending upon sample composition. For example, in the $x = 0.24$ sample the 'positive' signal remains fairly constant over a range of temperatures and it is only really the 'negative' signal that varies as a function of temperature. On the other hand, for the $x = 0.3$ sample the 'positive' and 'negative' signals both change as a function of temperature and it is likely that this different temperature dependence is related to the different levels of doping in the two samples.

B.4.3 Understanding the magnetic field dependence

In Figure B.15 we saw that field cooling the $x = 0.3$ samples in a 0.1T field caused both the positive and the negative signal to be suppressed. In the context of our model, however, we propose that the positive signal is associated with the ultrafast, sharp rise in 'conductivity' that occurs when the micropulse hits the sample and creates hot electrons that are in thermal non-equilibrium with their surroundings, and the negative signal is associated with the relaxation of these hot electrons as they come into thermal equilibrium with the lattice and the core spins.

Let us first consider the suppression of the relaxation processes. a possible explanation for the suppression is based on magnetic domains. If we consider that the spot-size of FELIX on the sample has a typical diameter of 450 μm, whereas the typical domain size (as discussed in Chapter 2) is 10 μm, then this means that the beam will encompass many magnetic domains.

The magnetic field introduced by placing the NdFeB magnets on either side of the sample mounting stage is relatively small. It is thought that the only effect such a small field can have is to remove the domain walls from the sample, so that in effect we have a single domain. The argument here is that if we have a single domain, then the hot electrons will no longer flip spins as they change domains and we effectively lose a mechanism by which disorder is introduced. Although the hot electrons still relax, they do not cause as much spin disorder and hence the FELIX response goes less 'negative'.

However, this theory does not explain why we also see a reduction in 'conductivity' when the magnetic field is applied. The Taylor view is that when the hot electrons scatter off the phonons, their spin is conserved due to the weak spin-orbit coupling. Yes, the spin has a chance to flip when the electron is scattered, but the chance of it doing so is very small indeed. If this view is correct, then the 'conductivity' should be independent of the applied field. However, this is not what we observe experimentally, since we see that both P(t) and N(t) are smaller when the field is applied, though we cannot tell if it is P(t) or N(t) that is changing. Our experimental results indicate that, contrary to the Taylor view, either the excitation or the relaxation processes are field or magnetisation dependent. If the excitation process is spin dependent, this would mean that the hot electrons are also generating spin disorder via an electron-spin interaction indicating that it is not just phonons that are heating up the lattice, but also that spin waves could play a significant role in these materials.

B.5 Conclusions

In this chapter I have presented the results of pump-probe experiments carried out at FELIX on samples of LBMO with $x = 0.14$, 0.24 and 0.3 in a reflection geometry. It was concluded that the power dependence of the signal could be understood in terms of the

doping of the sample, and that the fast rise in signal amplitude, that we have associated with an increase in 'conductivity' due to the presence of hot, non-equilibrium electrons, was only observed in samples with a sufficiently high number of free carriers. The slow decay, observed in all samples, is thought to be assisted by spin-disorder caused by hot electrons traversing between domains and flipping their spin, thus reducing the conductivity of the sample. Both the fast rise and the slow decay have been modelled using a simple sum of two exponentials with differing time constants. Such a simple model has also demonstrated that the position of the 'positive peak' is related to the way these exponentials combine, and that the 'peak' represents the time, which is always a finite time after t=0, when the relaxation processes start to dominate.

The wavelength dependence of the FELIX data has been explained in terms of how the reflectivity changes with both conductivity and wavelength (R(σ, λ)). The IR spectra have shown that the conductivity is wavelength dependent and that there are several nodes, either side of which R(σ) can change sign. If we are at a wavelength where the conductivity increase as the temperature increases, then we will observe a positive signal at FELIX. Conversely, if we are at a wavelength where the conductivity decreases as the temperature increases, then we will observe a negative signal. This change in the reflectivity as a function of wavelength explains why the signal from FELIX is observed to reverse at particular wavelengths.

The temperature dependence of the FELIX data has been explained for the 'negative' signal, where the sample is coming into thermal equilibrium due to relaxation processes, in terms of both the heating of the sample by the incident beam and increased spin disorder. A crude model based upon the energy input from FELIX and an estimation of the specific heat capacity of the sample can successfully explain the shape of the 'negative' signal observed experimentally as a function of temperature. The amplitude of the 'positive' signal is controlled by the relaxation processes that occur after the sample has been heated. At certain temperatures the increase in 'conductivity' induced by FELIX is dominant, but as the sample approaches the Curie temperature, the phase change provides an additional means for the system to relax, reducing the amplitude of the 'positive peak' as the relaxation processes begin to dominate. The relaxation processes can be fitted with an exponential decay and typically have a time constant of 20–30 ps.

The magnetic field dependence of the relaxation processes has been discussed in terms of magnetic domains. The small field removes any domain walls in the sample and removes a mechanism for spin-disorder in the sample and reduces the amplitude of the 'negative' signal. The reduction in amplitude of the 'positive' signal has not been explained, but it has been shown to be spin dependent, which is contrary to observations by Taylor *et al.* (166).

Future studies of these materials at FELIX should incorporate a variable magnetic field in the experimental setup. It is necessary to be able to vary the field and observe the changes in the signal amplitude as a function of field rather than relying on FC data. Applying a magnetic field and then cooling the sample may produce different results to cooling the sample and then applying the field, and this needs to be investigated. Field dependent measurements as a function of temperature should also be made.

It would also be interesting to study different series of manganite samples, e.g. LCMO and LSMO, and compare the results to those obtained for LBMO. LCMO and LSMO have different properties to LBMO, in particular regarding their bandwidth for conduction by double exchange and also they have different skin depths. LCMO has a lower conductivity than LBMO and LSMO, so it would be interesting to see if we observe the same features at FELIX, or whether the composition changes the observed effects.

Definitions

$\mathbf{a}_0$	Lattice parameter
A	Attenuation; trivalent rare earth cation
AFM	Antiferromagnetic
B	Divalent alkaline earth cation
C	Specific heat capacity
CMR	Colossal Magnetoresistance
CMR(%)	Percentage change in the CMR
CNI	Spin-canted insulator
CVD	Chemical Vapour Deposition
DE	Double Exchange
DW	Domain Wall
$\mathbf{e}_g$	High energy $3d$ orbital
FC	Field cooled
FELIX	Free Electron Laser for Infrared eXperiments
FI	Ferromagnetic and insulating
FM	Ferromagnetic and metallic
FTIR	Fourier Transform Infrared

GB Grain boundary

H Applied magnetic field

IR Infrared

J Intergrain exchange constant

$\mathbf{J}_H$ Intra-atomic Hund rule exchange

k Wavenumber of incident radiation (cm^{-1})

$\mathbf{k}_j$ Wavenumber of the j^{th} resonance

$\mathbf{k}_{Lj}$ Wavenumber of the j^{th} longitudinal optical phonon mode

$\mathbf{k}_{Tj}$ Wavenumber of the j^{th} tranverse optical phonon mode

KRS-5 Brand name for the chemical Thallium Bromo-Iodide TlBr-TlI, crystals of which are used for windows and polarizers in the infrared optical range.

LAO $LaAlO_3$

LBMO $La_{1-x}Ba_xMnO_3$

LCMO $La_{1-x}Ba_xMnO_3$

LO Longitudinal optical phonon mode

LSMO $La_{1-x}Sr_xMnO_3$

m Field dependent term (with values $0 < m < 1$) which gives a measure of the magnetization of the sample.

$\mathbf{m}_e^*$ Effective mass of the electrons

M Magnetisation

$\mathbf{M}_S$ Magnetisation at saturation

MCT Mercury-Cadmium-Telluride (HgCdTe) detector

MMRS Micro-miniature Refridgeration System

MR	Magnetoresistance
MRE	Magnetorefractive Effect
MRE(%)	Percentage change in the MRE
N	Number of free carriers per unit volume
N(t)	Negative exponential function used to model the relaxation processes observed at FELIX
NGO	$NdGaO_3$
P	Electron polarization
P(t)	Positive exponential function used to model the increase in conductivity observed at FELIX
$\mathbf{P}_d$	Power detected
$\mathbf{P}_s$	Power of the source
PI	Paramagnetic and insulating
PLD	Pulsed Laser Deposition
PM	Paramagnetic and metallic
$\mathbf{r}_A$	Radius of the trivalent rare earth cation
$\mathbf{r}_O$	Radius of the oxygen ion
$\mathbf{r}_{Mn}$	Radius of the manganese ion
R	Reflectivity
Δ**R**	Change in the reflectivity
$\mathbf{R}_0$	Reflectivity in zero field
$\mathbf{R}_H$	Reflectivity in an applied field, H
$\mathbf{r}_{P0}$	Reflection co-efficient for p-polarized light in zero field

$\mathbf{r}_{S0}$	Reflection co-efficient for s-polarized light in zero field
$\mathbf{r}_{P}$	Reflection co-efficient for p-polarized light in an applied field
$\mathbf{r}_{S}$	Reflection co-efficient for s-polarized light in an applied field
$\mathbf{R}_{P0}$	Reflectivity for for p-polarized light in zero field
$\mathbf{R}_{S0}$	Reflectivity for for s-polarized light in zero field
$\mathbf{R}_{P}$	Reflectivity for for p-polarized light in an applied field
$\mathbf{R}_{S}$	Reflectivity for for s-polarized light in an applied field
$\mathbf{S}_1$	Infrared spectra measured in zero field
$\mathbf{S}_2$	Infrared spectra measured in an applied field
$\mathbf{S}_3$	Infrared spectra measured in zero field
$\mathbf{S}_j$	Oscillator strength of the jth phonon mode
SE	Secondary electrons
SEM	Scanning Electron Microscope
SG	Sol-Gel: a preparation method for making bulk LSMO samples
SSR	Solid State Reaction: an alternative preparation method for making bulk LSMO samples
STO	$SrTiO_3$
t	time; thickness; hopping amplitude
T	Temperature
$\mathbf{T}_C$	Curie temperature
$\mathbf{T}_{M-I}$	Metal-Insulator transition temperature
$\mathbf{T}_N$	Néel temperature
TO	Tranverse optical phonon mode

VRH	Variable Range Hopping
VSM	Vibrating Sample Magnetometer
ZFC	Zero Field Cooled
γ	Damping term for the free carriers
γ_j	Damping term for the jth harmonic oscillator
γ_{Lj}	Damping term for the jth LO mode
γ_{Tj}	Damping term for the jth TO mode
ε_0	The permittivity of free space
$\varepsilon(\omega)$	Complex dielectric function
$\varepsilon_{Drude}(\omega)$	Drude-like term in the complex dielectric function
ε_∞	High frequency term in the complex dielectric function
$\varepsilon_{film\infty}$	High frequency term in thin film's complex dielectric function
$\varepsilon_{sub\infty}$	High frequency term in substrate's complex dielectric function
$\varepsilon_{film0}(\omega)$	Complex dielectric function of the thin film in zero field
$\varepsilon_{film}(\omega)$	Complex dielectric function of the thin film in an applied field
ε_{sub}	Complex dielectric function of the substrate
$\varepsilon_{total0}(\omega)$	Complex dielectric function of the film/substrate system in zero field
$\varepsilon_{total}(\omega)$	Complex dielectric function of the film/substrate system in an applied field
η	Scaling term for the magnetisation
θ	Angle of incidence of the IR light
θ_D	Debye temperature
ξ	Ferromagnetic correlation length

ρ	Resistivity
$\Delta\rho$	Change in the resistivity
$\sigma(\omega)$	Conductivity
σ^*	Antibond between s and p orbitals i.e. the two orbitals overlap but the bonding between them is such that their electron densities tend to repel one another.
ϕ	Angle between the Mn-O bonds
ω	Angular frequency of the incident radiation
ω_L	Angular frequency of the LO mode
ω_P	Plasma frequency
ω_T	Angular frequency of the TO mode
Γ	Tolerance factor

Bibliography

[1] Coey J. M. D., Viret M. and Von Molnár S., *Advances in Physics*, **48**, 167–293, (1999).

[2] Jonker G., and van Santen J., *Physica*, **16**, 337, (1950).

[3] Jonker G., and van Santen J., *Physica*, **16**, 599, (1950).

[4] Jonker G., *Physica*, **22**, 707, (1956).

[5] Jonker G., and van Santen J., *Physica*, **19**, 120, (1953).

[6] Volger J., *Physica*, **20**, 49, (1954).

[7] Wollan E. O., and Koehler W. C., *Phys. Rev.*, **100**, 545, (1955).

[8] Zener C., *Phys. Rev.*, **81**, 440, (1951).

[9] Zener C., *Phys. Rev.*, **82**, 403, (1951).

[10] Anderson P. W., Hasegawa, H., *Phys. Rev.*, **100**, 675, (1955).

[11] Kusters R.M., Singleton J., Keon D.A., Greedy R.M., Hayes W., *Physica B*, **155**, 362, (1989).

[12] von Helmholt R. *et al.*, *Phys. Rev. Lett.*, **71**, 2331, (1993).

[13] Chahara K. *et al.*, *Appl. Phys. Lett.*, **63**, (1990).

[14] Ju H.L., Kwon C., Li Q., Greene R.L., Venkatesan T., *Appl. Phys. Lett.*, **65**, 2108, (1994).

[15] Jin S. *et al.*, *Science*, **264**, 413, (1994).

[16] Edwards D. M., *Advances in Physics*, **51**, 1259–1318, (2002).

[17] T. Venkatesan T., M. Rajeswari M., Dong Z.-W., Ogale S.B., Ramesh R., *Phil. Trans. R. Soc. Lond. A*, **356**, 1661, (1998).

[18] Jacquet J. C. and Valet T., in *Magnetic Ultrathin Films, Multilayets and Surfaces*, edited by E. Marinero (Materials Research Society, Pittsburgh, 1995).

[19] Granovsky, A. B., *et al., Phys. Sol. State*, **45**, 911, (2003).

[20] Granovsky, A. B., Bykov I.V., Gánshina E.A., Gushchin V.S., Inoue M., Kalinin Yu. E., Kozlov A.A., Yurasov A.N., *JETP*, **96**, 1104, (2003).

[21] Bykov I., *et al., Phys. Sol. State*, **42**, 498, (2000).

[22] Bozec D. *et al., J. Appl. Phys.*, **91**, 8795, (2002).

[23] Gervais, F., *Mat, Sci. Eng.*, **R 39**, 29, (2002).

[24] Boris A.V., Kovaleva N.N., Bazhenov A.V., Samoilov A.V., Yeh N.C., Vasquez R.P., *J. Appl. Phys*, **81**(8), 5756, (1997).

[25] Okimoto Y. , *et al., Phys. Rev. Lett.*, **75**, 109, (1995).

[26] Kim K. H., *et al., Phys. Rev. Lett.*, **77**, 1877, (1996).

[27] Kim K.H., Gu J.Y., Choi H.S., Eom D.J., Jung J.H., Noh T.W., *Phys. Rev. B*, **55**, 4023, (1997).

[28] Okimoto Y., Katsufuji T., Ishikawa T., Arima T., Tokura Y., *Phys. Rev. B*, **55**, 4206, (1997).

[29] Lin K., Cheng R., Wang S., Zhang Y., *J. Phys. Cond. Matt.*, **10**, 4315, (1998).

[30] Kim K. H., *et al., Phys. Rev. Lett.*, **81**, 1517, (1998).

[31] Quijada M., Cerne J., Simpson J.R., Drew H.D., Ahn K.H., Millis A.J., *Phys. Rev. B*, **58**, 16093, (1998).

[32] Jung J.H., Kim K.H., Noh T.W., Choi E.J., Jaejun Yu, *Phys. Rev. B*, **57**, R11043, (1998).

[33] Yoon S., Liu H.L., Schollerer G., Cooper S.L., Han P.D., Payne D.A., Cheong S.-W., Fisk Z., *Phys. Rev. B*, **58**, 2795, (1998).

[34] Machinda A., Moritomo Y., Nakamura A., *Phys. Rev. B*, **58**, R4281, (1998).

[35] Simpson J.R., Drew H.D., Smolyanionova V.N., Greene R.L., Robson M.C., Biswas A., Rajeswari M., *Phys. Rev. B*, **60**, R16263, (1999).

[36] Jung J.H., Kim K.H., Lee H.J., Ahn J.S., Hur N.J., Noh T.W., Kim M.S., Park J.-G., *Phys. Rev. B*, **59**, 3793, (1999).

[37] Saitoh E., Okimoto Y., Tomioka Y., Katsufuji T., Tokura Y., *Phys. Rev. B*, **60**, 10362, (1999).

[38] Ishikawa T., Ookura K., Tokura Y.: *Phys. Rev. B*, **59**, 8367, (1999).

[39] Jung J.H., Lee H.J., Noh T.W., Moritomo Y., *J. Phys. Cond. Mat.*, **12**, 9799, (2000).

[40] Congeduti A., Postorino P., Dore P., Nucara A., Lupi S., Mercone S., Calvani P., Moro A., Kumar A. and Sarma D.D., *Phys. Rev. B*, **63**, 184410, (2001).

[41] Kim K.H., Lee S., Noh T.W., Cheong S.-W., *Phys. Rev. Lett.*, **88**, 167204, (2002).

[42] Nucara A., Perucchi A., Calvani P., Aselage T., Emin D., *Phys. Rev. B*, **68**, 174432, (2003).

[43] Hartinger Ch., Mayr F., Loidl A., Kopp T., *Phys. Rev. B*, **70**, 134415, (2004).

[44] Loshkareva N.N., Sukhorokov Yu.P., Gizhevskii B.A., *Phys. Stat. Sol. A*, **164**, 863, (1997).

[45] Boris A.V., Koraleva N.N., Bazhenov A.V., van Bentum P.J.M., Rasing Th., Cheong S.W., Samoilov A.V., Yeh N.C., *Phys. Rev. B*, **59**, R697, (1999).

[46] Sukhorokov Yu.P., Gáshina E.A., Belevtsev B.I., Loshkareva N.N.,Vinogradov A.N., Rathnayaka K.D.D., Parasiris A., Naugle D.G., *J. Appl. Phys.*, **91**, 4403, (2002).

[47] Marques R. F. C., Abernethy P. R.,*et al.*, *Journal of Magnetism and Magnetic Materials*, **272–276**, 1740–1741, (2004).

[48] Kravets V. G. *et al.*, *Phys. Rev. B*, **65**, 054415, (2002).

[49] Dagotto E. *et al.*, *Physics Reports*, **344**, 1–153, (2001).

[50] Gerloch M. , Slade R. C., *Ligand Field Parameters*, Cambridge, London, (1973).

[51] Yoshido K. , *Theory of Magnetism*, Springer, Berlin, (1998).

[52] Dagotto E., *Nanoscale Phase Separation and Colossal Magnetoresistance*, Springer, Berlin, (2003).

[53] Tokura Y., *et al., J. Phys. Soc. Japan*, **63**, 3931, (1994).

[54] Urushibara A., *et al., Phys. Rev. B*, **51**, 14103, (1995).

[55] Moreo A. , *et al., Science*, **283**, 2034, (1999).

[56] Nagaev E. L., *Phys. Uspekhi*, **39**, 781, (1996).

[57] Asamitsu A. , *et al., Nature*, **373**, 407, (1995).

[58] Campbell A. J., *et al., Phys. Rev. B*, **55**, R8622, (1997).

[59] Kubo K., Ohata N., *J. Phys. Soc. Japan*, **33**, 21, (1972).

[60] Shannon R.D. and Prewitt C.T., *Acta Cryst.*, **A32**, 785, (1976).

[61] Hwang H.Y., Cheong S.W., Radaelli P.G, Marezio M. and Batlogg B., *Phys. Rev. Lett.*, **75**, 914, (1995).

[62] Rodriguez-Martinez L.M, and Attfield J.P., *Phys. Rev. B*, **54**, R15622, (1996) and *Phys. Rev. B*, **58**, 2426, (1998).

[63] García-Muñoz J. L., *et al., J. Phys.: Condens. Matter*, **8**, L787–L793, (1996).

[64] Radaelli P. G., *et al., Phys. Rev. B*, **54**, 8992, (1996).

[65] Millis A. J., Littlewood P. B. and Shraiman B. I., *Phys. Rev. Lett.*, **74**, 5144, (1995).

[66] Jonker G. H., *Physica*, **20**, 1118, (1954).

[67] Young Sun, Xiaojun Xu and Yuheng Zhang, *J. Pys.: Condns. Matter*, **12**, 10475–10480, (2000).

[68] Coey J. M. D.,*et al., Phys. Rev. Lett.*, **75**, 3910, (1995).

[69] Louca D., *et al., Phys. Rev B*, **56**, R8475, (1997).

[70] Billinge S. J. L., *et al., Phys. Rev. Lett.*, **77**, 715, (1996).

[71] Tyson, T. A., *et al., Phys. Rev B*, **53**, 13985, (1996).

[72] Kaplan S. G., *et al., Phys. Rev. Lett.*, **77**, 2081, (1996).

[73] de Gennes P. G., *Physical Review*, **118**, 141, (1960).

[74] Koller W., *et al., Phys. Rev. B*, **67**, 174418, (2003).

[75] Honsuk Yi *et al.,, Phys. Rev. B*, **61**, 9501, (2000).

[76] De Teresa J. M., *et al., Nature*, **386**, 255, (1997).

[77] Varma C. P., *Phys. Rev. B*, **54**, 7328, (1996).

[78] Zhao G. *et al., Nature*, **381**, 676, (1996).

[79] Viret M., *et al., Europhys. Lett.*, **42**, 301, (1998).

[80] Radaelli, P. G., *et al., Physica B*, **241-243**, 295, (1998).

[81] Lynn J. W., *et al., Phys. Rev. Lett.*, **76**, 4046, (1996).

[82] Viret M., *et al., Phys. Rev. B*, **55**, 8067, (1997).

[83] Raquet B, Anane A, Wirth S, Xiong P and von Molnar S, *Phys. Rev. Lett.*, **84**, 4485 (2000).

[84] Fäth M, Freisem S, Menovsky A A, Tomioka Y, Aarts J and Mydosh J A, *Science*, **285**, 1540 (1999).

[85] Miller H and Biswaz A, http://www.phys.ufl.edu/REU/2003/reports/miller.pdf (2003).

[86] de Andrés A, García-Hernández M, Martínez J L, and Prieto C, *Appl. Phys. Lett.*, **74**, 3884 (1999).

[87] de Andrés A, Taboada S, Colino J M, Ramírez R, García-Hernández M, Martínez J L, *Appl. Phys. Lett.*, **81**, 319 (2002).

[88] Xiong G C *et al., Solid State Commun.*, **97**, 599 (1996).

[89] Ju H L *et al.*, *Phys. Rev. B*, **51**, 6143 (1995).

[90] Schiffer P *et al.*, *Phys. Rev. Lett.*, **75**, 3336 (1995).

[91] Hwang H Y, Cheong S-W,Ong N P and Batlogg B, *Phys. Rev. Lett.*, **77**, 2041 (1996).

[92] De Teresa J M, Ibarra M R, Blasco J, García J, Marquina C, Algarabel P A, Arnold Z, Kamenev K, Ritter C and von Helmolt R, *Phys. Rev. B*, **54**, 1187 (1996).

[93] Millis A. J., Littlewood P. B. and Shraiman B. I., *Phys. Rev. Lett.*, **77**, 175, (1996).

[94] Röder H. , Jun Zang and Bishop A. R., *Phys. Rev. Lett.*, **76**, 1356, (1996).

[95] Lee J. D. and Min B. I., *Phys. Rev. B*, **55**, 12454, (1997).

[96] Sboychakov A. O., *et al.*, *J. Exp. Theor. Phys.*, **95**, 753, (2002).

[97] Alexandrov A. S. and Bratovsky A. M., *J. Phys.: Condens. Matter*, **11**, 1989–2005, (1999).

[98] Nagaev E. L., *Phys. Letters A*, **258**, 65–73, (1999).

[99] Alexandrov A. S. and Bratovsky A. M., *J. Phys.: Condens. Matter*, **11**, L531–L539, (1999).

[100] Alexandrov A. S. and Bratovsky A. M., *Phys. Rev. Lett.*, **82**, 141, (1999).

[101] Nagaev E. L. *Phys. Rev. Lett.*, **84**, 2042, (2000).

[102] Horsch P., *et al.*, *Phys. Rev. B*, **59**, R14149, (1999).

[103] Banista C, *et al.*, *Phys. Rev. B*, **58**, R14689, (1998).

[104] Yi H. and Lee S., *Phys. Rev. B*, **60**, 6250, (1999).

[105] Yunoki S., *et al.*, *Phys. Rev. Lett.*, **80**, 845, (1998).

[106] Saitoh T., *et al.*, *Phys. Rev. Lett.*, **62**, 1039, (2000).

[107] Kebin Li, *et al.*, *J. Phys. Condens. Matter*, **10**, 4315–4322, (1998).

[108] Emin D., *Phys. Rev. B*, **48**(8), 13691, (1993).

[109] Perroni C. A., *et al. Phys. Rev. B*, **64**, 144302, (2001).

[110] Perroni C. A., *et al. Phys. Rev. B*, **66**, 184409, (2002).

[111] Bibes M., Valencia S., Balcells L.I., Martinez B., Fontcuberta J., Wojcik M., Nadolski S, Jedryka E., *Phys. Rev. B*, **66**, 134416, (2002)

[112] McIlroy D.N., Waldfried C., Zhang J., Choi J.-W., Foong F., Liou S.H., Dowben P.A., *Phys. Rev. B*, **54**(24), 17438, (1996).

[113] Maurice J.L., Pailloux F., Barthélémy A., Durond O., Imhoff D., Loynett R., Rocher A., Contout J.P., *Phil. M.*, **83**(28), 3201, (2003).

[114] Ju H.L., Nam Y.S., Lee J.E., Shin H.S., *J. Mag. Mag. Mat.*, **219**, 1, (2000).

[115] Vlasko-Vlasov V.K., Lin Y., Welp U., Crabtree G.W., Miller D.J. and Nikitenko V.I., *J. Appl. Phys.*, **87**(9), 5828, (2000).

[116] Millis A.J., Darling T., Migilori A., *J. Appl. Phys.*, **83**, 1588, (2000).

[117] Izumi M., Konishi Y., Nishihara T., Hayashi S., Shinohara M., Kawasaki M., Tokura Y., *Appl. Phys. Lett.*, **73**, 2497, (1998).

[118] Razavi F.S., Gross G., Habermeier H.U., Lebedev O., Amelinckx S., van Tendeloo G., Vigliante A., *Appl. Phys. Lett.*, **76**, 115, (2000).

[119] Vengails B., Maneikis A., Anisimovas F., Butkuté R., Dapkus L., Kindury A., *J. Mag. Mag. Mat.*, **211**, 35, (2000).

[120] Bibes M., Balcells L.I., Valencia S., Fontcuberta J., Wojcik M., Jedryka E., Nadolski S., *Phys. Rev. Lett.*, **87**(6), 067210, (2001).

[121] Kawasaki M., Takahashi K., Maeda T., Tsuchiya R., Shinohara M., Ishiyama O., Yonezawa T., Yoshimoto M. and Koinuma, H., *Science*, **266**, 1540, (1994).

[122] Zhang J., Tanaka H., Kanki T., Chou J.C., Kawai T., *Phys. Rev. B*, **64**, 184404, (2001).

[123] Yuan Q., *Phys. Rev. B*, **70**, 066401, (2004).

[124] Pradhan A.K.,Sahu D.R., Roul B.K., Feng Y., *Appl. Phys. Lett.*, **81**, 3597 (2002).

[125] Miniotas A., Vailionis A., Svedberg E.B., Karlsson U.O., *J. Appl. Phys.* **89**, 2134, (2001).

[126] Gupta A., Gong G.Q., Gang Xiao, Duncombe P.R., Lecoeur P., Trouilloud P., Wang Y.Y., Dravid V.P. and Sun J.Z., *Phys. Rev. B*, **54**, R15629, (1996).

[127] Li X.W., Gupta A., Gang Xiao and Gong G.Q., *App. Phys. Lett.*, **71**(8), 1124, (1997).

[128] Phillips J.C., *Phys. Rev.* **133A**, 1020 (1964).

[129] Tedrow P.M. and Meservey R. *Phys. Rev. B*, **7**, 318, (1973).

[130] Park J.-H., *et al.*, *Phys. Rev. Lett.*, **76**, 4215 (1996).

[131] Ziese M., Sena S.P. and Blythe H.J., *J. Mag. Mag. Mat.*, **202**, 292-300, (1999).

[132] Yamanaka M. and Nagaosa N., *J. Phys. Soc. Japan*, **65**, 3088, (1996).

[133] Yeong-Ah Soh, Aeppli G., Blamire M.G. and Mathur N.D., *J. Appl. Phys.*, **87**(9), 6743, (2000).

[134] Kwon C., Robson M.C., Kim K.C., Gu J.Y., Lofland S.E., Bhagat S.M., Trajanovic Z., Rajeswari M., Ventkatensan T., Ktartz A.R., Gomez R.D., Ramesh R., *J. Mag. Mag. Mat.*, **172**, 229, (1997).

[135] Lecoeur P., Trouilloud P.L., Xiao G., Gupta A., Gong G.Q. and Li X.W., *J. Appl. Phys.*, **82**, 3934 (1997).

[136] Ashcroft and Mermin, *Solid State Physics*, Thomson Learning, (1976).

[137] Hecht, E., *Optics*, Third edition, Addison-Wesley, (1998).

[138] Gervais, F., "High Temperature infrared reflectivity spectroscopy by scanning interferometry", edited by K.J. Button, New York: Academic Press, chapter 7 ,279-339, (1983).

[139] Mertz, L., "Auxiliary Computation for Fourier Spectroscopy." *Infrared Phys.*, **7**, 17–23, (1967).

[140] Vopsaroiu *et al.*, *Phys. Rev. B*, **70**, 214423, (2004)

[141] Almaz Optics, Inc., *http://www.almazoptics.com/KRS-5.html*

[142] Granovsky A. B., Inoue M., *Journal of Magnetism and Magnetic Materials*, **272-276**, e1601-e1605, (2004).

[143] Souche Y. and Wagner E., *http://lab-neel.grenoble.cnrs.fr/themes/micro/Imag1.htm♯toto1*

[144] MMR Technologies Inc. *http://www.mmr.com/jt.htm*

[145] Crystan Ltd. *http://www.crystran.co.uk/*

[146] Marques R. F. C., *et al.*, *IEEE Transactions on Magnetics*, **38**, 5, (2002).

[147] Marques R. F. C., *et al.*, *Journal of Magnetism and Magnetic Materials*, **226–230**, 812–814, (2001).

[148] Private communication with Prof. L. Cohen from Imperial College, London.

[149] Sukhorokov Yu.P., Gáshina E.A., Belevtsev B.I., Loshkareva N.N., Vinogradov A.N., Rathnayaka K.D.D., Parasiris A.and Naugle D.G. *J. Appl. Phys.*, **91**, 4403, (2002).

[150] Linke, J.L., *MSc. dissertation*, The University of York, (2005).

[151] Litvinchuk A.P., Chen S.Y., Iliev M.N., Chen C.L., Chu C.W. and Popov V.N., *Physica C*, **361**, 234, (2001).

[152] Zhang Z.M., Choi B.I., Flik, M.I., Anderson, A.C., *J. Opt. Soc. Am. B*, **11** (11), 2252, (1994).

[153] Abrashev M.V., Litvinchuk A.P., Iliev M.N., Meng R.L., Popov V.N., Ivanov V.G., Chakalov R.A., C. Thomsen, *Phys. Rev. B*, **59** (6), 4146, (1999).

[154] Spitzer W.G., Miller C.R., Kleinman D.A., Howarth L.E., *Phys. Rev.* **126** (5), 1710, (1962).

[155] Barker Jr., A.S., *Phys. Rev.*, **145** (2), 391, (1966).

[156] Kamarás, K., Barth, K.-L., Keilmann, F., Henn, R., Reedyk, M., Thomsen, C., Cardona, M., Kircher, J. Richards, P.L., Stehlé, J.-L., *J. Appl. Phys.*, **78** (2), 1235, (1995).

[157] Petzelt J., Ostapchuk T., Gregora I., Rychetsky I., Hoffmann-Eifert S., Pronin A.V., Yuzyuk Y., Gorshunov B.P., Kamba S., Bovtun V., Pokorny J., Savinov M., Porokhonskyy V., Rafaja D., Vanek P., Almeida A., Chaves M.R., Volkov A.A., Dressel M., Waser R., *Phys. Rev. B*, **64**, 184111, 2001.

[158] Orera V.M., Trinkler L.E., Merino R.I., Larrea A. , *J. Phys. Cond. Mat.*, **7**, 9657, (1995).

[159] Suda J., Mori T., Saito H., Kamishima O., Hattori T., Sato T., *Phys. Rev. B*, **66**, 174302, (2002).

[160] Kittel C., Einführung in die Festkörperphysik, 8th edition, Oldenbourg Verlag, 1989.

[161] Shirane G. and Yamada Y., *Phys. Rev.*, **177**, 858, (1969).

[162] Private communication with Prof. G. Gehring from the University of Sheffield.

[163] Dörr K, *J. Phys. D: Appl. Phys.*, **39**, R125-R150,(2006).

[164] Gross R *et al.*, *J. Magn. Magn. Mat.*, **211**, 150, (2000).

[165] http://www.rijnh.nl/molecular-and-laser-physics/felix/n2/f1234.htm

[166] Taylor A.J., Averitta R.D., Demsara J., Lobadb A.I., Sarraoa J.L., Trugman S.A., *Physica B*, **312-313**, 640, (2002).

[167] Private communication with Prof. G. Gehring at the University of Sheffield.